UNIVERSITÀ DI PARMA

Dottorato di Ricerca in Scienza e Tecnologia dei Materiali

Ciclo XXX

Development of Contacts for CZT-based X and Gamma Ray Detectors

Coordinatore:
Chiar.mo Prof. Enrico Dalcanale

Tutor:
Chiar.mo Prof. Andrea Zappettini

Dottorando: Manuele Bettelli

Anni 2014-2017

Outline

Acknowledgments

First of all I would like to express my gratitude to my supervisor Andrea Zappettini, for the support, the intellectual direction and the patience throughout my student career.

I would also like to thank the other members of my research group: Maurizio Culiolo, Davide Calestani, Michela Janni, Marco Villani and Nicola Coppedè. They were always present whenever I needed help. I would also like to thank all the people of IMEM institute that have shared their time with me.

I would also like to show my gratitude to Due2lab members: Giacomo Benassi and Nicola Zambelli. They were important landmarks during my PhD.

Thanks to the following people for the use of their facilities and generous time and effort: Andrea Santi, Maura Pavesi, Leonardo Abbene, Fabio Principato, Matt Veale, Giuseppe Allodi and Gianfranco Galli.

Thanks to my fellow students, the “Mensa” group, my colleagues and my university friends for their friendship and support in these years.

I especially thank my parents Fausto and Anna, my sister Lisa, my grandmother Maria and my girlfriend Elena for their love, their encouragement and their continuous support during my studies.

Finally I want especially show my gratitude to my friends of Barco and environs for all the moments of leisure and happiness spent together.

Introduction

Nowadays ionizing radiation detectors are widely employed in several application fields (Figure I-1). These include medical imaging (CT, SPECT), environmental monitoring (control of the background radiation and contaminated areas), homeland security (cargo and luggage control) and astrophysics (study of x- and γ-ray emission from celestial bodies).

In last decades the employment of semiconductor devices is getting more and more important and they have replaced classical scintillators in various application fields. Semiconductor based detectors can achieve better energy resolution thanks to the direct conversion of incident radiation into electrical signal. In addition semiconductor materials, compared to scintillators, allow to achieve higher spatial resolution in imaging detectors. These characteristics make semiconductors the more advance technology for radiation detection of x- and γ-photons in the energy range 1 keV - 10 MeV [1] [2] [3].

Figure I-1. Applications of ionizing radiation detectors

In 1945, Van Heerden [4] demonstrated that silver chloride crystals, when cooled to low temperatures, were capable of detect γ-rays, α-particles and β-particles. Taking into account the key demands of radiation detector applications, several semiconductor materials have been studied after that year. The main requests for such materials are: I) high stopping power even for energetic radiations; II) opportunity to make spectroscopy; III) imaging capability with good spatial resolution; IV) possibility to operate at room temperature; V) excellent mechanical rigidity to fabricate compact and stable systems.

Among the compound semiconductors Cadmium Zinc Telluride (CdZnTe or simply CZT) meets the listed above demands. CdZnTe represents the best compromise in terms of energy efficiency, high atomic number, resistivity, and room temperature operation capability.

In particular its attractive characteristics are:

- Bandgap of 1.57eV, that is at the same time wide enough to make high resistivity possible and narrow enough to ensure low pair-production energy.
- Mean atomic number of 50, which means a good stopping power also for high-energy radiation.
- Electron mobility-lifetime product sufficiently high.
- Possibility to growth large single crystals.

For these reasons with CZT material nowadays high performance detectors with good energy resolution, high detection efficiency and room temperature operation capability can be fabricated [2].

Unfortunately CZT shows some issues not yet overcome by the scientific community. In my PhD thesis I have focused my effort on the study of *contacts*. The two main aspects that I have addressed are constituent metal and electrode geometry. The constituent metal determines the contact type, blocking or ohmic nature of contacts are primarily dependent on the deposited metal. Comprehensive study of the band structure, electrical properties and physicochemical characteristics of the metal-semiconductor interface carried out on different metals is reported in this thesis. The other important aspect, covered during my PhD, is the geometric configuration of electrodes. With appropriate geometries, we are able to recover the deterioration of spectroscopic performance due to poor hole transport properties. Moreover, for each specific application, some contact layouts can be more performing than another, depending on the properties required such as collection efficiency, energetic resolution, imaging capability, etc.

This thesis includes some efforts and results, reached at IMEM-CNR and Physics Department of the University of Parma during the last three years, on devices for radiation detection applications.

This thesis starts with an overview of semiconductor-based detectors and radiation-matter interactions. Basic radiation detection physics is given and CZT strength and weaknesses are reported.

Chemical and physical properties of CZT, its main growth techniques and its typical defects are detailed in chapter 2.

Chapter 3 is about contacts. It sequentially reports electroless deposition technique, band theory of contacts and their current-voltage characteristics. The last part of this section theoretically treats the influence of electrode layout.

Readout electronic allows to convert the induced charge generated by ionizing radiations in a digital signal easily interpretable by a PC. Analog and digital approach and ASIC systems are the subjects of chapter 4.

Experimental setups used for measurements of this thesis are described in chapter 5. Some are located in IMEM CNR laboratory and others have been used thanks to collaboration with other research groups. Part of the instrumentations was developed and assembled by the author of this thesis.

In the sixth part of the work the detector preparation is presented. Preparation and characterization of CZT detectors fabricated at IMEM-CNR institute are treated. This part describes all the detector fabrication processes carried out by undersigned, these processes include: cutting, lapping and polishing, contact deposition and passivation.

Results and discussion of experiments carried out during my PhD are reported in chapter 7. Characterizations including I-V characteristic, resistivity measurement, adhesion test, transport

properties measurement and spectroscopic performance were performed on contacts deposited thanks to electroless depositions developed by undersigned. Investigation of charge sharing effects on small pixel arrays is reported and digital corrections are evaluated even under high radiation flux. Also, during my work, a complete prototype was developed, a prototypal UAV (Unmanned Aerial Vehicles) equipped with a CZT radiation detector realized in collaboration with RimLab (engineering group of Parma University) described at the end of chapter 7.

The last chapter summarizes the results achieved in the experiments and lists issues that deserve a better deepening.

1 Semiconductor-based X- and γ-ray detectors

Development of new materials more and more performing results in a continuous evolution of X and γ ray detectors for energy-dispersive spectroscopy. These detectors can be conveniently applied in several fields (*Figure 1-1*), for example medical diagnostic, astrophysics, cosmic radiation sources study, national security, airport baggage control, food-control scanner, etc.

Figure 1-1. Device applications

Scintillators were firstly employed in these fields, they work thanks the photon absorption and then conversion from X-radiation to light radiation through organic or inorganic crystals. A photomultiplier, after the first process (scintillation), collects the light pulses in electric pulses. The amplitude of these signals is directly correlated with photon energy, it is then possible to use these devices as X and γ ray detectors.

Scintillators have unfortunately some handicap that limit their possible applications:

- It is quietly easy obtain large single crystal but the absorption coefficient is related with maximum dopant concentration. This value (usually quite low) limits their conversion efficiency.
- Photon conversion in scintillators, contrary to semiconductors, happens in two steps decreasing the total process efficiency and then detector resolution.
- Statistic of light radiation generation is subjected to great fluctuation due to scattering processes of light.

Aforementioned limits are intrinsic, so that new solutions and particularly new materials for detection of high energy radiations were considered: semiconductors.

In the case of semiconductor detectors the detection mechanism is fundamental different. Photoelectric absorption in semiconductors is performed in a single step process where the high-

energy photon interacts with matter and releases free carriers proportionally to its energy. Free carriers drift in an applied electric field and are collected by electrodes. Carriers' flight induces at the electrodes a current transient whose time-integral gives the X-photon energy. Furthermore, semiconductor absorption depends not on the impurity concentration but on the material density, thus resulting efficiency is far greater than scintillators (in same condition of volume and density).

In the light of these points, semiconductors are employed more and more frequently instead of scintillators. The main advantages are in particular:

- High absorption efficiencies
- Better energetic resolutions
- Compact devises
- Possibility to realize high spatial resolution devices (impossible for light scattering in scintillators).

1.1 Nuclear radiations

Semiconductor detectors can detect different type of radiation, electromagnetic waves or sub-atomic particles and can be either uncharged or charged. Protons, β-particles (electrons and positrons) and alpha particles are included in charged radiations; while γ-rays, X-rays and neutrons are included in uncharged radiations. All these radiations are also known as ionizing radiations because they carry enough energy to liberate electrons from atoms or molecules, thereby ionizing them.

Uncharged radiation can be produced in different ways, such as:

- Relaxation of an excited atom to ground state (Ionization or emission of an orbital electron)
- Spontaneous decay of heavy nucleus (alpha particle, fission fragments or neutrons)
- Relaxation to a lower energy state of excited nucleus (γ-rays)
- Annihilation of electrons or positrons (γ-rays)

The typical energy of ionizing radiation is different from type to type:

- Ionizing electromagnetic radiation has a wide spectrum, from few keV for X-ray up to tens of MeV for cosmic radiation
- Alpha particles typical range is 3 to 7 MeV
- Neutron (fast ones) energy is from 10keV to 15MeV
- β radiation comes to some keV to 100MeV

1.2 Radiation-matter interaction

For applications it is important that radiation is detected in the relevant spectrum of energy, so that interaction length is the parameter that allows to calculate the detector thickness for the interested radiation energy.

Obviously charged particles (α and β) have a strong interaction with matter and typically are stopped and detected in the firsts hundreds microns of material. Neutrons have low interaction with typical semiconductors used for detectors, so a converter material is necessary to convert neutrons into γ rays or alpha particles. These are easily detected by the semiconductor detector.

Here we concentrate on the interaction of electromagnetic radiation with matter that can happen according to the four mechanisms described below.

1.2.1 Photoelectric absorption

In this process the incident photon is completely absorbed by a bonded electron, to which transfers all its energy (Figure 1-2). Excited electron (called photoelectron) interacts quickly with the crystalline lattice through Coulomb's interactions that generate electron-hole pairs. The number of pairs is proportional to the initial photon energy and depends on the mean formation energy for electron-hole pair that is different for each semiconductor. In this process the entire photon energy is deposited in the detector and to obtain its energy, it is enough to measure the whole photo-generated charge. For this reason photoelectric absorption is the ideal process for X and γ spectroscopy. Cross section is directly proportional to interaction probability and follows the following law:

$$\sigma_{fotoelettrico} = 4\sqrt{2}\sigma_T \alpha^4 Z^5 \left(\frac{m_e c^2}{\nu}\right)^{\frac{7}{2}} \quad 1\text{-}1$$

$$\sigma_T = \frac{8\pi}{3}\left(\frac{e^2}{4\pi\epsilon_0 m_e c^2}\right)^2 \quad 1\text{-}2$$

Where σ_T is Thomson cross section, α is fine-structure constant, Z is atomic number of lattice atoms, m_e is electron mass, e is electron charge, c is light speed, ν is radiation frequency and ϵ_0 is vacuum permittivity. Because cross section is proportional to the fifth power of Z semiconductors with high atomic number are preferred; because cross section is proportional to $\nu^{-7/2}$: photoelectric absorption decrease strongly when energy of incident photon increase.

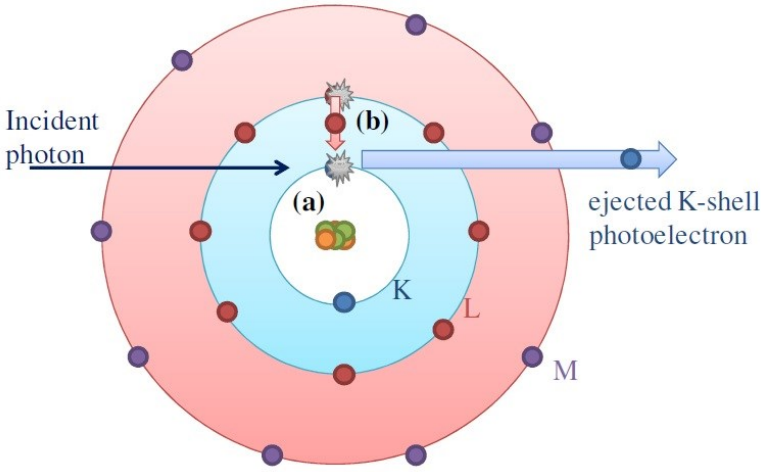

Figure 1-2. Photoelectric effect, (a) the ejection of K-shell electron and (b) jumping of L-shell electron to fill the hole [5]

1.2.2 Elastic scattering

Rayleigh scattering is the a process where a photon is elastically diffused inside the material (without energy losses) at low angle with respect to incident direction. No energy deposited means no electric signal detected from the device, therefore this mechanism will be neglected in the following.

1.2.3 Compton scattering

Inelastic scattering happens when incident photon energy is far greater than the electron boundary energy (Figure 1-3). If this energy is sufficiently high we can neglect the force that bonds electron and nucleus and so, we can consider the electron a free electron. Part of photon energy is transferred to the electron and the photon is deflected to an angle θ in a new direction. The energy transferred to the electron depends on the scattering angle that can change from 0 (with $\theta = 0$) to a maximum value when $\theta = \pi$.

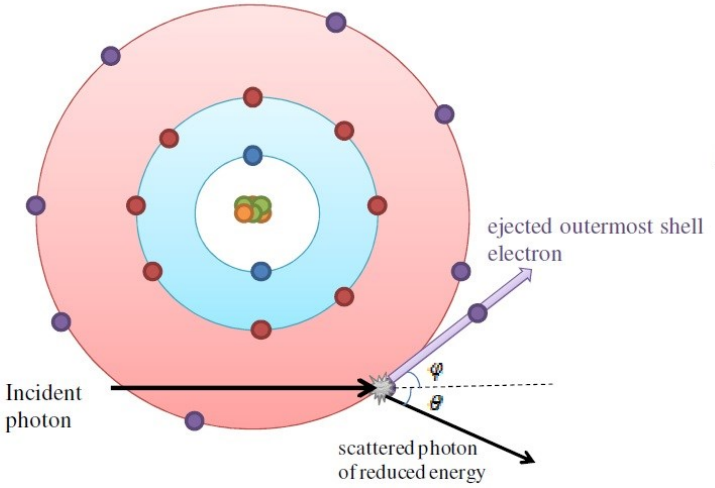

Figure 1-3. Compton scattering mechanism [5]

The scattered electron interacts with crystalline lattice generating an amount of electron-hole pairs proportional to its energy. Random energy is deposited at the detector coherently with random scattering angle, for this reason gamma spectroscopy is not possible under Compton interaction. Cross section (σ) for a single electron can be integrated for all scattering angles (Figure 1-4), resulting value depends only on the incident photon energy (Klein-Nishina law [6]):

$$\sigma_{Compton}^{single\ e} = 2\pi r_0^2 \left\{ \frac{1+\epsilon}{\epsilon} \left[\frac{2+2\epsilon}{1+2\epsilon} - \frac{\ln(1+2\epsilon)}{\epsilon} \right] + \frac{\ln(1+2\epsilon)}{2\epsilon} - \frac{1+3\epsilon}{(1+2\epsilon)^2} \right\} \quad 1\text{-}3$$

$$\epsilon = \frac{E}{m_e c^2} \quad 1\text{-}4$$

Where r_0 is classical electron radio ($r_0 = \frac{e^2}{m_e c^2} = 2.8 * 10^{-13} cm$), m_e is electron mass, e is electron charge and E is incident-photon energy.

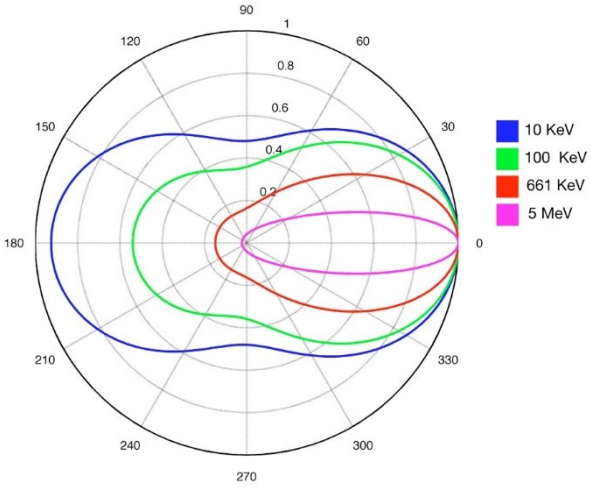

Figure 1-4. Plot of Klein-Nishina differential for Compton scattering cross section at different energies [7]

The atomic number Z is equal to electrons number present in that atom, then the total Compton cross section is:

$$\sigma_{Compton} = Z\,\sigma_{Compton}^{single\ e} \qquad 1\text{-}5$$

The Compton cross section depends on Z but the power law is very weak compared to the photoelectric one. Semiconductors with high atomic number have better ratio between photoelectric and Compton probability, for this reason semiconductors with high atomic number are preferred.

1.2.4 Electron-positron pair production

When a high-energy incident photon interacts with the nuclear electrical field, e^+e^- pair created after its disappearance (Figure 1-5). A minimum of incident energy is required for this process, photon energy superior of the mass of two electrons (1022keV) is necessary. The excess energy is transferred to the electron or positron as kinetic energy. Now the positron annihilates with another electron producing two 0.511 MeV photons that interact with the semiconductor according to the processes described above.

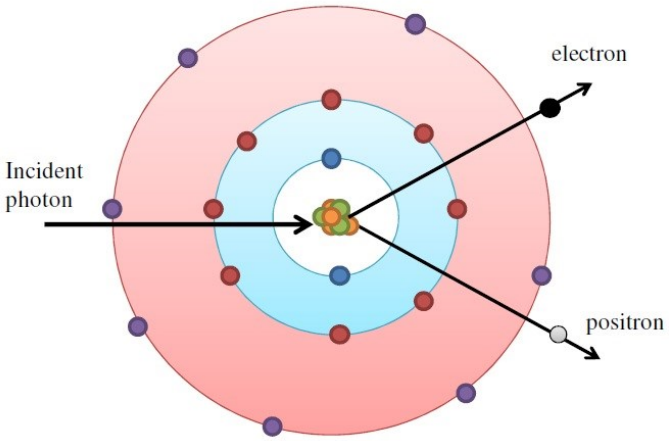

Figure 1-5. Schematic pair production mechanism [5]

1.2.5 Global absorption

Interaction processes between radiation and matter are competitive and total absorption is the result of all the described processes (Figure 1-6). Accurate material selection is important in order to obtain good detectors.

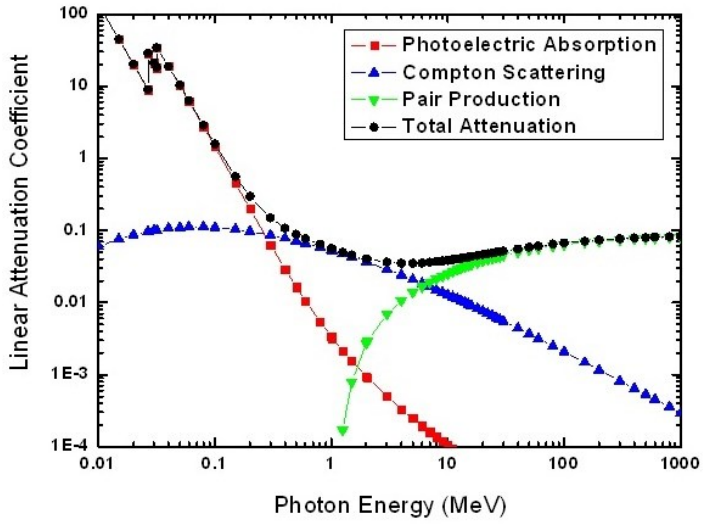

Figure 1-6. The behaviors of the attenuation coefficient of CdTe/CZT for photoelectric absorption, Compton scattering, and pair production [8]

The energy-range of photons studied in this thesis focuses is 10 keV - 1 MeV, so, photoelectric absorption and Compton scattering are the main processes involved. Both processes depends on photon energy and atomic number. From the respective cross sections for interested interaction follows that, to maximize photoelectric absorption at the expense of the Compton scattering high Z it is necessary. Compared with typical semiconductors for detector manufacture, CZT and CdTe have high atomic number (the mean value is around 50). In Figure 1-7 it is possible to understand the strong relation between attenuation coefficient and atomic number for different semiconductors.

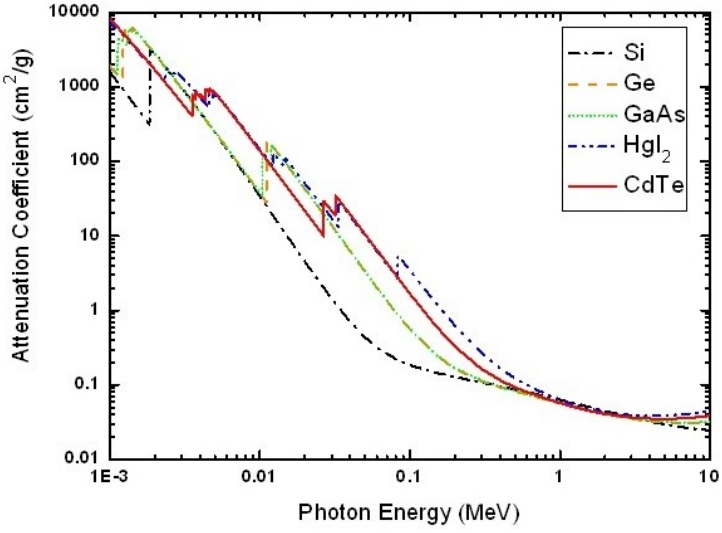

Figure 1-7. Attenuation coefficients as a function of photon energy for different materials [8]

1.3 CZT for detectors

In this chapter it is described which are the main characteristics that a semiconductor should have to became a good radiation detector.

These characteristics are:

- High atomic number: in the previous chapter it was shown that cross section for photoelectric absorption goes as Z^5.
- A bandgap wide enough (more than 1.4eV) to decrease thermally generated charge. High resistivity (more than $10^9 \Omega cm$) allows low leakage current and so low electric noise. The material resistivity depends on bandgap energy and doping: wide bandgap and appropriate doping lead to high resistivity materials.
- A bandgap narrow enough to limit electron-hole pairs energy production (less than 5eV). Large number of produced pairs decrease statistic fluctuation and increase signal-noise ratio (energetic resolution is increased).
- High $\mu\tau$ product, where μ is mobility and τ is mean lifetime of carriers. The mean free path $\lambda = \mu\tau E$ of carriers must be comparable (better if bigger) with detector thickness; in order to obtain high λ with relatively low electric field value (E) $\mu\tau$ product must be high. Condition on λ is necessary to minimize charge losses inside the device and maximize induced current at electrodes.
- Good crystal quality. To minimize recombination and trapping of carriers large single crystals with low defects density are required. $\mu\tau$ product is strongly influenced by material quality. In addition a good material without extended defects are also mechanically stable and stronger, this characteristic is fundamental in several application of radiation detectors.

At the light of characteristics listed above, some materials seem to be particularly interesting, such as germanium, silicon, gallium arsenide, silicon carbide, thallium bromide, cadmium telluride and cadmium zinc telluride.

Ge and Si had been historically the first materials employed to realize spectroscopic detector. The low value of their bandgap ($E_{gap}^{Si} = 1.11eV$, $E_{gap}^{Ge} = 0.66eV$) is a double-edged sword: whilst allows the realization of detector with extremely high resolution, does not allow to employ them at room temperature (high thermal generation of pairs) and continuous freezing at cryogenic temperature is required (typically liquid nitrogen). In order to collect carriers in silicon detector it is also necessary to generate a depletion region with appropriate doping, so the active region of silicon detectors is in the range of millimeter fractions [9]. This reason together with its low atomic number results in a low absorption efficiency of high-energy radiation.

Bandgap ($E_{gap}^{SiC} = 3.0eV$) and mechanical resistance make SiC really an interesting material for radiation detector, particularly in dosimetry applications because silicon and carbon fit well atomic number of living beings [10]. Sadly high bandgap results in high energy for pairs production (low signal-noise ratio) and low Z doesn't allows the creation of efficient detector for high-energy radiation.

Interesting material for detectors realization is GaAs; it has optimal bandgap for room temperature use, large Z, and can be obtained in large crystals. Unfortunately, GaAs crystals still present a large concentration of defects, that shield the externally applied electric field for detectors whose thickness is larger [9].

TlBr exhibits weak ionic conductivity at room temperature, which negatively affects the leakage current of detectors and leads to device degradation over time.

Cadmium telluride (CdTe) and mercuric iodide (HgI_2) are the main materials that satisfy the above criteria. HgI_2 has disadvantages in terms of stability and toxicity [9]: this semiconductor requires encapsulation to prevent deterioration of the crystal surfaces on air exposure over periods of months. In the following table are shown the important characteristics described above for typical semiconductors for radiation detectors.

Compound	Si	Ge	GaAs	SiC	CdTe	CZT	HgI_2	TlBr
Mean atomic number	14	32	32	10	50	49.1	62	58
Mean atomic mass (u)	28.09	72.59	72.34	20.05	120	114.71	151	142
Density(g/cm^3)	2.33	5.32	5.32	3.21	5.85	5.78	6.4	7.56
Bandgap (eV)	1.12	0.66	1.42	3.0	1.5	1.57	2.13	2.68
Energy of pair production (eV)	3.65	2.85	4.2	~8.5	4.43	4.64	4.2	-
Electrons mobility (cm^2/Vs)	1500	3900	8500	1000	1100	1100	100	50
holes mobility (cm^2/Vs)	450	1900	400	100	100	50-80	4	5
$\mu\tau$ electrons (cm^2/V)	2-5	5	10^{-4}	10^{-3}	10^{-3}	10^{-3}	10^{-4}	$5\ 10^{-4}$
$\mu\tau$ holes (cm^2/V)	1-2	2	10^{-5}	10^{-4}	$5\ 10^{-4}$	$3\ 10^{-5}$	10^{-5}	$5\ 10^{-5}$
Resistivity (Ωcm)	$2.3\ 10^5$	47	10^8	$>10^{12}$	10^8-10^9	10^{10}	10^{10}	-
Thickens to absorption (90%) of 60keV radiation (cm)	130	2.6	2.6	~140	0.5	0.5		-

Table 1.1. Property of some important semiconductors for X and γ rays detectors [11] [12]

CdTe and CdZnTe represent the best compromise in terms of energy efficiency, high atomic number, resistivity, and room temperature operation capability:

- Bandgap of 1.57eV that is in the right value to have at the same time a low pair-production energy and high resistivity.
- Mean atomic number of 50, that means a good stopping power also for high energy radiation.
- Good electron mobility.
- Possibility to growth large single crystal (even with much more difficulties in the case of Si and Ge).

1.3.1 CZT detector applications

Homeland security is one of the growing application field [13]. The fear of terrorist attacks, airplane security, the increase of traveling people and object shipping all over the world are some of the main reasons for the research and the realization of detectors with fast and accurate response. Realization of increasingly fast and safety body and baggage scanner is critical for airport security [14]. The need of a response in a few seconds is necessary especially considering actual volumes of people and goods that every day cross the main airports. The use of highly sophisticated devices can reduce scanning time and also the total dose requested for dangerous object revelation.

Another important application field is medical imaging. Semiconductor detectors can be employed for medical devices with far greater performances compared with scintillators. SPECT (Single Photon Emission Computed Tomography) [15] or CT (Computed Tomography) [16] are techniques that are becoming more and more common in the preventative medicine or surgical applications and the use of new and more sensitive detectors could be a great help in the cure and detection of diseases.

Environmental monitoring is historically performed using Geiger Mueller counters, but this equipment are not able to acquire energy information of incident radiation, so the nature of contaminant sources remains unknown. Thus, the use of spectroscopic detectors would be highly welcome in this filed. Radiation monitoring is divided in two main applications: control of background radiation (controlling natural X and γ ray emitted by the soil) [17] and control of areas around nuclear facilities (where constant control is need to avoid poisonings) [18].

CZT has always been a focus material in the detection of γ-ray emission from sources in the deep space. Reduce the dimensions and weight of radiation detector is crucial point for astronomical equipment. It was demonstrated that the use of CdZnTe detectors is extremely convenient for such applications.

2 CZT chemical and physical characteristics

$Cd_{1-x}Zn_xTe$ (CZT) is obtained from CdTe in order to improve material characteristics for the detector realization with a little addition of zinc. Atomic number of CZT elements is high enough to allow a strong photoelectric absorption ($Z_{Cd} = 48, Z_{Zn} = 30, Z_{Te} = 52$), the mass attenuation coefficient of CZT is 4-5 times that of Ge and even 100 times that of silicon.

$Cd_{1-x}Zn_xTe$ is a ternary compounds where the zinc amount is in range 0.02:0.2. With this range the band gap is larger than 1.5 eV (if zinc amount, x, is 10% the exact value of band gap is 1.572eV) that allows a very low leakage current at room temperature. Anyway, this value, is sufficiently low to allow the photogeneration of a great number of electron-hole pairs and then to obtain detectors with a good signal-noise ratio and accordingly high energetic resolution.

One of the most important novelty of CZT (compared to CdTe) is that it is less prone to polarization effects [9], the polarization is a phenomenon related to carrier trapping by trapping centers (impurities and defects): trapped carriers distort electric field in the device resulting in a bad carrier collection that change during the time [19] [20] [21]. This is a very important issue when the detector undergoes long working times. Also, because of polarization effects, CdTe detectors can hardly be thicker than 2mm.

CZT it is also more rigid than CdTe, this characteristics is important for many applications.

Another point of strength of CZT is that, with the Zn addition, the band gap is increased and with it resistivity too. A typical value of CZT resistivity is in order to $10^{10}\Omega$cm. With these values the leakage current is very low also with typical electric field values of hundreds V/mm, that increase the carriers collection and the signal *shaping* speed.

2.1 Crystalline structure

CdTe and CZT have the same crystalline structures; these crystals have a building block composed by two interpenetrating face center cubic (*FCC*) sub-lattices shifted on the cell diagonal by one-quarter. In CZT Cd and Zn occupy vertexes of one of these sub-lattices and Te occupy the vertexes of the other one. The resulting structures is zinc-blende (Figure 2-1-right).

$Cd_{1-x}Zn_xTe$ can be ideally seen as CdTe where x cadmium atoms has been randomly substituted with zinc ones. The structures obtained with total cadmium substitution is also stable, in other terms CdTe and ZnTe are completely miscible (how is shown in the double lens diagram in Figure 2-1-left) but typically the Zn amount adopted for applications is not so high (2-20%). The lattice constant of CZT can be estimated with a linear interpolation from two binary compounds ($a_{CdTe} = 6.4823\text{Å}\ and\ a_{ZnTe} = 6.102\text{Å}$) with Vegard's law [22]:

$$a(\text{Å}) = 6.4823 - 0.3803x \xrightarrow{x=10\%} a(\text{Å}) = 6.44427\ (at\ room\text{-}temperature) \qquad 2\text{-}1$$

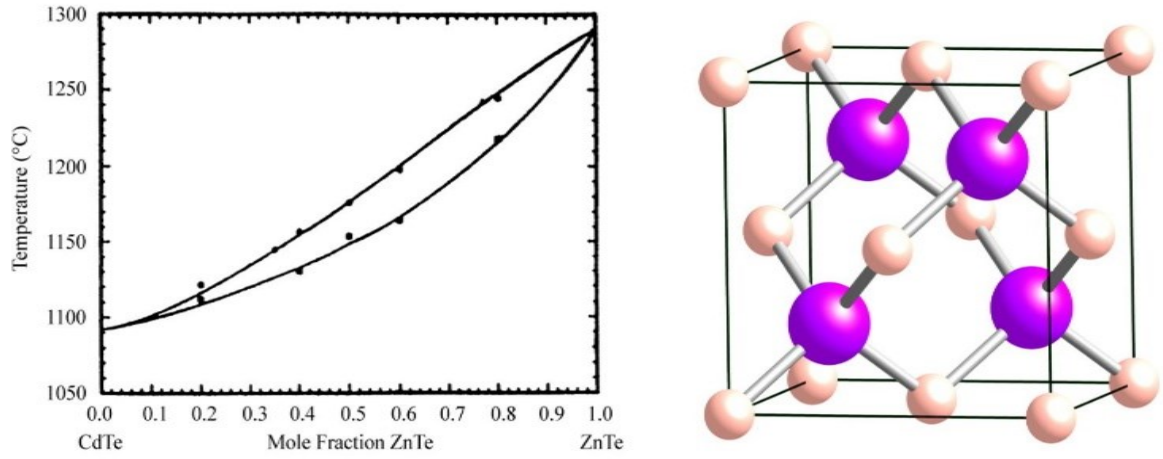

Figure 2-1. CdTe -ZnTe double lens phase diagram (left) and crystalline structure of CdTe and CZT (right) [23]

2.2 Band structure

The band structure of CZT is usually studied starting from the those of CdTe and ZnTe. These two compounds have a direct bandgap at room temperature of 1.5eV and 2.2eV respectively. In Figure 2-2 is shown the band structure of CdTe calculated with pseudopotential. The one of ZnTe is qualitatively similar.

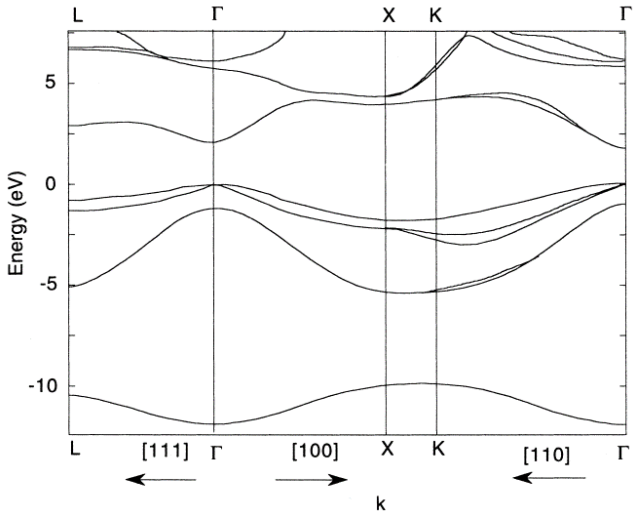

Figure 2-2. Band structure of CdTe [23]

To calculate the effective masses (m^*) of holes and electrons can be use

$$\frac{1}{m^*} = \frac{2\pi}{h^2}\frac{\partial^2 E}{\partial k^2} \qquad 2\text{-}2$$

In the spherical constant energy surface approximation, the m^* value can be achieved from the reciprocal of the curvature of the energy band calculated in $k = 0$. Effective mass for electrons is $m^*_{CdTe} = 0.11m_0$ and $m^*_{ZnTe} = 0.15m_0$ [24], instead holes value is $0.70m_0$ for heavy and $0.103m_0$ for light ones. Two values must be taken into account for holes due to the separation in valence band [25]. It is not easy perform the same calculation for CZT because the band theory is based on

periodicity of the lattice, whose assumption is violated in case of alloys because equivalent compounds (CdTe and ZnTe) are randomly disposed.

Actually, to fit well the dependence of band gap from the zinc amount (x), quadratic curvature is preferred to linear interpolation. [26]

	$E_g(x)[eV] = 1.51 + 0.606x + 0.139x^2 \xrightarrow{x=0.10} 1.572eV$	2-3

CZT with $x = 10\%$ have a typical bandgap value of $1.572eV$ at 300K. Furthermore, after an appropriate doping and an auto-compensation mechanism, the obtained compound is highly resistive. Thanks the compensation it is reasonable to assume the Fermi levels in the mid gap.

2.3 Electrical and carriers transport properties

To obtain good detectors is very important to use a semiconductor with high resistivity to limit leakage current and increase the electric field. CdZnTe resistivity is around $10^{10}\Omega$cm, this value is sufficiently high to ensure performant detectors.

Other important characteristics are μ and τ values, their contribution is more explicit in terms of mean free path ($\lambda_{n,p} = \mu_{n,p}\tau_{n,p}E$, where E is the electric field). Mean free path is the distance that the carriers can cross through the semiconductor before they are trapped and indirectly suggests the amount of charge loss inside the semiconductor during the carriers flight. Higher μτ values allow thicker detectors and good charge collection at the electrodes.

μ and τ are influenced by the band diagram, the crystalline lattice, defects, and trapping centers. The product of these transport parameters (μτ) for CZT is generally better than the parameters of other semiconductor with high Z used in X-ray detector field. However, in CZT, the μτ product for holes is 2 orders of magnitude lower than the one of electrons; the respective value at 300K are: $\mu\tau_h \sim 10^{-(4\div5)}\frac{cm^2}{V}$ and $\mu\tau_e \sim 10^{-(2\div3)}\frac{cm^2}{V}$.

This large difference between electrons and holes restrict detector performance in particular decreasing energy resolution. The most evident impacts are photopeak broadening and tailing effect [27].

Photopeak broadening is due to charge trapped in the semiconductor. To limit that it is possible to increase the applied voltage keeping in mind that contemporarily also leakage current increases. The high resistivity of CZT fortunately helps us because, on the contrary of CdTe, we can apply hundreds V/mm.

Moreover, asymmetric photopeak is frequently observed (Figure 2-3), due to the large difference of electrons and holes transport properties. This is named *tailing effects* and it is caused by the incomplete collection of holes, whose trapping decreases the signal generated at the electrode originates a tail at the low energy side of the peak. The tailing effect is more

intense in the case of more energetic radiation, because it penetrates deeper in the detector and the amount of charge loss changes according to the random penetration of each photon.

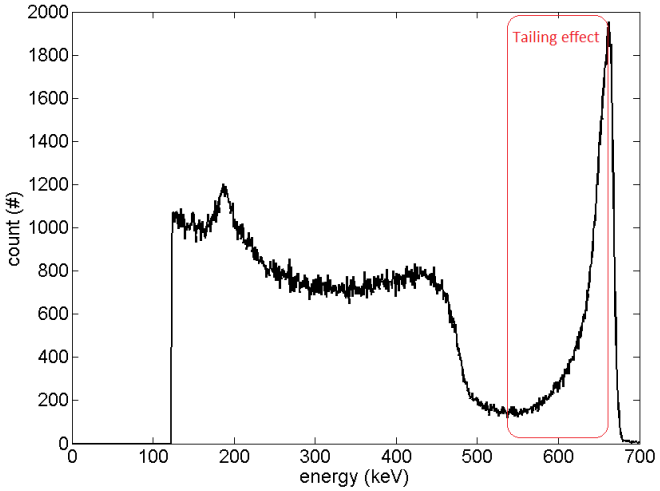

Figure 2-3. Typical CZT spectrum with tailing effect

For high-energy applications, contacts with particular geometries are necessary to reduce this effect; in particular, it is known that it is possible to dispose electrodes in a way to seriously reduce the tail. They are called single carrier geometries, and they will be discussed with more details in chapter 3.3.3.

2.4 Crystal growth

An important challenge is to obtain large CZT single crystal volumes. To have good X and γ ray detection capabilities it is essential to employ monocrystalline material because polycrystalline one has poor charge transport properties due to recombination of charge carriers at grain boundaries.

To growth monocrystalline CZT is important to use really pure precursors (Cd, Zn and Te more than 6N) and avoid contamination during the procedure. Actually, the most used techniques are traveling heater method (THM) and Bridgman (high and low pressure and boron-encapsulated vertical Bridgman). In this thesis I employed commercial THM (powered by REDLEN) and boron-encapsulated Vertical Bridgman (powered by our IMEM-CNR laboratory) crystals [28].

2.4.1 Traveling heating method

THM exploits a region of melt tellurium as solvent through which cadmium and zinc diffuse toward the solid seed of CZT where the crystal growth happens (Figure 2-4). This method is possible at ~ 600-900°C as it occurs under non-stoichiometric conditions [29]. Melt tellurium is preferred at cadmium as solvent because CdTe solubility in Cd is poor. A benefit of THM is that impurities with low segregation coefficients are confined in melt-Te zone. Industrial growers, such as Redlen, are able to produce CZT crystal with electron $\mu\tau_e$ in the order of $10^{-2}cm^2/V$ and very large single crystal volumes (110cm^3) [30].

Schematic THM growth process is shown in Figure 2-4, the tellurium-rich solvent is obtained by melting CdTe and ZnTe source materials above the seed crystal. The seed crystal is used to control nucleation, improve lattice matching, and grow crystals in the correct crystallographic

orientation. Inside the ampoule is maintained a temperature gradient to promote the element diffusion toward the seed crystal. The ampoule is moved through the heater and rotated. The rotation induces a convection current that reduces solidification at the edges and migration of zinc away from the center of the boule.

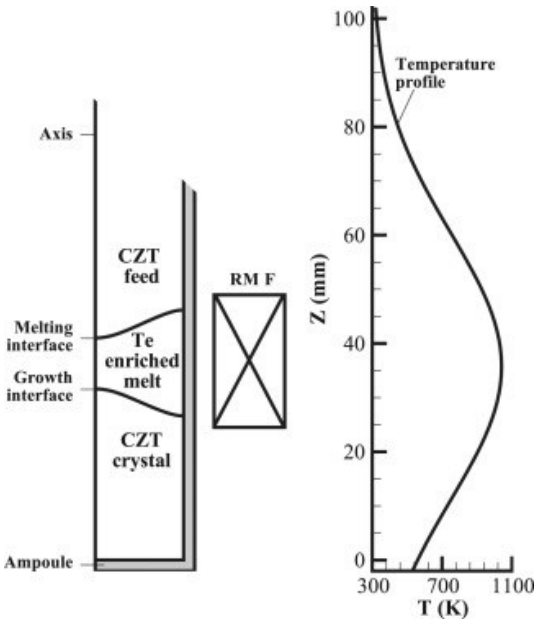

Figure 2-4. Scheme of THM growth system [31]

The main defects of crystal grown by THM are cadmium vacancies and tellurium inclusions. Cadmium vacancies are acceptors, so that in order to get high resistivity, the crystal must be compensated with an additional doping of indium or aluminum. The reason for the formation of tellurium inclusions is that when local supercooling occurs at the growth interface, tellurium could be included in the crystal. To avoid, or least reduce Te inclusions a convex growth interface must be created to promote nucleation close to ampoule wall and keep the inclusions away from the ingot center. To create this interface type it is crucial a careful control of axial/lateral heating and of the pulling speed.

2.4.2 Bridgman

Bridgman growth is a controlled freezing process occurring at the liquid-solid equilibrium condition. With the aim of producing single large crystals, growth occurs under a controlled temperature gradient that allows single nucleus growth. It is possible to charge the ampoule with single elements powdered or with a pre-synthesized compound. The *sealed* ampoule is moved in a temperature gradient that slowly solidifies the melted content in order to minimize the crystalline defects and avoid interfacial instability (Figure 2-5). Several configuration were suggested:

- Moving ampoule through the oven
- Moving oven keeping the ampoule steady
- Vertical configuration
- Horizontal configuration

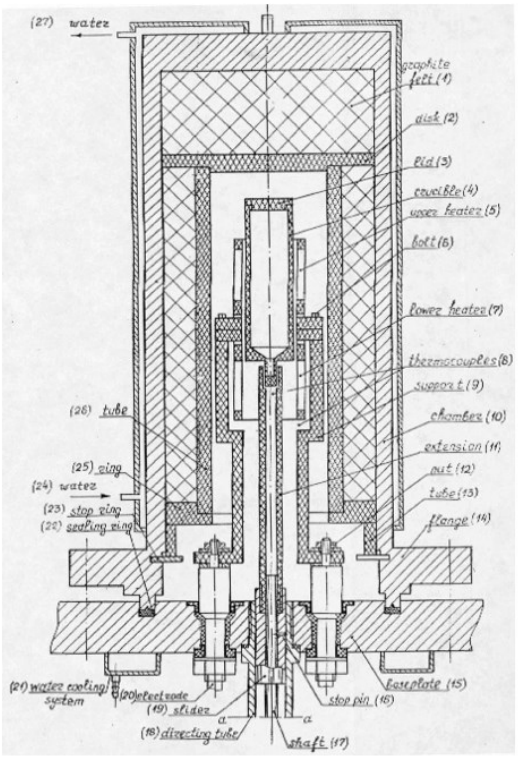

Figure 2-5. Schematic diagram of HPB [23]

The IMEM-CNR growth system is a vertical Bridgman where ampoule is moved inside the oven tunnel.

The large difference of vapor pressure between cadmium and tellurium causes that the gaseous part is meanly composed by cadmium, this is an issue of this process. Most of losses are of Cd and the result is that the crystal is tellurium-rich, even if the starting charge is stoichiometric.

2.4.3 High Pressure Bridgman

In the case of High pressure Bridgman growth, the graphite ampoule is not sealed, and cadmium losses are limited by the injection of inert gas (generally argon) at high pressure in the external chamber. Typical values of pressure may vary from 10 to 150 atmospheres [32]. This overpressure decreases the diffusion coefficient of Cd and Te vapors, and thus minimize CZT losses that spread in the growth chamber.

2.4.4 Boron-encapsulated Bridgman

To avoid Cd losses it was also developed a variant of Bridgman technique: *Boron encapsulated Bridgman.* This growth technique allows to obtain high quality CZT crystals without sealing the quartz ampule and without using high pressure gas.

This technique is performed using no-sealed ampoule where B_2O_3 is added over the CdZnTe charge as encapsulant. The oxide has low fusion temperature (~450°C) and low density. For these reasons, before CZT is completely melt, boron oxide is already liquid and covers the CZT charge. Furthermore, B_2O_3 creates a thin layer all around the internal side of ampoule between CZT and quartz because it is slightly reactive with the last one (Figure 2-6).

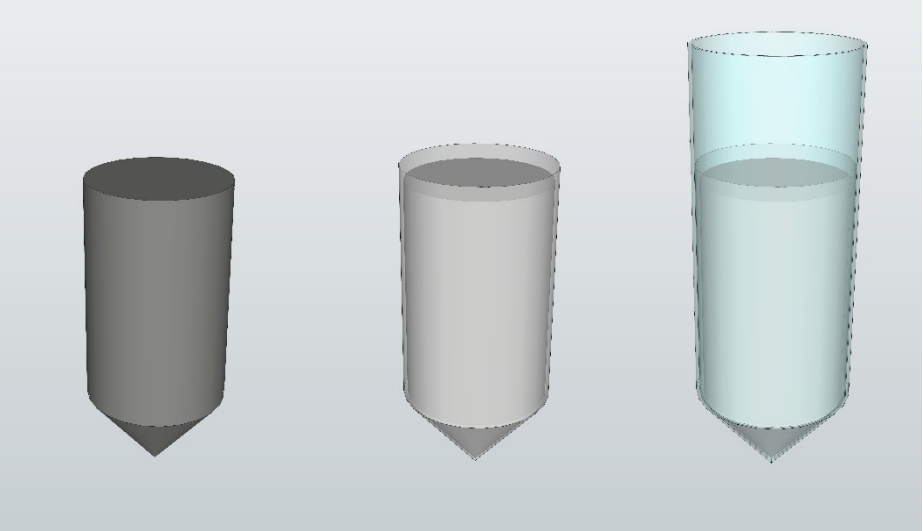

Figure 2-6. Only CZT ingot (left), B_2O_3 fully encapsulates the melt (center) and CZT ingot with B_2O_3 in quartz ampoule (right) [33]

B_2O_3 have two fundamental effects:

- Decreases surface evaporation of CZT, because it is under a thick layer of boron oxide that avoids evaporation.
- Minimizes sticking between ampoule and CZT [33], reactivity between CZT and boron oxide is less than reactivity with quartz. Furthermore, preventing contact on quartz, it avoids oxygen contaminations that create impurity inside the final crystal.

First of all high purity cadmium, zinc and tellurium (7N) in the right stoichiometry are charged in a quartz ampoule and heated up to induce the chemical reaction that produces polycrystalline CZT.

The direct synthesis is carried out at quiet high pressure (20-40 bar) of inert gas (argon). Extremely pure argon (6N) is used to avoid any type oxidation. The overpressure helps to contain the evaporated material inside the quartz ampoule and to minimize material losses.

The second step is a thermal treatment. Weighing errors and material loss via evaporation could cause a deviation from the correct stoichiometry. A thermal treatment is thus necessary to allow the evaporation of excess components and to set the right stoichiometry. This is realized at 800°C in low pressure of inert gas, without any overpressure of Cd or Te.

The last step is the crystal growth. The treated polycrystalline CZT is located in the quartz ampoule with the exact indium amount for semiconductor compensation (necessary to obtain high resistivity material). Boron oxide is introduced in the ampoule on top of the charge. The growth ampoule is brought above melting temperature and, after a stabilization time, it is moved slowly through the oven temperature gradient where the seeding (before) and growth (after) start. The last step of the process takes 15 days, but the real growth time is more or less seven days; in this time a 7 cm long ingot is obtained (Figure 2-7-a).

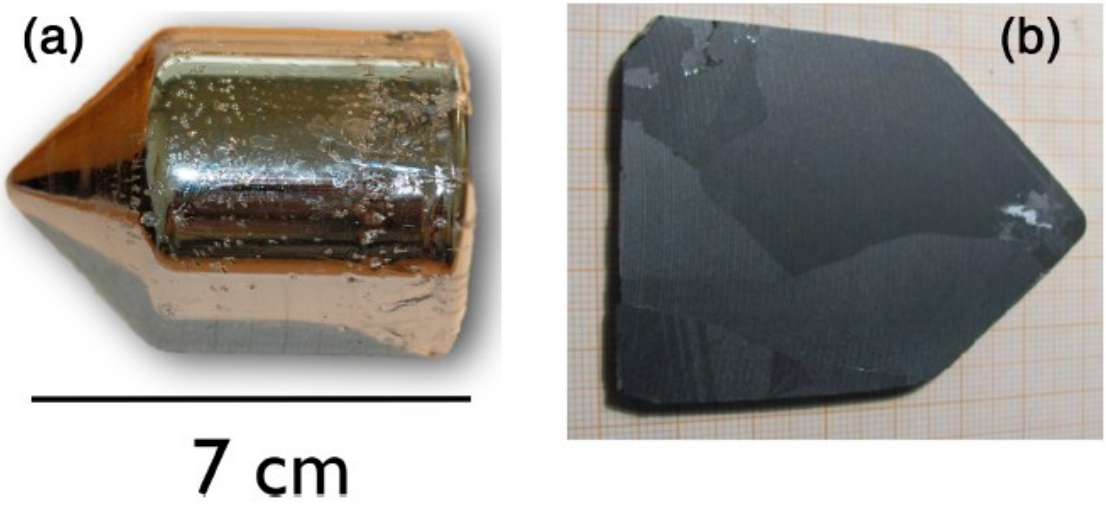

Figure 2-7. a) 2 inches ingot growth at IMEM-CNR institute, by using B2O3 very smooth surfaces were obtained [7]

IMEM ingots are typically around 2 inches and around 600g of weight.

Despite all these precautions CZT ingots are not fully single-crystal. Moreover, typically a large number of defects of different type and nature are found. Some of the typical CZT defects are described in the next paragraph (2.5).

2.5 Defects and inhomogeneity

An important challenge of CZT grower is to decrease as much as possible defects and inhomogeneity, as they play a crucial role in carriers transport.

One of the problem is to maintain the right stoichiometry uniformly throughout the ingot. This aspect is an issue for CZT because the segregation coefficient for zinc is 1.35, the latter is defined as the ratio between the concentration of Zn in solid phase versus concentration in liquid one.

$$K_{Zn} = \frac{C_S}{C_L} = 1.35 \qquad 2\text{-}4$$

This means that there is a lower concentration of zinc in the molten material compared to the solid phase. So during the growth the quantity of solidified Zn changes through the ingot axis. This characteristic is intrinsic of all melt-growth techniques and therefore it cannot be avoid. The variation of zinc concentration changes lattice properties and bandgap width, result of this inhomogeneity is the deterioration of spectroscopic properties.

CZT defects can be broken down in two macro categories:

- Point defects
- Extended defects

Point defects generate shallow and deep levels. In a perfect crystal electron and holes occupy only the energy levels in conduction and valence band; interstitial defects and vacancies promote additional energy levels at different depths. In other word, point defects are the main creators of carrier traps with a subsequent lowering of their lifetime.

Most common extended defects are:

- Grain boundaries
- Cracks
- Pipes
- Te inclusions
- Voids
- Twins

Grain boundaries (Figure 2-8) can be formed during the growth when local temperature gradients or high growth speeds occurs. These defects are more probable in the first stage of an unseeded growth when nucleation of several grains appears, or may be originated by an instable growth interface. Close to the grain boundaries interface many other defects are forming such as impurities and dislocations, so that electrical and mechanical properties are locally changed. Mechanical weakening and charge transport limitations are typical of these defects, trapping and recombination effects are also expected in these regions.

Thermal and mechanical stresses due to the cooling down after crystal growth are perpetrators of cracks. Cracks are typically few centimeters of length and about 25 microns in width and typically start at the edges of the ingot and sometimes can propagate inside the ingot. Cracks can also be created in the subsequent stages of device preparation such as cutting and lapping processes. Therefore cracks can be avoided thanks to appropriate choices of: thermal profile, crucible material and cooling down process.

Another frequent defects in CZT are twins (Figure 2-8). Twin boundaries occur when two crystals of the same type intergrow, so that only a slight misorientation exists between them. It is a highly symmetrical interface, often with one crystal the mirror image of the other; also, atoms are shared by the two crystals at regular intervals. The formation energy of this process is quiet low in CZT, this is why a large number of twins can be found in a ingot. Twins are due to temperature fluctuations during growth, thus to diminish their number is necessary improve the temperature profile and temperature stability of the furnace.

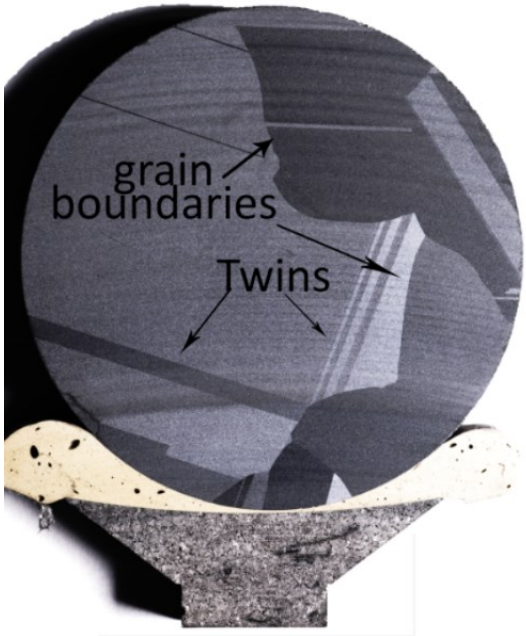

Figure 2-8. CZT slice with defects marked

High resistivity CZT is usually obtained by doping with group III elements a tellurium deviated charge. Thus, CZT crystal for detector application always are obtained a Te-rich charge. During the growth a little amount of tellurium is included inside the ingot in the form of Te inclusions. Typical diameters of these inclusions are between 1 and 3 microns but larger ones up to 30 microns observed, especially close to twin planes or to grain boundary interfaces. Tellurium electrical resistivity is several orders of magnitude lower than surrounding semiconductor, so that higher leakage current (and then field distortion) is found in the volumes with large amount of inclusions. For this reasons Te inclusions strongly limit CZT devices performances, in particular imaging devices. So monitoring these defects is crucial to obtain high quality material.

Charge transport properties depend on impurities and defects of the semiconductor. They operate like scattering centers by changing mobility and by reducing lifetime. Defects are also the cause of carriers recombination and electric field distortions.

3 Contacts

The role of contacts is crucial to fabricate good CdZnTe detectors. Not optimized contacts result in low detector performance, even starting with high quality material. Hence optimized engineering of contacts in terms of geometry and constituent metal is required.

Contacts must be able to reduce total leakage current, and, at the same time, they must be chemically and mechanically stable. Another important point is the quality of metal-semiconductor interface to avoid carriers trapping and recombination.

Contacts realization must be careful at some expedient:

- CZT surface is not stable at high temperature: with $T > 100 - 120°C$ a decrease of resistivity is found. All high temperature techniques and annealing with the aim to improve electrical and mechanical properties of contact are then forbidden.
- Metal-semiconductor interface must be homogenous and the deposition must avoid oxide layer and impurities under the contact.
- Thick and uniform conductive layer is required to allow uniform conductivity all over contact area.
- Metal contact have to be able to overcame stress.
- Time resistance is required for contact because electrical properties must be maintained.

The fact that CZT can not withstand relatively low temperatures (100-120°C) precludes the use of several techniques and in particular prevents the use of interdiffusion between metal and CZT that usually increases the adhesion of contacts.

An appropriate geometry is necessary in order to maximize spectral resolution and carrier collection. The best contact geometry changes application-by-application and a specific study is unavoidable for competitive detector manufacture. Different thicknesses of CZT and different radiation energy ranges require simulations with the aim to choose right electrode disposition. In this thesis it will be explained how contacts geometry change carriers collection and how it is possible to set the correct parameters to improve spectroscopy in different application fields.

3.1 Typical deposition techniques

Several deposition techniques have been developed over the years, actually the main are electroless deposition [34], sputtering [35] and evaporation [36]. Different concepts were exploited and several metals (Au, Pt, W, Al, Rd, In, Ag) were considered to realize optimal contacts on CZT [34] [37].

In my thesis work, I was focused mainly on electroless deposition with some interesting results with nickel, gold and platinum deposition.

3.1.1 Electroless deposition

This deposition technique (also called *chemical* or *autocatalytic plating*) is a non-galvanic plating method that involves numerous simultaneous reactions (both in solution and the interface). This reaction happens without electrical helps from an external field, exploiting only the differences of electrochemical potentials and is catalyzed by the careful selection of experimental conditions such as temperature, solution pH, and solvent mixture. Electroless deposition for CZT involves really complicated reactions that are not fully clarified in literature yet [38] [39]. For these reasons empirical approach is still requested for process optimization.

Electroless deposition have several advantages:

- Economy: complex vacuum systems or expensive evaporation and spattering systems are not request.
- Reproducibility: when process has been optimized, electroless technique ensures high grades of stability and reproducibility.
- Scalability: it is possible to apply this technique also for large surfaces maintaining contact quality.
- Quickness: this technique allows deposition of hundreds nanometers in few minutes.

In chapter 6.3 the standard process and the new developments will be explained in the detail.

3.2 Contacts and band theory

Contacts are very important for a semiconductor device because both extraction of carriers and induced signal depend on them. Understand the different behavior due to their nature or formation characteristic is important in devices fabrication to optimize them according to final application.

Metal-semiconductor junction has been studied for several years and numerous models were developed. This section is focused only on the model that fits well the voltage characteristics of our devices. Firstly though, we must know the behavior of different metal in contact with CZT using the band theory.

3.2.1 Metal-CZT: band theory and carriers transport

To understand better the nature of metal-semiconductor junction it should be considered the CZT band diagram before and after the coupling with the metal. CZT has the Fermi level at mid gap, for this reason, contacts will show a different behavior according to carriers choice.

Different metals could show extremely different characteristics under bias. Carrier injection and extraction is influenced until the point to exhibit *ohmic* or *blocking* behavior [40].

Ohmic-like contacts do not prevent the current flux through the detector: so, they will show greater dark current but prevent any charge accumulation close to the interface. on the contrary, blocking contacts are characterized by the presence of a potential barrier (also called Schottky barrier) that limits the current flow inside the device. Blocking electrodes show a rectifying current-voltage behavior (like the diode) and could accumulate charge close to interface.

The two contact types are discernible by the metal work function ϕ_M if interface defects and inhomogeneity and interfacial oxide are negligible. The *work function* is defined as the minimum energy required to extract an electron from the metal. For metals, it corresponds to the difference between Fermi and vacuum levels.

In Table 3.1 the work function value is listed for several metals.

	Element	ϕ_M (eV)	Element	ϕ_M (eV)	Element	ϕ_M (eV)	Element	ϕ_M (eV)
	Ag	4.52-4.74	Cs	2.14	Mg	3.66	Si	4.6-4.85
	Al	4.06-4.26	Cu	4.53-5.1	Mn	4.1	Sr	2.59
	Au	**5.1-5.47**	Gd	2.9	Na	2.36	Te	4.95
	Ba	2.52-2.7	Hg	4.475	**Ni**	**5.04-5.35**	Ti	4.33
	Bi	4.34	In	4.09	Pd	5.22-5.6	V	4.3
	Cd	4.08	K	2.29	**Pt**	**5.12-5.93**	W	4.32-5.22
	Cr	4.5	Li	2.93	Sb	4.55-4.7	Zn	3.63-4.9

Table 3.1 Work function of different metals [40]

In semiconductors, the definition of "work function" loses completely meaning because the Fermi level is inside the forbidden region (in the gap). Then it is preferable to use the electron affinity X defined as the difference between conduction band and vacuum state. However, also work function is relevant for semiconductors (for CZT ϕ_S=5.1eV): the comparison of semiconductor and metal work functions determine the contact type.

Detector is, in first approximation, a couple of metal-CZT junctions back to back. The strong difference between μτ of electrons and holes brings to consider principally electron contribute. When metal-semiconductor-metal (MSM) structure is created, the bands of semiconductor (close to the metal) bend to achieve a new thermodynamic equilibrium. With following equations it is easy calculate the resulting barrier heights for electrons and holes [40].

$$\phi_n = \phi_M - \chi = \phi_M - \phi_S + \frac{E_{gap}}{2} \qquad 3\text{-}1$$

$$\phi_p = E_{gap} - \phi_n \qquad 3\text{-}2$$

In Figure 3-1 the band diagrams before and after the thermodynamic equilibrium established for two different systems are shown: on the left $\phi_M < \phi_{CZT}$ and on the right $\phi_M > \phi_{CZT}$. The equilibrium is reached thanks an electrons transfer from metal to semiconductor with a consequent band spiking.

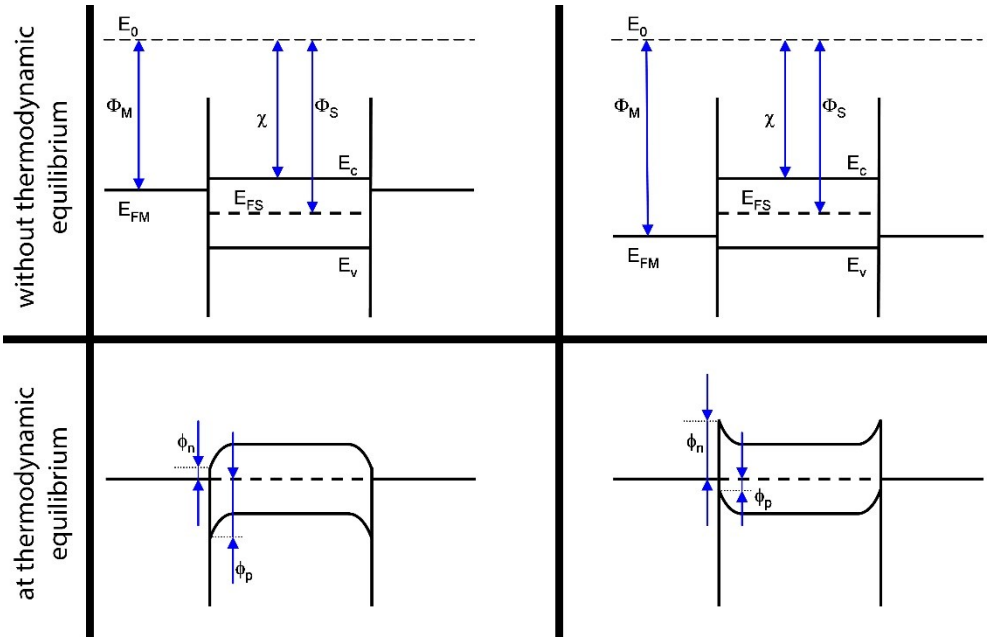

Figure 3-1. Bands diagram before (top) and after (bottom) thermodynamic equilibrium [40]

In the left case, the Schottky barrier is higher for holes: the behavior of contacts will be ohmic for electrons and blocking for holes. In the right case, the exact opposite happens: ohmic for holes and blocking for electrons.

When high voltage is applied at the electrodes (classical configuration of CZT device), bands are stretched and barriers change their shapes (Figure 3-2). Notable effect is that the stretching is able to remove the electron barriers near the positive contact (for both cases). This effect is also important for the treatment of current-voltage (IV) characteristic.

Top-left diagram of Figure 3-2 shows that:

- Injected electrons that enter from the cathode (-) will have a low contact potential to overcome: cathode behaves as ohmic contact for electrons.
- Electrons that attain the anode (+) flow without problem toward the metal.
- Injected holes meet a high Schottky barrier: anode behaves as blocking contact for holes.
- Holes that reach the cathode flow without obstacles up to the metal.

Besides, top-right diagram of Figure 3-2 shows that:

- Injected electrons that enter from the cathode (-) have a high contact potential to overcome: cathode behaves as blocking contact for electrons.
- Electrons that attain the anode (+) flow without problem toward the metal.
- Injected holes meet a low barrier: anodes behaves as ohmic contact for holes.
- Holes that reach the cathode flow without obstacles up to the metal.

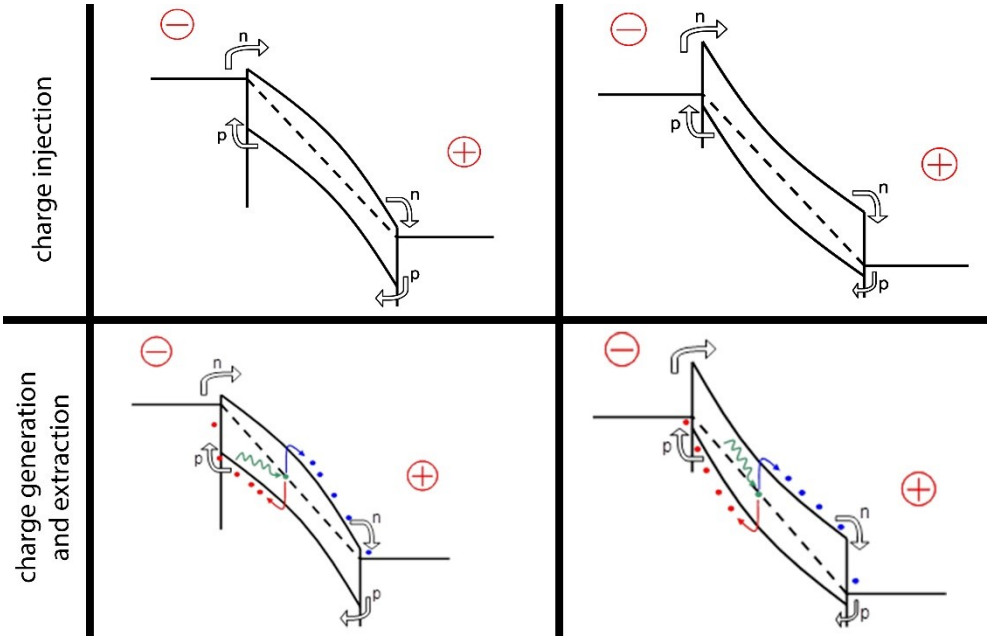

Figure 3-2. Charge injection (top) and generation (bottom) under high voltage applied [40]

Therefore, contacts with $\phi_M < \phi_S$ limit the hole dark current at the anode causing that the total leakage current is dominated by electrons. Contacts with $\phi_M > \phi_S$ limit the electron dark current at the cathode by making a bit more significant the hole contribution compared to the previous case.

Bottom diagrams in Figure 3-2 show the transport through the barriers when the charge is generated inside the device (for example for X-ray absorption). Photoelectrons and photoholes will not meet potential barriers and they will be collect without problems. Thus, metal work

function does not affect the charge collection: each generated carrier will always flow through the outgoing electrode without hitting any barrier [40].

From this handing we can conclude that the ideal system is composed by a couple of different junctions: a cathode with $\phi_M > \phi_S$ and an anode with $\phi_M < \phi_S$. This system minimizes the dark current and ensures excellent charge collection.

This holds for a generic MSM system without any assumption on the semiconductor type and its properties. If a strong difference between electron and hole μτ-products is considered holes are more likely to be trapped: considering the mean free path under a typical field of 1000V/cm we obtain:

$$d_h = (\mu\tau)_h E < 1mm \quad 3\text{-}3$$

$$d_e = (\mu\tau)_e E > 10mm \quad 3\text{-}4$$

Typical thickness of devices is few millimeters, then injected holes and holes generated near the anode will never reach the cathode. As a result, the charge storages under the cathode. Normally the injected electrons compensate that quantity but, when the flux of radiation is high, the trapped charges inevitably increase and also the outgoing holes Schottky barrier. This mechanism gradually distorts the electric field by changing charge collection. To limit the problem it is possible to change the metal at the cathode (replace it in such a way that $\phi_M < \phi_S$) generating a more injective contact that, by supplying more electrons, can compensate the trapped holes.

From band theory and transport properties two different configurations are found (Figure 3-3):

- For low radiation flux the ideal configuration is with $\phi_{cathode} > \phi_{CZT} > \phi_{anode}$ in order to limit the leakage current and decrease the electronic noise.
- For high radiation flux the ideal configuration is with the same type of contacts both at the anode and at the cathode and $\phi_M < \phi_{CZT}$, in order to limit the polarization effect due to charge trapping.

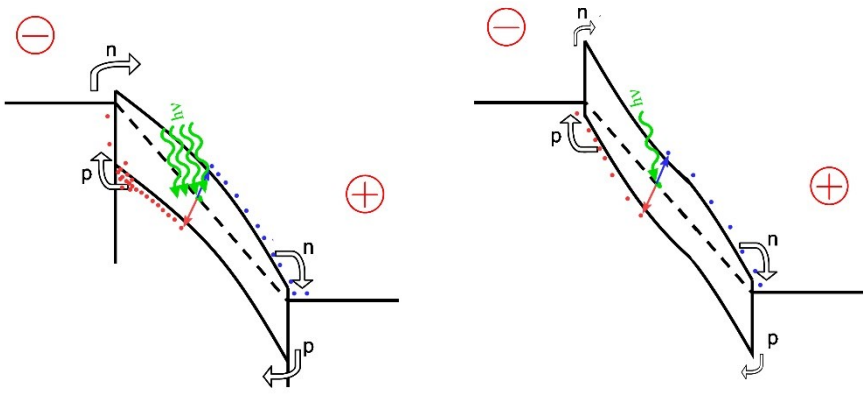

Figure 3-3. Ideal electrode configuration for: high flux (left) and low flux (right) incident radiation

Several challenges are present in the process of surface preparation and in the contact deposition. For these reasons it is not easy to understand in advance the behavior of a metal deposited with a particular technique. Surface contamination, oxidation, and dead layer associated with improper lapping/polishing can change the work function of a metal or lowering the barrier height by as much as 0.5 to 1 eV [40]. Anyway, thanks at IV and spectroscopic measurements it is possible to define if a deposited layer behaves as ohmic or blocking contact.

In the following chapter it is described a model to define the barrier height and other important contact characteristics by using current-voltage curve.

3.2.2 Current-Voltage characteristic

From a complete IV several important information of the sample can be extracted. Using a guard ring surrounded device (the aim of this special element will be described further) it is possible to isolate the bulk contribution from the surface one and study only the real effect of contacts. We have previously outlined the device as a couple of metal-semiconductor junctions; neglecting the holes contribution (for CZT is very low with respect to the electrons one) and remembering that the outgoing contacts normally do not show barriers, we can simplify further the treatment. The unique contact that contributes to the IV curve is the one negatively biased. If the applied voltage changes in a range with positive and negative values we have to consider both contacts but one for bias region. Ohmic-like contacts do not change the IV curve and can be neglected in the treatment.

In a simple view we have three main cases:

- Both ohmic-like contacts: the IV is linear with a slope that depend on the CZT resistance.
- Both blocking contacts: the IV shows an "S" behavior as two diode coupled back-to-back.
- Only one blocking: the IV is similar to that of the diode in series with a high resistance (given by CZT).

Grounding the contact named *anode* and changing the bias of the other contact, *cathode*, from negative to positive, we can study both contacts. Detectors are typically polarized with cathode at negative voltage (for the better transport properties of electrons), so the following treatment and the data in this thesis concern only the negative branch. The model is obviously applicable with positive one but it would be less interesting for applications.

The IV characteristic is conveniently measured at different temperatures allowing to calculate the barrier height by means of Arrhenius plot of a fitting parameter.

At very low voltage (up to half volt) it is estimable the bulk resistivity of CZT crystal, the IV curve following a linear trend when the bias voltage approaches zero. This behavior indicates that in this range (region I) the series resistance of the bulk CZT dominates the charge transport mechanism [41].

Increasing voltage there is a sublinear region (region II) due to the formation of a depletion region in CZT [41]. With few volts the device is fully depleted, so a new region starts (region III) where current, at low voltage, follows a linear trend with higher resistivity value than that of region I, notably due to the fully depleted region. At higher voltage the current starts to increase exponentially due to the lowering of potential barrier as a result of the presence of a thin interfacial layer between metal and CZT (firstly modelled by Wu in general case [42], and after elaborated by Bolotnikov in [41] for CZT).

Region II and III can be explained by taking into account the interfacial layer-thermionic-diffusion (ITD) model developed by Wu [42]. This model explains the deviation from the standard theories of the electrical conduction at the Schottky metal/ semiconductor barrier, due to the specific influence of an interfacial layer between the deposited metal and the semiconductor surface, by including in the Schottky barrier model the effects of both voltage drop and transmission coefficient across interfacial layer. Actually, during the fabrication process, surface treatment could generate a Te-rich layer that rapidly oxidizes generating a thin layer of TeO_2; ITD model takes into account this interfacial layer.

In the following rows it is used this standard for the quantities:

J_R reverse current density
V_R reverse bias voltage
k Boltzmann constant
T temperature
A^* effective Richardson constant
v_t thermal velocity
θ_n transmission coefficient through the interfacial layer
ϵ_i and δ_i permittivity and thickness of interfacial layer
D_s density of surface states per unit of energy and area
ϕ_{B_0} height of Schottky barriers of junction
V_{RT} required voltage to fully deplete the crystal
v_D effective diffusion velocity
W width of the depleted layer
μ electron mobility
V_{bi} diffusion potential at cathode
ΔV potential at the edge of the depleted layer
E_A electric field inside the undepleted layer
E_0 electric field at the anode when $V_R = V_{RT}$
L detector thickness

According to the ITD model, when bulk resistance can be neglected (region II and III), the reverse current density J_R can be expressed as a function of reverse voltage V_R [41]:

$$J_R = \left(\frac{C_0}{1 + \frac{\theta_n v_t}{v_D}} \right) \exp\left(\frac{q C_2 V_R}{kT} \right) \qquad 3\text{-}5$$

Where $C_0 = \theta_n A^* T^2 \exp(q\phi_{B_0}/kT)$ and $C_2 = 1 - \epsilon_i/(\epsilon_i + 2q\delta_i D_S)$.

In the second region ($V_R < V_{RT}$, where crystal is not fully depleted) equation 3-5 becomes:

$$J_R = \left(\frac{C_0}{1 + \frac{C_1}{C_3 + 2V_R}} \right) \exp\left(\frac{q C_2 V_R}{kT} \right) \qquad 3\text{-}6$$

Where $C_1 = \theta_n W v_t/\mu$ and $C_3 = 2V_{bi} - 2\Delta V + E_A W$.

When $V_R > V_{RT}$, the detector is fully depleted and equation 3-5 becomes:

$$J_R = \left(\frac{C_0}{1 + \frac{C_4}{C_5 + V_R}} \right) \exp\left(\frac{q C_2 V_R}{kT} \right) \qquad 3\text{-}7$$

Where $C_4 = \theta_n L v_t/\mu$ and $C_5 = V_{RT} - E_0 L$.

Fitting equation 3-7 at high voltage and different temperatures, we obtain several parameters:

- C_0, from which it is possible to extract ϕ_{B_0} from the slope of the Arrhenius plot $\ln(C_0/T^2)$ versus 1/kT.
- C_4, from which, considering typical value of v_t and μ are respectively 8.5 10^6 cm/s and 1000 cm^2/Vs [41], it is possible to extract θ_n.
- C_2, used in the next step.

Fitting equations 3-6 at $V_R < V_{RT}$ and considering C_2 from the previous fit, we can verify the consistency of the model comparing obtained ϕ_{B_0} with the previous one.

In region III two different transport mechanisms can be distinguished, according to the value of $\frac{\theta_n v_t}{v_D(V_R)}$:

- If it is lower than one, leakage current is dominated by *thermionic emission*.
- If it is greater than one, leakage current is dominated by *diffusion*.

The two mechanisms are competitive, in particular: diffusion is dominant at low voltage, while thermionic transport is dominant at high bias. The "critical value" of voltage is related to the transmission coefficient through oxide layer (θ_n) so indirectly with the thickness of the layer.

Finally a fourth region of space charge limited current (SCLC) transport is also possible [43]. At very high voltage, the current follows the power law:

$$J_R \propto V_R^m \qquad 3\text{-}8$$

Where m is larger than two; this behavior is related to the presence of deep traps.

From the IV analysis we can obtain important information about interfacial layer, the bulk resistivity and the height of the Schottky barrier of the contact.

3.3 Contact geometries

Other than metal contacts choice, it is really important to select appropriate contact geometry. Due to the wide application fields of CZT detectors it doesn't exist a unique electrode configuration. On the contrary, changing detection requests lead to a consequent change of detector geometry.

With *detection requests* shall it is meant for example: energy range of expected radiation, sensibility of detector in terms of acquired event rate, intensity of radiation flux, spatial resolution.

Appropriate electrodes configuration can also give the possibility to realize *single carrier detectors*. This could be a good point of strength having regards to the strong difference of μτ product between electrons and holes. With single carrier detector, hole effects are neglected thanks to an only rearrange electrodes rearrange.

To optimize detector geometry it is crucial to study and fully understand charge collection phenomena at electrodes.

The following subchapter will discuss charge collection or rather *charge induction* at electrodes and in which way geometry influence this process.

3.3.1 Ramo-Shockley theorem

Ramo-Shockley theorem describe how moving charges induce current on electrodes.

The Shockley–Ramo theorem allows to calculate the instantaneous electric current induced by a moving charge. It is based on the concept that current induced at the electrode is due to the instantaneous change of electrostatic flux lines on the electrode and not to the amount of charge received by the electrode per second. The theorem appeared in William Shockley's 1938 paper "Currents to Conductors Induced by a Moving Point Charge" [44] and a year later in Simon Ramo's 1939 paper entitled "Currents Induced by Electron Motion" [45].

Shockley and Ramo independently derived a highly useful formula for electrode current calculation induced by charged carriers moving in a three dimensional structure with multiple contacts:

$$I^k = \sum_j q_j \boldsymbol{W}_j^k \cdot \boldsymbol{v}_j \qquad 3\text{-}9$$

Where j are the particles with charge q_j and speed $\boldsymbol{v}_j$, k indicates the contact for which the current is to be evaluated. The physical $\boldsymbol{W}_j^k$ has dimensions of inverse of length and its value is the electric field evaluated on the position of particle j which would result if all terminals are grounded except the k-th that is biased at 1 Volt.

Application of this theorem has been extensive, from hot carrier noise in bulk semiconductor and submicron semiconductor structure to generators and detectors of electromagnetic radiation to terminal currents in Monte Carlo device transport simulation [46].

This formula was derived from Green's reciprocity theorem:

$$\sum_i Q_i^A V_i^B = \sum_i Q_i^B V_i^A \qquad 3\text{-}10$$

Where A, B are two possible sets of {charges, potentials} of the system of electrodes.

Demonstration starts considering case A with all terminals grounded and charge q_p placed inside the space, and case B with all electrodes grounded except for $V_k = V_k^B$. It is possible deduce that all $V_i^A = 0$ and then summary is null. In case A it is possible obtain the value of induced charge at k electrode Q_k^A. Figure 3-1 shows A and B configurations.

$$q_p V_p^B + Q_k^A V_k^B = 0 \rightarrow Q_k^A = -q_p \frac{V_p^B}{V_k^B} = -q_p V_w \qquad 3\text{-}11$$

Setting $V_k^B = 1$ we can define a new "pseudo-potenital" (pseudo because is dimensionless) called *weighting potential* $V_w(\boldsymbol{r})$ all over the space. This potential is typical for k terminal and represents the weight with which electrode feel charge located in $\boldsymbol{r}$.

If charge q_p are in motion it is possible define induced current as the derivate of induced charge and then deduce:

$$I_k(t) = \frac{d}{dt} Q_k(t) = -q_p \frac{dV_w}{dt} \cdot \frac{d\boldsymbol{r}}{d\boldsymbol{r}} = -q_p \frac{d\boldsymbol{r}}{dt} \frac{dV_w}{d\boldsymbol{r}} = -q_p \boldsymbol{v}_p(-\boldsymbol{W}) \qquad 3\text{-}12$$

$$I_k(t) = q_p \boldsymbol{v}_p(t) \boldsymbol{W}(\boldsymbol{r}) \qquad 3\text{-}13$$

Where $\boldsymbol{v}_p(t)$ is speed of charge q_p and $\boldsymbol{W}(\boldsymbol{r})$ represent the *weighting field* defined as $-\boldsymbol{\nabla}_{\mathbf{r}} V_w(\boldsymbol{r})$.

Weighting field depend only on electrode configuration. It is easily calculable solving Laplace equation for each specific geometry grounding all electrodes, except the electrode upon which induced current will be calculated that is set to 1 (Figure 3-4).

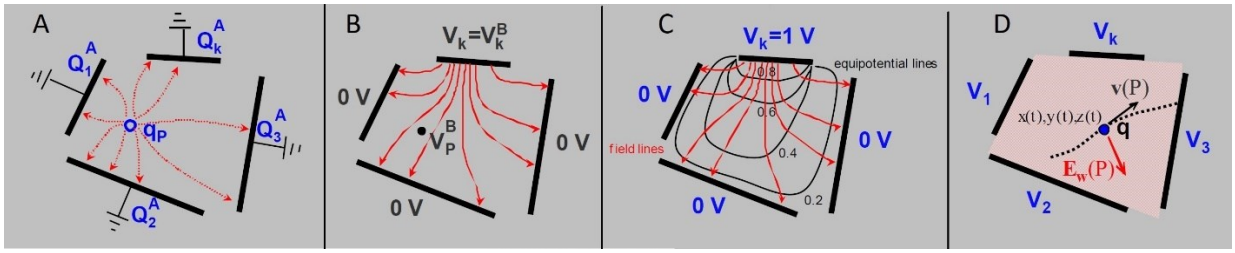

Figure 3-4. A) configuration A; B) configuration B; C) weighting field line (red) and equipotential line (black) D) charge in motion and local weighting field [47]

Ramo-Shockley theorem is fundamental to calculate the current induced at the collecting electrode in a radiation detector. Its strength is that weighting field is independent by the real field and the material characteristic but depends only on geometrical disposition of electrodes in the device.

Because in general charge is not homogeneously distributed q_p is conveniently substituted with charge distribution ρ. Furthermore it is possible to write charge spatial velocity $\boldsymbol{v}_p$ as $\boldsymbol{v}_p = \mu \boldsymbol{E}(\boldsymbol{r})$ where μ is mobility of carriers and $\boldsymbol{E}(\boldsymbol{r})$ is the real electric field. So now induced current (3-13) is written as:

$$I(t) = \iiint_V \rho\big(\boldsymbol{r}(t)\big)\mu \boldsymbol{E}\big(\boldsymbol{r}(t)\big) \cdot \boldsymbol{W}\big(\boldsymbol{r}(t)\big) dV \qquad 3\text{-}14$$

Where $\boldsymbol{r}(t)$ is the equation of motion of carriers in the volume dV. Trajectory of charge is determined by the actual operating electric field, and mobility of traveling carriers.

If we consider the point-like charge motion, equation 3-14 is splitted in two highlighting electrons (e) and holes (h) contribution.

$$I(t) = q_e \mu_e \boldsymbol{E}\big(\boldsymbol{r}_e(t)\big) \cdot \boldsymbol{W}\big(\boldsymbol{r}_e(t)\big) + q_h \mu_h \boldsymbol{E}\big(\boldsymbol{r}_h(t)\big) \cdot \boldsymbol{W}\big(\boldsymbol{r}_h(t)\big) \qquad 3\text{-}15$$

Generally the first step of detector readout electronics (see section 4.1) integrates inducted current in time. It is performed by a charge sensitive amplifier (CSP) and mathematically is described by equation 3-16. Simulation of induced total charge is crucial to optimize devices.

$$Q_{tot} = \int_0^{t_F} I(t) \qquad 3\text{-}16$$

Where t_F is the fly time of carriers.

3.3.2 Real electric field vs weighting field

Ramo-Shockley theorem suggest that two important fields must be taken into account for the evaluation of a device:

- **Electric field $\boldsymbol{E}(\boldsymbol{r})$**: this depends on several parameters such as: bias voltage, trapping, spatial charge, barrier height at contacts, defects. All these elements could change and distorts the externally applied electric field, sometimes in a way also hard to compute. Some methods have been developed to know the real electric field inside a device. A well known technique is based on the use of the Pockels effect that exploits rotation of polarized IR light induced by electrical field [48]. However, it is known that IR light distorts the electric field in CZT devices [49]. A novel technique is reported in this thesis at chapter 5.4 (LI-TCT) that allows to obtain real electric field with laser photo-generated carriers ([50] [51] [52]). Field distortions are avoidable in LI-TCT using appropriate expedients.
- **Weighting field $\boldsymbol{W}(\boldsymbol{r})$**: this depends only on geometrical factors. So, once optimized the geometry for the specific application, the weighting field for each detector realized with this electrodes configuration is the same. It is also independent by applied voltage and contact metal. The previous sub-chapter (3.3.1) explains how it is possible to obtain the weighting field, several programs are able to solve Laplace equation to compute it. For simulations in my PhD, I have used Comsol multiphysics, a smart program that makes FEM (Finite Element Method) computation with interactive graphic interface.

Making some assumptions it is also possible to simulate the real electric field using Comsol, considering a perfect detector without spatial charge and contact defects. Obviously, this simulation has not the demand to reproduce the real electric field, anyways it gives important suggestion from the point of view of carriers trajectory and flight time.

3.3.3 Type of contact geometries

Material with high atomic number are required for the realization of efficient X and γ-ray detectors. HgI_2, CdTe and CdZnTe are materials that have attracted most attention to date. However, due to trapping of charges, the output signal of a conventional detector having planar electrodes depends not only on the deposited energy, but also on the position of that interaction. This effect is more relevant when the difference between μτ product for electrons and holes is great (as in the case of CZT).
The output signal is proportional to the total induced charge (equation 3-16) that contains the contribution of both carrier types. In order to overcome the effects of severe trapping of holes in wide band-gap semiconductors, researchers have been investigating techniques in which the pulse amplitude is sensitive only to one type of charge carriers, normally just the electrons (and not the holes). These techniques are called single polarity charge sensing, which can alleviate the charge trapping problem if the drift length of just one type of charge (such as electrons) can be long compared with the detector thickness.

With appropriate contact geometries it is possible to realize single carrier detectors [53]; the shape of the weighting field is important to understand better why these detectors are only sensitive to electrons. In this paragraph, I want to show different contact configurations and the respective simulation of weighting and electric fields. The top contacts of detectors represented in the images of the next paragraph are the anodes while the bottom ones are the cathodes.

Simulations of weighting and electric potentials are also shown, they are plotted respectively in the central and right sides of images (Figure 3-5, Figure 3-6, Figure 3-7, Figure 3-9, Figure 3-10, Figure 3-11 and Figure 3-12). In these figures cathode is in the bottom side while anode in the top side. Strong potential variations are represented by intense color-gradients in 2D maps.

Planar-planar electrodes
The configuration of a planar-planar detector is illustrated in Figure 3-5-left. The anode is connected to the CSP and the cathode is biased. For a slab geometry, the weighting potential is simply a linear function of depth *z* and it is 0 at the cathode and 1 at the anode. The resulting weighting field, that is the gradient of the weighting potential, is uniform and its value is 1/L (where L is the detector thickness). If the loss of charge carriers during the drift time can be ignored, such as is usually the case in a high purity germanium detector (HPGe), the induced charge on the anode does not depend on the depth of interaction. But in CZT case, the μτ product of holes is low and with typical electric fields (about 500V/mm), the charge loss is not negligible. For this reason the induced charge depend strongly on the interaction depth: in the limit of holes mean free path tending to zero, the total induced charge is a linear function of depth *z*. Planar-planar CZT detectors is not recommended to detect radiation with high-energy that would interact deeply thereby generating a bad spectrum.

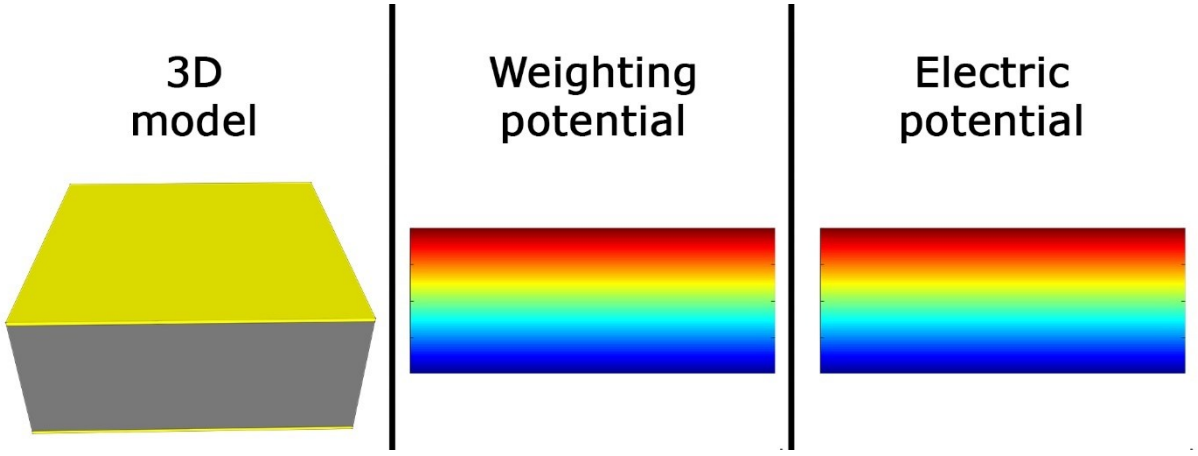

Figure 3-5. Example of planar-planar detector (left), and related weighting (center) and electric potential (right)

Virtual Frisch-grid electrodes

The first single polarity charge sensing technique was implemented in gas detectors by Frisch [54] who used a grid contact between the anode and the cathode to overcome the problem of slow drift and loss of ions. In a semiconductor detector it is not possible to realize the grid contact. So, a virtual grid is realized as follows. The lateral surface of the detector is covered with an insulating layer; a metallic layer, that covers the insulation, plays the role of the grid (this configuration is called virtual Frisch-grid [55]). The lateral metallic layer gets very close (P≪L) to the anode as shown in Figure 3-6-left. Generated electrons travel in CZT and are collected by the anode. The weighting potential of the anode is obtained by applying a unit potential on the anode, and zero potential on both the lateral layer and the cathode. The resulting weighting potential is close to zero at the cathode and in the region of CZT covered by the layer, and strongly increases near the anode (Figure 3-6-center). The induced charge is close to zero until the carriers do not enter into the region where weighting field increases. If the thickness of the detector is far greater than the penetration length of the incoming radiation the induced charge does not depend on the depth of interaction *z*.

Bolotnikov at al. [56] observed that detectors with rougher lateral surfaces yielded better spectra, even though they had higher electronic noise and leakage current. These observations have a straightforward explanation: the less polished crystal surfaces cause a higher surface leakage current, which, in turn, results in more uniform electric field distribution inside a detector, thereby improving the charge collection efficiency. However, reliable surface control is difficult to achieve with simple mechanical polishing. A more reliable method of producing such a conducting channel upon the surface is with a chemical process. The simulation of real electric field (Figure 3-6-right) is realized considering high leakage current on later surfaces.

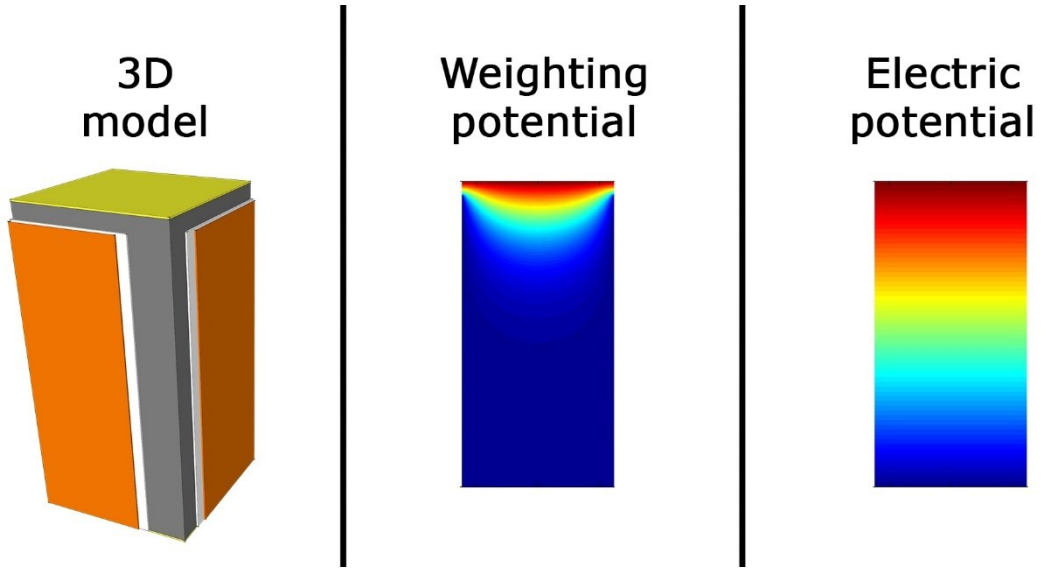

Figure 3-6. Example of virtual Frisch-grid detector (left), and related weighting (center) and electric potential (right)

Coplanar grid electrodes

Single polarity charge sensing was implemented on semiconductor detectors by Luke based on the use of coplanar grid electrodes in 1994 [57] [58]. The concept is illustrated in Figure 3-7-left. Instead of a single electrode on the anode, parallel strip electrodes are used and the strips are connected in an alternate manner to give two banks of grid electrodes (electrodes A and B). A voltage difference between these two banks of electrodes is applied so that the selected charge carriers (in this case electrons) are always collected by one electrode, say electrode A. The weighting potential of electrode A (V_w^A) within the device is calculated by letting the potential on electrode A be 1 and potentials on cathode and electrode B to be zero [59], and solving the Laplace equation (since there is no space charge). Similarly, the weighting potential of electrode B (V_w^B) is

calculated by letting the potential on electrode B be 1 and potentials on cathode and electrode A to be zero.

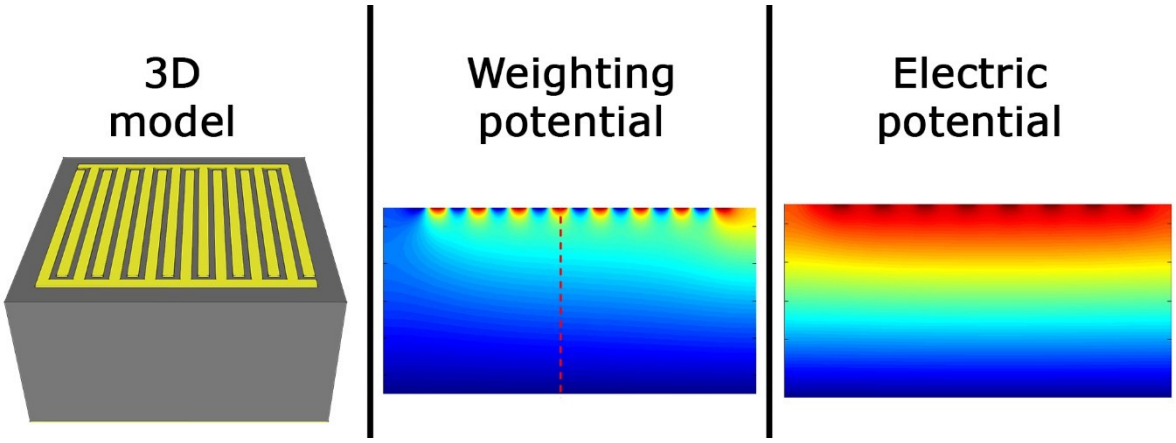

Figure 3-7. Example of coplanar detector (left), and related weighting (center) and electric potential (right)

Figure 3-8 shows the weighting potentials of each electrode along a line perpendicular to the electrode surfaces and intersecting with one strip of the collecting anode (A) at its center, such as along the red dotted line (*line r*) in the center of Figure 3-7. Notice, V_w^A and V_w^B are practically identical for 0<z<L-P, and then V_w^A approaches 1 and V_w^B drops back to zero rapidly. P is the period of coplanar grid electrodes and is much smaller than the thickness of the device L (P≪ L). Induced charges on the two grids are identical when electrons travel far from them (from 0 to L-P). This regime is followed by the rapid increase on electrode A and drop on electrode B back to zero when electrons approach grid A and deviate away from the B (from L-P to L). Single polarity charge sensing is implemented by reading out the difference signal between electrode A (collecting anode) and B (non-collecting anode). This differential signal corresponds to the weighting potential of $V_w^A - V_w^B$. It has zero net value for 0<z<L-P and rises from 0 to 1 when the charge travels from z=L-P to L. The shape of differential weighting potential is very similar than that of Frisch-grid and, with it, also the benefits.

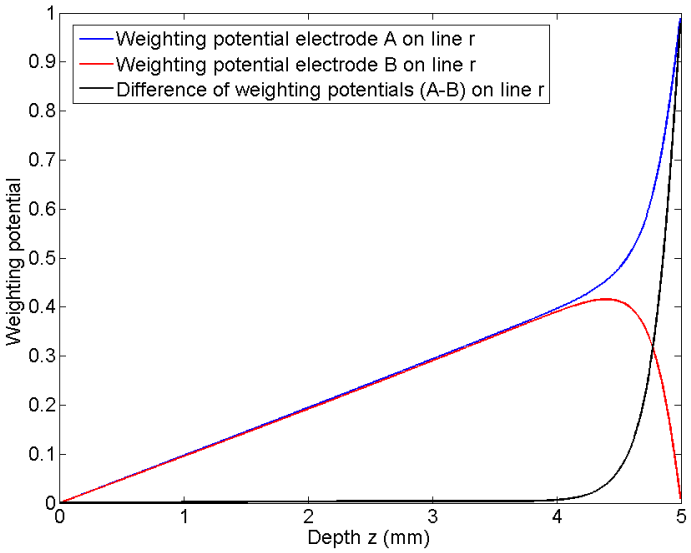

Figure 3-8. Weighting potential calculated on line r for electrode A and B. The black line represent the difference between the blue and the red one

Strip electrodes

Semiconductor detectors using strip electrodes were first motivated for two-dimensional position sensing [60] [61], and it was later realized that single polarity charge sensing can also be achieved by reading out signals from individual strip electrodes [59] [60] [61]. The induced charge on any particular strip is very low when charge carriers move far away (when the distance to the strip is much larger than the pitch of strip electrodes P) from the electrode. This can be understood by noting that the weighting potential of the specific strip electrode is determined by applying a unit potential on the strip electrode and zero potential on all other electrodes (other stripes and cathode). The weighting potential is very low in most of the detector volume except very close to the strip electrode. Furthermore, the bias voltages applied at the stripes are set in order to create an electric field that drives electrons to the collecting stripe. The resulting electric field increases moving towards to the collecting electrode, this means that the electrons induce charge only very close to the anode.

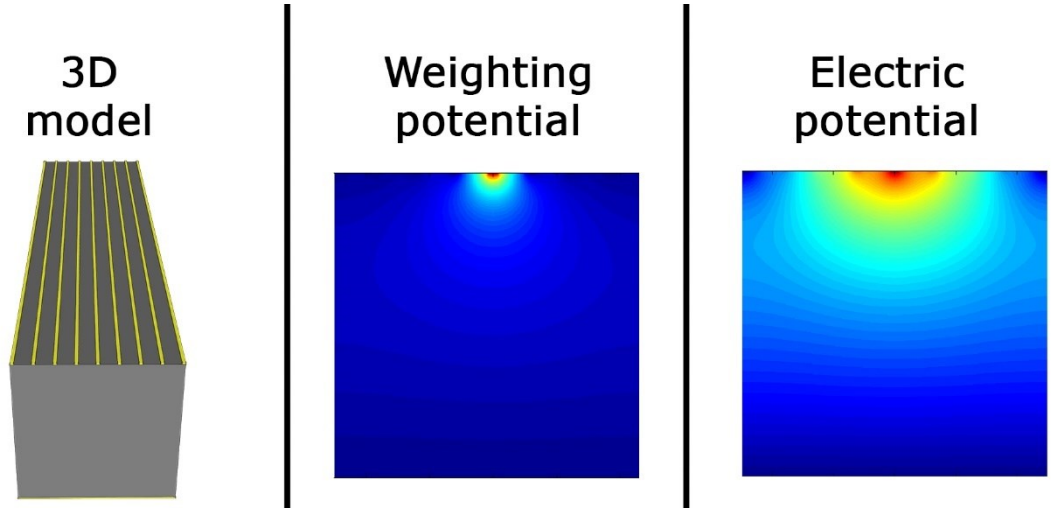

Figure 3-9. Example of stripes detector (left), and related weighting (center) and electric potential (right)

Hemispheric-like electrodes

The earliest single polarity charge sensing technique implemented on semiconductor γ-ray detectors was the development of hemispherical devices [62]. On those devices, a small dot anode was placed in the focus of the hemispheric cathode electrode (Figure 3-10-left) and the signal was read out from the small-area anode. The weighting potential of this small anode is calculated by applying a unit potential on the anode and grounding the cathode. The resulting weighting potential is very low within most volume of the detector and rises rapidly to 1 approaching the anode. Therefore, the induced charge on the anode is dominated by the movement of charge carriers close to the anode. Although significant improvement in γ-ray energy resolution was demonstrated, the realization of this type of detectors is not easy: the shaping of CZT to obtain a hemispheric cathode requires appropriate instruments.

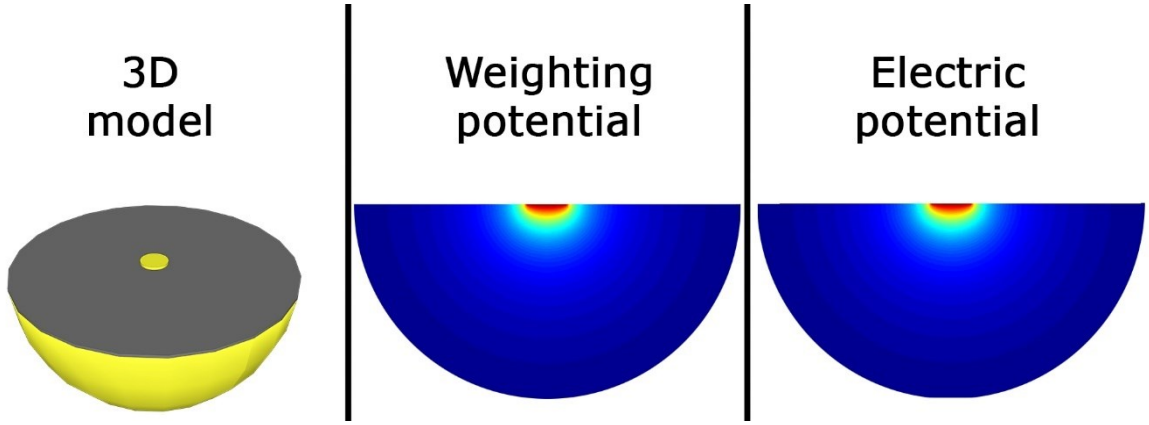

Figure 3-10. Example of hemispheric detector (left), and related weighting (center) and electric potential (right)

Quasi-hemispheric detector was proposed to overcome this problem [63]. The shape of weighting potential and also the electric field is very similar to the hemispheric one and it is easy to realize. The idea is to realize the hemispheric detector on a parallelepiped CZT block. This is achieved by maintaining the same shape of the anode and by simulating the hemispherical electrode covering the lateral surface and the cathode with metal.

A novel geometry, called *hemispheric-like,* (Figure 3-11-left) is proposed to simplify procedures even further. Hemispheric-like detector (that it is shown in Figure 3-11-left) is composed of a small circular pixel surrounded by a thin guarding at the anode, and a full area contact at the cathode (lateral surfaces are not contacted). Charge collection is optimized with a large gap between pixel and guard ring because in this way the thickness of guarding decrease and, with it, also the region with weak electric field under the guard ring. To best simulate the electric field of hemispheric detector, it is necessary to apply the same negative voltage at both cathode and guard ring and grounding the pixel. Hemispheric detector are also more versatile because it is possible set a different electric field between cathode and guard ring. In some cases, for example, with low-energetic incoming radiation, the best spectrum could be obtained setting differently the voltage of guard ring and cathode. Current that flows between pixel and guard ring ensures more uniform electric field distribution as in virtual Frisch-grid geometry.

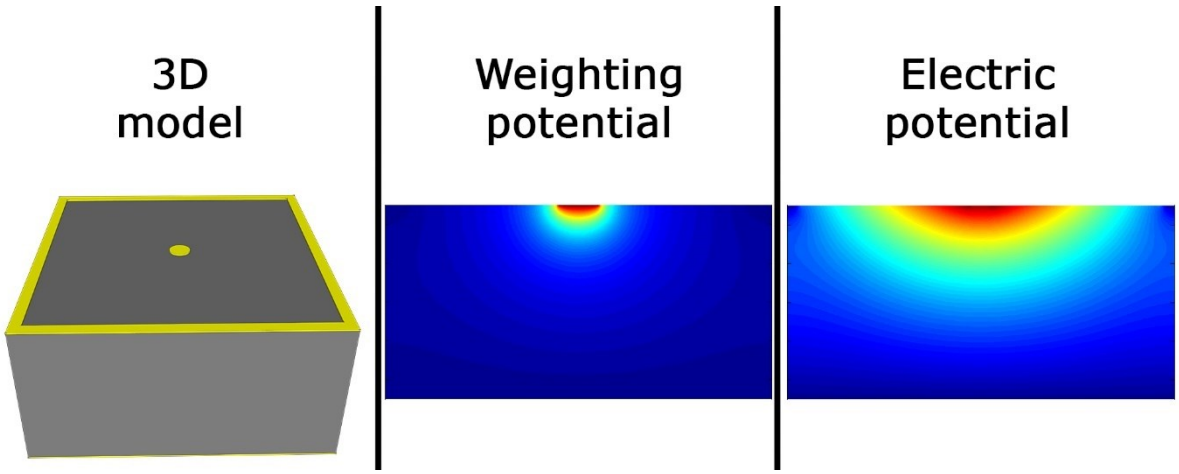

Figure 3-11. Example of hemispheric-like detector (left), and related weighting (center) and electric potential (right)

Pixelated detectors

Detectors that exploit pixelated anode arrays were also realized for two-dimensional position sensitive imaging applications [64] [65]. It was found that γ-ray energy resolution obtained from individual anode pixels on a CdZnTe detector was significantly improved compared to that from a conventional detector using planar electrodes. The readout signal of an individual pixel of an anode array suggests that pixelated detector is another form of single polarity charge sensing [66]. The induced charge on a particular anode pixel from the moving charge is very small when it is far away (the distance to the pixel is much greater than the pixel pitch P) and increases rapidly when the charge approaches the pixel. The weighting potential of an anode pixel along a plane passing through the center of that pixel is shown in Figure 3-12.

Anode layout can be:

- 2D array of small pixels that is widely employed in imaging applications [67] [68].
- 1D array of small pixels that is typically used in scanner applications [69].
- Mono-pixel anode that is often exploited for the experimentation [70].

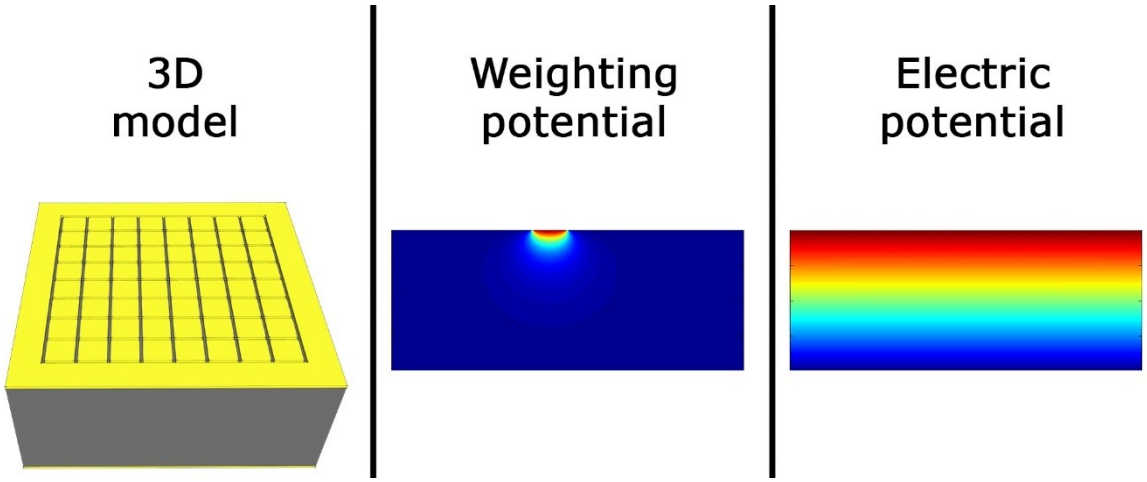

Figure 3-12. Example of pixelated detector (left), and related weighting (center) and electric potential (right)

Detectors with mono- or multi-pixelated anode are typically equipped with the guard ring electrode as shown in Figure 3-12-left. The utility of this special electrode is essentially the minimization of surface effects. It works by removing the contribution of lateral surfaces from the current that flows through pixels. Guarding becomes so important when the application requires high bias voltage because, by limiting the readout current, it reduces the electronic noise and improves the spectral resolution of detector.

4 Readout electronic

Until now the attention has been focused only on the properties of CZT and on the relevance of contacts (metal and geometry), but once developed the device with specific characteristics for the desired application, how is it possible to read the signal in order to obtain a spectrum? To answer this question it is important to know the type of output signal that is expected. When the radiation interact with CZT, electron and hole clouds are generated. A strong electric field is applied to avoid instantaneous recombination of photo-induced carriers. The two clouds drift in opposite direction under the effect of field and, thanks to Ramo-Shockley theorem (chapter 3.3.1), current transient is induced at device electrodes. The aim of readout electronic is to convert these weak current transients in an energy-resolved spectrum.

The wide range of applications leads to different solution to solve readout issue: for example in case of extremely high radiation flux (in excess of hundreds Mcps, typical of computer tomography) a spectroscopic response is not allowed but only a monochromatic imaging (obtained only by total current and not by the induced current of each event) is ensured.

4.1 Analog approach

Historically, the readout chain was completely analogical and composed by several stages.

Analog approach is employed even now for several applications when only few channels are required and radiation flux is low (up to dozens of kcps). This because electronics like that is easy to realize, low-cost and industrially-produced by companies such as Amptek and Cremat.

Figure 4-1 shows analog readout stages outlined in detail in the following sub-chapters.

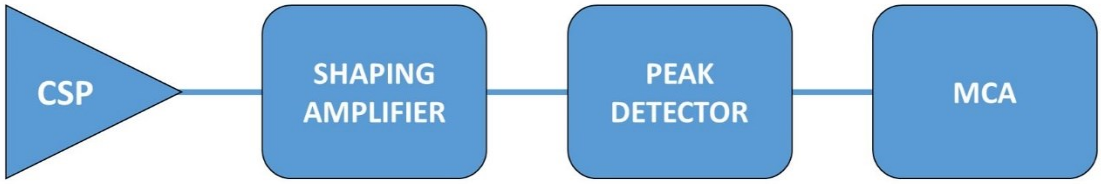

Figure 4-1. Readout stages

4.1.1 Charge Sensitive Preamplifier

The first stage of the chain is the charge sensitive preamplifier (CSP). Its design offers low noise, stability, and its integrating nature provides an output signal that is proportional to the total charge induced by the detector during the pulse event. It is for these reasons that CSPs are used in radiation detector applications where an individual detection pulse is needed.

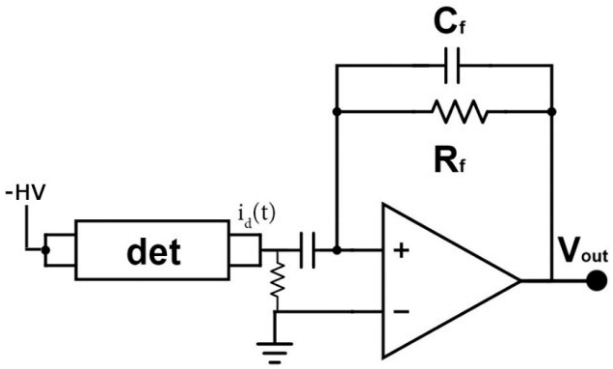

Figure 4-2. Basic CSP

The basic circuit of a CSP is shown in Figure 4-2. The output voltage is proportional to the integral of detector current and the gain of preamplifier is given by the feedback capacitor C_f. The feedback resistor R_f is needed to reset the signal: without this resistor the output would increase until the charge sensitive preamplifier reaches its maximum output. Feedback resistor is also named bleed resistor and typically has a high value (hundreds of MΩ) to ensure reset time about a hundred of microseconds long (Cremat board configuration in Figure 4-2).

$$V_{out}(t) = \frac{Q(t)}{C_f} = \frac{1}{C_f}\int_0^t i_d d\tau \qquad 4\text{-}1$$

$$\tau_{RC} = R_f C_f \overset{e.g.}{\Longrightarrow} 100M\Omega \cdot 1.4\text{pF} = 140\mu\text{s} \qquad 4\text{-}2$$

Equation 4-1 is true in high gain approximation.

Figure 4-3 shows the typical signal generated by the CSP: a) the detector pulse is generated by inducted charge, b) the "fast" CSP response due to integration process, c) the "slow" CSP response with exponential shape due to RC feedback.

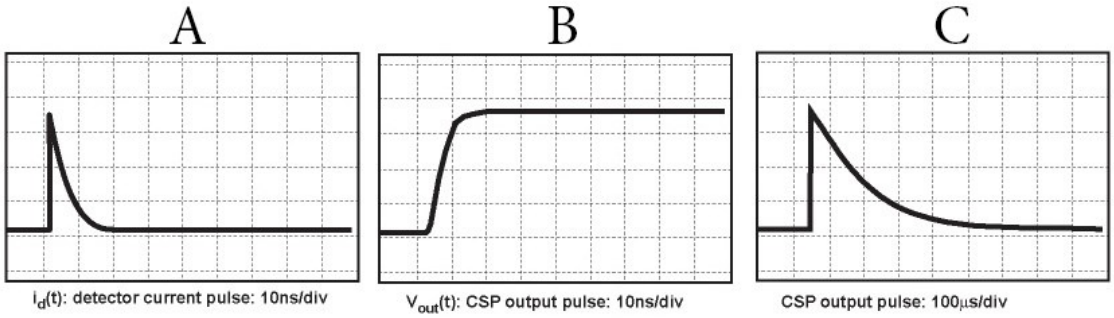

Figure 4-3. Typical shape of signals in commercial CSP [71]

4.1.2 Shaping Amplifier

Shaping amplifier is often used after the charge sensitive preamplifier stage. It has three main functions:

- Ti provides an output pulse that returns to baseline much faster than CSP output; this is important in high flux applications to avoid pile up.
- It filters noise coming from preamplifier stage.
- T gives extra gain to the signal, which may still be very small after CSP stage.

In Figure 4-4 it is schematically represented how the shaping amplifier processes the input signal. Typically shaping amplifier provides a Gaussian output. A dedicated trimmer mounted on this stage allows to improve the Gaussian shape of the signal. Shaping time of these amplifiers are variable in the range from 50 nanoseconds to few microseconds. The longer the shaping time , the better will be the signals in terms of low noise. The drawback is that a long shaping does not allow to increase input flux.

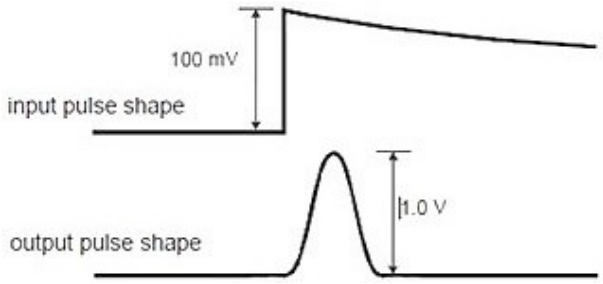

Figure 4-4. Signal processing in shaping amplifier [72]

4.1.3 Peak-Detector

Peak detectors capture and hold the maximum of the voltage signal. Ideally, the output of the peak detector circuit tracks or follows the input voltage until the maximum point is reached and then holds that value when the input decreases. Its aim is to hold the maximum value exiting from the shaping amplifier until the next stage, typically a multichannel analyzer (MCA), has read it and, after the digital resetting signal given by MCA, returns to the baseline pending for the next pulse.

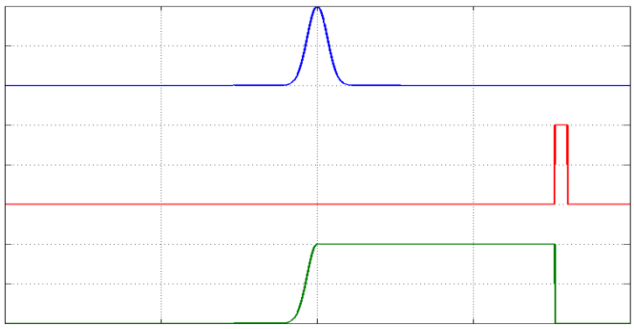

Figure 4-5. Shaping amplifier output (blue), digital reset signal (red), output signal of peak-detector

4.1.4 Multi-Channel Analyzer

The multichannel analyzer (MCA) is an important laboratory instrument, which can measure distributions of input signals.

It operates in two different modes: pulse height analyzer (PHA) mode, and multichannel scaler (MCS) mode. In PHA mode, the input pulses are sorted into bins (channels) according to their amplitude, while in MCS mode pulses are sorted according to their arrival time. Usually for detector application it is used in PHA mode.

MCA can have a digital output connectible to a computer for further analysis. The characteristics of a good MCA are:

- Fast reading of pulse signals (hold up by peak-detector)
- High number of channels in order to provide good resolution
- High input voltage range.

4.2 Digital approach

As it was discussed in the previous paragraph, the acquisition chain is usually ended by a logical unit (MCA) that convert analog signals in a digital output.

Analog chain described before only allows the readout the energy of incident radiation (photon, α or β particle). More information regarding the pulse are required in order to improve spectral energy resolution and to "clean" spectra by unwanted contributions. In order to make the system able to read all these information, several blocks of the chain must be interconnected. This approach is rather rigid because changing the hardware blocks is necessary in case other types of acquisition or measurement different parameters is required.

Another approach to readout systems for radiation devices is to digitalize the signal as soon as possible. The signal digitalization must be achieved by a fast ADC (analogic digital converter) to avoid information losses during the digitalization. Then analysis can be carried out in two different ways:

- Saving the whole waveform without any losses of information but widely using storage memory (all points of signal are acquired and stored).
- Making a fast online analysis and extrapolating only characterizing information of each pulse.

The first digital systems had an analog frontend electronics composed by a CSP and a shaping amplifier; after that, Gaussian-like signals were digitalized and analyzed in order to extract height and shaping time for each pulse.

Today thanks to the availability of fast digitizers (up to 100MS/s), it is also possible to acquire directly the CSP signal. Several benefits result from this approach. First of all, having directly the waveform of inducted charge, strong improvement on energy resolution due to pulse discrimination is possible.

Digital analysis is essential when radiation flux is greater than hundreds of kcps, because in these conditions with an analog chain pile up degrades completely the spectrum.

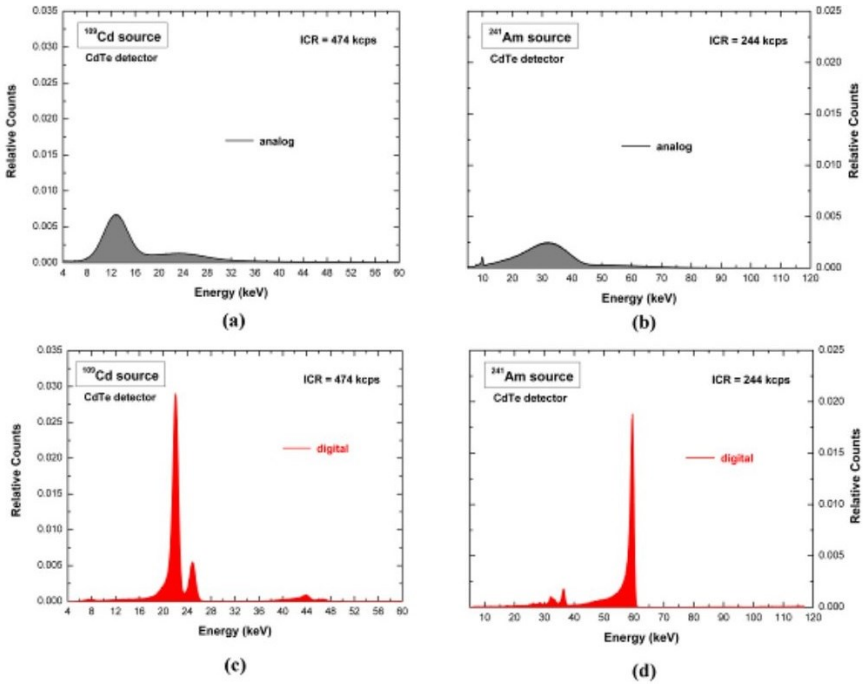

Figure 4-6. Spectra of ^{109}Cd (left) and ^{241}Am (right) with high radiation flux, analogic (up) and digital (down) approach [73]

Other important corrections are permitted with pixelated detector: time coincidence analysis of pulses on different pixels allows several improvement on spectrum and on spatial resolution. In the next chapters, the advantages of the digital approach will be experimentally demonstrated.

4.2.1 Digital Pulse Processing

Digital Pulse Shaping (DPP) systems, by digitizing and processing the output waveform from radiation detectors (i.e. the output CSP waveform), are able to save and perform multi-parameter analysis (arrival time, pulse width, pulse height pulse peaking time, etc.) even at high input counting rates (ICRs). With modern digitizer the DPP is achievable also onboard: this makes possible further increment of ICR because it is not necessary to save the whole waveform but only the main data of each peak.

Custom DPP developed by Abbene at al [70] [73] [74] and used for several spectra of this thesis is schematized in Figure 4-7. It is based on two pipelined shaping steps: a fast and a slow shaping. In the following paragraphs the two signal processing chains will be described.

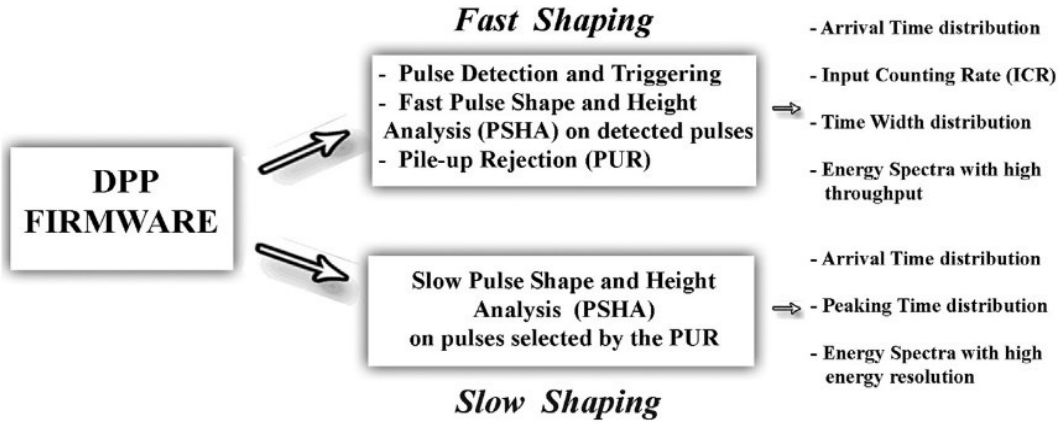

Figure 4-7. The main operations and output data of Abbene DPP system [74]

The CSP output waveform is shaped by using the classical single delay line (SDL) shaping technique [9]. SDL shaping is obtained by subtracting from the original pulse an attenuated fraction of the delayed replica. SDL shaping gives short rectangular output pulses with fast rise and fall times. Generally, two main features characterize the SDL shaping:

- The time width of each SDL shaped pulse is well defined.
- If the delay time is larger than the peaking time of the CSP pulse, the SDL shaping also preserves the leading edge (pulse height and peaking time) of each CSP output pulse.

These features make SDL shaping very appealing for timing and PSHA (pulse shape and height analysis) at both low and high ICRs. Through the fast SDL shaping the following operations are performed:

1. Pulse detection and time-tag triggering.
2. Fast pulse shape and height analysis (fast PSHA), that provides energy spectra with high throughputs (i.e. the OCR/ICR ratio, where OCR is the output-counting rate). The fast PSHA is performed on the SDL pulses by using a short delay time (but greater than the peaking time of the CSP pulses to avoid ballistic deficit) and a fast baseline recovery by using a running average value of a fixed number of samples preceding the SDL pulse, where no further pulses are present. Due to the short delay time, used to ensure high throughputs, the energy resolution of energy spectra is generally poorer than the resolution of the spectra obtained from the slow PSHA; the time width (one of the shape related parameters) of the SDL shaped pulses is also measured.

3. Pile-up rejection (PUR) for the slow analysis; the PUR is used to select time windows of the CSP waveform for the slow PSHA. Each selected time window of the CSP waveform is termed Snapshot, while the width of this window, user-selected, is termed Snapshot Time (ST). If two detected fast SDL pulses are within ST/2 of each other, then neither pulse will be selected; i.e. a pulse is accepted if it is not preceded and not followed by another pulse in the ST/2 time window periods.

The main feature of the slow SDL shaping is that the pulse height and shape analysis (PSHA) is performed on each PUR selected snapshot, containing only one CSP pulse. The pulse height analysis is performed by applying a SDL shaping with a delay time longer than the delay time of the fast SDL shaping. Automatic baseline restoration and optimized low-pass filter (trapezoidal filter) are applied for each slow SDL shaped pulse. The energy resolution strongly depends on the ST values, as the shaping time of classic analog systems. Through the slow SDL shaping, the system is able to provide, for each selected CSP pulse, the following results:

- Trigger time.
- Pulse height
- Peaking time.

The shape related parameters (the peaking time of the slow SDL shaped pulses and the time width of the fast SDL shaped pulses) and their relation with the pulse height are very helpful to improve the detector performance. Pulse shape discrimination (PSD) allows to minimize incomplete charge collection effects, pile-up and charge sharing. The output results from both channels are provided in listing mode, where each list is characterized by a user-selected number of event-sequences (typical fast channel sequence: arrival time, fast energy and pulse width; typical slow channel sequence: arrival time, slow energy and peaking time).

Both the time width of the pulses from the fast shaping and the ST are dead times for the system with a well-defined modeling [75](paralyzable deadtime, [76]). Figure 4-8 shows the throughput of the DPP system: the output photon counting rates (OCRs) from fast and slow shaping versus the true input counting rate (ICR). The purple and green lines are the paralyzable dead time model functions for the fast shaping (dead time of 200 ns) and slow shaping (with a snapshot time of 6 μs).

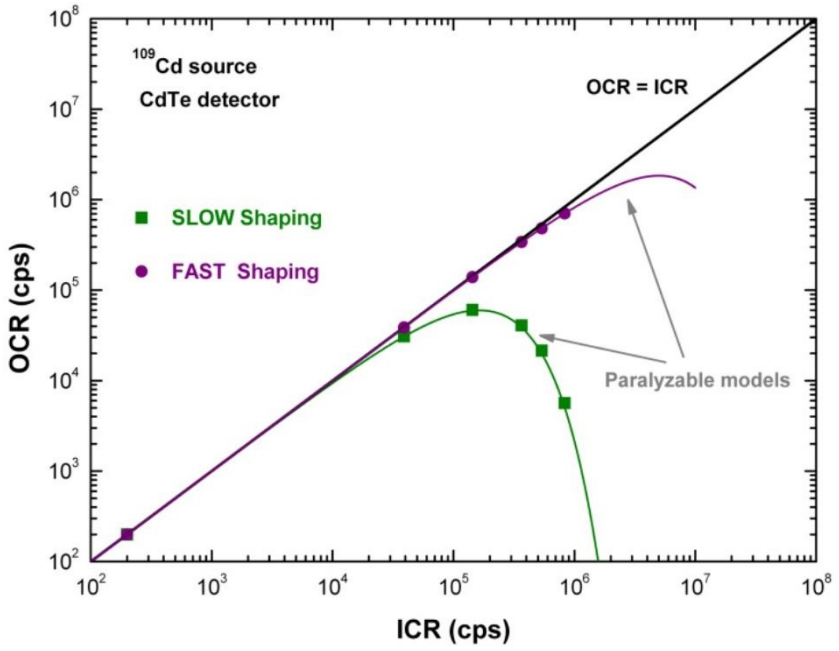

Figure 4-8. Throughput difference between fast and slow shaping [73]

For imaging applications several x-ray camera have been developed [77]. The research aim is to realize detectors increasingly spatial resolved. With this in mind pixel pitches are reduced year by year. This results in two main aspect:

- *Charge sharing* increment. The lower the pixels pitch the higher is the probability that the electron cloud is shared by two or more neighboring pixels.
- *Small pixel effect*. The weighting field for small pixels is close to zero until the anode vicinity: this is favorable because no induced charge is achieved when the weighting field is close to zero. Small pixel effect results in *single carriers devices* (avoiding the contribution of holes that in CZT have poor transport properties) and in independence of the depth of interaction of the induced charge. This means that these detectors have high-energy resolution and more symmetric peaks.

Two different corrections have been developed to avoid the spectral distortion due to charge sharing: *charge sharing discrimination* (CSD) and *addition* (CSA) [78].

Each frame of data recorded by the detector is inspected for multiple events that may occur in neighboring pixels. CSD algorithm removes shared event and not includes them in the processed spectra: this increases energy resolution but reduces the effective counting sensitivity defined as the ratio between events in the spectrum vs total events detected. In the CSA algorithm, the energy deposited in each pixel involved in the shared event is summed together and assigned to the pixel that originally received the largest proportion of the energy. Improvement of sensitivity compared to raw data is achieved, but algorithm suffers from a reduction of energy resolution due to an increase in noise and errors in the addition process. In Figure 4-9 are shown effects of these corrections.

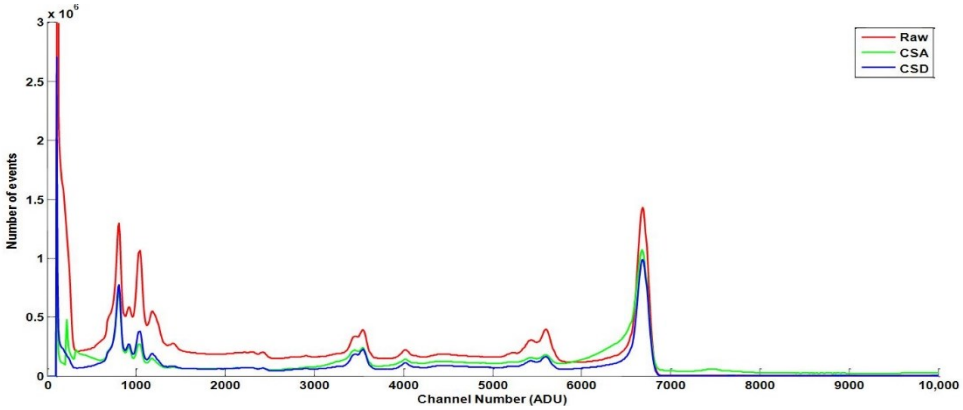

Figure 4-9. Spectra of raw data, charge sharing addition and charge sharing discrimination [79]

Frames of data with sharing information combined with those of timing are fundamental also for a new type of correction which seeks to reduce spatial resolution under the pixel size: the *subpixel positioning*. In the last decade several efforts are made to achieve position resolution better than the pitch of charge collecting electrodes in semiconductor detectors. Warburton [80], Burks et al. [81] and Williams et al. [22] proposed and demonstrated a method to obtain improved position resolution based on induced transient signals on non-charge-collecting electrodes in striped CdZnTe and HPGe detectors. Marks et al. [82], Vickersa and Chakrabarti [83] and Jakubek and Uher [84] studied several algorithms to achieve sub-pixel position resolution when an electron cloud is collected by several pixels in pixelated detectors. Narita et al. [85] showed the difference in the transient signals on neighboring non-charge-collecting pixels in pixelated CdZnTe detectors when the gamma-ray interaction position was changed [86].

Data acquired during the session at Diamond synchrotron are discussed in this thesis, even corrections described before (CSA, CSD and subpixel positioning) have been tested and results are shown in chapter 7.4.

4.3 ASIC

In the previous paragraphs devices for x-ray cameras have been mentioned. This device requires a detector with a large number (thousands) of very small pixels (down to 50 μm) [87] [88]. Standard electronics cannot reach these miniaturizations, so new systems had been developed. Application Specific Integrated Circuits (*ASICs*) were developed for solid state radiation detectors to miniaturize readout circuitry; ASICs implement several and parallel readout electronics, one channel for each pixel. Figure 4-10 shows the evolution of ASICs: in the years technology improvements have allowed to integrate all stages of the electronic chain (from CSP to MCA).

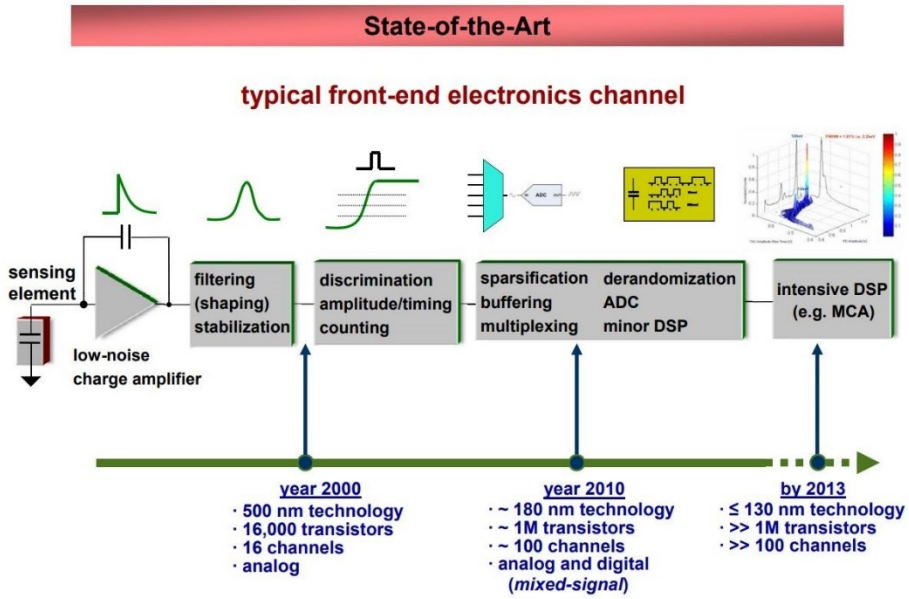

Figure 4-10. ASICs evolution [89]

For example a work on CMOS readout ASICs carried out at Brookhaven National Laboratory was presented in 1991 [89]. ASIC applications present significantly different challenges including readout for proportional chambers and silicon drift detectors. The techniques and insights acquired in the development of these new ASICs are also helpful in the readout of other radiation sensors like CdZnTe (CZT). The sections that follow describe two ASICs I worked on in the last year of my PhD: *PIXIE* and *HEXITEC*.

4.3.1 PIXIE

PIXIE ASIC consists of four arrays of 3x3 pixels matrix on which a single detector can be bonded. The detector anode consists of four different array of pixels as shown in Figure 4-11-B. Pitch of the largest array is 500 μm while the other three have 250 μm pitch. These pixel dimensions were chosen to be compatible with existing detectors allowing tests of different geometries. For each pixels it is present only the charge preamplifier (not the shaping one) and then an output buffer which is multiplexed directly off the chip. The chip has 2 selectable range: up to 150keV and up to 1.5MeV.

In Figure 4-11-C (on the top) the calibration circuit in the central pixel of each array can be seen. It allows to test ASIC sending a pulse signal through the preamplifier. This figure shows also a block diagram of individual pixel electronics. The feedback circuit was designed to permit detector leakage current up to 250 pA per pixel. The nine outputs from each arrays are multiplexed on to a common nine track analogue bus. The individual arrays can be selected modifying a 2-bit digital input. The outputs of all nine channel can be read out simultaneously to

study directly the CSP waveforms for each event. A total of 0.3W is required by the ASIC the majority of which is used by the buffer unit.

The PIXIE ASIC has a great advantage: the ability to mount detectors directly to low-noise electronics reducing noise source of wiring. Another advantage of the PIXIE ASIC is that multiple contact geometries can be tested on the same crystal. The use of a single piece of CdZnTe removes some of the uncertainty introduced from comparing different contact structures on different pieces of material. By digitizing the output of each channel it is also possible to directly study the effect of contact geometry on the shape of pulses generated by X-ray events.

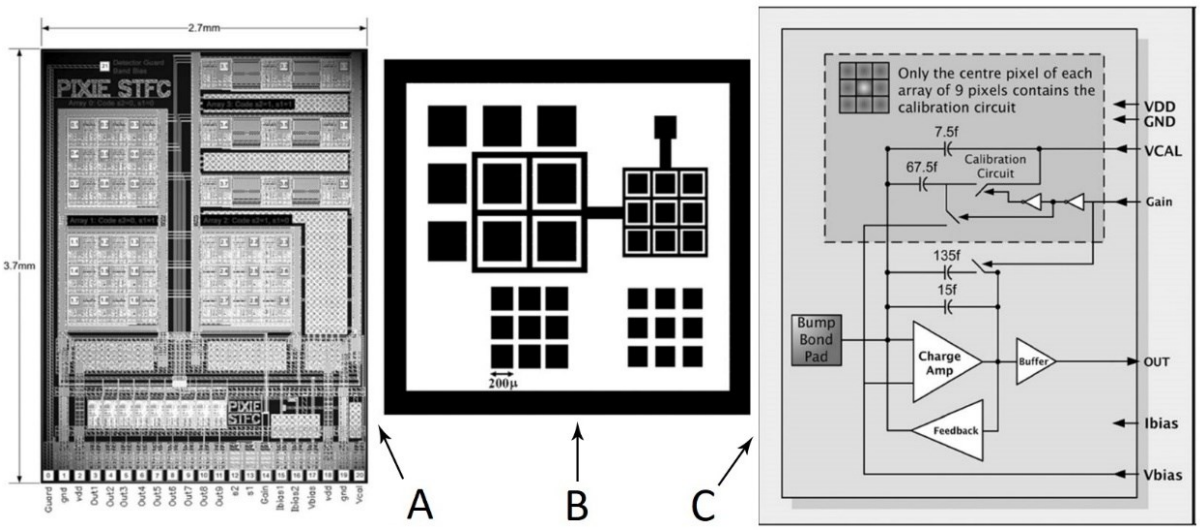

Figure 4-11. PIXIE ASIC: A) photo of circuit, B) detector geometry of four pixels array, C) schematic circuitry [90]

4.3.2 HEXITEC

The HEXITEC ASIC was developed for the readout of spectroscopic grade CdTe and CdZnTe detectors [91]. The ASIC works in two different gain range: 5–150 keV and 0.05–1.5 MeV. The original test structure consisted of an array of 20 × 20 channels on a 250 µm pitch but this has been extended to 80 × 80 channels in the final ASIC. Each parallel channel has identical pixel circuitry (Figure 4-12-right) with charge preamplifier, shaping amplifier (shaping time of 2µs) and peak-hold circuit. The charge preamplifier stands leakage current up to 50 pA per pixel. The detectors are controlled using a dedicated DAQ system: the ADCs digitize the analogue voltages from each peak hold and then store data locally by the FPGA before transfer to a control PC via Camera-Link. The DAQ system includes a temperature stabilizer able to register and hold the detector temperature in a range from -10 °C to 30 °C with a precision of ±0.1 °C. The ASIC has an on-chip monitoring circuit that records the temperature during operation.

The system gives as output one 2D-frame (80x80) every 25 µs (40 kHz) with the voltage value for each channel. The frames are sent to the PC for post-processing. Data stored on PC are saved in RAW format and can be processed with custom software or Matlab script in order to apply proper correction (such as CSD, CSA or subpixel positioning) and extract spectra or γ-images.

The system used in my PhD mounts a CZT detector realized by myself. It is shown in Figure 4-12-left. The realized detector is 2 mm thick and does not cover completely the 80x80 ASIC chip but about a quarter of it.

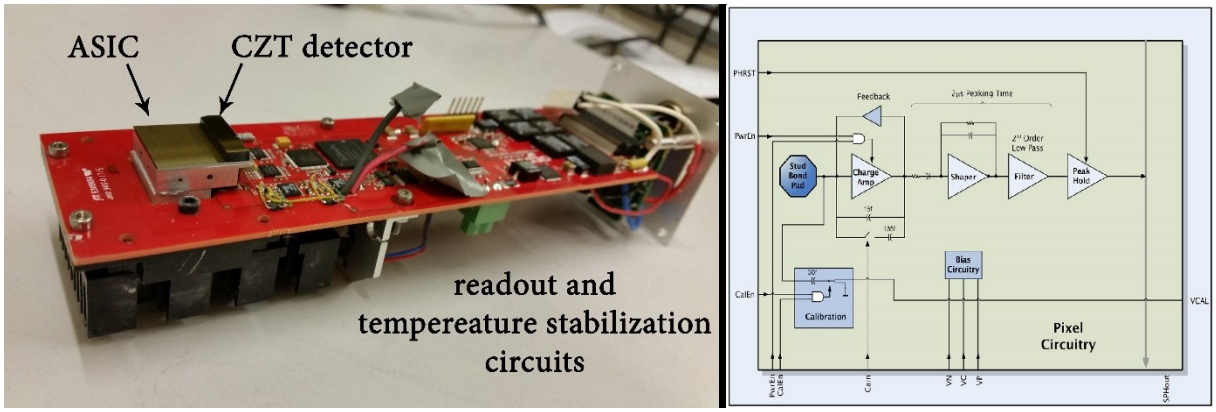

Figure 4-12. On the left: Hexitec ASIC with mounted CZT crystal (the detector do not cover all chip area) and on right: the circuitry for each pixel [91]

5 Experimental setups

In this chapter the experimental setups used for measurements of this thesis are described. Some are located in IMEM CNR laboratory and others have been used thanks to collaboration with other research groups. The development of some setups was part of my work.

5.1 Probe station (JV characteristic)

To study samples and, particularly their contacts, JV characteristics are fundamental. They provide important information on the detector characteristics and its functioning as radiation detector.

It is no trivial to perform this measurement on CZT device because of the high resistivity of the material: high resistivity results in very low measured currents (up to few pA); this is the reason why special instrumentation is required. It is necessary to perform this measurement inside a shielded box and use coaxial cable to minimize electric noise. The metal box guarantees conditions of total darkness, necessary due to the intrinsic photoconductivity of samples.

The *probe station* (Figure 5-1) used in our laboratory was realized during the period that I spent in IMEM for master degree thesis. Especially, I focused my effort on data acquisition achieved by PC, that automatically controls two Keithley instruments: sourcemeter 2410 and picoammeter 6548. Realized instrumentation allows us to perform measure at the state of art.

Figure 5-1. Probe station for JV characterization

Pixel detectors are typically realized with a surrounding guard ring at the anode. Guarding provides to limit the leakage current, which is the main responsible for base-line fluctuations in the CSP stage.

Measurements realized on detectors with a single pixel and guard ring (Figure 5-2-B) are achievable by using two amperometers and a voltage generator. In Figure 5-2 it is shown the used setup for monopixel detectors. Thanks to the presence of the guard ring, current that flows through the pixel is only due to carriers that travel inside the CZT.

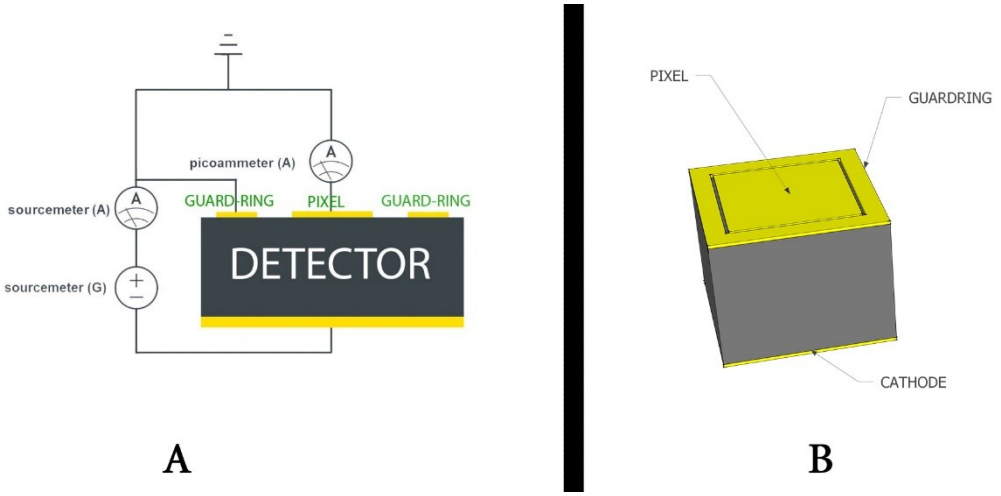

Figure 5-2. A) Standard electrical setting of detector measurements, B) typical monopixel detector

Monopixel detectors are used for several experiments in this thesis because they are easy to realize and, at the same time, allow to study several characteristics of final devices, such as: the metal of which contacts are made of, surface treatments, influence of geometry on detector performance, weighting field, electric field and properties of the CZT we used.

To connect electrodes:

- Samples are located on the brass support on the cathode-side (full area contact), the support is electrically connected at sourcemeter.
- Guard ring and pixel electrodes are connected by means of two tungsten tips and each tip is fixed on a three axial micro-positioner.

By using this system, it is possible to measure unbounded sample, because the electrical contact is ensured by the tips. To allow the right positioning of tips on electrodes it is used a *micro-stereoscope*. This is a fundamental instrument because sometimes tips must be located on a very small pixel such as 50µm.

Micro-stereoscope is a particular type of microscope that does not allow large zoom (up to 40x) but is equipped with large focus distance. This distance allows to work under the microscope with cumbersome instrumentation, as in our case. Under the stereoscope are located the brass support and the two micro-positioners. These last positioners are composed of three orthogonal sleds coupled with three micrometric screws in order to ensure high precision in all the three spatial dimensions. All these components are inside a cubic box with aluminum walls and two doors, that give the possibility to operate inside the box. The metallic box has two important functions: to electrically shield samples and to ensure their complete obscuration by the external light, that increases currents with photo-generation. All the measurement instrumentations (Keithleys and PC) are connected between them and placed out of the aluminum shell to avoid any electric noise. A capacitive-thermometer is placed inside box to monitor the temperature and, in order to better operate, is also placed a led light.

Tungsten tips and brass support are connected with BNC connectors outside the box, and then shielded cables (to not collect noise from the environment) carry signals at Keithleys. In the electrical scheme of Figure 5-2-A we have sourcemeter 2410 which is able to apply voltage (from 5μV to 1.1kV) and measure current (with a maximal resolution of ±10pA) simultaneously, and picoammeter 6485 that ensures a resolution three order of magnitude greater than sourcemeter (±10fA).

The use of these instruments is driven by their characteristics: picoammeter measures the weak current that goes through the detector bulk while the sourcemeter applies the selected voltage between cathode and anode and measures current that flows on lateral surface. Computer is connected with the instruments by using PCIB-USB module, that allows to control the instruments thanks to VISA commands.

To build IV curve, it is necessary to change the applied voltage and to measure the relative currents. This is achieved thanks to a custom software developed in LabView (by myself in master degree). During my PhD I have implemented it in Matlab, that ensures larger degree of freedom in terms of programming and data analysis. With this software, it is possible to produce non-linear ramps of voltage and to automatically save the IV curves of bulk and surface.

Non-linear ramp permits to acquire all requested data in a single swept, furthermore it allows to thicken points close to zero volt, with the aim to better calculate the resistivity of CZT. It is possible to directly set the value of potentials used for the sweep thanks to the use of Matlab. However a default ramp is defined and used for mostly samples. Default ramp requires two parameters: maximum of voltage to reach V_{max} (that is reached for both positive and negative voltages) and number of steps N.

$$V_{actual}(i) = V_{\max}\left(\frac{2i-N}{N}\right)^3 \qquad 5\text{-}1$$

V_{max} is set taking into account the total current that flows in detector: this voltage is set in order to have a maximum current of 10μA to avoid any danger for samples. Between the change of voltage and the readout of current, a preselected delay time is used to let equilibrate the detector and typical value such of delay is about 8-10 seconds. After the delay, each Keithley measures current and saves a selectable number of points (default value is 20) on which Matlab averages and saves the medium value.

This system was used to acquire all the IV curves shown in this thesis. The system has not a temperature control yet. In order to have JV characteristics at different temperatures, some measurements in this thesis were performed by Abbene and Principato the laboratory of Dipartimento di Fisica e Chimica (DiFC) of Palermo University. The cooperation with DiFC was carried out also in the frame of the PRIN Project No. 2012WM9MEP founded by the Italian Ministry for Education, University and Research (MIUR).

The DiFC system is composed by a Keithley 2410 Source Meter Unit (SMU) and a Keithley 236 SMU synchronized via external trigger link lines. In particular, the 2410 SMU, after the source value setting, sends a trigger to the 236 SMU, which starts the source-delay-measurement cycle. At the end of the AD conversion, the 236 SMU sends the trigger to the 2410 unit to start the setting of the new value. During each sweep operation, a maximum number of 101points was used. The time required to gather the data of a single IV curve mainly depends on the time delay value. Different delay time values, between the setting of the bias voltage and the starting of the current measuring phase, were used. The detectors were enclosed in a shielded box with a temperature control. So it was possible to perform IV curves at different temperatures with the guard ring of the detector held at the same zero potential of the pixel. The detector was enclosed in a shielded box placed on a Peltier thermal stage with temperature control within 0.1°C, and filled with nitrogen gas to prevent condensation. Further details of the experimental setup are reported in these papers [92] [93].

5.2 Tape test

Mechanical resistance of contacts deposited on CZT is still one of the great issues of these detectors. The problem is worsened by the impossibility of anneal them at high temperature; despite this is a well-known problem in CZT word, the weak adhesion of contacts is scarcely studied. This issue is aggravated in the case of electroless depositions.

ISO 2409 describes an easy test to evaluate film adhesion on a general substrate; the ISO outlines the method of a technique called *tape test.* If a film overcomes tape test, this means that it is stronger than a minimum value defined by the standard tape used.

The passages of tape test are:

- To apply a piece of tape at the metal surface and press it in order to optimize adhesion.
- To gently lift off the tape.
- To control the surface of substrate and of tape in order to discover the result of the test.

If the tape is clean and metal is not peeled by tape, the test is overcame, otherwise the test is failed. It is only a qualitative test, however it defines an adhesion threshold of contacts, that allows to compare different type of electroless deposition techniques.

Standard tapes have been fixed in order to make test reproducible [94] [95]. I have used adhesive 3M's tape, model *600 crystal* (transparent and with good adhesive quality). In the experimental chapter are reported several results of this test with different metal layers.

5.3 Readout electronics and radioactive sources

During my PhD, I have made several samples to study the influence of geometry and of constituent metal contacts and to validate theoretical prediction. A system to take spectra from samples it is needed to better characterize them. I built two different electronic readouts in order to test spectroscopy of manufactured detectors. These chains are completely analogic and are both composed of a commercial and a "homemade" part.

Both electronic chains are made up of elements that carry out the same duties but come from different vendors. In the following rows it is described in details only one of the two chains to better understand their working principle.

The electrical signals generated by detectors are very weak: e.g. if the energy of incident radiation is 100 keV, the amount of photogenerated pairs for each photon is about 21000 that is to say 3.4 fC of charge due to electrons. It means that electronics must be completely engineered to minimize electrical noise if we want to achieve spectra good signal to noise ration. In Figure 5-3 is shown a picture of the readout box where the different stages described below are highlighted:

- *Shielded box*, to avoid external noise.
- *Power supply and filters:* both external and internal alimentation are allowed. It is filtered with an active stage, anyway the internal one is less noising.
- *HV generator and filters:* in this case the high voltage applied to the detector is generated by a lab instrument and is driven inside the box by BNC connector. The HV is filtered with a simple RC passive circuit.
- *Detector plug:* the socket where the standard detector boards are plugged.
- *Test-in line:* it is a BNC connector on which it is possible to send a square wave to measure the electronic noise of the readout circuit.
- *CSP*, the preamplifier is manufactured by Amptek (model A250 mounted on PC250).

- *Shaping amplifier*, also manufactured by Amptek (The PC-275 Test Board accommodates three A275s and a BLR1 and produces a 5-pole pulse with 1 µs risetime).
- *MCA*, also manufactured by Amptek (model MCA8000D) composed of a peak-detector and a digitizer that sends data at computer via USB.

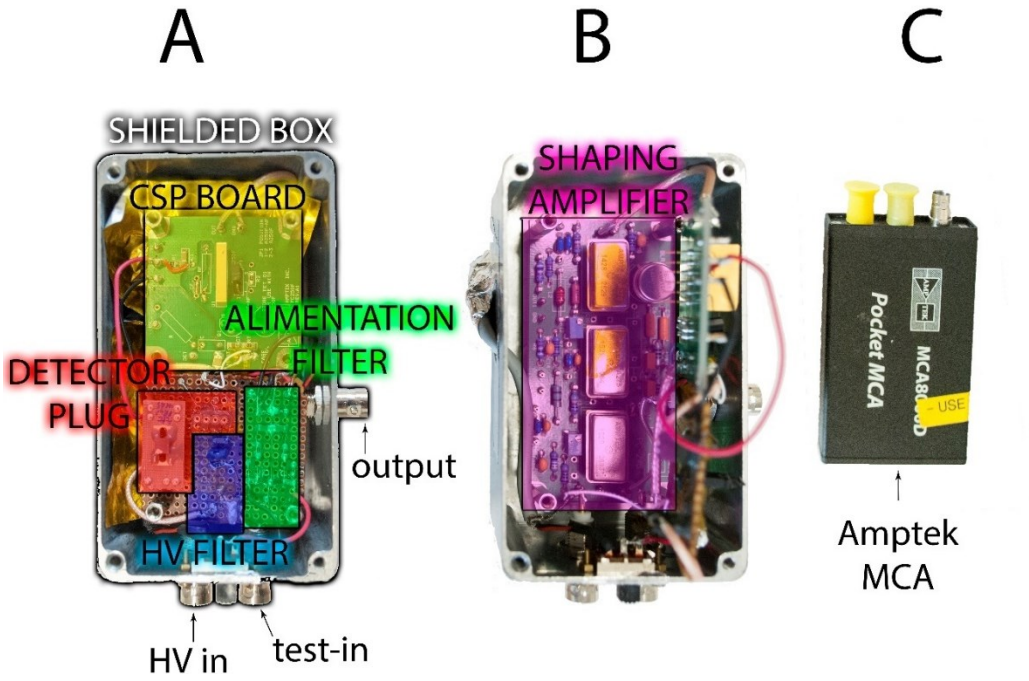

Figure 5-3. A) filters, plug board, CSP and B) shaping amplifier of Readout box. C) Amptek MCA

To test the detector performances and obtain energy resolution value, nuclear sources are required. The preliminary assays made on the majority of samples are obtained by using two sources shown in Figure 5-4:

- ^{57}Cobalt, gently divested by physic laboratory of Mössbauer's spectroscopy by researcher Gianfranco Galli. ^{57}Co is a gamma emitter with two main photoemission lines at 122.1 keV and 136.5 keV. Its half-life is 271 days and the activity of our source we used is about 10 µCi and this ensures spectra with discreet statistics in few minutes.
- ^{137}Cesium, it is located in physics lab under the supervision of professor Giuseppe Allodi, that kindly allows me to benefit from source. ^{137}Cs beta decays in ^{137m}Ba that in turn, after few minutes, decays with gamma emission at 662 keV. Its half-life is about 30 years.

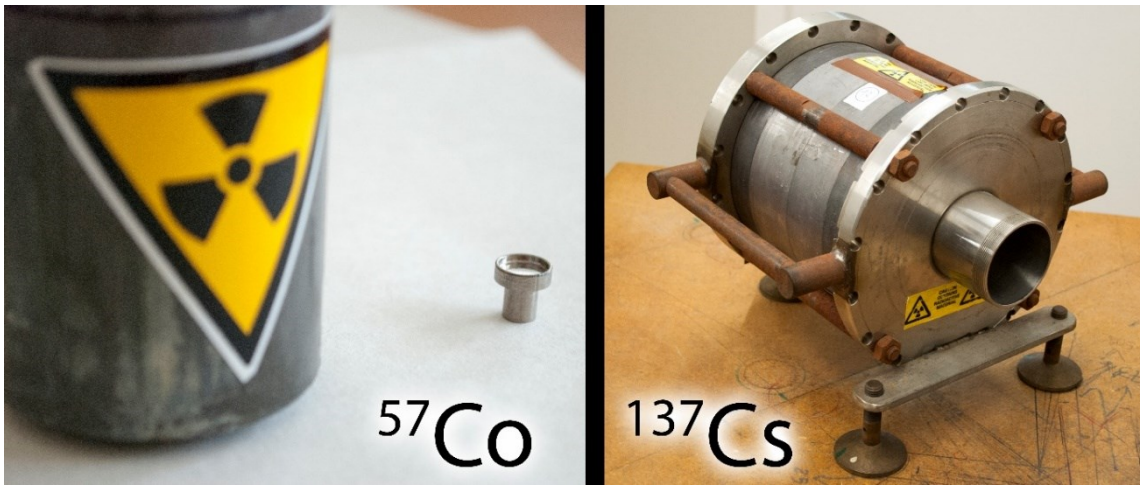

Figure 5-4. Nuclear sources used in my PhD, cobalt 57 on the left and cesium 137 on the right

Other sources are used for data acquired in this thesis, in particular X- and γ-ray calibration sources are employed at DiFC to collect several spectra reported in the experimental section 7. In particular:

- ^{109}Cd with emissions at 22.1 keV, 24.9 keV and 88.1 keV.
- ^{241}Am with emissions at 26.3 keV and 59.5 keV, two sources with different activities (0.1 MBq and 370 MBq). The neptunium L X-rays of the strongest source are shielded by the source holder.
- ^{57}Co with emissions at 122.1 keV and 136.5 keV, tungsten fluorescent lines produced by the source backing are present: $K_{\alpha 1}$=59.3keV, $K_{\alpha 2}$=58.0keV, $K_{\beta 1}$=67.2keV and $K_{\beta 3}$=66.9keV.

Another important employed source is the one used to test our UAV prototype described in section (7.5). The aim was to demonstrate that our drone is able to individuate a hidden source. To allow this experiment the source had to be strong enough to be felt by a 2.4 cm^3 detector up to 30 meters. Emiltest s.r.l. (company of Fidenza (PR) engaged on non destructive control on thick tubes for pipelines) provided us a powerful ^{192}Ir nuclear source of some dozens Curie (about 10^6 MBq) of intensity. Several emission lines are present in iridium spectrum: the main emissions are at: 300 keV (group of peaks), 468 keV, 600 keV (group of peaks), 880 keV and 1050 keV (group of peaks).

5.4 Setup of LI-TCT

Electric field profile inside the device can be measured by means of Pockels effect [96] [97]. An alternative method is the measure of the time of flight of charge carriers that cross the whole detector thickness. The current transient, induced by the charge generated as a consequence of irradiation with photons or alpha particles, can be fitted to evaluate the two most important transport physicals: mobility μ and lifetime τ. Under the strong assumption of a linear electric field profile or by imposing an infinite carrier lifetime, several efforts were spent to reconstruct the electric field from time of flight measurements [98] [99].

In collaboration with Pavesi's group of physics department in Parma, we have developed a new self-consistent method (described in subchapter 5.4.1) based on the laser induced transient current technique (LI-TCT). The procedure allows to reconstruct the spatial profile of the electric field along the thickness of CZT detectors and to extract one by one the transport parameters (μ mobility and τ life-time) without any assumption on the electric field profile [100]. Therefore, with this technique it is possible to study the quality of the material and polarization effects in different conditions of bias voltage and temperature.

Making use of a Nd:YAG Polaris II laser system, samples have been optically excited impinging an area of about some dozens of μm in diameter, at the center of the cathode (see Figure 5-5). 532nm pulses (second harmonic of Nd:YAG laser) are 10 ns long, and with maximum repetition rate of 20Hz. Light is simultaneously brought with two optical fibers of the same length on the sample and on a fast photodiode that acts as trigger for the pulses. The pulse energy released on the CZT is the same for all the acquired current transients. The energy value has been estimated less than 100pJ, anyway the value of output energy of laser is simply tunable by using the laser control. Due to the short penetration depth at energies above the energy gap, the pair generation takes place immediately beneath the electrode and the current pulse arises from the drift of a single carrier type. In order to reduce noise contribution and little fluctuation of photogenerated charge, a few thousands of current pulses have been averaged thanks to the trigger system. The samples are totally encapsulated with a special epoxy, except a little hole where the optical fiber is connected. This prevents absorption of reflected or diffused light through lateral surfaces. It is important to

prevent unwanted charge generation if not only under the metal contact where the laser is focused. The diameter of laser spot that hits the sample is about 200 μm.

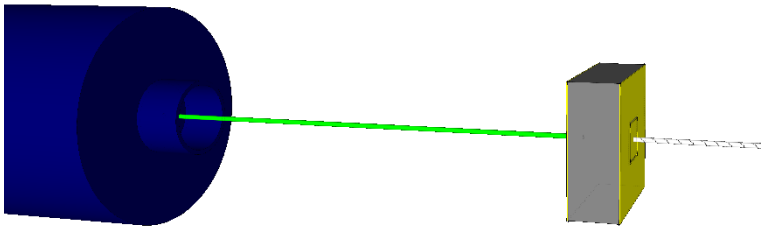

Figure 5-5. Schematically representation of TCT: the laser light hit the cathode in correspondence of center of the anodic pixel

The output signals have been amplified by a homemade amplifier with bandwidth of 80 MHz, that ensures a time constant of 2 ns that is comparable with the nominal laser pulse width. The signal is converted into a voltage pulse with a conversion factor of 105 V/A and acquired by a Digital Storage Oscilloscope Owon SDS8202 (200 MHz of bandwidth and 2 GS/s of sample rate). The oscilloscope is connected to a PC that downloads transient data and averages them by means of Matlab program. Approximately 10^4 signals are acquired to reduce random noise by a factor of 100. Bias voltage has been supplied by a Keithley 2400 High Voltage Source-Measure Unit. The experimental setup for LI-TCT is shown in Figure 5-6.

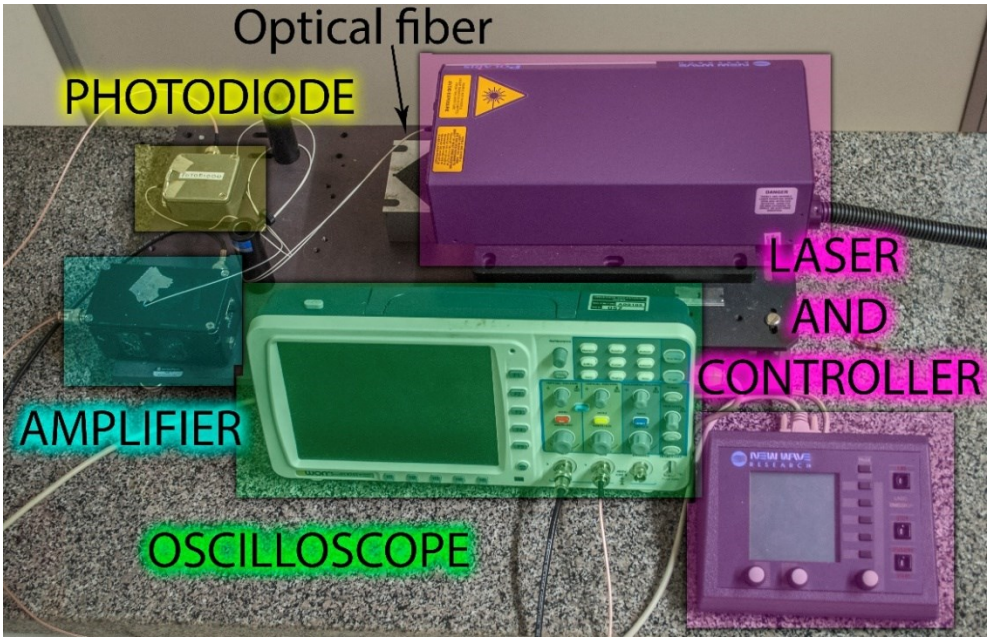

Figure 5-6. Experimental Setup of LI-TCT with highlighted the different stages

5.4.1 Self-consistent method for the analysis of experimental data

In the following rows I want to briefly explain the self-consistent method developed in collaboration with Andrea Santi during my PhD. The method allows to extract electric field profile and transport parameters for electrons and holes in a generic CZT detectors. The power of this method is that it is applicable directly on the final device and does not damage it. In addition, thanks to the simulation of weighting field, no geometric constricts on contacts are required (it means that we can measure samples with any contact geometry). Moreover, both electron and

hole parameters are simply achievable by changing sign of bias voltage. The aim of following description is only to underline the main steps of the method. Further details and exhaustive description were reported in PhD thesis of Andrea Santi [52].

The Diffusion of photogenerated charge is not very influential: the final spatial spread of the charge package is much less of the thickness of the sample. For example, the spatial spread of charge density in a sample 1 mm thick and biased with 100 V is about 15 μm [52].

Also detrapping phenomena are negligible since the characteristic times are greater than 100 μs, values about 100 times greater than typical times of flight in our experiments [52]. Only an infinitesimal fraction of trapped carriers are able to escape from the traps and to take part in the signal.

Tacking into account previous evaluations, diffusion of charge during drift and detrapping phenomena are assumed to be negligible. In these conditions, charge is only subjected to:

- Generation close to the illuminated electrode.
- Drift toward the collecting electrode with a speed proportional to the local electric field.
- Trapping during its flight with a rate related to the inverse of life-time τ.

Since the carriers are generated immediately under the illuminated electrode, a single carrier equation can be obtained from 3-15:

$$I(t) = q(t)\mu \boldsymbol{E}\big(\boldsymbol{r}(t)\big) \cdot \boldsymbol{W}\big(\boldsymbol{r}(t)\big) \qquad 5\text{-}2$$

And finally, by introducing trapping:

$$I(t) = q_0 e^{-\frac{t}{\tau}} \mu \boldsymbol{E}\big(\boldsymbol{r}(t)\big) \cdot \boldsymbol{W}\big(\boldsymbol{r}(t)\big) \qquad 5\text{-}3$$

where q_0 is the initial charge of photogenerated cloud and τ is the life-time of selected carriers. By neglecting diffusion, the trajectory of carriers ($\boldsymbol{r}(t)$) becomes one dimensional and the math treatment results simplified. For these reasons, in the further formula, we consider a mono-dimensional motion with law $r(t)$.

A set of current transients with different applied voltage V_i and with same generated total charge (that means acquired with the same laser pulse energy) is required. Sub-index i indicates that the relative physical is related to i-th transient with related applied voltage.

The transit time is established thanks to the first derivative of the transient signal: the local minimum of the derivate matches the inflection point in the transient decreasing. This point is considered as the end of the transient.

The method could be summarized in four steps:

1. Achievement of $\boldsymbol{q_{tot}}$ and $\boldsymbol{\tau}$: from the definition of weighting potential we know that $\int_0^L W(r_i)dr_i \stackrel{\text{def}}{=} 1$. The differential dr_i is rewritable as $v(r_i)dt$ then, by replacing it in the previous formula, we obtain $\int_0^{T_{R_i}} W\big(r_i(t)\big)\mu E_i\big(r_i(t)\big)dt = 1$. The argument of integral is similar to induced current (5-3) so, with another substitution, we obtain $\int_0^{T_{R_i}} \frac{I_i(t)}{q_0 e^{-t/\tau}} dt = 1$. Finally we can write $q_0 = \int_0^{T_{R_i}} I_i(t) e^{\frac{t}{\tau}} dt$. q_0 and τ is independent by the index i, then we can obtain their value looking for the τ value that minimizes the q_0 chi square.
2. By replacing $v_i(t) = \mu E_i\big(r_i(t)\big)$ in the integral form of hourly law $r_i(t) = \int_0^t v(t')dt'$, we obtain $r_i(t) = \int_0^t \mu E_i\big(r_i(t')\big)dt'$. So, by using the 5-3 in the same way of step 1, the formula becomes:

$$r_i(t) = \int_0^t \frac{I_i(t')e^{t'/\tau}}{q_0 W\left(r_i(t')\right)} dt' \quad 5\text{-}4$$

To know $W\left(r_i(t)\right)$, that is the weighting field that carriers feel in time t, we must know the hourly law $r_i(t)$ in order to turn the time dependence into spatial one ($W(x)$) that is obtained by numerical simulation.

3. The third step is to solve the self-consistent problem in equation 5-4 and to obtain simultaneously $\boldsymbol{r_i}(t)$ and $\boldsymbol{W}\left(\boldsymbol{r_i}(t)\right)$. Self-consistent problem is solved by using a *while* cycle that improves step by step the $r_i(t)$. The cycle ends when the square deviation of last two hourly laws ($r_i(t)$ and $r_{i-1}(t)$) reaches a preset threshold. A uniform electric field is assumed as initial condition, so carrier speed is constant and $r_i^0\ (t) = L\frac{t}{T_{r_i}}$. In the k-th iteration hourly law is calculated by $r_i^k(t) = \int_0^t \frac{I_i(t')e^{\frac{t'}{\tau}}}{q_{tot} W\left(r_i^{k-1}(t')\right)} dt'$. This process is applied for all transients $I_i(t)$.
4. By knowing the hourly law we can write the inverse function $t(r_i)$ and we can obtain value of $\boldsymbol{\mu}$ and electric field profile $\boldsymbol{E}(\boldsymbol{r})$**.** From equation 5-3 it follows that:

$$\mu E_i(r) = \frac{I_i\left(t(r_i)\right)e^{\frac{t(r_i)}{\tau}}}{q_{tot} W(r)} \quad 5\text{-}5$$

Now we can obtain mobility as average of $\mu_i = \frac{\int_0^L \mu E_i(r)dr}{\int_0^L E_i dr} = \frac{\int_0^L \mu E_i(r)dr}{V_i}$ on i and thanks to 5-5 $E(r)$ is also achieved.

The described procedure was implemented with Matlab and was optimized in collaboration with Andrea Santi. Several samples were analyzed in my PhD by using this method. A large amount of data obtained from measures were published or presented at IEEE conference [101] [50] [102].

5.5 Diamond synchrotron

In the February of 2017, I had the pleasure to take part in an experiment at the synchrotron near Oxford in collaboration with Abbene's group (university of Palermo) and Veale's group (Rutherford Appleton Laboratory). In 2016 our proposal was accepted and we had five days of beam-time at line B16. After the analysis of results originating from the experiment, we reapplied and we were selected for carrying on other experiments in 2018.

In the following rows, I want to describe firstly diamond synchrotron and then the setup of our experiment.

Diamond Light Source (Figure 5-7) is a 3GeV synchrotron inside the Harwell Science and Innovation Campus in South Oxfordshire, UK. It was founded by UK government thanks to Wellcome Trust and Science and Technology Facilities Council. Diamond activities started in January 2007 and currently has 22 operative beamlines. The facility welcomes either industrial companies or academic scientists from both UK and international research groups.

Figure 5-7. Above view of Diamond facility

Diamond works like a giant microscope. By exploiting the bright light produced by fast electrons, it is possible to study with high resolution anything: from fossils to jet engines to viruses and vaccines.

The synchrotron accelerates electrons close to light speed on a circular trajectory and, thanks to the centripetal acceleration, electrons give off brighter light composed by high-energy photons. These photon beams are then directed into laboratories known as 'beamlines' that are tangential to the ring and all around it (Figure 5-8-left). Here scientists have at their disposal a bright and strongly collimated (up to few square microns) beam that can be made monochromatic.

We worked in beamline B16, that is a flexible and versatile beamline for testing new developments in optics and detector technology and for trialing new experimental techniques. B16 provides both white and monochromatic X-rays from 4 up to 50 keV in several operational modes.

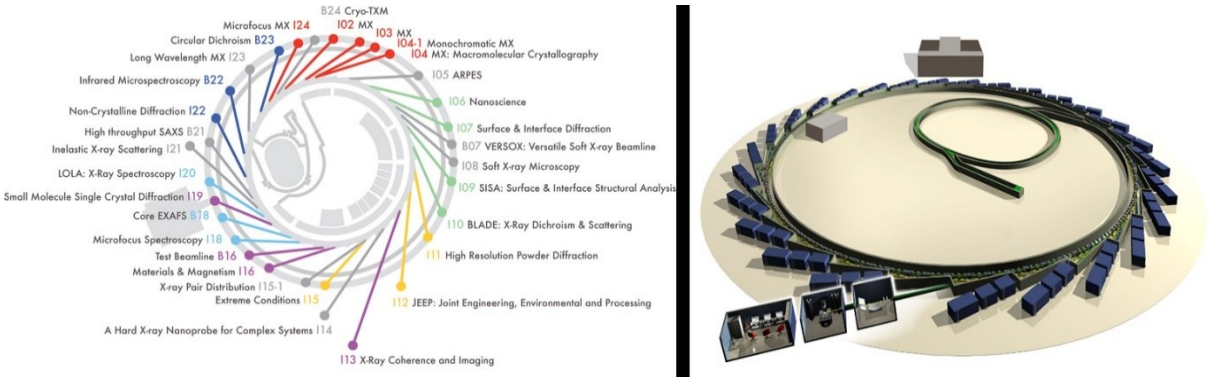

Figure 5-8. Beamlines map of Diamond (left) and 3D render of typical beamline lab (right)

In beamline B16 we mounted our instrumentation for the experiment. The experiment was completed using the PIXIE system (chapter 4.3.1) with two different CZT devices. The first was 1 mm thick and fabricated by myself by using material from Redlen, the second was purchased from Redlen Technologies and was produced using a new high-flux grade CdZnTe material.

The first detector was realized to be bonded on a PIXIE ASIC. The PIXIE ASIC have a standard contact design: full area cathode and pixelated anode (see Figure 5-9). The anode has four pixel arrays 3x3, three of them have a pixel pitch of 250 μm and the last of 500 μm. The detectors were realized with the standard procedure described in chapter 6.

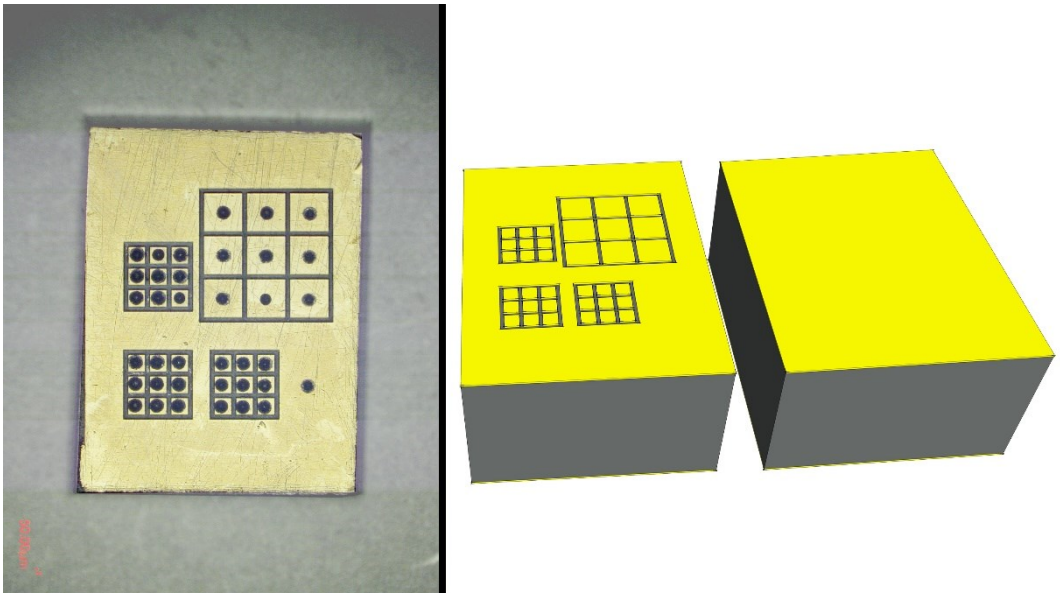

Figure 5-9. PIXIE detector produced by myself with the bonding spots on the anode surface (left), 3D design of PIXIE detectors (right)

Detectors operated at ~2 °C. Signals from PIXIE-ASIC were digitized using CAEN instrumentation and after analyzed using Labview and Matlab custom programs. Software and firmware, developed by Leonardo Abbene at DiFC, allowed to save pulse height, arrival time and time width for each X-ray interaction up to 1 Mcps rate.

The system was located in the optic table of beamline and a fine beam of 10x10 μm^2 was defined using JJ-slits. A second set of anti-scatter slits, that were mounted on the optic table, were also used to ensure clean beam profile. Two different energies, obtained by means of channel cut monochromator, were used for the experiment: 10 keV and 50 keV. The beam spot was moved on the detector by using the sample stages with step sizes of 12.5 µm and 25 µm. We performed with this setup 1D and 2D scans for both array types of both samples. Figure 5-10 shows the experimental setup in two different views.

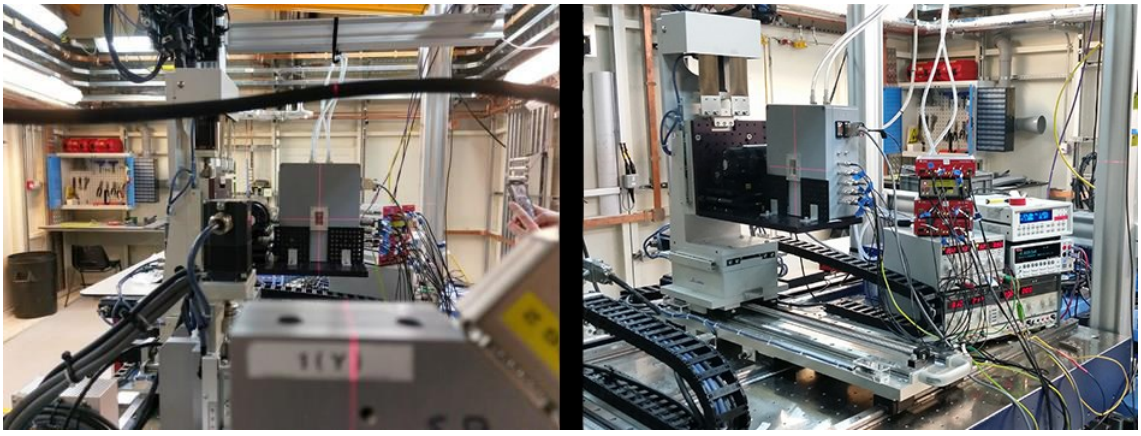

Figure 5-10. "Beam" view with red laser lines to assist the sample centering (left), PIXIE box and readout electronics (right)

Also HEXITEC system was tested. The ASIC, equipped with IMEM detector, was mounted on the same support of PIXIE board. The HEXITEC detector is 2.5 mm thick with a full area cathode and pixelated anode (Figure 5-11). The latter is compound by a 20x75 pixels array surrounded by guard ring. Firstly the beam was aligned at the center of pixel 11,48 (row, column) and after a 1D scan was performed up to pixel 11,52. We used beam energy of 25 keV and 50 keV for this

experiment. Finally ^{57}Co and ^{241}Am spectra were measured in a lead-shielded box. All data were taken in RAW mode for further analysis and studies.

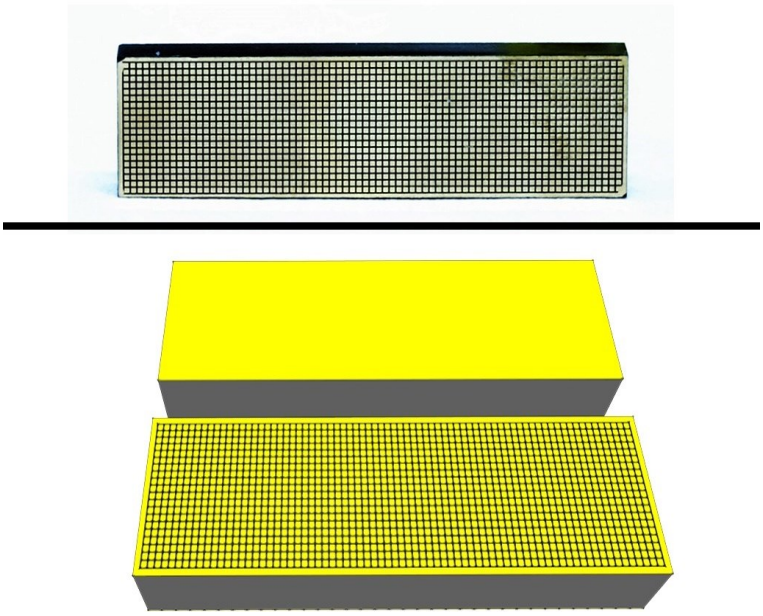

Figure 5-11. HEXITEC detector manufactured by myself (top), and its 3D model (bottom)

6 Detector realization

Some rules should be kept in mind during sample preparation:

- Processing temperature must always be lower than 120°C.
- Work must be performed in a clean room.
- High purity solvent and chemicals must be used.

The complete process to realize CZT-based γ-ray detectors will be carefully described in this chapter starting from the material selection up to detector bounding on its breadboard.

6.1 Material selection

An accurate selection of material is needed to obtain detector with good transport properties and consequently high resolution.

CZT must have high resistivity (greater than $10^{10}\Omega$cm) and shall not contain extended defects such as grain boundaries, cracks or twins.

We work with two different CZT materials: one type is commercial purchased by Redlen supplier and the other coming from the ingots growth in IMEM-CNR by boron encapsulated vertical Bridgman (described in 2.4.4).

The material bought from Redlen is already selected and tested. Purchased detectors are monolithic and monocrystalline with typical size of 20x20x6 mm^3 and they only need to be cut in order to minimize material waste.

When we process IMEM material we have to select monocrystalline regions and to optimize the cutting step to minimize CZT waste. Two-inches ingots are generally cut in wafers 3 or 5 mm thick perpendicularly to the growth direction (Figure 6-1). If we cut them in slices alongside the growth direction we would get larger single samples but strongly heterogeneous because of zinc segregation.

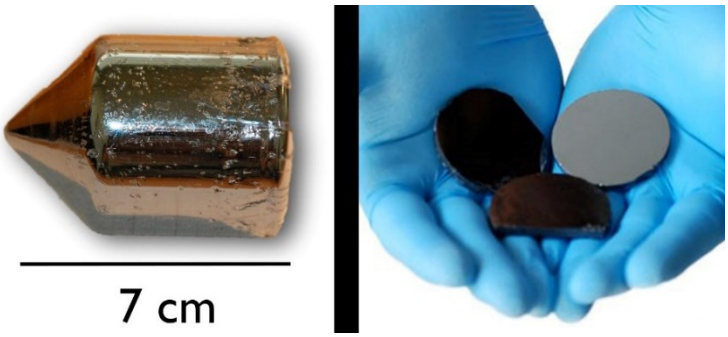

Figure 6-1. CZT ingots grown at IMEM (left), cut wafers (right)

A simple but functional method is used to highlight with precision the monocrystalline blocks. Both faces of all wafers are photographed by placing the illumination in order to maximize the contrast between different grains. In post-processing, the images are cleaned and photo-

parameters are tuned in order to better point out different grains. One of the two faces of wafer is mirrored and overlapped at the other one. In this way, it is possible to highlight on the image the monocrystalline border and to take the cutting measure with precision. Figure 6-2 shows the partial photos and the final result of process (bottom).

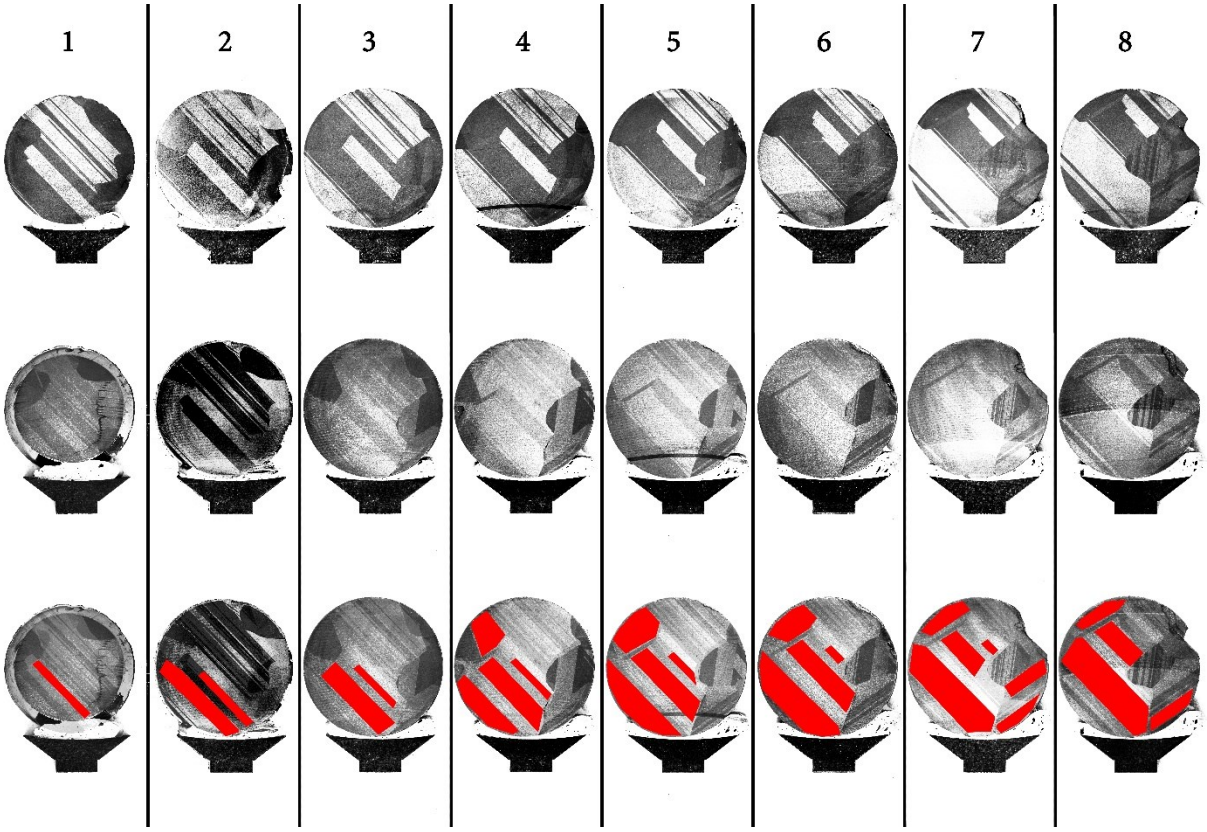

Figure 6-2. top view of wafers (top), bottom view of wafer reflected (middle) and monocrystalline zone selection red colored (bottom)

Cutting follows the material selection step. It is used a static circular saw with internal blade (Meyer Burger Annular Saw TS 23) shown in Figure 6-3. This machine is able to make accurate cuts and, by using specific arrangement, avoids the generation of new extended cracks on the sample border (although in the first microns are present some defects due to mechanical stress).

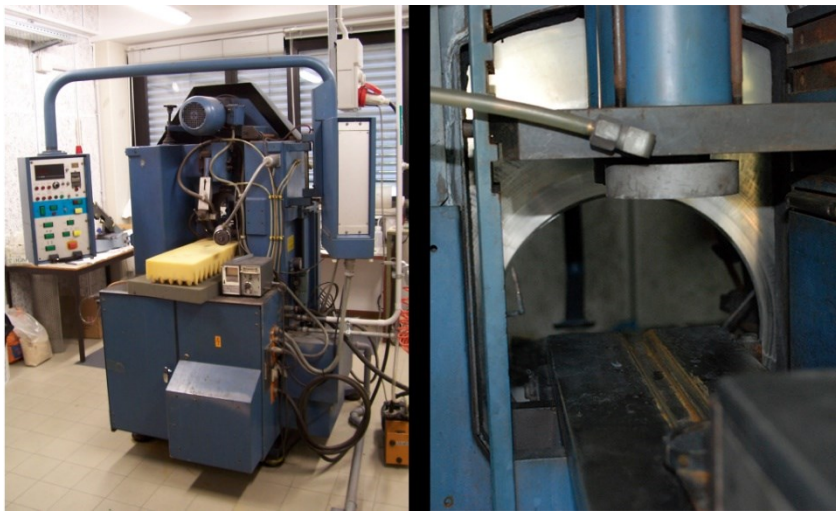

Figure 6-3. Meyer circular saw, in the right image it is visible the internal blade and the moving stage

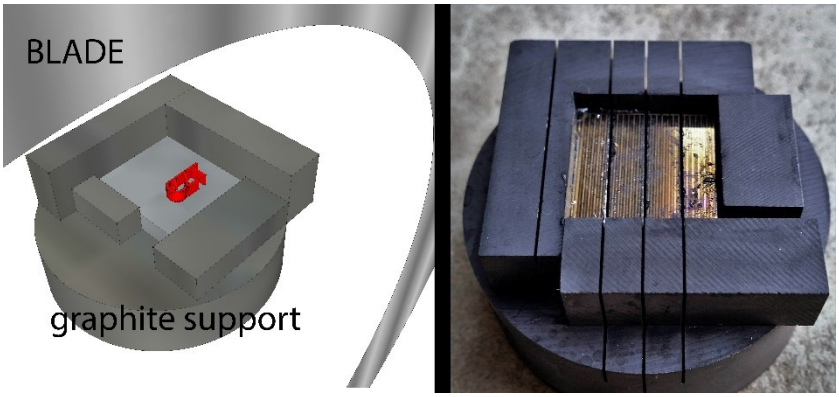

Figure 6-4. Cutting scheme (left), cut CZT sample (right)

6.2 Surface treatments

A critical issue on realization of CZT-based detectors is the preparation of surfaces on which contacts are deposited. They should be homogenous, low roughness and un-oxidized as much as possible. A meticulous two-step process of lapping and polishing is required to reduce roughness; this process leaves surfaces very clean and ready for contact deposition. Polished CZT surface is terribly reactive and the oxide starts to grow in a couple of seconds and it is mainly composed of TeO_2 (black and opaque). The surfaces must be left in air the minimum time before metallization to avoid oxide formation [103]. In this chapter the preparation steps to obtain high quality contacts are described.

6.2.1 Lapping and polishing

It is necessary to excise a thin layer of CZT in order to make surface flat and smooth and to remove its defects. We use a special machine called lapping machine to do this. It is composed by a circular horizontal plate where sandpapers are applied. The plate turn on itself with a tunable speed. Samples are glued on a custom support and are located on its top. The support is equipped with a micrometric screw, to define how much material we want to remove, and a ring of silicon-carbide spacers (visible in Figure 6-6-B). Spacers, that are not eroded by sandpapers, ensure flat and homogeneous final surfaces. Two different machines are located in our laboratory:

- Remet LS2 (Figure 6-5-left). The abrasive plate is motorized and the samples support is controlled and held by hand. Plate diameter is 20cm and its speed is tunable from 0 to 300rpm (typically is 250rpm). Available surface for samples is 30x30mm^2 and it is used only for research purposes.
- ECOMET 4 (Figure 6-5-right). It is completely automatic: both abrasive dish and samples support are motorized. Motor speed and perpendicular strength, that presses samples on dish, are tunable. Plate diameter is 30.5cm and its speed is tunable from 0 to 500rpm. The available surface for sample is about 200cm^2 so the machine is able to produce a large number of samples in a single time.

Figure 6-5. Lapping machines: Remet LS2 (left) and ECOMET 4 (right)

I have mostly used Remet LS2 for realization of samples reported in this thesis. Cut samples are cleaned in boiling acetone and are glued (with Joel crystalbond 509) on the glass surface of lapping support. Glass is used because is flat and presents a smooth surface, so there is not risk to ruin the already lapped face of samples.

To ensure clean surfaces and to reduce surface leakage current, the following procedures was used:

1. The first contact surface is prepared and contact immediately deposited; we minimize exposure at air and avoid surface contamination by depositing contacts immediately after the polishing.
2. The second contact surface is prepared on the opposite side and the second contact is immediately deposited.
3. The four lateral faces are lapped one by one to remove metal excess deposited during the previews steps and to reduce surface defects that worse the spectroscopic response by changing local electric field and increasing leakage current.

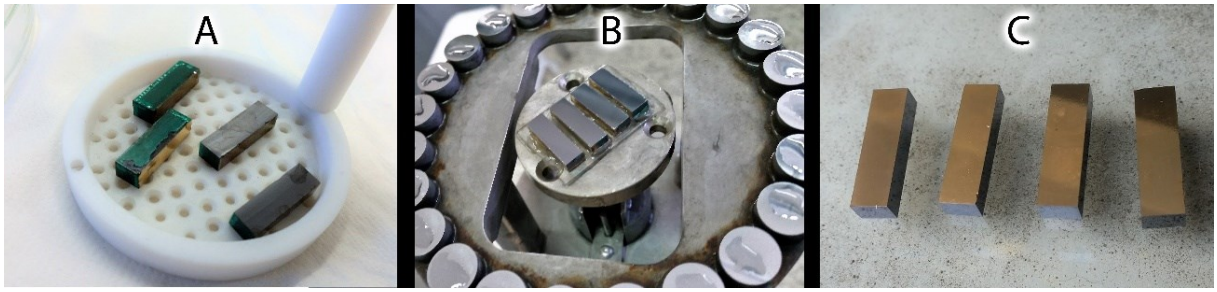

Figure 6-6. Sample after cutting (A), after lapping and polishing (B) and after lapping of lateral faces (C)

Samples are glued on the support surface. The lapping process starts by using course sandpaper to rapidly remove at least 100-150 μm of CZT. This process completely removes the surface damage induced by cutting. We generally use sandpaper p2500 or p600 (respective particle size of 8.4 and 25.8 μm) for few minutes. Now sandpaper p4000 (particle size of 5 μm) is used to

remove about 50 μm of material; this fine cleaning required at least 5 minutes. Lapping process is followed by polishing one. The abrasive dish is replaced by synthetic cloth sprayed with diamond suspensions. to finish well the surfaces. Polishing is divided in 2 steps: the first with 3 μm suspension and the second with 1 μm suspension. Both steps last at least 5 minutes to ensure extremely clean surfaces.

After lapping and polishing stages, samples are unglued from the support and washed in boiling acetone and after in boiling isopropanol with the aim to remove glue residuals and surface halos.

Contact deposition occurs immediately after the polishing of contact surfaces; gold and platinum depositions are made directly on the lapping support. During my PhD, I have optimized deposition of gold and nickel, and developed a procedure to deposit platinum. All the processes are electroless based and described in 6.3.

6.2.2 Etching

The etching is typically used as the last step of surface preparation, before contact deposition [104]. It is a chemical attack of the surface of CZT that removes most of unwanted residuals and waste. Several etching solutions were developed in the years: bromide solved in methanol is one of the mainly used solution and it is proposed in different concentrations and etching times [104]; also mixed solution of H_2O_2-HI-citric acid is used in literature [105]. Another important use of etching is to "draw" the selected electrode layout on contact face. In this case, the process is used to remove the metal from the areas where we want to uncover CZT in order to have electrical insulation. The etching of gold is indirect because bromide is not able to dissolve gold. The deposited gold layer is porous, so bromide passes through it by falling on CZT under the metal. In this case the following reaction happens [104]:

$$Cd_{0.9}Zn_{0.1}Te_{(surface)} + 3Br_2 \Rightarrow 0.9CdBr_2 + 0.1ZnBr_2 + TeBr_4$$

The gold is also removed from CZT surface in few seconds. To remove the contact only in the selected areas, it is necessary to apply a mask in order to put etching solution in touch only with desired areas. To obtain selected geometries, a photolithograph process is necessary. Firstly a cover layer of photoresist (Microposit SP15 positive photoresist) is deposited over the entire surface. The next step is the UV illumination: UV light passes through a negative mask and lights up photoresist layer only where we want to weaken it. A developing bath removes the photoresist leaving on metal surface a protection layer that avoids the contact of metal with bromide.

We use the following recipe: I) preparation of solution of bromide in ethylene glycol (6% in volume), II) immersion of masked samples in the solution for 5 minutes. This procedure allows contemporary high resolution (pixels with 55 μm pitch were made with good results) and large area (up to 20x20 mm^2). These performances are achievable only by working in a clean room in order to avoid any surface contamination that could compromise the final result.

6.2.3 Passivation

Passivation is the last process of sample realization and it consists in the oxidation of non-metallized CZT surfaces. The oxide obviously has higher resistivity than CZT, so the leakage current that flows between different contacts is strongly decreased (sometimes over two degree of magnitude [103]). This decreases electrical noise and improves the spectral energy resolution of the detectors. Passivation reaction of CZT produces mainly tellurium oxide (TeO_2) that is a black and opaque compound arranged all over the free CZT surfaces. Several techniques of passivation were developed in past: water based bath with KOH, NH_4F or H_2O_2 [106]; solution of bromide and lactic acid [106]; plasma oxidation [107].

Samples studied in my PhD were passivated following this recipe: firstly samples are dipped in a water solution of sodium hypochlorite at 15% for 1 minutes; after the rinse with water, samples are immersed in a solution at 10% of hydrogen peroxide for 5 minutes. Samples are washed with water and lastly dried.

6.2.4 Lateral surface: field distortion and leakage current

Last step of lapping process is performed on lateral surfaces. Detectors with very rough faces usually show bad spectroscopy. Defects related to a rough surface could deflect the electric field lines and promote charge losses for events happened close to the surfaces. Those events with incomplete collection of carriers worse the spectroscopy because the induced current is decreased by the trapped charge. Lapping process decreases also the leakage current by removing surface defects. This process is able to reduce the surface current up to three orders of magnitude [23]. Babalola [12] has proved that leakage currents increase with the roughness. Electronic noise is strongly linked with spectroscopic performance then, to optimize resolution, we have to minimize leakage current. Passivation and lateral face polishing are extremely important but not enough to reach high performances. It is necessary to adopt a special geometric element that subtracts surface current from the signal sent to CSP. This geometric element (called guard ring) is described in section 3.3.3 and consists of a metallic layer all around the anode boundaries. It is at the same voltage of the collecting electrode but is not electrically connected to it.

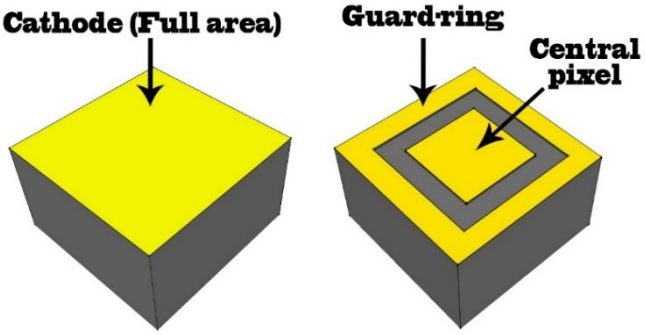

Figure 6-7. Typical monopixel device configuration with guard ring

6.3 Electroless deposition

The technique that I have used to realize contacts is mainly the electroless deposition. In the following paragraphs, solutions and reactions that allow the deposition of metal layer on CZT are described in details.

6.3.1 Gold

Electroless deposition of gold is achieved with a single reagent: hydrate gold chloride ($HAuCl_4 \cdot xH_2O$). All chemical reactions involved in the process that reduce ion Au^{3+} in metallic Au occur by engaging Cd or Te, so they take place at the solution-semiconductor interface. Chemical potential is associated at each reaction:

$$2AuCl_4^- + 3Cd_{(s)} \Rightarrow 2Au_{(s)} + 8Cl^- + 3Cd^{2+} \gg \Delta E = +1.40V \quad 6\text{-}1$$

$$4AuCl_4^- + 3Te_{(s)} \Rightarrow 4Au_{(s)} + 16Cl^- + 3Te^{4+} \gg \Delta E = +0.43V \quad 6\text{-}2$$

$$4AuCl_4^- + 3Te_{(s)} + 6H_2O \Rightarrow 4Au_{(s)} + 16Cl^- + 3TeO_2 + 12H^+ \gg \Delta E = +0.41V \quad 6\text{-}3$$

The reaction with the largest chemical potential (ΔE) is the most favorite, so evaluating all the possible redox, it results that 6-1 is the main reaction. This reaction deprives Cd from CZT, releasing the ions Cd^{2+} [38].

Reaction 6-3, although less probable than 6-1, suggests that a little amount of tellurium dioxide could be produced by gold salt that reacts with Te and water; this reaction is potentially dangerous for detector performances (for example changing solvent). To avoid this reaction it is necessary to remove water from the depositing solution.

High acidity (pH<1) is a point for the solution because low pH inhibits oxide formation at the interface (except the little amount caused by reaction 6-3): tellurium oxide is catalyzed in alkaline environments [108].

Gold electroless deposition is possible in different solvents, so several solvents were tested. In this work I am focused in particular on two solvents: water and alcohol-based solvents.

The classical solution that can be found in literature is gold chloride solved in **water** with different concentrations [38]. Solution at 4% of weight is take as reference for the comparison of the effectiveness among depositing solutions.

After polishing, samples are dried with compressed air and a little amount of electroless solution is dropped on the clean and dry CZT surface. By doing this, we obtain a unique large drop that covers completely the sample surface and deposits gold homogeneously; after one minute, we discard the electroless solution and wash with water the samples. Solution discard is minimized because only the volume of drop is wasted. By using this approach it is always possible to deposit gold with freshly solution.

The final layer is compact and shiny and with golden color (it is not trivial because thin gold layers have different colors due to different optical properties).

Positive aspects of this solution are that:

- Gold chloride is strongly soluble in water.
- Gold layer is enough thick and homogenous.
- The deposition is fast and achieved at room temperature.
- Water is the safest solvent.

However, it has some crucial defects:

- The solution reacts also with water producing oxide.
- Mechanical stability of the metallic layer is low, then detector life is limited.

Solubility of gold chloride is high also in alcoholic environment. To deposit contacts we also use an electroless solution based on **methanol**. In order to allow a better comparison we have not changed the concentration fixing it at 4% in weight. Chemical reactions are the same that in aqueous medium except for the undesirable reaction 6-3, but kinetic could change.

The final layer turns out to be more homogeneous and highly shiny, sign that methanol deposition is really uniform and the metal layer is more compact. The film obtained with the methanol solution is mechanically stable and allows the realization of long-life detectors.

In the chapter 7.1 the adhesion of contacts achieved with water and methanol solutions is studied and discussed.

6.3.2 Platinum

Also in case of platinum deposition the electroless solution is only composed by a unique reagent: platinum chloride ($PtCl_4$) solved in different solvents. Chemical potentials of reactions between Pt and Cd or Te are:

$$PtCl_6^{2-} + Cd_{(s)} \Rightarrow PtCl_4^{2-} + 2Cl^- + Cd^{2+} \gg \Delta E = +1.09V \quad 6\text{-}4$$

$$PtCl_4^{2-} + Cd_{(s)} \Rightarrow Pt_{(s)} + 4Cl^- + Cd^{2+} \gg \Delta E = +1.16V \quad 6\text{-}5$$

$$2PtCl_6^{2-} + Te_{(s)} \Rightarrow 2PtCl_4^{2-} + 4Cl^- + Te^{4+} \gg \Delta E = +0.11V \quad 6\text{-}6$$

$$2PtCl_4^{2-} + Te_{(s)} \Rightarrow Pt_{(s)} + 8Cl^- + Te^{4+} \gg \Delta E = +0.19V \quad 6\text{-}7$$

Both Cd reactions are more favorite than Te ones, as revealed by the values of ΔE. Therefore platinum will react mostly with cadmium getting free Cd^{2+} ions.

The development of platinum deposition was complicated. In literature the only parameters reported [34] [38] are very similar to gold ones but, by using the same conditions adopted for gold electroless (room temperature, water or methanol solutions), platinum layer results inhomogeneous and weak, even if solution concentration and deposition time are changed.

After several tests and failures, I found the right conditions to allow the deposition of homogeneous and stable layer. Platinum chloride is solved in a mix solution of methanol and dimethylformamide (DMF) at 4% in weight. To solve that large quantity of salt in the solvent it is necessary to warm up the compound at 60-70°C and to shake until the salt is completely solved.

Samples are placed on a hotplate and heated up to 90-100 °C and over them a 300 W lamp is placed. The cooled electroless solution is dropped on samples in the same way of gold deposition. The deposition takes place in 5 minutes. The procedure is repeated 2 or 3 times. Then, samples are cooled down and rinsed in water.

The deposited layer is homogeneous, mechanically strong, shiny and off-white. This color means that the layer is quite thick. By using water solution the final film becomes hazel and opaque, indicating that the layer deposited in aqueous solution is very thin.

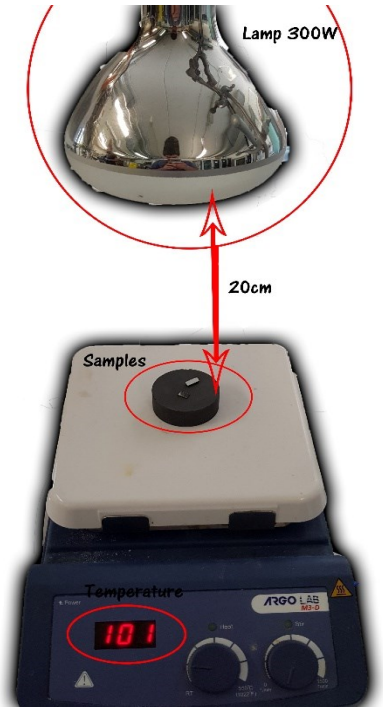

Figure 6-8. Deposition setup for platinum electroless

6.3.3 Nickel

Gold and platinum work functions are larger than the one of CZT; in chapter 3.2 it is apparent that a metal with work function lower than CZT could be interesting for the realization of ohmic contacts. Nickel work function is in range 5.04÷5.35 (Table 3.1), so ohmic contacts are expected.

As for platinum, a clear nickel electroless deposition for CZT is not reported in literature. Nevertheless, by exploiting several papers and patents [109] [110] [111] [112], a novel technique has been developed. In this section, the electroless deposition of nickel, optimized after several tests, will be illustrated.

The depositing solution is composed by 550 mg of $NiCl_2 \cdot 6H_2O$ (nickel chloride hexahydrate) and 400 mg of NaH_2PO_2 (sodium hypophosphite) solved in 5 ml of water. The high concentration of hypophosphite leads to a final layer with a discreet amount of phosphorus, about 6-7% (confirmed also by X-ray microanalysis).

The solution is put inside a little ABS cylinder realized with a 3D printer; cylinder temperature is set at 100 °C with a boiling water bath. Samples are removed from the lapping support, washed with boiling acetone and isopropanol and inserted in the cylinder. Now the container is closed to limit the evaporation of solvent and held in these conditions for 15 minutes.

The obtained film is uniform but the metallic layer is not shiny and with a hazel color tending to gray (Figure 6-9). However the layer is thick and strong, and the conduction properties are good. A lapping process is necessary to remove nickel from lateral surfaces.

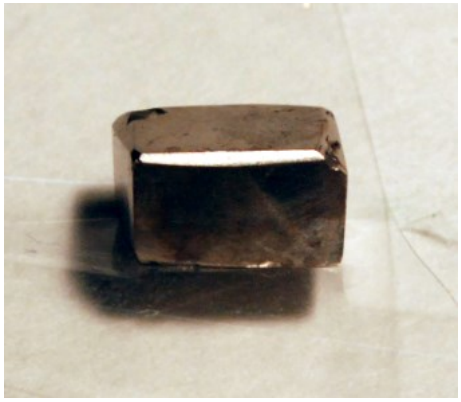

Figure 6-9. Nickel covered samples

Chemical reactions that happen are the following [109]:

$$Ni^{2+} + H_2PO_2^- + H_2O = Ni_{(s)} + 3H^+ + HPO_3^{2-} \quad 6\text{-}8$$

$$H_2PO_2^- + H_2O = HPO_3^{2-} + H^+ + 2H_{ads} \quad 6\text{-}9$$

$$H_2PO_2^- + H_{ads} = P_{(s)} + H_2O + OH^- \quad 6\text{-}10$$

Reactions for the nickel deposition do not involve Cd or Te, so they occur in the entire solution and not only on CZT (as in gold and platinum case). The reduction of nickel ions is initially catalyzed by CZT surface and after by the nickel layer itself (autocatalysis). Anyway a little amount of nickel is deposited on the entire backer; disposable supports are preferred at glass (for this reason we use ABS cylinders).

6.4 Bonding

After passivation, samples are ready to be tested or bonded to obtain the final devices. Some of them are directly bonded on dedicated electronics (such as PIXIE or HEXITEC ASICs), so they were directly shipped to the group that handles flipchip-bonding. The other samples were bonded on standard breadboards.

The breadboard (Figure 6-10, A and B) is rectangular and based on Diclad 870 (composed of Teflon) and it was chosen because it is really insulating and easy to be processed. Breadboards were tested under high voltage and different temperatures and humidity conditions to access their quality. Breadboards show copper paths on both sides:

- Top paths are used only to solder pins, to increase mechanical stability, and to realize a solid plane where glue can cling and hold the sample.
- Bottom paths drive the electrical contacts close to the anode to make the connection with device electrodes easy (generally pixel and guard ring).

After a rapid electrical control to check currents, the samples are glued on the top side of breadboards by using a special glue (3M epoxy adhesive 2216 B/A gray) with cathodes pointing upwards. The cathode is connected with a thin gold wire (25µm section) to the corresponding pin using epoxy conductive glue with silver (8331 Silver Conductive Epoxy Adhesive). When the glue is hardened, the breadboard is flipped and locked on a ABS printed support (visible in Figure 6-10-E). The support is moved under a stereoscope and other two thin wires of gold are used to connect pixel and guard ring to respective copper contacts by using silver based epoxy. When glue is hardened, samples are ready to be measured.

Samples mounted on these breadboards can be studied by most of the techniques used in this thesis.

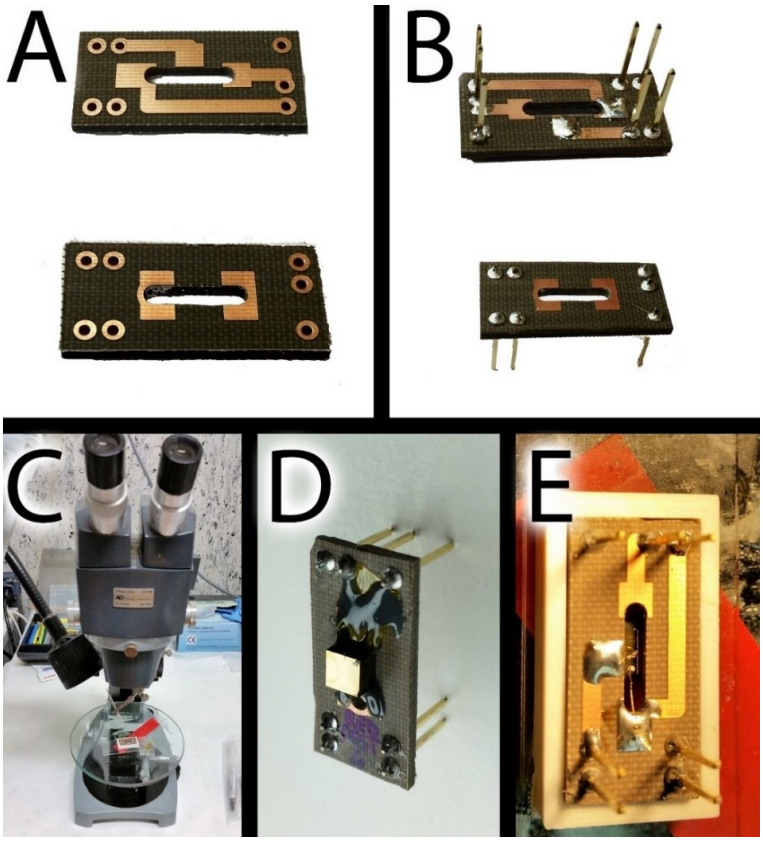

Figure 6-10. A) standard breadboard, B) standard breadboard with pin soldered, C) bounding stereoscope system, D) bounding of cathode, E) bounding of anode

7 Results and discussion

In this chapter, experimental results obtained during my PhD thesis are shown and discussed.

In the first paragraph, the properties of the electroless gold contact realized in alcoholic solutions and of the detectors realized with this new technology are shown [70] [74] [113] [114].

The following section questions of novel nickel and platinum contacts [115] [102].

The third part of this chapter concerns the important results performed with LI-TCT [50] [101] [102] [116].

The fourth sections concerns the results we obtained. We performed several 1D and 2D scan with the tiny x-ray beam in order to study charge-sharing effects in small pixel array by using PIXIE ASIC thanks to the digital system developed in Palermo. Another detector was tested on HEXITEC electronic, results are described in the mentioned section. By employing these data we wrote an internal report for the synchrotron committee and a under-review paper [117]. A new proposal to perform a new experiment in the next year was already won.

In the last section, it is described the development of Unmanned Arial Vehicle (UAV) equipped with a CZT detector for the localization and identification of nuclear sources. The prototype was realized in the frame of the project Xdrone, part of the flagship project "Fabbrica del Futuro" [118] [119].

7.1 Electroless *gold* contacts obtained in alcoholic solutions

In this chapter I want to present the full characterization of the electrical, mechanical, charge transport and spectroscopic properties of THM-grown CZT detector equipped with new gold contacts deposited by using alcoholic electroless solution (the technique is described in chapter 6.3.1). The detector, based on CZT crystals provided by Redlen Technologies, is characterized by low leakage current allowing high bias voltage operation even at room temperature. The main transport mechanisms of the new device was investigated by modelling the measured IV curves (under reverse bias voltages) with the interfacial layer thermionic-diffusion (ITD) model described in section 3.2.2. An accurate characterization of the spectroscopic response of the detector, at both low and high rates, was performed by using custom-designed digital readout electronics and monochromatic X-ray and γ-ray sources (^{109}Cd, ^{241}Am and ^{57}Co). The readout electronics is able to continuously digitize and process the signals from the detector (i.e. the preamplifier output signals) and to perform a fine pulse shape and height analysis even at high radiation fluxes.

My contributions are in particular the optimization of new electroless deposition and the realization of the detector. Furthermore, I made preliminary measurements of the device and I carried out the tape test on dedicated samples.

The detector are based on CZT crystals (4.1x4.1x3 mm^3), grown by Redlen Technologies using THM technique. The cathode is a planar electrode that cover completely the detector surface (4.1x4.1 mm^2) and the anode surface is characterized by a central electrode (2x2 mm^2)

surrounded by guard ring (Figure 7-1). The width of the guard ring is 950 μm and the gap between the electrodes is 50 μm. As shown in Figure 7-1, detector is bonded onto standard breadboard.

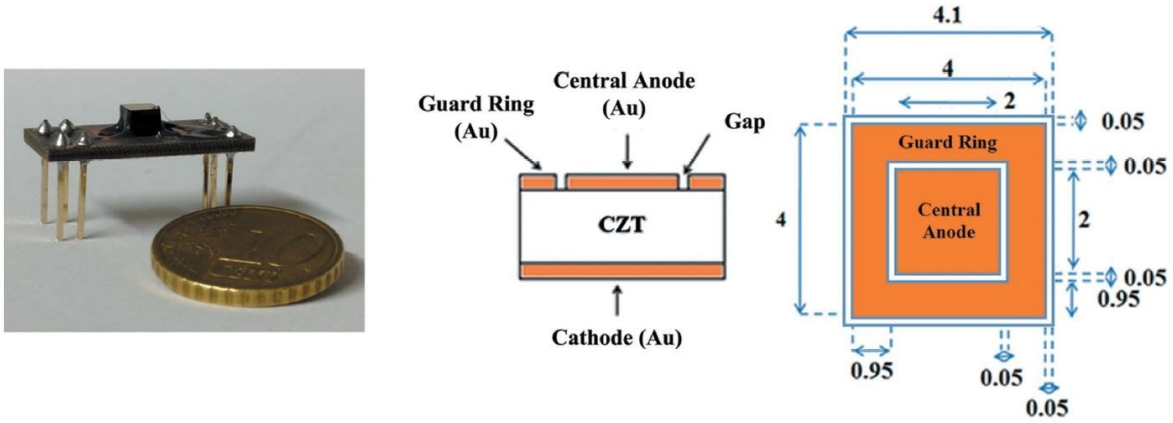

Figure 7-1. New 3mm thick THM-grown CZT detector (left), schematic cross-section view of the detectors (center) and anode electrode layout (right)

Gold contacts were realized on both the anode and the cathode of detector. The new gold electroless deposition performed in alcoholic environment was used. The anode pattern (guard ring and pixel) was obtained thanks to photolithography process and the passivation procedure was performed in order to reduce the surface leakage current.

The device is characterized by very low leakage currents and allows high bias voltage operation (>7000 V/cm) even at room temperature with excellent prospective for high-flux radiation measurements.

7.1.1 Mechanical stability

Tape test is used to check the mechanical resistance of contacts, it provides a seal threshold of electrodes. Tests were performed on dedicated samples: the contact deposited with the new electroless deposition based on methanol solution was compared to a standard contact deposited with aqueous solution.

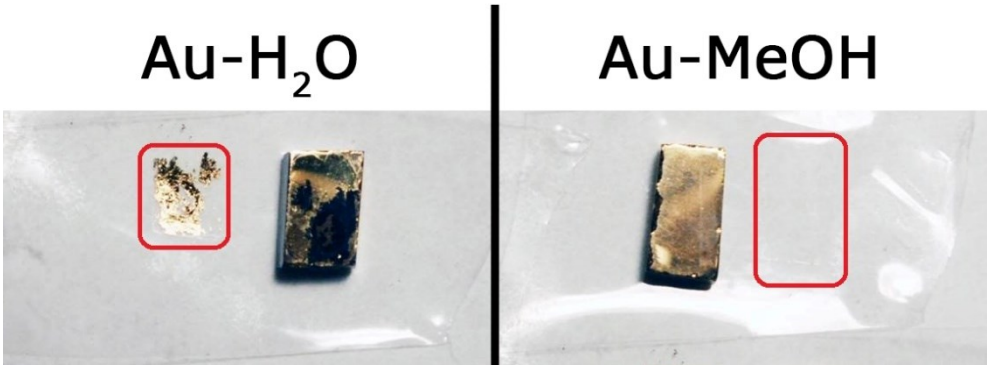

Figure 7-2. Tape test results for old water based contact (left) and the new one based on methanol solution (right)

From Figure 7-2 results that contact deposited with water-based solution (solution mostly used in literature) do not overcome tape test (left side of the image). The new contact deposited with methanol solution, on the contrary, overcome tape test (right side of the image). The gold contact are able to withstand several test repetitions. The contact surface is not changed and any gold or CZT trace are found on the tape. Instead, using aqueous solution, part of the deposited material is left on the tape leaving bare the CZT. The metal is completely removed by the tape.

7.1.2 Current-voltage characteristic

Figure 7-3-left shows the current–voltage (IV) characteristics of the sample 3 mm thick equipped with 2x2 mm² central pixel. IV curves are measured at different temperatures (from 40 °C to 15 °C, with temperature steps of 5 °C). The behavior of the IV curves is typical of the Au/CZT/Au contacts, i.e. of a metal–semiconductor–metal device with two back-to-back Schottky junctions.

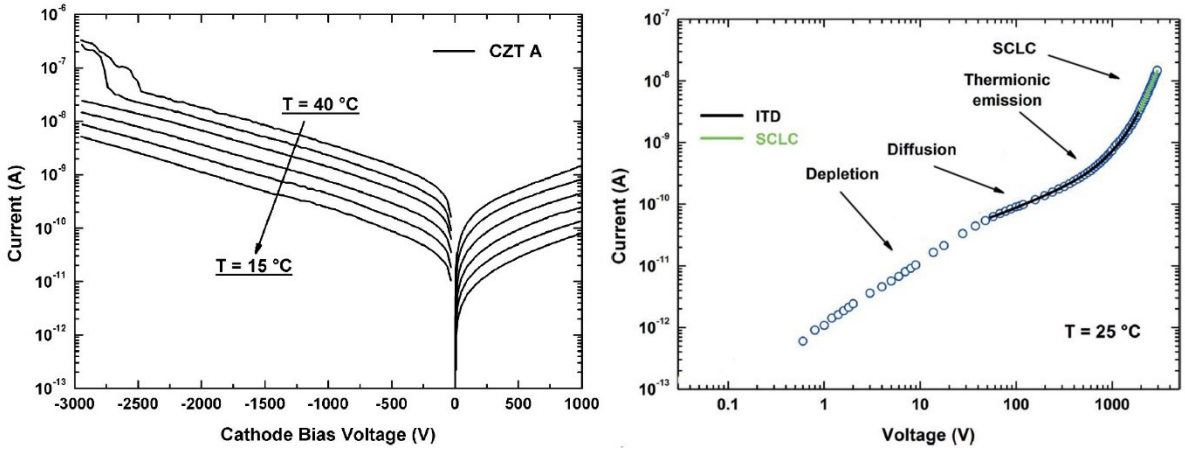

Figure 7-3. IV characteristics measured at different temperature (from 40 °C to 15 °C, 5 °C steps) (left) and fit of measured IV curve at 25 °C (right). Main transport mechanisms are highilghted in right plot

As clearly visible in the figure, the detector is characterized by very low leakage current in the reverse bias region: 4.7 nA/cm² at 300 V (1000 V/cm) at 25 °C and 1.4 nA/cm² at 300 V at 15 °C. Moreover, the detector ensures moderate leakage currents, at room temperature (25°C), even at high bias voltages: 93 nA/cm² at 2000 V (6700 V/cm) and 370 nA/cm² at 3000 V (10000 V/cm). To better understand these experimental results, we described the measured IV curves (under reverse bias voltage) through the ITD model.

Figure 7-3-right shows the measured IV curves, under reverse bias voltages, where main transport mechanisms are highlighted. the IV curve is characterized by the formation of the depletion region even at low voltages (<1 V), precluding the possibility to estimate the bulk resistivity. Diffusion and thermionic emission mechanisms occur at high voltages, in particular the thermionic emission occurs at about 200 V. This means that leakage current is limited even at high voltages.

In order to perform a quantitative evaluation of these differences, we fit the IV characteristics with ITD model. The estimated barrier height under thermal equilibrium (ϕ_{B_0}) is 0.92 eV and is consistent with the literature [120]. The transmission coefficient through the interfacial layer (θ_n) and the parameter C_2 turn out to be 0.063 and 4.0 10^{-5} respectively. Due to the C_2 dependence on D_s (density of surface states), the new contact seems to be characterized by a low density of surface states. The C_2 parameter is related to the effective barrier height (ϕ_{eff}) with the following equation [41]:

$$\phi_{eff} = \phi_{B_0} - C_2 V \qquad 7\text{-}1$$

The effective barrier height decreases slowly with the bias voltage, so the leakage current is limited even at high voltages. The weak effect of the interfacial layer is pointed out by the high θ_n value and explains how the leakage current is diffusion-limited up to high voltages.

Electrical properties of a similar detector with contacts deposited via standard aqueous electroless solution were compared with the detector previously mentioned. Both the two samples show very high resistivity. The obtained barrier height in the case of water based solution (0.85 eV) is very similar to the one obtained in the case of methanol based solution (0.92 eV). Moreover, the characteristic shows a linear dependence at high voltage also in the case of water

based solution, that means that the oxide layer thickness is very small. Basically, we can say that the I-V characteristics of the contacts are qualitatively very similar, and so that the electrical behavior of the contacts is not particularly affected by the use of methanol instead of water.

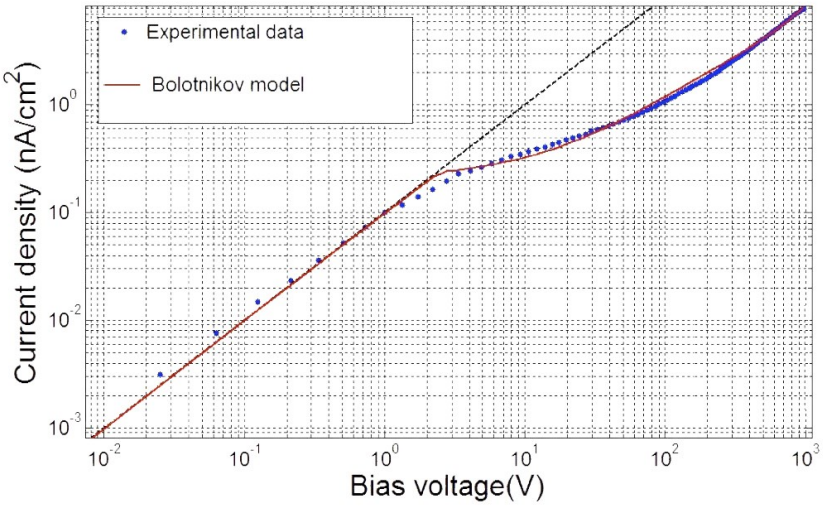

Figure 7-4. IV characteristics of sample equipped with standard water-based gold contacts

In the following pages, I want to show the spectroscopic performances of the CZT detector, especially under high radiation fluxes.

7.1.3 Spectra

The spectroscopic performance of the detectors was measured by using standard front-end electronics. We used a commercial AC-coupled charge-sensitive preamplifier (CSP; A250F/NF with external FET SK152) with a nominal equivalent noise charge of about 100 electrons RMS. The CSP is characterized by a resistive feedback with a decay time of 250 µs. The detectors and the CSP were mounted on a custom PCB board based on a polytetrafluoroethylene (PTFE) substrate. The PCB board was enclosed in a shielded box and the detectors were irradiated through a light-tight beryllium window. The height analysis of the CSP output pulses was performed through custom DPP electronics. The DPP system, by digitizing and processing the CSP output waveforms, is able to perform an accurate pulse shape and height (PSHA) analysis (e.g. arrival time, pulse height and pulse shape) even at high input counting rates (ICRs). The DPP system consists of a digitizer (DT5724, 16 bit, 100 MS/s, CAEN SpA) and a PC, which controls digitizing functions, the acquisition and the analysis. The pulse-processing analysis was performed by using a custom DPP firmware uploaded to the digitizer. A general overview of digital corrections is reported in section 4.2.1.

The time-stability of the detector, at low rates (ICR = 200 cps), was first investigated. ^{241}Am and ^{57}Co spectra were measured, by using an electric field of 1500 V/cm, and the detector showed good time-stability within a time window of 30 minutes. All energy spectra were measured by using the slow PSHA, which gives the best energy resolution values. Figure 7-5 shows the measured energy resolution (FWHM) at 59.5 keV of the detector at different bias voltages obtained under low (left) and high (right) ICR. Similar low-rate performances (energy resolution around 4% at 59.5 keV) were obtained from other researchers with planar CZT detector coupled to the A250 preamplifier [121].

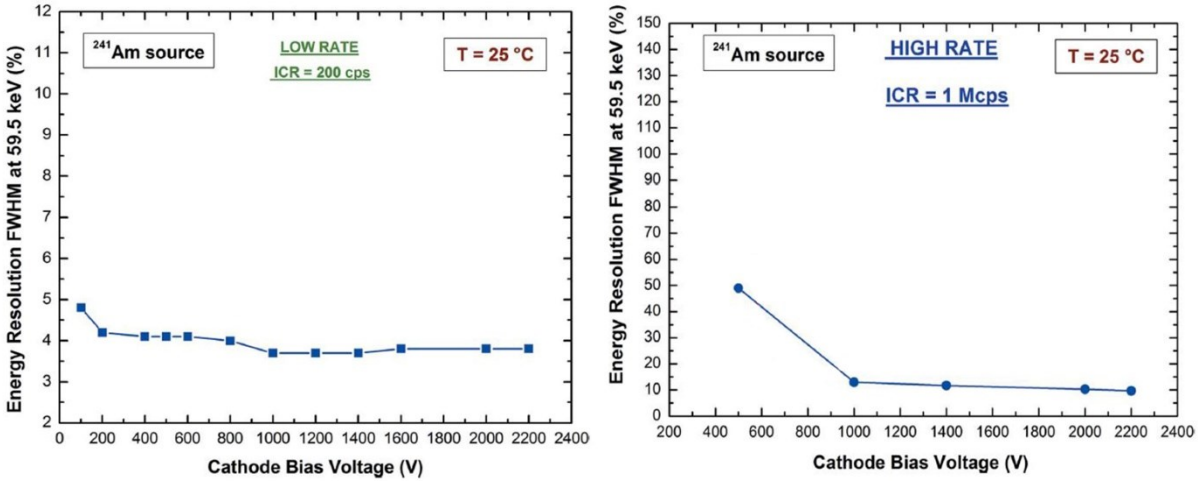

Figure 7-5. FWHM values obtained with different voltages. Low rate (200 cps) on the left high rate (1 Mcps) on the right

The detector allows high bias voltage operation (>7000 V/cm) in agreement with the measured electrical characteristics. Despite the best energy resolution (3.7% FWHM at 59.5 keV) is obtained at voltages between 1000 V and 1400 V, I prefer to (Figure 7-6) show the ^{241}Am and ^{57}Co spectra measured at the maximum bias voltage of 2200 V (7300 V/cm). The maximum voltage of 2200 V was fixed by the electronic components of the bias voltage filters.

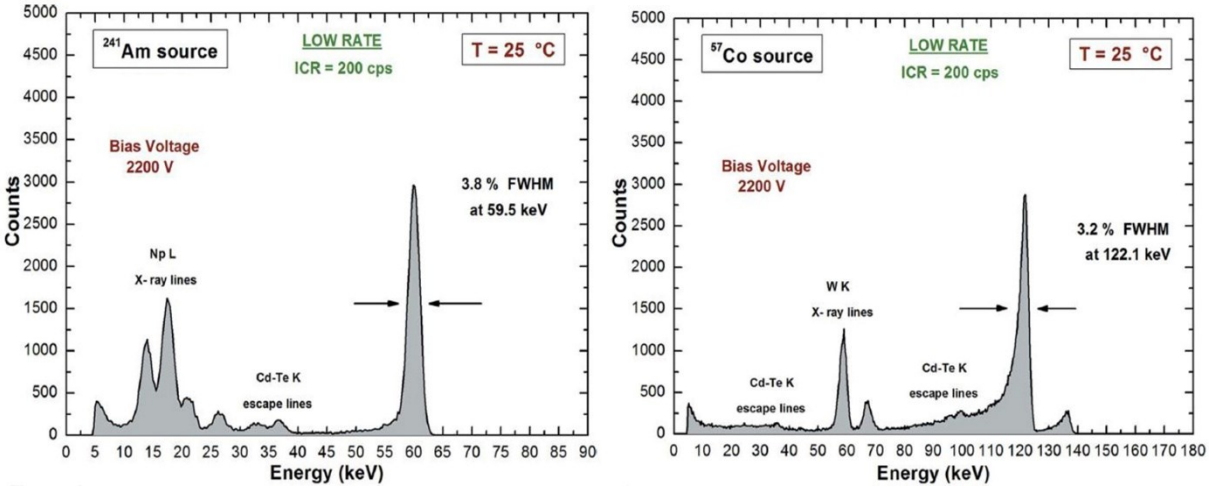

Figure 7-6. ^{241}Am (left) and ^{57}Co (right) low-rate spectra performed using 2200 V

At high rates, the time-stability of the detector was verified, within a time window of 30 minutes, up to 1 Mcps (^{241}Am source). The optimal bias voltages of detectors are generally greater than the optimal bias voltages obtained at low rates (Figure 7-5). This is due to the high-flux radiation-induced polarization phenomena [122] [97] [123], producing a degradation of the electric field within the detectors. The electric field distortions are caused by a charge buildup created within the detector that strongly depends on the radiation characteristics (flux and energy), the detector properties (thickness, contacts, bias voltage and charge transport properties) and the operating conditions (temperature). Recently, Bale et al. [122] theoretically investigated the mechanism of the high-flux polarization effects in CZT detectors, obtaining an analytical dependence of the critical flux (above which polarization effects dominate) on material, detector and operating parameters. Polarization degradations are more marked at low temperatures and by increasing the detector thickness and the photon energy; these effects can be mitigated by increasing the bias voltage and by using CZT materials with high charge transport properties (high holes $\mu\tau$ values).

Main results of digital correction of the spectra at high rate are reported below. The digital system is able to provide two different types of energy spectra: energy spectra from the slow PSHA, characterized by a fine energy resolution and a low throughput, and energy spectra from the fast PSHA, characterized by poorer energy resolution but higher throughput. Moreover, both corrections depend on the statistical distribution of pulses shape, expressed through the peaking time (slow PSHA) or the time width (fast PSHA).

Figure 7-7 shows that with high ICRs, pulse shape analysis mitigates the pile-up effects in energy spectrum (peak pile-up).

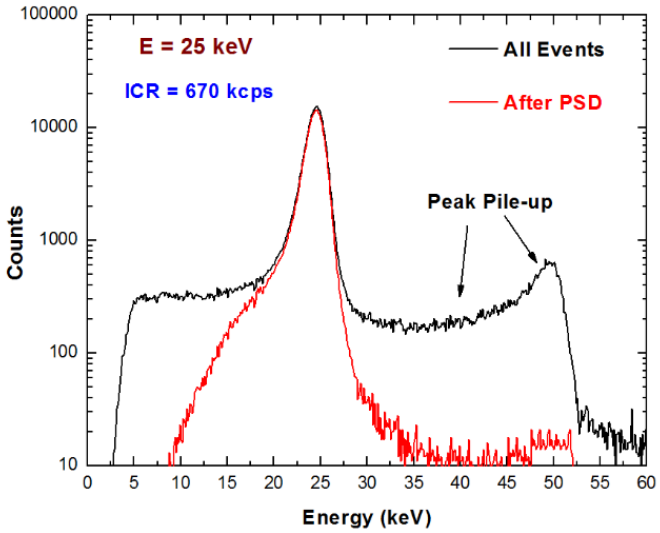

Figure 7-7. Effect of PSD on a spectrum measured under high ICR

Figure 7-8 shows ^{241}Am spectra measured with the detector by using pulse shape discrimination (PSD) combined with slow (left side) and fast (right side) PSHA. The spectral resolution is better in the case of slow PSHA: using 1 Mcps the FWHM at 59.5 keV is 8% against the 9.7% for the fast analysis. The slow PSHA at 550 kcps shows a relatively high throughput (ratio between Output Counting Rate and Input Counting Rate) of 49%, but by increasing the ICR up to 1Mcps the resulting throughput drops becoming 0.4%. To maintain high throughput even at 1 Mcps it is necessary use the fast PSHA, Figure 7-8 shows that the throughput of fast PSHA using ICR of 1 Mcps is 57%.

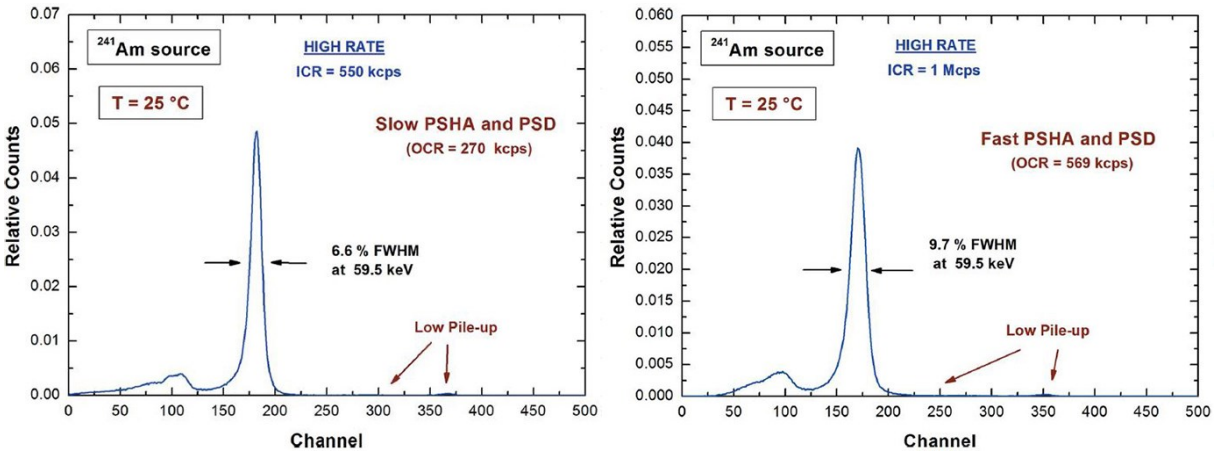

Figure 7-8. ^{241}Am spectra measured under high flux. They are corrected using slow (left) and fast (right) PSHA and PSD

7.1.4 Conclusions

The performance of the detector equipped with gold contacts deposited via alcoholic electroless solution was presented. The detector, characterized by low leakage current even at room temperature, allow high bias voltage operation (>7000 V/cm), which is very important for high-flux radiation measurements.

The detector, coupled to an innovative digital pulse processing electronics are characterized by excellent high-rate performance and, even under high radiation flux, it does not present polarization phenomena up to 1 Mcps (tested with ^{241}Am source).

The results give important indications on the use of these devices with pixelated electrode structures for high-flux energy-resolved X-ray imaging. E.g. a 500 µm pitch-pixel structure (typical of several X-ray imaging applications), based on these CZT detectors, would allow high flux rates greater than 4 10^6 photons/cm^{2}s without excessive spectral distortions. We have realized other detectors based on this technique, some of them were mounted on PIXIE and HEXITEC ASIC. Measurements are reported in section concerning the Diamond experience (chapter 7.4).

New pixelated detectors with gold contacts deposited by means of this technique were realized (Figure 7-9) but not yet fully characterized. Charge-sharing effects, through coincidence measurements and pulse-shape analysis, will be investigated. The realized devices will be used to investigate phenomena of different application fields. The Geometrical characteristics of detectors are:

- Detector 500 µm thick and with pixel-pitch of 80 µm for low energy application.
- Detector 3 mm thick and with pixel-pitch of 450 µm for high energy application.

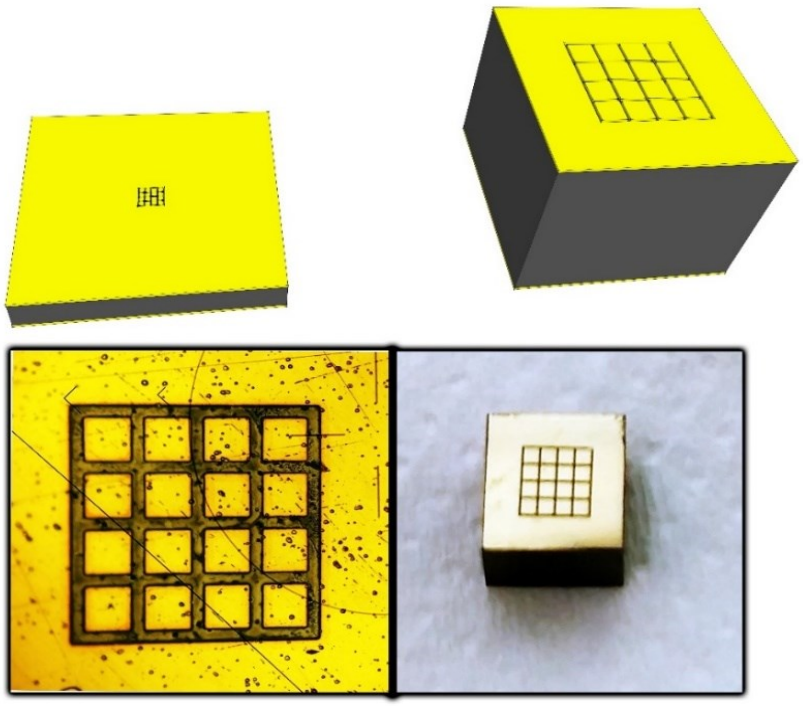

Figure 7-9. New developed pixelated detectors: 80 µm pixel-pitch (left) and 450 µm pixel-pitch (right)

7.2 *Nickel* and *platinum* contacts

Nickel and platinum contacts on CZT were tested. In particular, nickel work function could provide low electronic Schottky barriers that could generate ohmic contacts. As seen for gold, blocking contacts are adopted to realize high-resolution spectrometers, where it is required the minimization of dark current. On the other hand, one of the main exploitation fields for CdZnTe detectors is related to high flux applications [124] [68]. In this case, the use of ohmic contacts is preferred due to their capability to extract with high efficiency photo-generated carriers. Indium is traditionally employed to realize ohmic contacts on high resistivity CdZnTe crystals. However, indium electroless deposition is not easy, and evaporated indium contacts usually show poor adhesion. Obtaining a stable ohmic contact able to overcome tape test would be interesting for several applications.

Also platinum shows interesting properties: resulting Schottky barriers for electrons should be greater that in the gold case, then the leakage current should be even lower. This could be important to increase bias voltage and to further reduce the signal noise at the CSP input. Moreover, the bigger the electron barrier, the smaller the hole ones will be. This could be interesting to study hole properties.

Detailed description of the deposition techniques is reported in chapter 6.3.

My contributions in this section are:

I. Devolvement of depositing solutions and depositing systems for both metals;
II. Realization and characterization of all mentioned detectors;
III. Realization of tape test.

7.2.1 Mechanical stability

In order to test the mechanical stability of Pt and Ni contacts, tape test was performed using standard tape (model 3M 600). Figure 7-5 shows results of the tape test on nickel (left) and platinum (right) contacts deposited both via electroless. It is evident that both contacts withstand the tape test. It means that the contacts are mechanical stable and promising for long-term application.

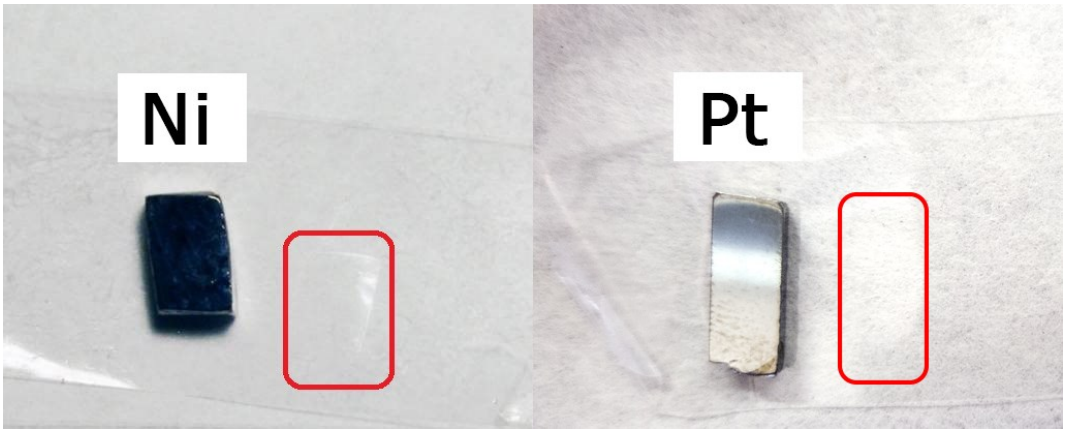

Figure 7-10. Tape test performed on nickel (left) and platinum (right) contacts

For the first time we have deposited nickel and platinum contacts that are able to overcome the tape test.

7.2.2 Characterization of Nickel contact

Surface resistance of contact was measured in order to evaluate the conductivity of deposited layer. The two multimeter tips were leaning on the sample surface at about 1 centimeter of distance. As reference we consider the typical surface resistance of gold contacts that is around 10 Ω. This measurement performed on nickel contacts is about 50 Ω. The obtained value is low enough to ensure performing contacts. Further study on electrical properties and spectral characterizations are reported below.

Four identical detectors were realized to characterize nickel contacts. All detectors have full-area cathode and a large central pixel (2x2 mm^2) surrounded by a guard ring as anode (Figure 7-11-left). Detector with all possible contact configurations were realized (Au/CZT/Au, Au/CZT/Ni, Ni/CZT/Ni and Ni/CZT/Au; where the metal before "CZT" indicates the cathode and that after the anode). The gold contacts were made by using methanol solution. Samples were bounded on standard breadboards (Figure 7-11-right) and measured with probe station.

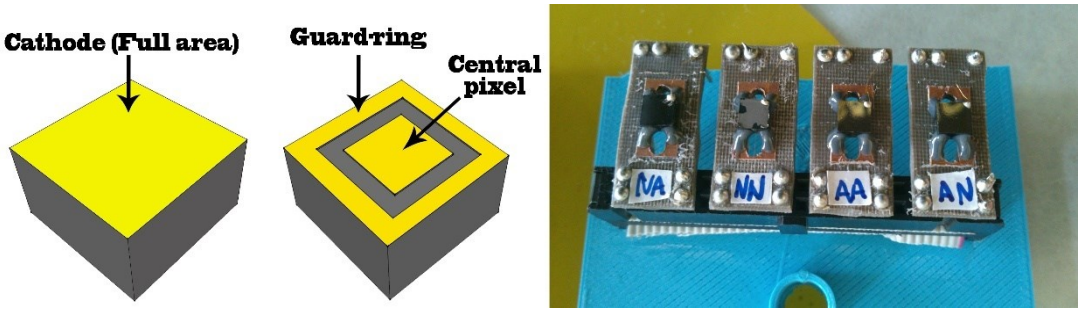

Figure 7-11. Detectors geometry (left) and detectors bounded on their breadboards ready to be characterized (right)

In Figure 7-12-left the IV curves of the four samples are plotted (only reverse currents). A resistivity of about 2 10^{10}Ωcm was obtained for all the devices. Prediction that the electrons Schottky barrier of nickel is lower than the gold one is consistent with these results: the leakage current order is in agreement with respective contact configuration. Au/CZT/Ni (shortened AN) has the lowest leakage current because both the contacts have the maximum barrier for entering carriers (electrons encounter barrier generated by gold contact and holes that generated by nickel contact). Au/CZT/Au (shortened AA) have the second lowest current because the contacts are blocking only for electrons. Similar condition for NN sample but in this case electrons (that are the mainly contributors at the total current) encounter a lower barrier. NA is the case where any carrier encounters a Schottky barrier, indeed the resulting current is the largest. Figure 7-12-right shows the entire IV curves of samples AA and AN. The Au/CZT/Au sample shows the "S" curve that is typical for two back-to-back blocking contacts on high resistivity material [125]. Indeed, the Au/CZT/Ni sample shows asymmetric behavior similar to the diode characteristic that could be due to the effect of a blocking (gold) and an ohmic-like contact (nickel). This means that the barrier height generated by nickel contact is low enough to consider the contact as ohmic.

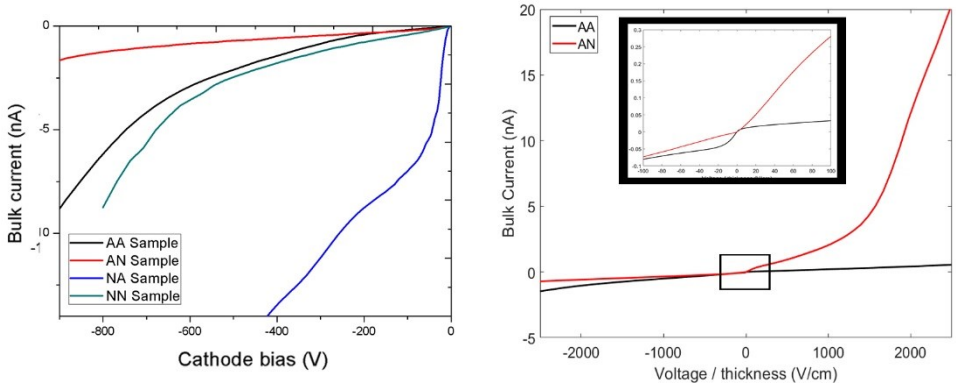

Figure 7-12. Reverse leakage current of the four samples (left). Entire IV curves for AA and AN samples (right),

Figure 7-13 reports spectra measured at DiFC in Palermo. Devices were measured by using uncollimated ^{241}Am source with a bias of 1000 V/cm at 25 °C. AA and AN samples show a good resolution at low radiation rate (both 3.9% at 59.5 keV), this means that the nickel contacts is comparable with gold as far as charge collection is considered. Samples NA and NN show the worst energy resolution (respectively 6.2% and 4.4% at 59.5 keV) due to the high dark current that induce electric noise. High dark current also causes the noise at low-energy visible in the first part of bottom plots. In a future work it could be investigated to measure these detectors under high radiation flux, in order to evaluate the beneficial effect of the nickel contact.

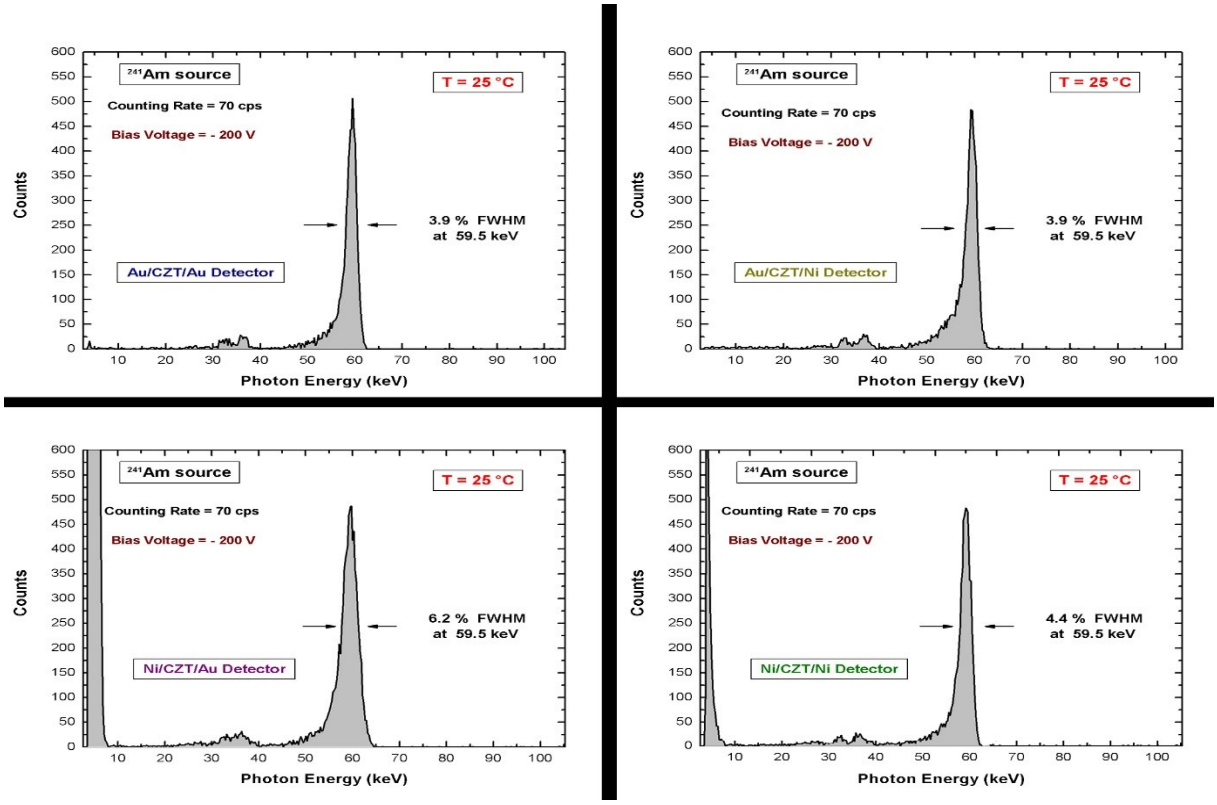

Figure 7-13. ^{241}Am spectra measured with the four samples biased at 200 V and with ICR=70 cps

7.2.3 Characterization of Platinum contact

Surface resistance was measured with the procedure described in the previous section. The resistance value obtained from platinum contacts is in range 100-300 Ω. This value is larger than platinum the one measured for gold contacts but low enough to ensure high-performing contacts.

Comparative study between gold and platinum contact is detailed below. Two detectors were realized with REDLEN material. First detector (called *AA*) with dimension of 5.5x5.5 mm^2 and 2 millimeter thick presents a full-area cathode and a large central pixel (4x4 mm^2) as anode surrounded by guard ring. Gold was deposited on both CZT faces by using methanol electroless deposition. The second sample (called *PP*) is 6x5.7mm^2 and 1.1 millimeter thick, it is equipped with full-area cathode and with a large central pixel (4x4 mm^2) surrounded by the guarding as anode. The new platinum deposition technique already described was used for both contacts.

The behavior of the two detectors is compared as a function of the electric field (V/L) instead of the bias voltage because the thickness of two detectors is different and the comparison is more accurate (Figure 7-14). Data were collected by using the instrumentation already described: IV curves were collected by means of the probe station described in 5.1 and spectra by using Amptek electronics chain and ^{57}Co nuclear source (5.3).

Figure 7-14 shows the IV curves for both samples with electric field at the abscissa and current density at ordinate. The large plot shows the behavior up to high voltage while in the insert in bottom-right corner is displayed the curves close to zero. In both samples is visible the "S" behavior typical of a couple of back-to-back blocking contacts; the "S" is more squeezed for PP, moreover this detector shows lower leakage current than the AA sample at low voltage. When electric field increases the exponential behavior is visible on both the curves. This effect is higher in PP sample as visible in the larger plot. In section 3.2.2 we have seen that the exponential behavior is more pronounced when the oxide is thicker. From preliminary analysis it seems that the platinum deposition exhibits a thicker unwanted oxide interfacial layer.

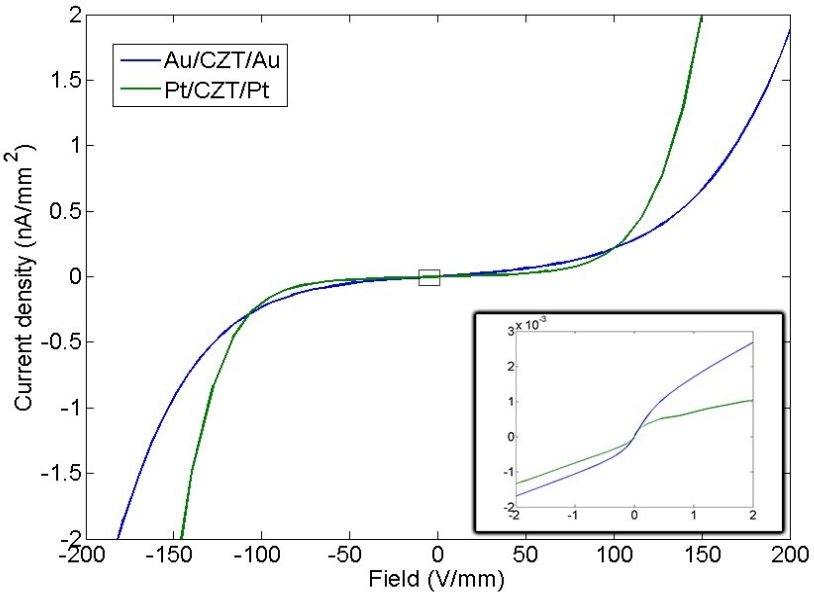

Figure 7-14. JV comparison for AA and PP samples. In the small pane are shown the JV between ±2V/mm

Carrier mobility and lifetime of samples with platinum contacts were achieved by using the LI-TCT and are reported and discussed in chapter 7.3.3.

Spectra reported in Figure 7-15 were performed thanks to the electronic chain described in 5.3 and using ^{57}Co nuclear source. The bias voltage was set in order to apply the same electric field to both samples (1500 V/cm); energy resolution and also charge collection efficiency of PP sample

are comparable with the AA one. FWHM of samples are 9% and 10.5% respectively for samples AA and PP. The noise of Amptek chain is convoluted with detector response, so the chain contribution must be taken in consideration for the evaluation of FWHM. Amptek chain shows a high internal noise (8% at 122keV). Furthermore, large pixel area does not allow high performance. The little difference between FWHM values could be due to the difference of thickness. Charge collection in Redlen material does not change so much between 1 and 2 mm thick detectors, especially if the applied electric field is equal and strong enough. The weighting field of a detector equipped with a large single pixel (as 4x4 mm^2) results to be flat when the thickness is about one millimeter, while shows a little increment when thickness is about 2 millimeters. When weighting field is not flat the energy resolution of detector is better (this could be seen as a weak "small pixel effect").

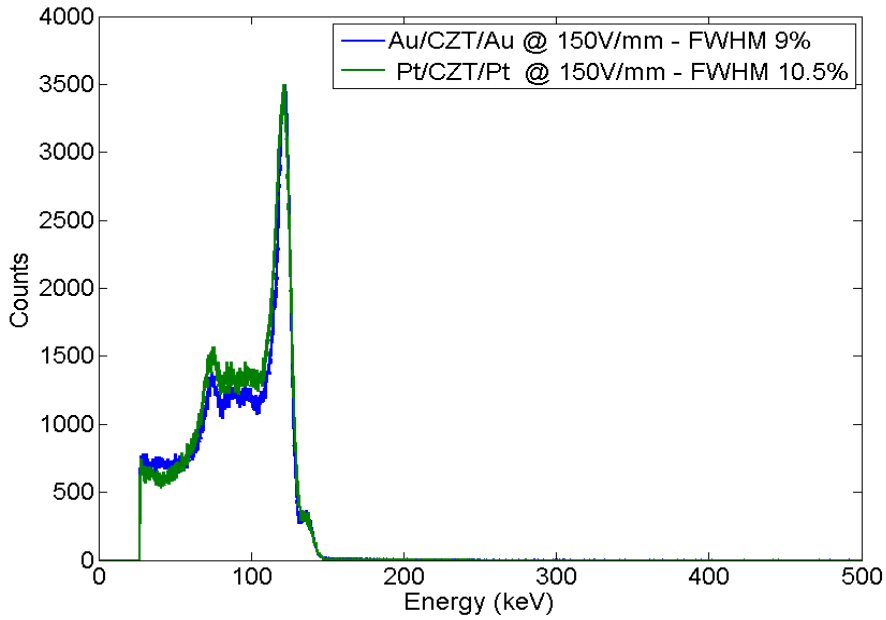

Figure 7-15. Comparison of ^{57}Co spectra between samples AA and PP, both samples biased at 150V/mm

Measurements are in progress in Palermo, to acquire IV curves at different temperature to obtain accurate value of barrier height in PP detector. Furthermore, corrected spectra using digital pulse analysis will be measured both at low and high flux to fully understand the behavior of platinum contacts.

7.2.4 Conclusions

We have realized mechanically stable nickel and platinum electroless contacts deposited with new procedures. Platinum contacts show a blocking behavior, while nickel contacts behave as ohmic. However, more investigations are necessary to make clear this point. In any case, by using nickel as anode contact, a high-energy resolution detector was achieved. We think nickel contacts could be useful for high flux applications.

By using platinum contacts we have achieved good results: leakage current and even energy resolution is comparable with gold contacts. Both nickel and platinum contacts appear to be promising for future application. Further analysis are necessary to extract the barrier height of platinum-CZT junction and to understand the cause of the strong exponential behavior of JV curves of detectors with platinum contacts. Also low and high rate spectra will be acquired by means of digital system for both nickel and platinum detectors.

7.3 Current transient analysis (LI-TCT)

Laser Induction Transient Current Technique was detailed in chapter 5.4. It allows to achieve transport parameters and electric field profile of CZT detectors. The power of this method is that is a non-destructive technique and it is potentially applicable to every sample. Thanks to the standard breadboards we have tested several samples with different dimensions, geometries, base material, and contact metals. The most significant results about LI-TCT are reported in this chapter.

I devoted myself particularly to realization, bonding and encapsulation of all studied detectors. Weighing field simulations were also carried out by myself. Undersigned took part also at optimization of experimental setup and development of self-consistent method.

7.3.1 Samples encapsulation

The system works with any type of detector but when more accurate measurements are requested (detectors with particular geometries or when output signal is extremely weak), a further sample processing is necessary.

To achieve accurate and reproducible measurements we developed the following method. The sample, bounded on the standard breadboard, is almost entirely encapsulated with the glue (3M epoxy adhesive). A little hole is left free on the cathode to allow the photogeneration by means of the laser guided with the optical fiber. To obtain this hole a little rubber tube is glued in the middle of the cathode. The glue is also applied all around the sample (Figure 7-16). By doing so we avoid light excitation due to external light because the device is completely blacked out. Furthermore the optical fiber is mechanically locked in the rubber tube so that laser hits every time the same small area (diameter about 200 μm) determined by the tube. The combination of these two advantages results in reproducible and low noise measurements.

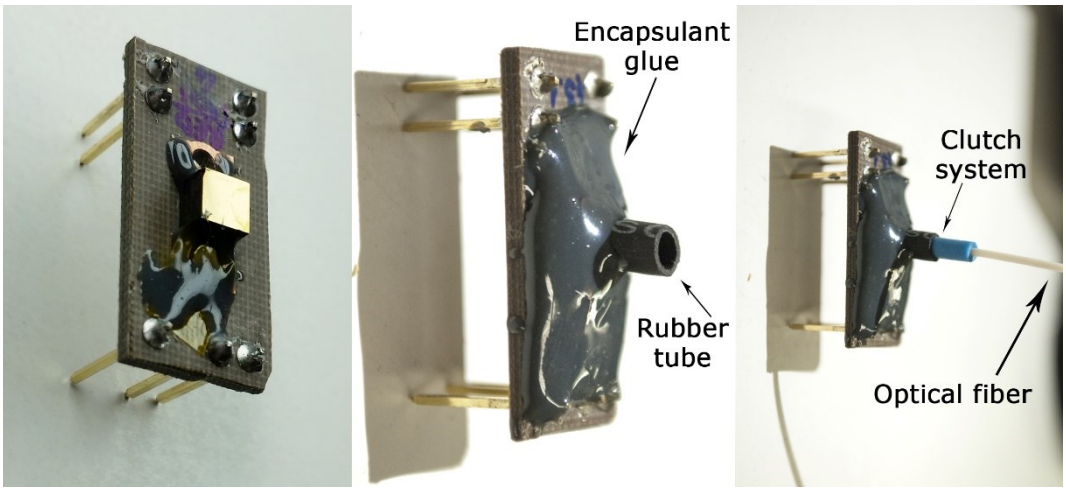

Figure 7-16. Sample before encapsulation (left), encapsulated sample (center), encapsulated sample with optical fiber locked in the rubber tube

Measurements reported in the following sections were acquired using encapsulated detectors. Firstly, I present a validation test of the model by using single pixel detectors with the same dimensions but different pixel size, then measurements performed for both electrons and holes are made on different detectors. Results from detector manufactured using different materials (IMEM and REDLEN) are reported.

7.3.2 Single pixel detectors

Several experiments were made in order to prove the self-consistent method described in chapter 5.4.1, the most significant is the following. Three identical samples were obtained from the same block of REDLEN CZT. The three samples were prepared together in the standard way but with different geometries: three single pixel devices are equipped with pixels of different sizes. Because devices come from the same CZT block, REDLEN material generally shows very high homogeneity, and, in addition, samples are prepared together, we expect similar transport properties and electric field profiles. On the opposite, the weighting field is different for the three detectors, so that the capability of the method to take into account the weighting field can be tested.

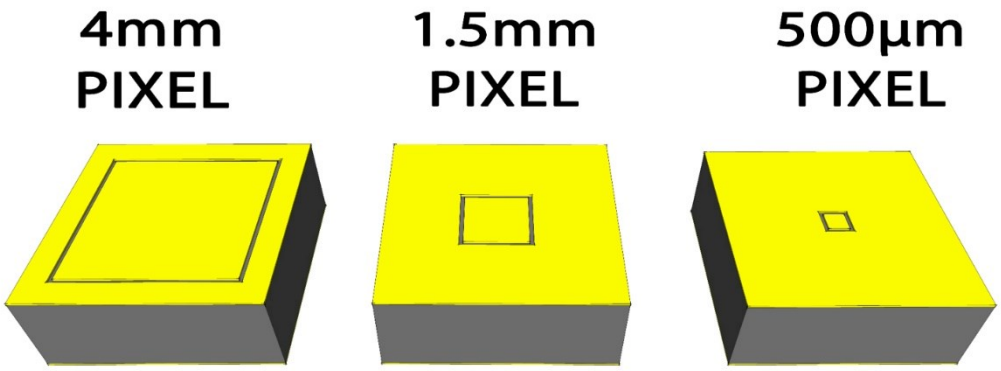

Figure 7-17. Three detectors realized by myself to test the self-consistent model. They have full area cathodes and, at the anode, a monopixel with different dimension: 4 mm, 1.5 mm and 500 µm

The three samples (see Figure 7-17) are 2 mm thick and with square 5.4x5.4 mm^2 cathode. They are equipped with gold contacts: full area cathodes and single pixel anodes surrounded by guard ring. The dimensions of square central pixels are: 4 mm 1.5 mm and 500 µm respectively. Pixel dimension strongly influence the weighting potential and presumably the current transient. In Figure 7-18 the weighting potentials of samples obtained by COMSOL simulations are shown. The top images represent 2D sections that cross the middle of pixel, while in the bottom are plotted the weighting field profile along the 1D line traveled by electrons.

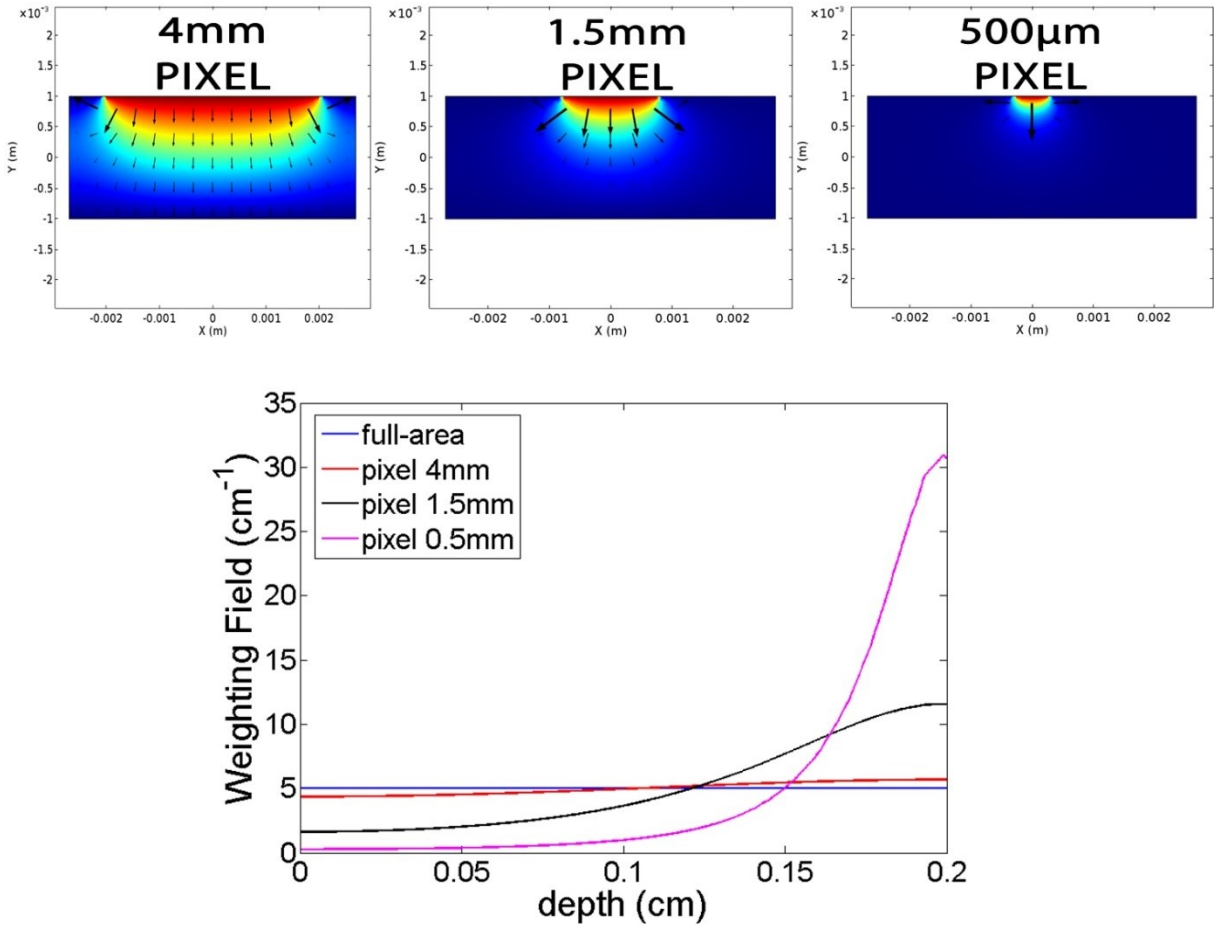

Figure 7-18. Weighting field of three samples: plot on 2D section passing in the middle of pixels (top) and its 1D profile on the line travelled by electrons (bottom)

Current transients (CTs) are amplified and saved by means of an oscilloscope. All CTs, obtained with different potential, are taken using the same laser intensity. This is fundamental because the model requires that the generated charge is the same for each voltage.

In Figure 7-19 the current transients (on the left) and the electric field profiles are shown, achieved from the data analysis (on the right) for the sample with 4 mm pixel. It is typical that close to the contacts the electric field profile change rapidly. The origin of this distortion could be or a real bending of electric field near the contacts or an error due to the determination of initial and final times or due to neglect of diffusion. Probably the distortion is the combination of these effects, anyway the central and largest part of the curves is not affected by that. The transport parameters obtained for electrons are:

$$\mu = 970 \pm 40\ cm^2/Vs \qquad \tau = 1.35 \pm 0.05\ \mu s \qquad \mu\tau = 1.3 \cdot 10^{-3} cm^2/V$$

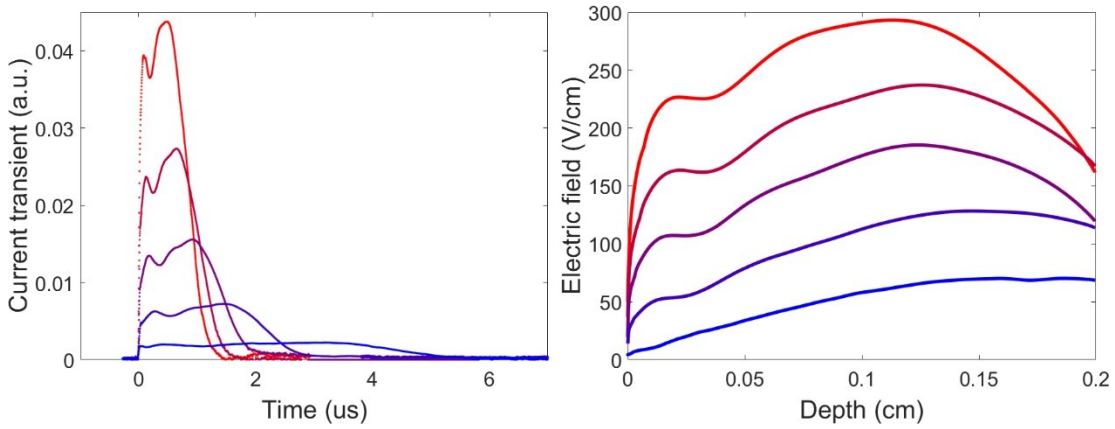

Figure 7-19. Current transient and electric field profile achieved for the sample with 4 mm pixel: the gradient of color between the curves represent the different bias voltages (from 10 V to 50 V, 10 V steps)

Figure 7-20 reports CTs and field profiles obtained from the detector with 1.5 mm pixel. The weighting field is less uniform than the one of the first sample and this is reflected on the increment of the last part of CTs. Transients show the typical "pixel effect": the current increases while carriers travel towards the pixel. The term that increases in time is the weighting field probed by the carriers, it increases approaching the pixel. This effect is purely due to the detector geometry.

This effect is not present in field profile and does not influence the evaluation of μ and τ because they are not influenced by weighting field. Below are reported values of transport parameters.

$$\mu = 990 \pm 30\ cm^2/Vs \qquad \tau = 0.98 \pm 0.07\ \mu s \qquad \mu\tau = 0.97 \cdot 10^{-3} cm^2/V$$

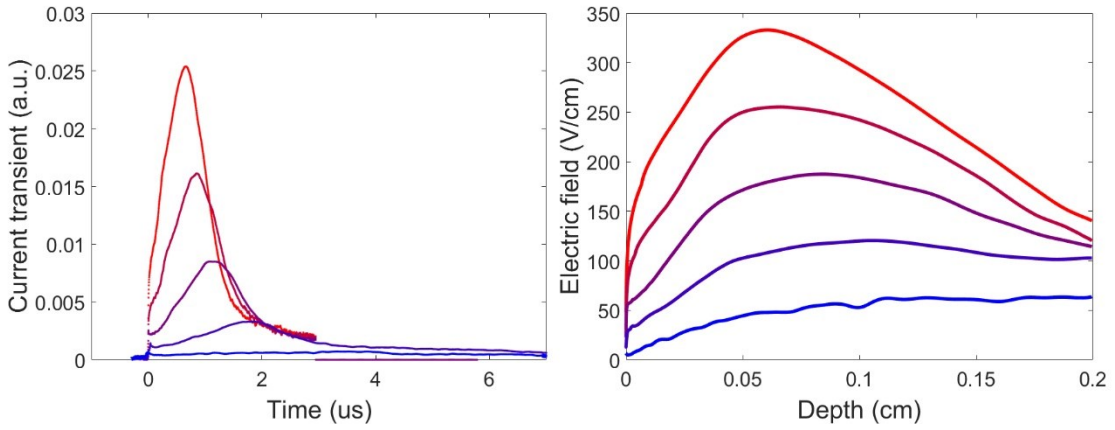

Figure 7-20. Current transient and electric field profile achieved for the sample with 1.5 mm pixel: the gradient of color between the curves represent the different bias voltages (from 10 V to 50 V, 10 V steps)

Lastly we measured sample with pixel of 500 μm (see Figure 7-21). Transport parameters achieved from this sample are:

$$\mu = 980 \pm 50\ cm^2/Vs \qquad \tau = 1.40 \pm 0.05\ \mu s \qquad \mu\tau = 1.37 \cdot 10^{-3} cm^2/V$$

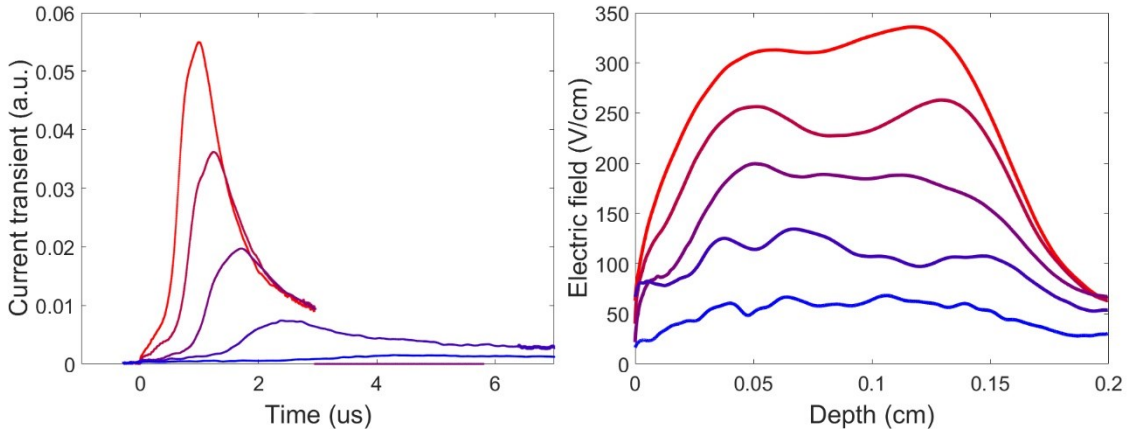

Figure 7-21. Current transient and electric field profile achieved for the sample with 500 µm pixel: the gradient of color between the curves represent the different bias voltages (from 10 V to 50 V, 10 V steps)

The transport parameters are very similar for the first and the third sample, the second one has a different lifetime. That is in accordance with the slope of electric field: slope of the electric field in second sample is higher than in the others. The lifetime and the slope of electric field depend indeed on the presence of negative fixed charge. The fixed charge bends the electric field and further it increases the carrier trapping, decreasing the lifetime. This effect can be generated by several variable. The parameter that we are expecting to be constant for all samples is the mobility because it depends meanly on material properties and samples are produced using the same CZT crystal. The three mobility values obtained are very similar. Furthermore the electric field profiles among the three samples does not change so much.

Data were analyzed also neglecting the effects of weighting field (its value is set 1/L, constant on the whole detector thickness). Electric field profiles show in Figure 7-22 are achieved by imposing uniform weighting field. Electric fields show strong differences between them. Also mobility of the three samples would be different at all (Table 7.1). From these results we can confirm the accuracy of new model also when weighting field becomes significant.

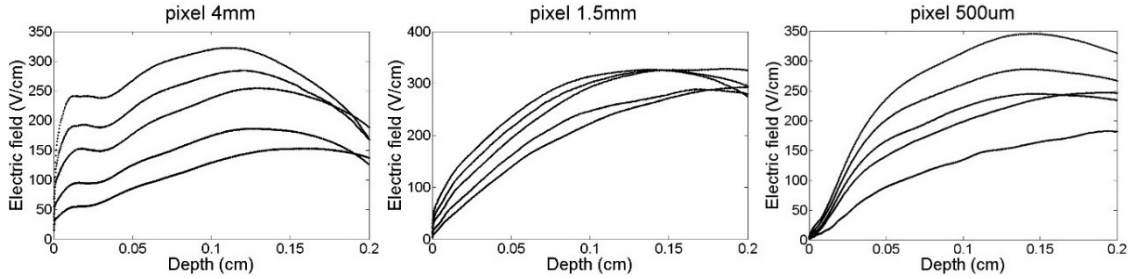

Figure 7-22. Electric field profiles obtained by using the wrong model that does not include weighting field effects (from 10 V to 50 V, 10 V steps)

Sample	Mobility μ (cm^2/Vs)
4mm pixel	987
1.5mm pixel	1070
500µm pixel	1200

Table 7.1

7.3.3 Electrons and holes

LI-TCT potentially allows measuring both electron and hole transport properties. Several samples were studied but unfortunately, the hole signal was too weak and hidden into the noise. Then, we tried to measure the current transient on a sample equipped with platinum contacts and we had a good news: platinum contacts enable to see hole signals, probably because the holes barrier generated by the platinum contact is lower that in the gold case.

Several detectors with platinum contacts were manufactured, some of them were studied in order to achieve hole properties. In the following pages I want to show most significant results obtained using 3 different samples:

- *Sample A*: based on IMEM material, the detector dimensions are 4x4mm^2 and 3 mm thick. The anode shows a central 2x2 mm^2 pixel surrounded by the guard ring.
- *Sample B*: based on REDLEN material, the detector dimensions are and 2 mm thick. Both contacts are full-area without any guard ring.
- *Sample C*: based on REDLEN material, the detector dimensions are 6x6 mm^2 and 1 mm thick. The anode shows a central 4x4 mm^2 pixel surrounded by the guard ring.

Every sample was encapsulated and both electron and hole current transients were stored for different bias voltages. The applied voltages were different in electron and hole cases: their transport parameters are strongly different so we typically set from few volts up to one hundred volts for electrons and in the region of hundreds volts for holes.

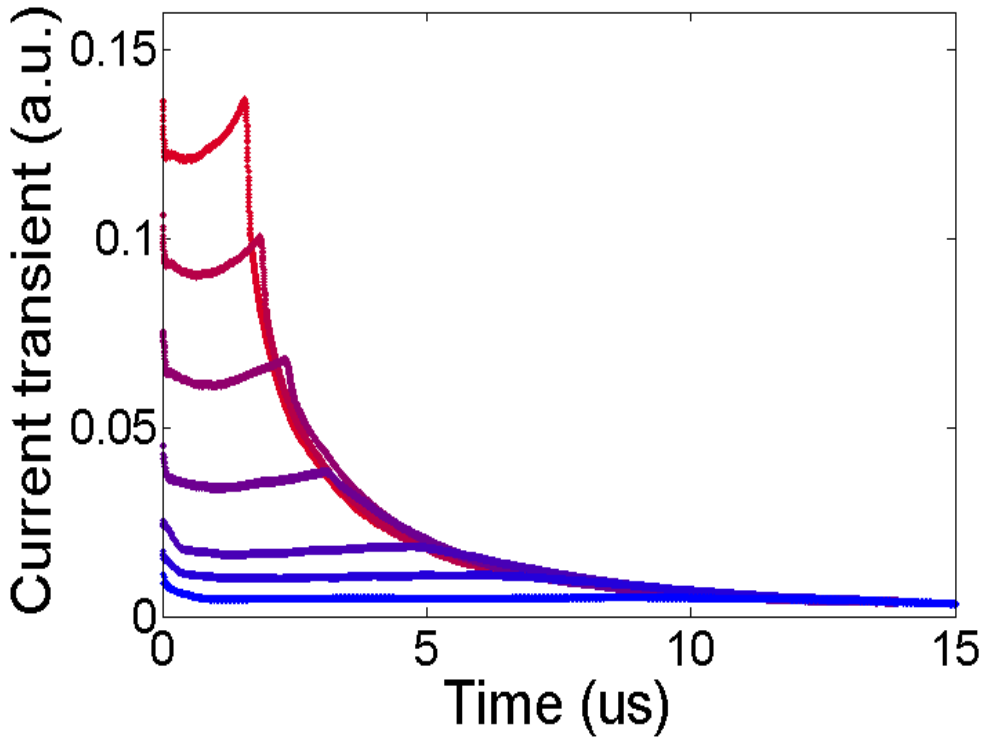

Figure 7-23. Hole current transients for sample B, the color gradient represents the different bias voltages (70 V, 100 V, 150 V, 200 V, 300 V, 400 V, 500 V)

Figure 7-23 shows the CTs for holes in detector B; CTs information are evaluable only after the analysis, then for the other samples are reported only electric field profile and transport properties.

The three figures (Figure 7-24, Figure 7-25 and Figure 7-26) report resulting electric field profile of three samples for both electrons (left) and holes (right).

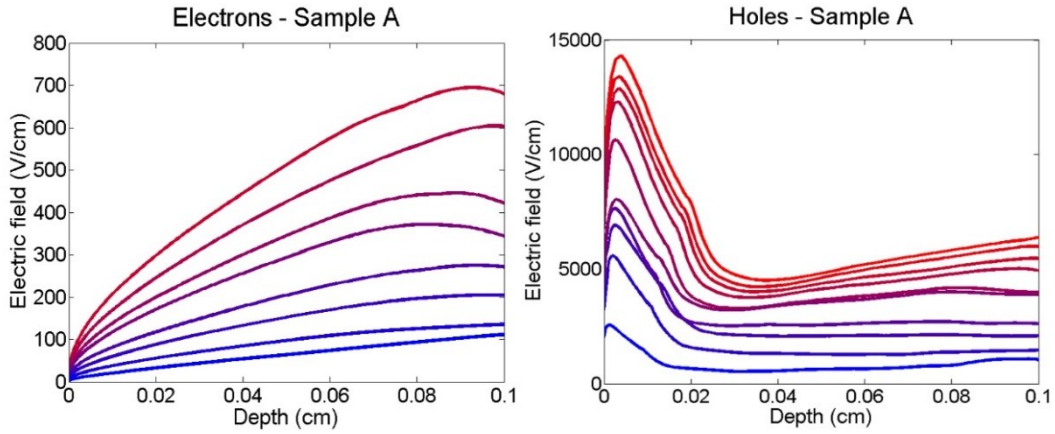

Figure 7-24. Electric field profiles for electrons (left) and for holes (right) of sample A. The color gradient represents the different bias voltages: for electrons (from 5 V to 40 V, 5 V steps) and for holes (from 200 V to 650 V, 50 V steps)

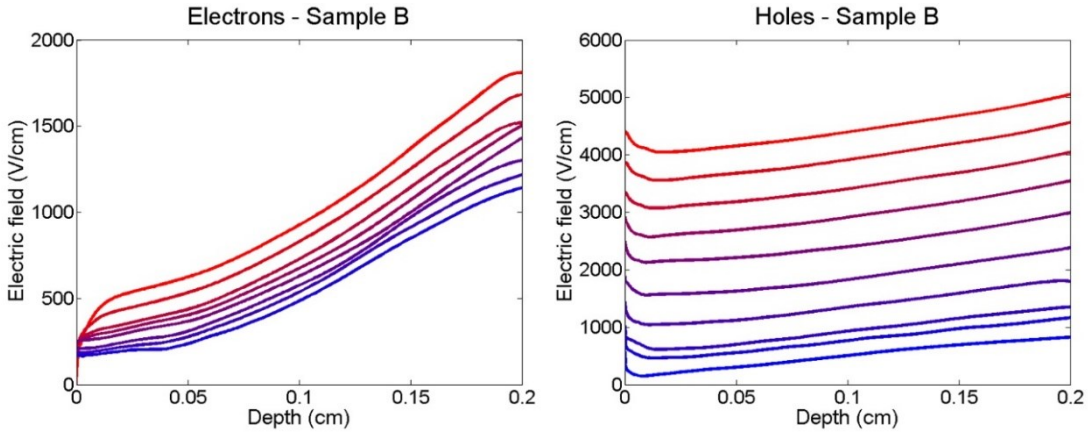

Figure 7-25. Electric field profiles for electrons (left) and for holes (right) of sample B. The color gradient represents the different bias voltages: for electrons (from 100 V to 160 V with 10 V steps, and 180 V) and for holes (100 V, 150 V, and from 200 V to 900 V with 100 V steps)

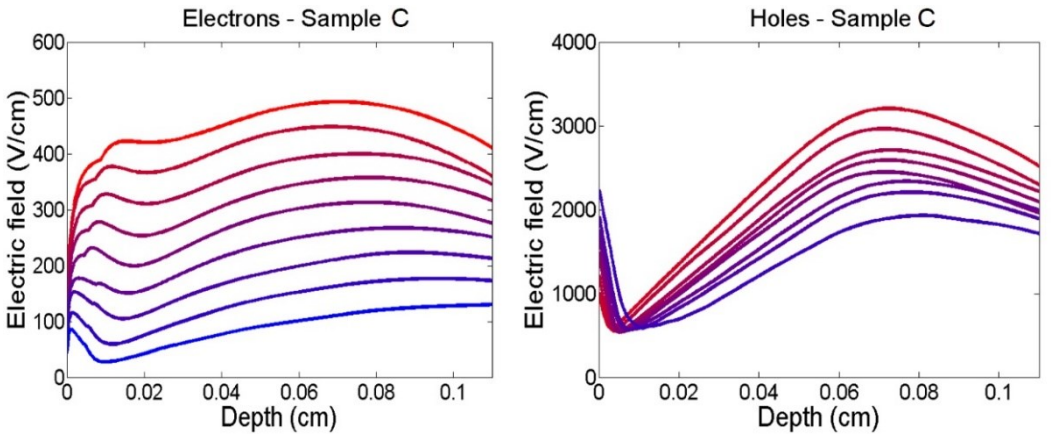

Figure 7-26. Electric field profiles for electrons (left) and for holes (right) of sample C. The color gradient represents the different bias voltages: for electrons (from 5 V to 50 V with 5 V steps) and for holes (160 V, 180 V, 190 V, 200 V, 210 V, 220 V, 240 V, 260 V)

Electric field measured with holes exhibit a strong slope in the first hundreds micron close to the illuminated electrode. This phenomenon is stronger in sample A and it could be due to fixed

charges localized under the cathode. This is probably due to the holes trapped near this electrode, when the distance is higher than about 100 micrometers from the illuminated electrode, the fixed charge changes in sign and electric field begins to increase. This phenomenon is found only with platinum contacts and using holes.

Transport parameters obtained for both carriers are reported in Table 7.2.

Sample	Electrons mobility μ_e (cm²/Vs)	Electrons life-time τ_e(μs)	Holes mobility μ_h (cm²/Vs)	Holes life-time τ_h(μs)
A	1408	0.65	36	1.97
B	976	-	47	5.8
C	1032	0.65	28	>5

Table 7.2

Sample A shows an anomalous value of electrons mobility, another sample of the same ingots had a mobility about 1000 cm²/Vs. The hole lifetime of sample A is consistent with the hypothesis of fixed charge deduced from electric field profile. For sample B we are not able to calculate the lifetime for electrons because the standard deviation of q_0 does not show the minimum necessary for the determination of lifetime (see step 1 of the method described in chapter 5.4.1). The values of hole mobility in the three samples are similar as expected.

The model is unable to give the lifetime of holes for sample C: times of flight for applied voltages are shorter than hole lifetime then we have not enough data to reconstruct well the carrier trapping process. The only way to increase flight time is to decrease the bias voltage but it is very difficult measure transients with voltages lower than 100 V: the signal becomes comparable with the noise and it is not possible to estimate the correct time of flight and the model results inapplicable. We can only assume that the lifetime is greater than the highest time of flight, then larger that 5 μs for sample C.

Lifetimes for holes slightly change among different detectors; the greater variation is from sample A and the other two, this difference could be due to the different CZT materials (sample A is from IMEM and other two are from REDLEN).

Thanks to platinum contacts we have measured for the first time mobility and hole lifetime using LI-TCT. Further analysis are required to increase statistic and to understand better the behavior of platinum contact.

7.3.4 Conclusions

LI-TCT, when applied on pixel detectors, needs a preliminary study of contact geometry. Current transients are strongly influenced by the weighting field.

The proposed self-consistent model enabling to measure μ, τ and E directly on final devices, taking into account the weighting proper field. The method was used to measure both electron and hole properties. The method was validated on devices having different weighting fields. The “pixel effect” changes the transients shape but not influence transport parameters and electric field.

7.4 Diamond session

The aim of this experiment was to investigate the performances of a prototypal high-flux spectroscopic imaging detector system based on CZT. One of the issues with this type of system is that the use of small pixels (<500 μm) leads to charge being shared between multiple channels leading to a reduction in spectroscopic performance. As the flux of X-rays on the detector becomes higher it becomes increasingly more difficult to correct the sharing effect. In this experiment the prototype system is used to demonstrate a novel digital pulse processing technique that, taking into account both x-ray energy and timing information, allows charge sharing correction for much higher rates.

The experimental setup has been fully described in section 5.5. Firstly we had to calibrate 1 millimeter detector and the digital system and then we started the scans. 1D and 2D scans were performed for both the array sizes (250 μm and 500 μm pitch). The same experiment was realized for the 2 millimeter detector produced by Redlen. By using the digitizer system developed by university of Palermo we made both snapshots and fast PSA for each scan. Finally, we performed a linear scan and spectroscopic measurements with nuclear sources on HEXITEC device.

PIXIE and HEXITEC detectors were carried out by the undersigned and I was also directly involved in the measurement campaign at the diamond synchrotron. Part of data analysis and, in particular, study of subpixel positioning were part of my work.

7.4.1 Detector calibration – detector IMEM 1 mm thick

Before starting mapping measurements, each pixel in the region of interest was energy calibrated by irradiating the center of each pixel with a 10x10 μm^2 beam at different energies. Only the center of the pixel was irradiated to avoid charge sharing between the neighboring pixels. Figure 7-27 compares the spectroscopic performance of the pixels of the 500 μm pitch array of the 1 millimeter thick CZT detector. All presented data were processed thanks to the fast-pulse-processing technique.

The performance at 20 keV and 50 keV was compared for the same array and typical FWHM measured at these two energies was 1.5 keV and 1.7 keV respectively. The increment at the higher energy may be in part due to the generation of Cd and Te florescence line. The K-edge of these two elements is 23.2 keV and 27.5 keV respectively and, at 50 keV, it is possible to generate florescence which leads to the formation of escape peaks which are clearly visible in Figure 7-27 (Bottom).

From these measurements it was possible to achieve the input count rate (ICR) at 20 keV and 50 keV which had values of 6.0 kcps and 0.3 kcps respectively. Knowing the size of the beam, 10x10 μm^2, this can simply be converted to flux which gives values of 6.0 10^7 photons $s^{-1}mm^{-2}$ and 0.3 10^7 photons $s^{-1}mm^{-2}$. These measured fluxes are consistent with what is expected from the output of the channel cut monochromator.

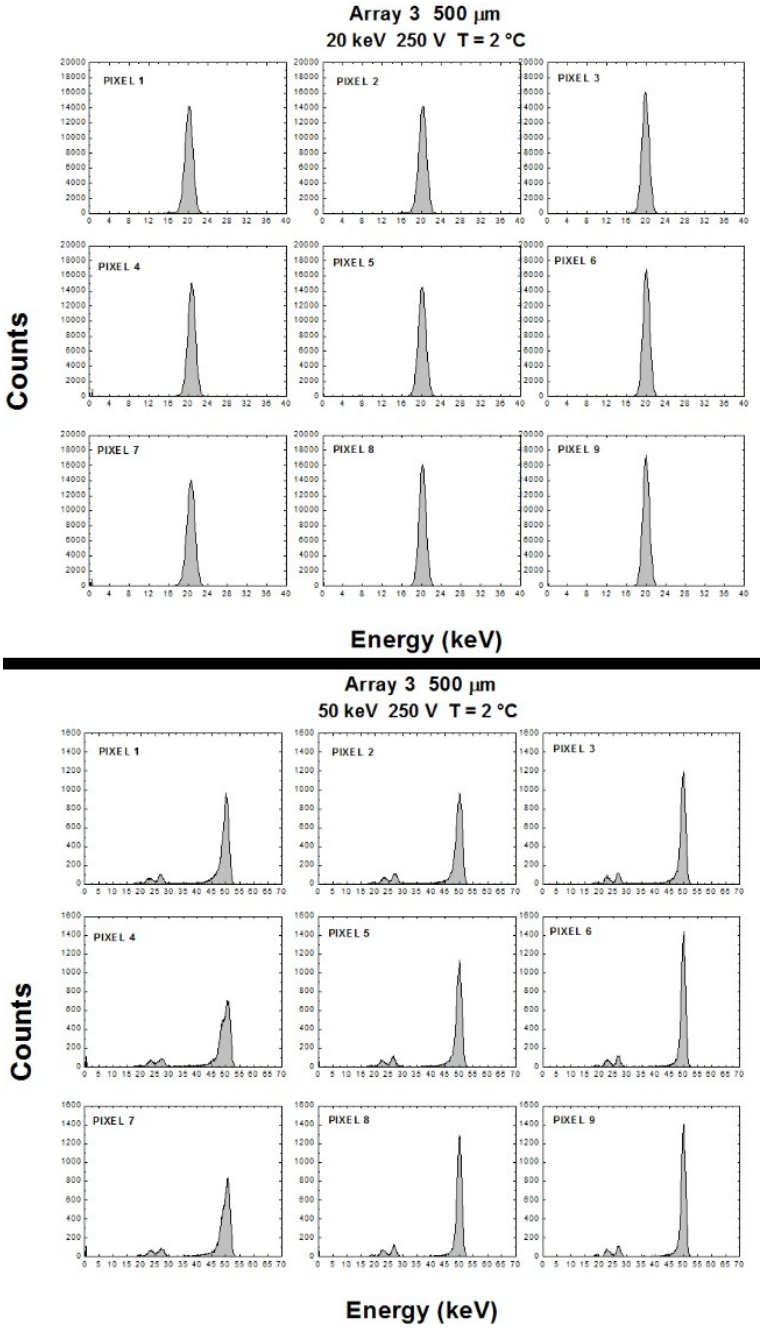

Figure 7-27. Calibration of each pixel at 20 keV (top) and 50 keV (bottom)

To test the robustness of the digital pulse processing technique, the beam dimensions were changed using the JJ-slits to produce a lozenge with dimensions 10x500 µm^2. The beam center was positioned over the middle pixel and data collected at 25 keV. The measured ICR was 670 kcps which corresponds to a flux of the order of 10.0 10^7 photons $s^{-1}mm^{-2}$. Figure 7-28 shows a histogram of the pulse "time width (TW)" which is proportional to the measured rise time of the pulse which can be used to discriminate both charge sharing and pulse pileup.

The TW histogram shows that the majority of events have a width of 280 ns which corresponds to real interactions occurring in a single pixel. Events are also detected with widths of <260 ns and these are consistent with events that have experienced charge sharing. There are also significant numbers of events that have TW values exceeding 300 ns and these are due to the pile-up of multiple X-rays.

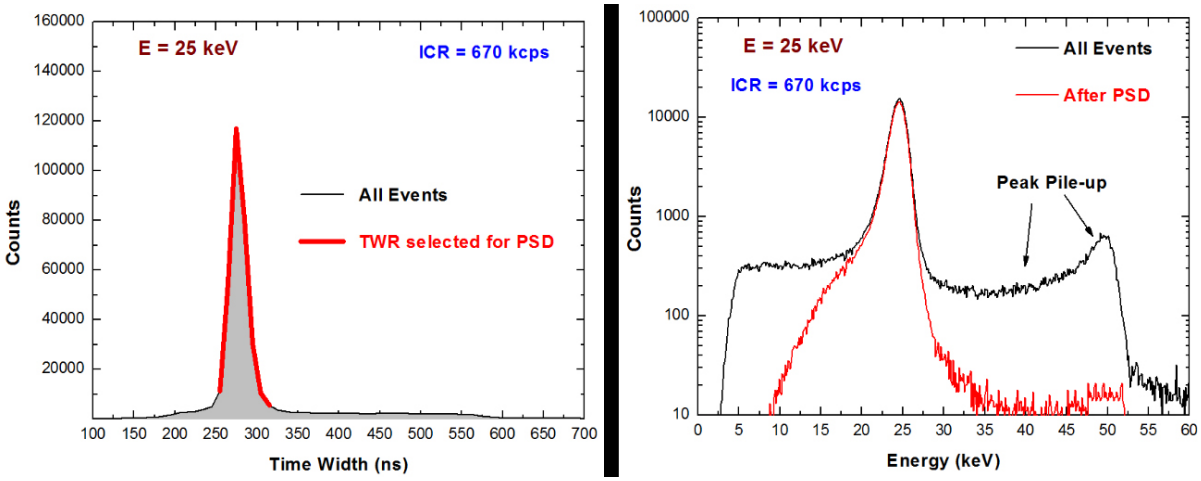

Figure 7-28. Time width of pulses (left) and spectrum before and after PSD correction (right)

Using the TW histogram shown in Figure 7-28-left it's possible to filter the resulting spectra to reduce charge sharing and pulse pile-up. The resulting improvement in the spectroscopic performance can be seen in Figure 7-28-right. FWHM of the 25 keV photo-peak is about 2keV after the correction. These results demonstrate that the digital pulse processing technique is working to reduce pile-up and charge sharing even at fluxes approaching 1 Mcps.

7.4.2 1D scan – detector IMEM 1 mm thick

After the calibration of PIXIE system and pulse processing technique, the effect of the interaction position on the detector performance was investigated performing 1D scan measurements. A 10x10 μm^2 microbeam was scanned between two pixels in steps of 10 µm and the detector output studied. Figure 7-29-top shows how the ICR changed in each position for each of the pixels involved, while Figure 7-29-bottom shows the resulting effect on the position of the photo-peak measured by each pixel.

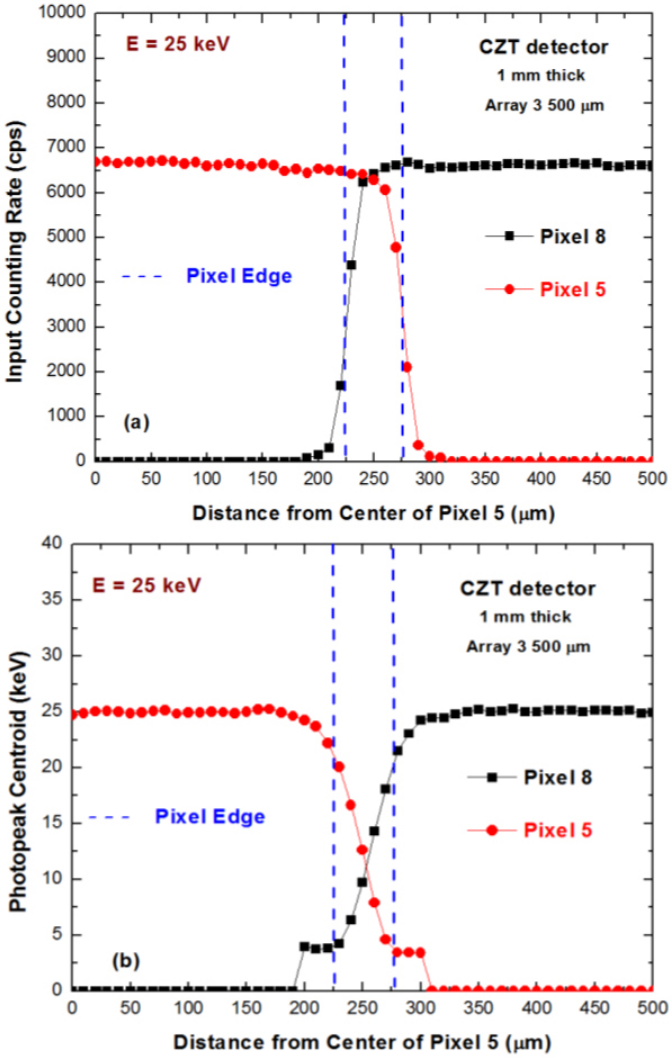

Figure 7-29. 1D scan: Input Counting Rate (top) and centroid energy (bottom) for two adjacent pixels

While the ICR is consistent along the length of the line-scan, the peak centroid shows a reduction in energy close to the edge of the physical electrode and in the inter-pixel region. Figure 7-30 shows examples of the spectra produced in the central pixel for three different interaction positions and also demonstrates how, as expected, the measured TW changes depending on the position.

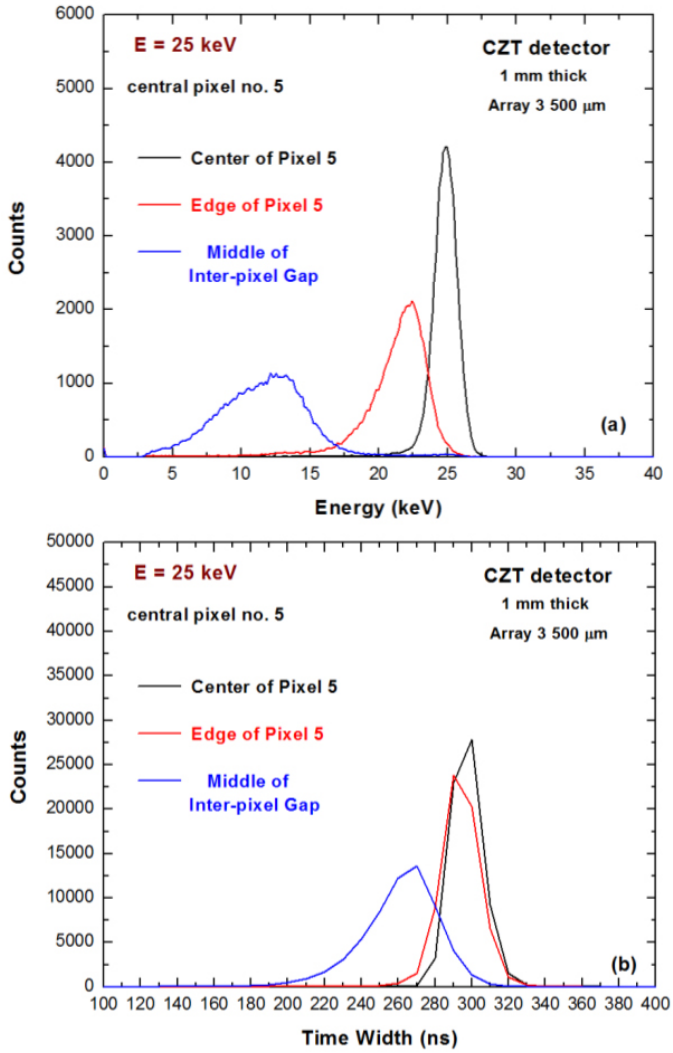

Figure 7-30. Energy spectra measured at three different positions along the 1D line scan (top). TW histograms measured at the same positions (bottom)

The extent of the charge sharing in the 1D line scan was also investigated by studying the percentage of events that displayed sharing at each position. Figure 7-31-top shows the multiplicity (m): the number of pixels involved in an interaction, as a function of position. The measurements show that charge sharing occurs up to a distance of 120 µm which is much larger than the 50 µm inter-pixel spacing. The reason for this difference is due to the diffusion of the charge cloud as it drifts from the X-ray interaction position to the anode.

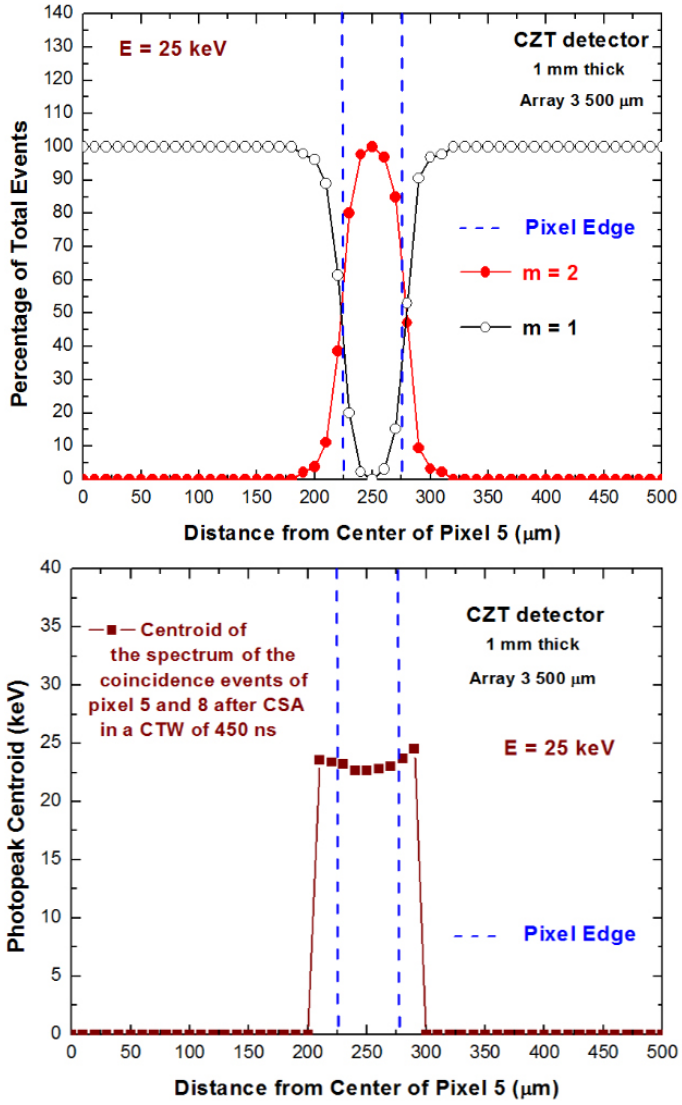

Figure 7-31. Top: percentage of single (m=1) and charge sharing (m=2) events as a function of position in the pixel pitch. Bottom: variation of peak centroid (energy) after charge sharing reconstruction

In the inter-pixel where the multiplicity is equal to 2, the signal measured in each pixel were summed together to recover the energy of the original X-ray. Figure 7-31-bottom shows how the reconstructed peak centroid (energy) varies across the inter-pixel region. At the center of the pixel the peak centroid is 22.7 keV which represents a charge loss of 2.3 keV. Rather than trapping in a low field region between pixels, this charge loss is likely to be due to the low energy threshold per pixel which has a value about 2 keV.

7.4.3 2D map – detector IMEM 1 mm thick

In the previous sections the performance of the digital pulse processing technique has been demonstrated for different energies, fluxes and charge sharing contributions. The next set of experiments focused on the uniformity of the CdZnTe detector as a function of energy and pixel pitch. To do this a 10x10 µm² beam was scanned across the detector for both the 500 µm and 250 µm pitch arrays. The step size for these scans was 25 µm and 12.5 µm respectively. The scans were carried out at 25 keV (below the Cd and Te K-edge) and at 40 keV.

Figure 7-32 shows the 2D map, on the 500 µm array at an energy of 25 keV. The map has a number of notable features; the first is that the measured response varies slightly from the expected pixel geometry. In reality, the physical pixels of the detectors have a uniform geometry with 500 µm pitch and a 50 µm spacing yet in the measured response of the detector, in some regions, the inter-pixel regions are no longer parallel and perpendicular. These measurements suggest that the electric field in the detector may contain non-uniformities that affect the collection volume of individual pixels. In the same image one of the lower pixels also shows a region of charge loss which corresponds to some non-uniformity of the electric field. The cause of this non-uniformity is unclear but may be due to either a crystalline defect (inclusion) or perhaps some issues with the electrode.

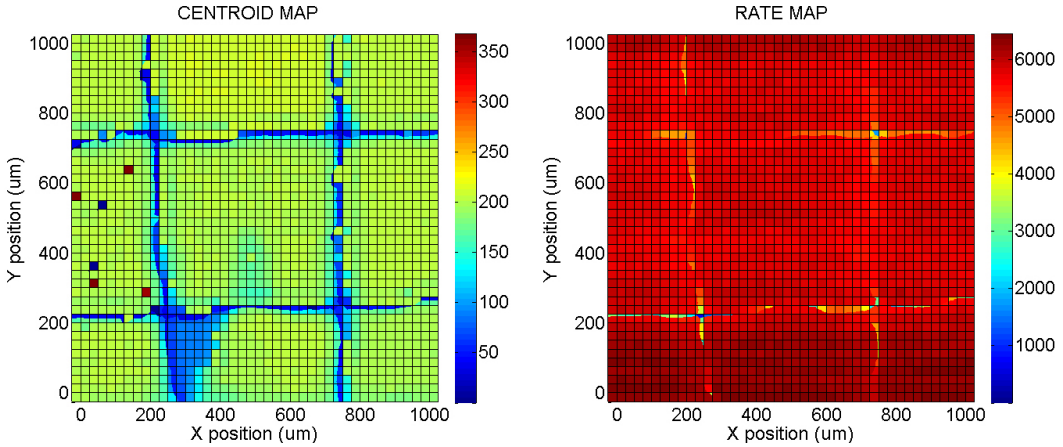

Figure 7-32. 2D scan of 500 µm array pitch performed with 25x25 µm² and 25 keV beam. Map of photopeak centroid (left) and ICR (right) as a function of beam position

The same scan was repeated but this time at an increased energy of 40 keV as shown in Figure 7-33. The main difference that could be observed was in the maps of the total count rate per position (the sum of counts from all pixels per position) which is shown in Figure 7-34. At the higher energy of 40 keV the regions of charge sharing that occur between pixels appear broader and this is due to the generation of Cd and Te florescence X-rays that lead to an increase in the overall charge sharing. This charge sharing region has a width of 50 µm and 75 µm at 25 keV and 40 keV respectively.

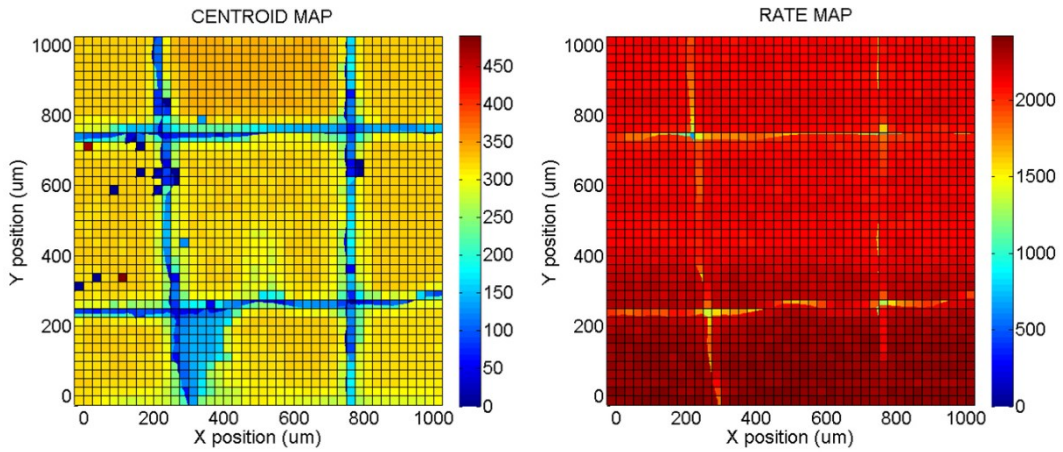

Figure 7-33. 2D scan of 500 µm array pitch performed with 25x25 µm² and 40 keV beam. Map of photopeak centroid (left) and ICR (right) as a function of beam position

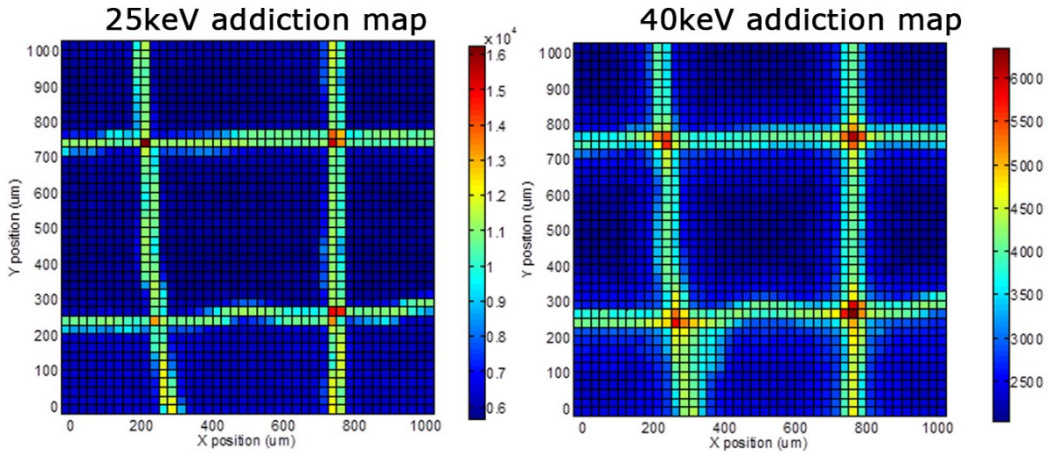

Figure 7-34. 2D scan of 500µm array pitch performed with 25x25µm² beam at 25keV (left) and 40keV (right) photon energy. Maps show the total ICR for each pixel

The same mapping procedure was also repeated for one of the 250 µm pitch pixel arrays of the same detector this time with a map resolution of 12.5 µm. Figure 7-35 shows the results of this 2D mapping at an energy of 25 keV. The maps show considerable non-uniformities in the images with the pixel borders being far from parallel or perpendicular suggesting that there are significant electric field non-uniformities on the scale of 100 µm. The bottom right hand corner of the central pixel also shows a large defect that affects not only the peak centroid but also the ICR in these positions.

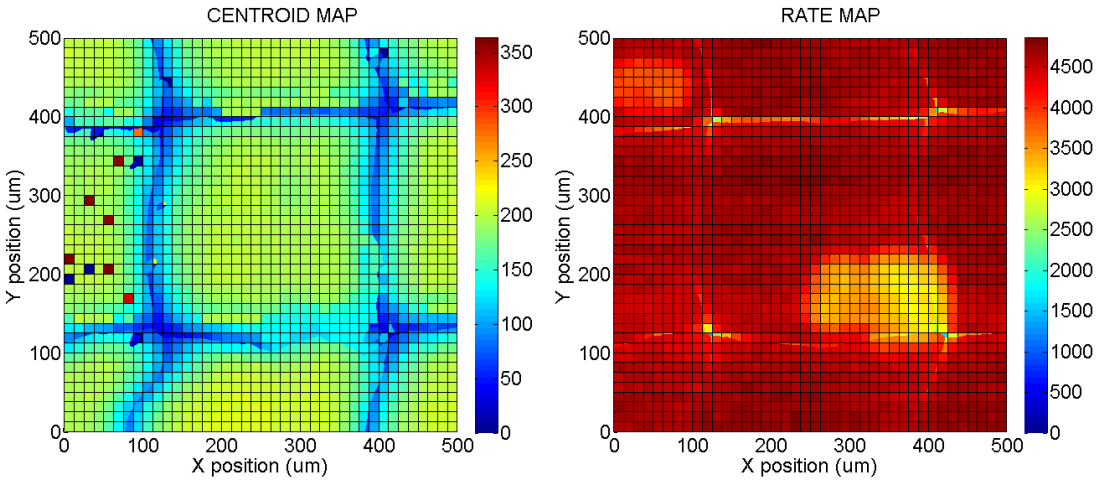

Figure 7-35. 2D scan of 250 µm array pitch performed with 12.5x12.5 µm² and 25 keV beam. Map of photopeak centroid (left) and ICR (right) as a function of beam position

Figure 7-36 shows a map of the same area this time repeated at an X-ray energy of 40 keV, above the Cd and Te K-edges. In this instance the map shows the same non-uniformities but with a much greater amount of charge sharing between pixels. This is clearly visible in Figure 7-37 which compares the total ICR per scan position. The measured width of the charge-sharing region between pixels for 25 keV and 40 keV were 75 µm and 100 µm respectively. The difference at the two energies, as with the 500 µm pitch, is due to the generation of florescence X-rays from the detector material itself.

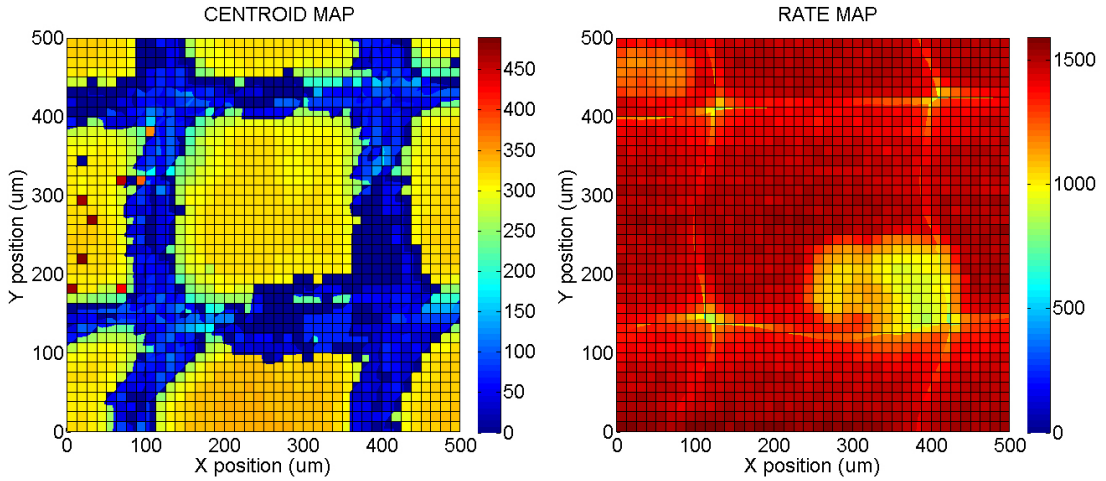

Figure 7-36. 2D scan of 250 µm array pitch performed with 12.5x12.5 µm² and 40 keV beam. Map of photopeak centroid (left) and ICR (right) as a function of beam position

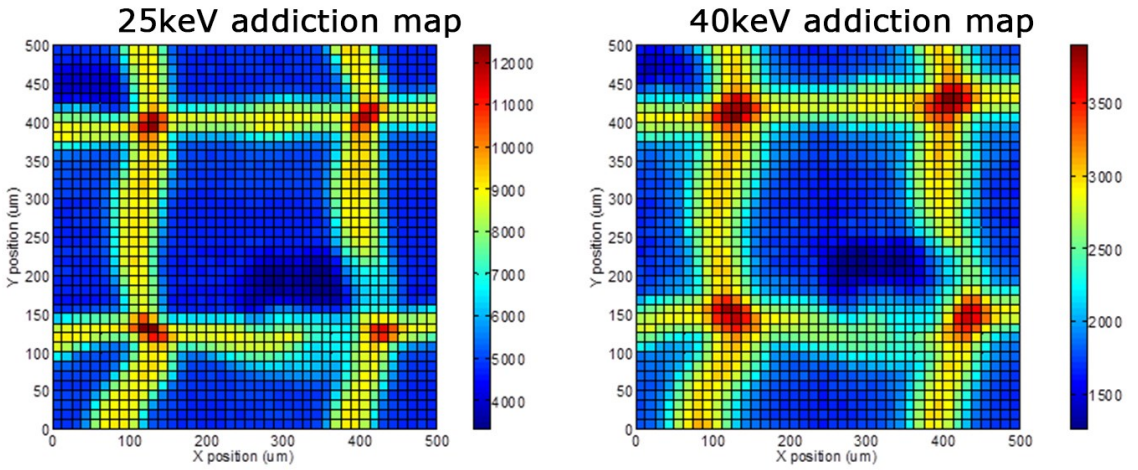

Figure 7-37. 2D scan of 250 µm array pitch performed with 12.5x12.5 µm² beam at 25 keV (left) and 40 keV (right) photon energy. Maps show the total ICR for each pixel

7.4.4 2D map – High-flux REDLEN 2 mm thick

The 2D mapping measurements were repeated but this time using a 2 mm thick CdZnTe detector that had been fabricated by Redlen Technologies from high flux grade CdZnTe material. Figure 7-38 shows the results of mapping at 25 keV of the 500 µm pitch array with a resolution of 25 µm per positon. The resulting map appears very uniform with the pixel laid out on a regular grid as would be expected from the physical geometry of the pixel electrodes. Charge sharing is observed over a 75 µm region which is consistent with the size of the inter-pixel region (50 µm) and the fact that the charge cloud will have diffused during the drift over the 2 mm of the detector.

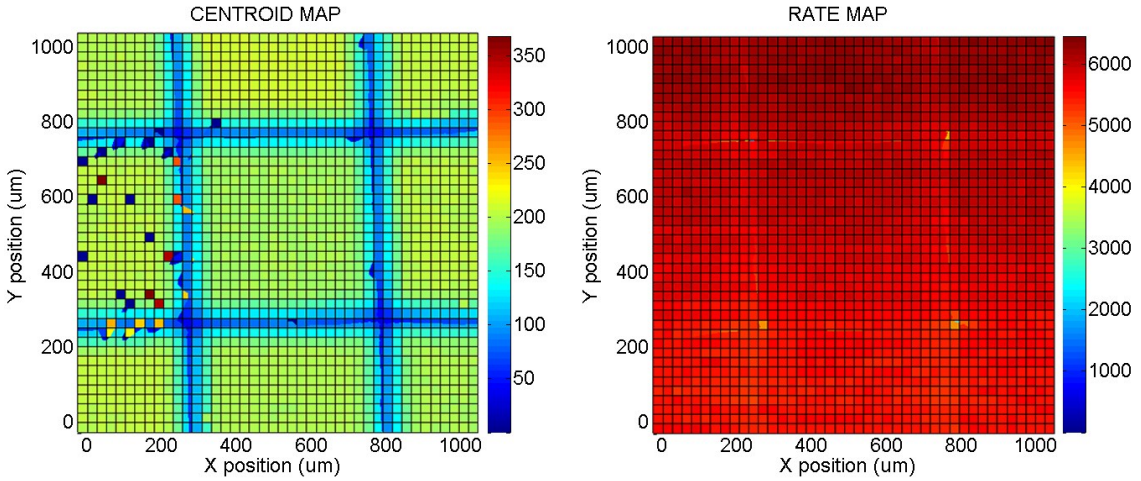

Figure 7-38. 2D scan of 500 µm array pitch performed with 25x25 µm² and 25 keV beam. Map of photopeak centroid (left) and ICR (right) as a function of beam position

The mapping was repeated at 40 keV as shown in Figure 7-39, thickness of sharing region is similar to that with 25 keV. Both the ICR maps display a little change in the uniformity of the detector response during the measure, as found also in Figure 7-33.

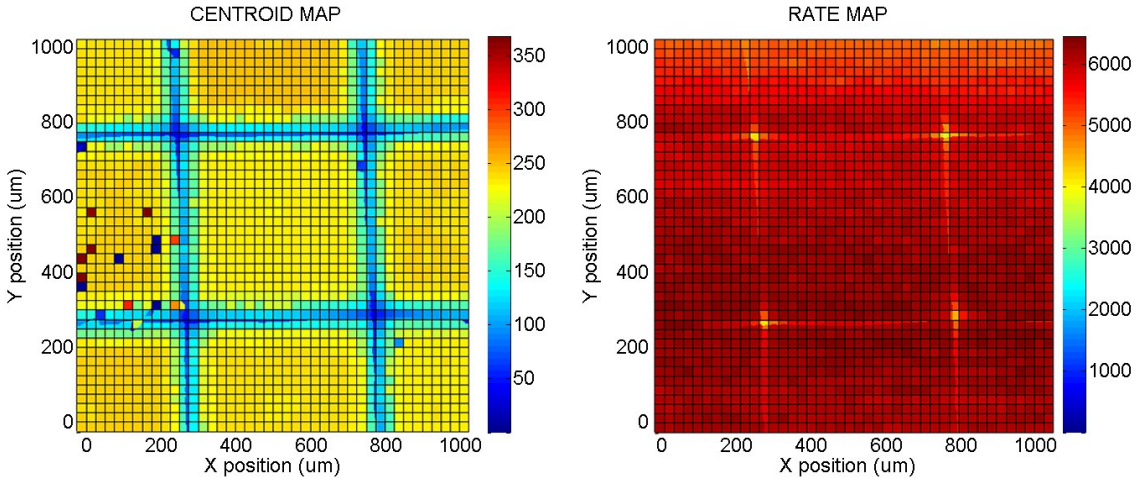

Figure 7-39. 2D scan of 500 µm array pitch performed with 25x25 µm² and 40 keV beam. Map of photopeak centroid (left) and ICR (right) as a function of beam position

Remaining at 40 keV, 2D mapping of one of the 250 µm pixel arrays was completed with a resolution of 12.5 µm which can be seen in Figure 7-40. The imaging of the pixels shows a regular grid as expected from the detector electrode geometry and is consistent with the response of the larger pixels. The measured charge sharing region between pixels was about 62 µm, similar to the inter-pixel gap size. These results suggest that the electric field inside the Redlen Technologies 2 mm thick detector is more uniform than that of the 1 mm device.

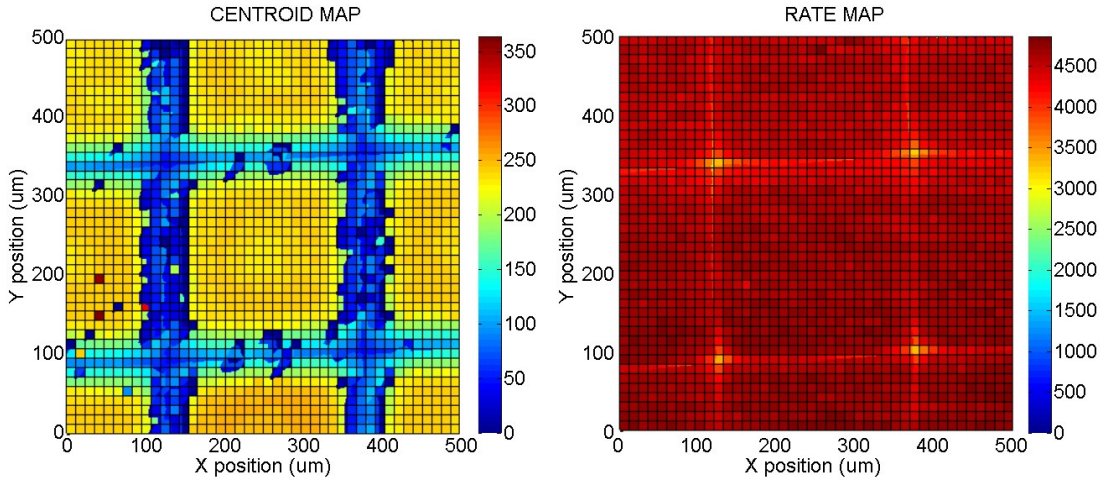

Figure 7-40. 2D scan of 250 µm array pitch performed with 12.5x12.5 µm² and 40 keV beam. Map of photopeak centroid (left) and ICR (right) as a function of beam position

7.4.5 HEXITEC

With the aim to study sharing effects in a multi-pixel system we measured the HEXITEC detector (described in chapter 4.3.2). Firstly we performed a 1D scan from pixel 11,48 to pixel 11,52 using a 10x10 µm² micro beam; the beam is moved 10 µm at each step, We have saved RAW data for each position and then the data have been analyzed using Matlab programs. This type of scan was performed for both 25 and 50keV for the same pixels. Saved data are 2D-frame 80x80 every 25µs containing only the energy information for each pixel; so the analysis performed with PIXIE on the time width are not possible. We can perform Charge Sharing Addition or Discrimination for each frame. When two or more neighboring pixels detect an event in the same frame, the event is classified as shared event.

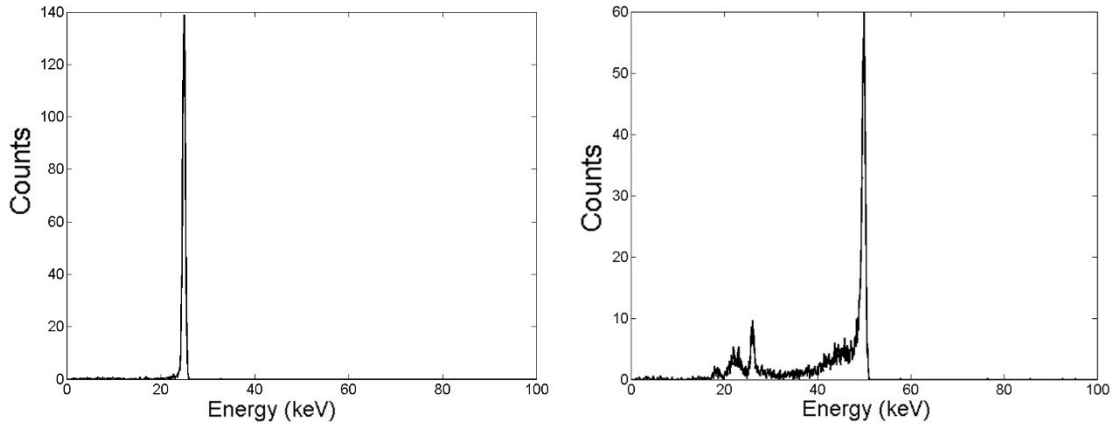

Figure 7-41. Typical spectra obtained with 25 keV (left) and 50 keV (right) beam located at the center of pixel

In the following figures (from Figure 7-42 to Figure 7-48) the centroid (on the left) and the counts (on the right) for each scanned pixel, represented in the plots with different colors, are shown. The energy of the beam was set to 25 keV for these scans. Figure 7-42 shows the RAW data plots. If any correction is applied, the regions of overlapping between pixels have a lower value of centroid and of counts. This means that the final spectrum is distorted by shared events as an increment of low-energy counts which is reflected also in total counts increment (a single event is counted twice). Distortion is greater when the overlapped region increases and, as seen in PIXIE

with small pixel pitch (250 μm), the shared events are numerous also at low energy. At 25 keV a pixel feels the charge generated by the interaction up to 95 μm from its border.

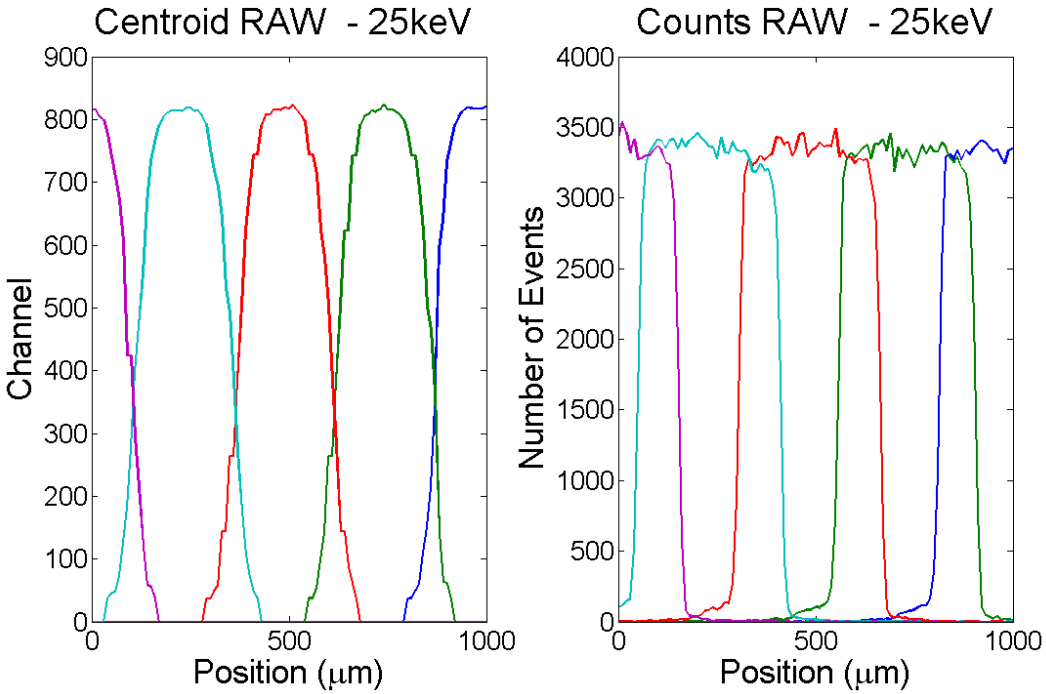

Figure 7-42. RAW data of 1D scan at 25 keV: centroid (left) and counts (right) values for each pixels

To overcome this problem we have applied CSA and CSD correction explained in detail in chapter 4.2.1. With the first one, the measured energies (centroid) of shared events are added and the sum value is allocated at pixel that had the highest value. In this way the total counts and centroid are more homogeneous in the regions between pixels. RAW data of previous figure are corrected with CSA and reported in Figure 7-43.

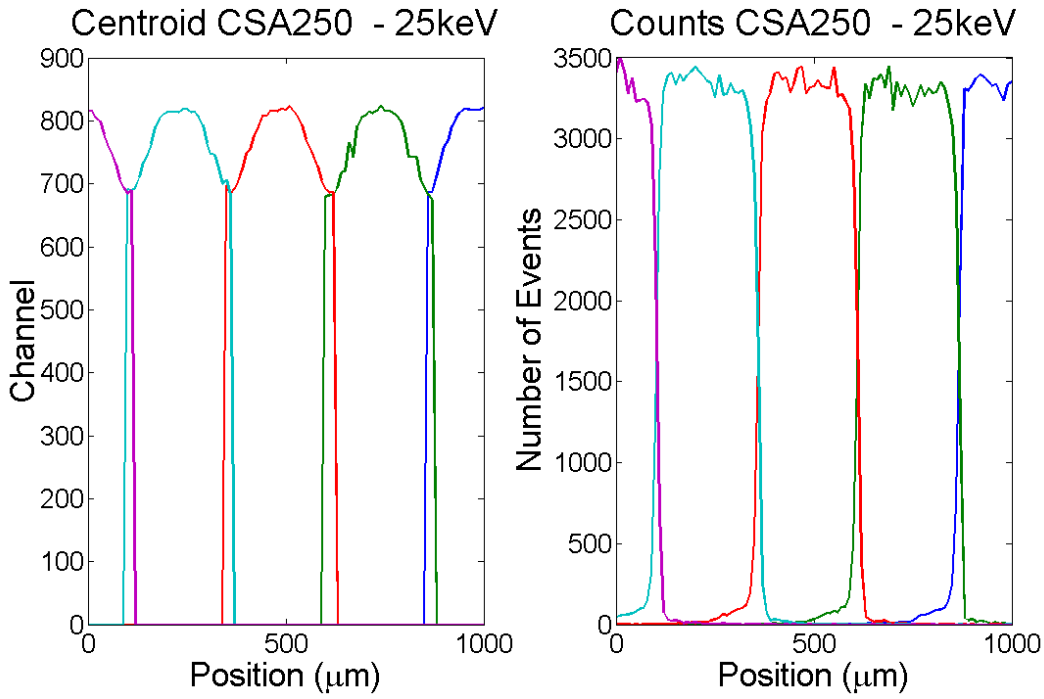

Figure 7-43. CSA results for 1D scan at 25 keV: centroid (left) and counts (right) values for each pixels

CSD consists in the elimination of shared events. In this way the final spectra is not affected by fake low-energy events (generated by the sharing) but total counts in the region between pixels become zero. RAW data are corrected with CSD and reported in Figure 7-44.

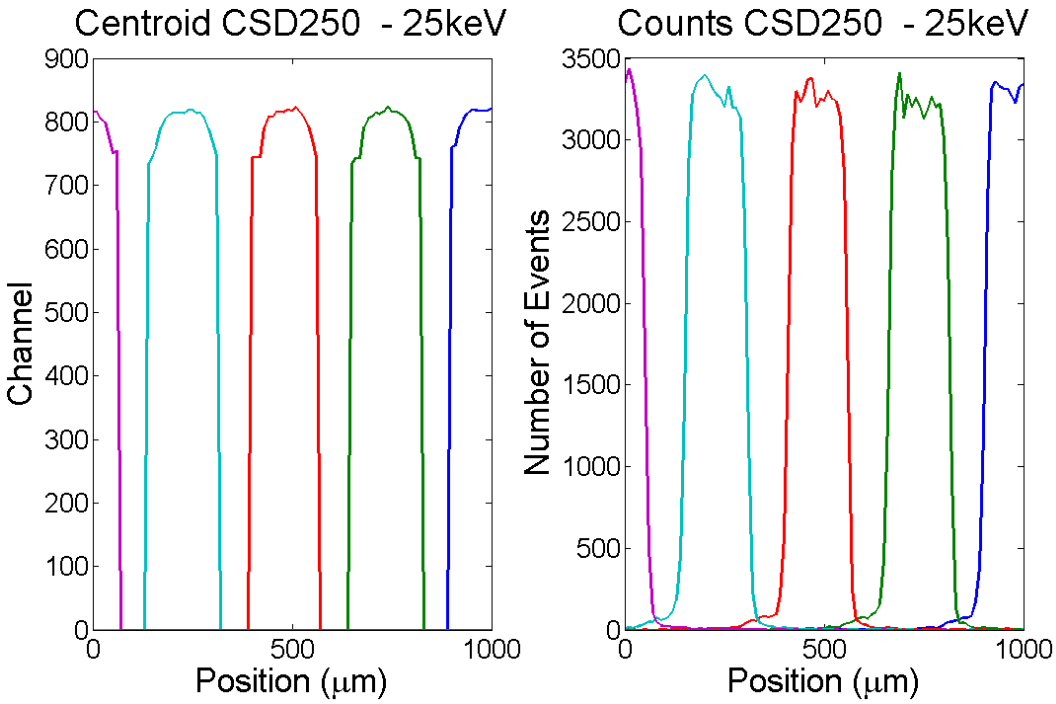

Figure 7-44. CSD results for 1D scan at 25 keV: centroid (left) and counts (right) values for each pixels

The 1D scan was performed also at 50 keV and in this case the scan was made only for the last three pixels. RAW data were acquired and after corrected with the previous techniques. Unelaborated data are reported in Figure 7-45. In accordance with the prediction the region of overlapping is greater than in the 25 keV case. The maximum distance from the pixel at which an event is detected is about 260 μm (more than the pixel pitch), this means that correction with first neighbor could be insufficient. For high energies we have to introduce a correction considering also the pixel around first neighbors. Counts have a decreasing trend during the measurements, this is probably due to the decreasing of the incident radiation flux.

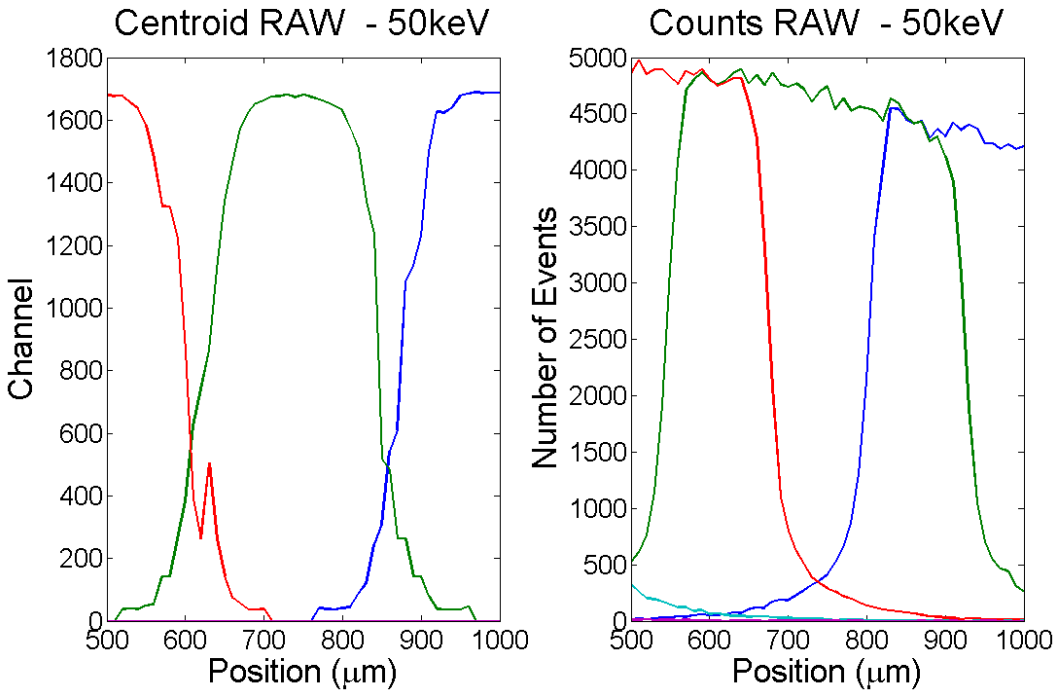

Figure 7-45. RAW data of 1D scan at 50 keV: centroid (left) and counts (right) values for each pixels

With classical CSA we obtain an improvement on the energy resolution and on the homogeneity of counts (Figure 7-46). Using the second-neighbor correction snCSA (Figure 7-47) we are able to remove the tails of far pixels but no important improvement are noted in terms of centroid or total counts.

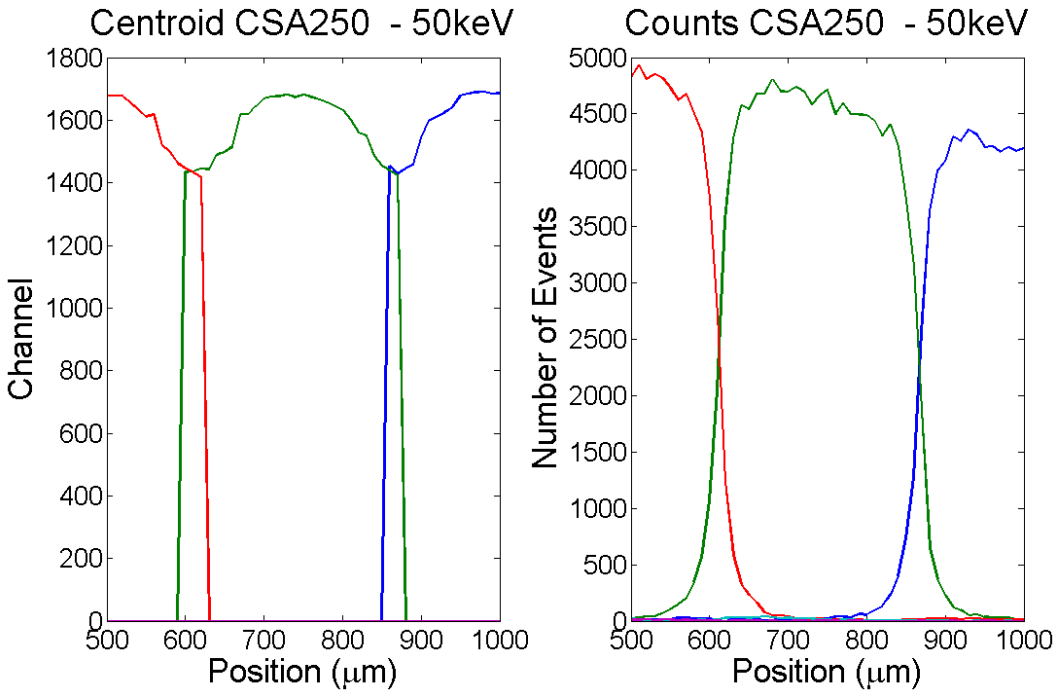

Figure 7-46. CSA results for 1D scan at 50 keV: centroid (left) and counts (right) values for each pixels

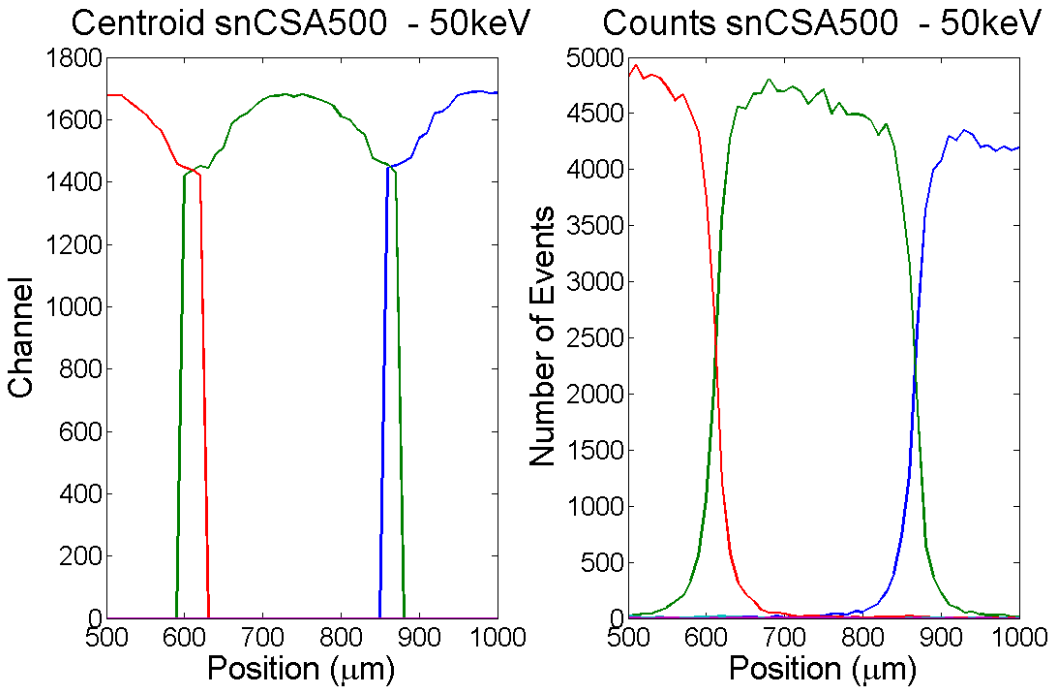

Figure 7-47. Results of snCSA for 1D scan at 50 keV using also second neighbors: centroid (left) and counts (right) values for each pixels

Same analysis is performed also with CSD. the results are similar to 25 keV case and also here second neighbors correction has negligible effect. For this reason only the classical CSD is reported Figure 7-48.

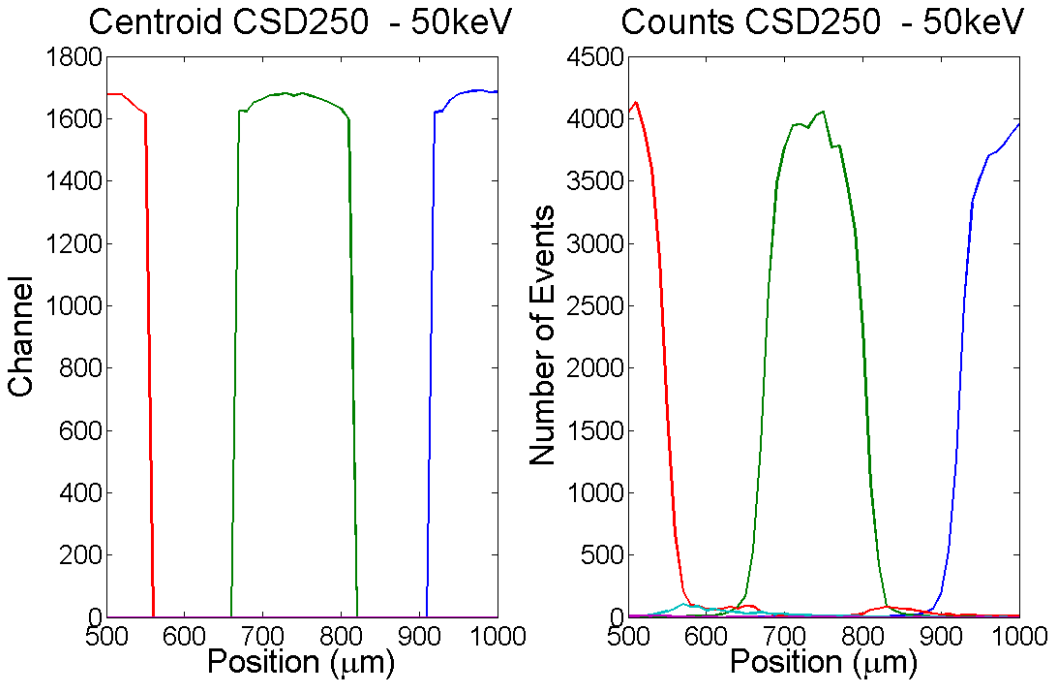

Figure 7-48. CSD results for 1D scan at 50 keV: centroid (left) and counts (right) values for each pixels

Figure 7-49 shows the counts during the 1D scan after CSA and CSD corrections, the dotted black lines represent the total counts obtained in each position. Theoretically this curve should be flat

because the photon flux does not change during the measure, then CSA reproduces more faithfully the real measure.

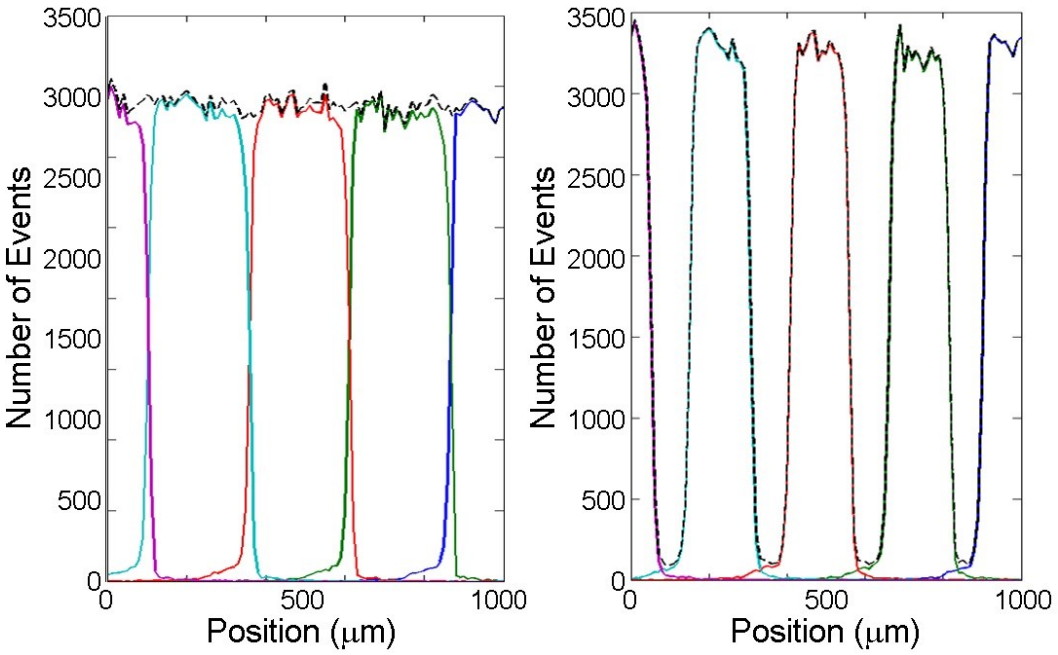

Figure 7-49. Number of counts as showed in previous images for 1D scan at 25 keV in case of CSA (left) and CSD (right) with in black the total counts obtained in each position

The sum of the spectra obtained during the 1D scan suggests the spectral response in case of full irradiated detector. Figure 7-50 shows this comparison for both employed energies. The best spectra seem to be the CSD ones: this correction produces a greater decrease in the total counts than the CSA, but improves the final spectra removing the low energy contribution due to the shared events.

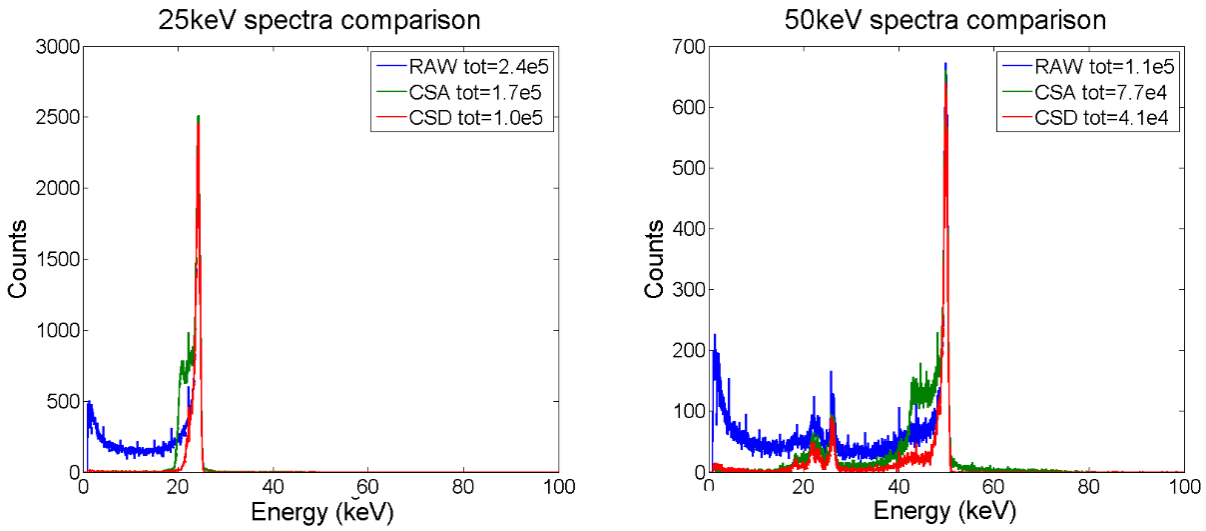

Figure 7-50. Comparison between RAW and corrected data of the sum of spectra obtained in 1D scan. The legends report the total counts for each curve

After 1D scans in beamline B16, we measured nuclear sources and applied CSD correction. We used two different nuclear sources: Americium 241 and Cobalt 57, whose respective brightest photopeaks are at 60 keV and 122 keV. Total spectra are reported in Figure 7-51, each single pixel

spectrum is calibrated in energy and after summed together. The figure reports these sums for both the sources.

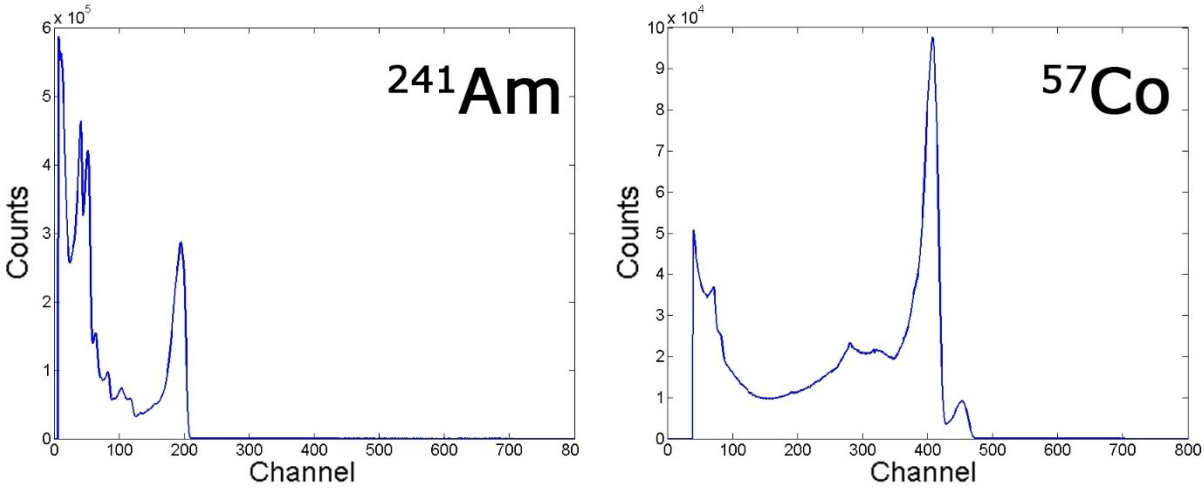

Figure 7-51. Acquisition with HEXITEC device, nuclear sources spectra corrected with CSD: total spectrum of americium 241 (left) and cobalt 57 (right)

Pixels with different resolution are added together and in the multitude of pixels some of them work better than others. The FWHM of global spectra for ^{241}Am and ^{57}Co are 12% and 6.5% respectively. However some pixels show a better resolution: in particular the best pixel of this detector has a really high resolution (FWHM ^{57}Co = 1.0% and ^{241}Am = 1.8%). These spectra are reported in Figure 7-52.

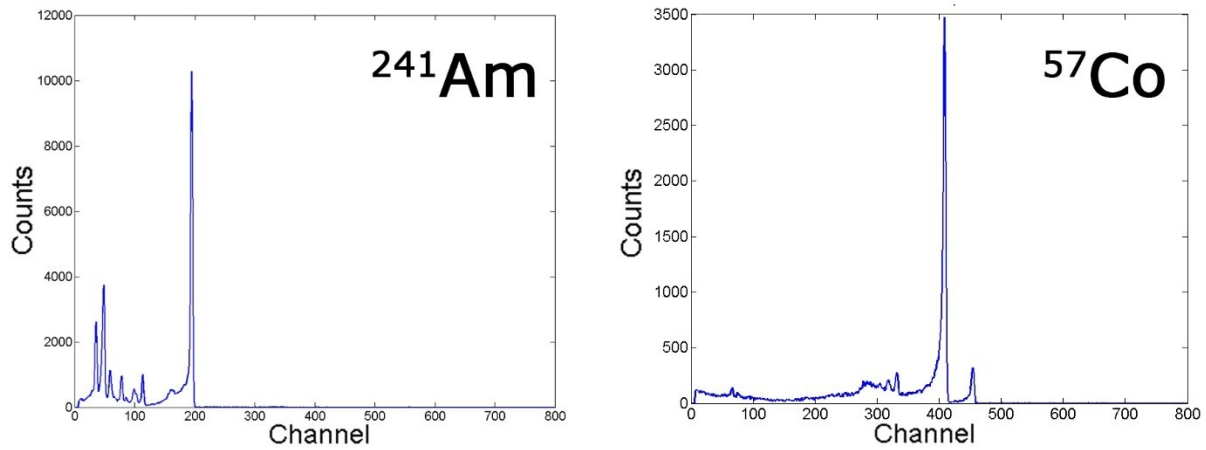

Figure 7-52. Acquisition with HEXITEC device, nuclear sources spectra corrected with CSD: best pixel spectrum of americium 241 (left) and cobalt 57 (right)

Using these data a novel analysis to achieve subpixel spatial resolution is proposed. Several scientists are studying different ways to obtain spatial resolution lower than the pixel [80] [86] [126] [127] [128]. In the following rows I propose the subpixel analysis achieved on HEXITEC device based on the collected charge ratio of shared events. To perform this correction it is necessary to separate in two dimensions the pixel array (we have only 1D scan so we cannot exploit the information of diagonal pixels). From previous data we can extract a "calibration" curve for subpixel correction: ratio between centroid was calculated for three adjacent pixels for

each beam position. Using equation 7-2 we can obtain the calibration curve $R(d)$ that is related to the distance of the interaction from the center of central pixel.

$$R(d) = -\frac{E_L(d)}{E_C(d)} + \frac{E_R(d)}{E_C(d)} \qquad 7\text{-}2$$

where d is the distance from the center of central pixel and $E_L(d)$, $E_C(d)$, $E_R(d)$ are respectively the value of the centroid in position d for left, central and right pixel. Using the inverse function of $R(d)$ and calculating R by using the value of shared charge from the real measurement it is possible to estimate the real position of interaction.

80x80 frames are taken one by one and, for each frame, elements of 80x80 matrix are sorted in descending order. Each event is considered on the central pixel of the triplet in equation 7-2 and R is evaluated for both X and Y axis: R is directly correlated with the interaction position, so that the position of each event with subpixel resolution can be calculated using the aforementioned method. During the analysis we eliminate from the sorted array the pixel already considered in previous shared events.

Calibration curve is calculated for both 1D scan: 25 keV and 50 keV and reported in Figure 7-53.

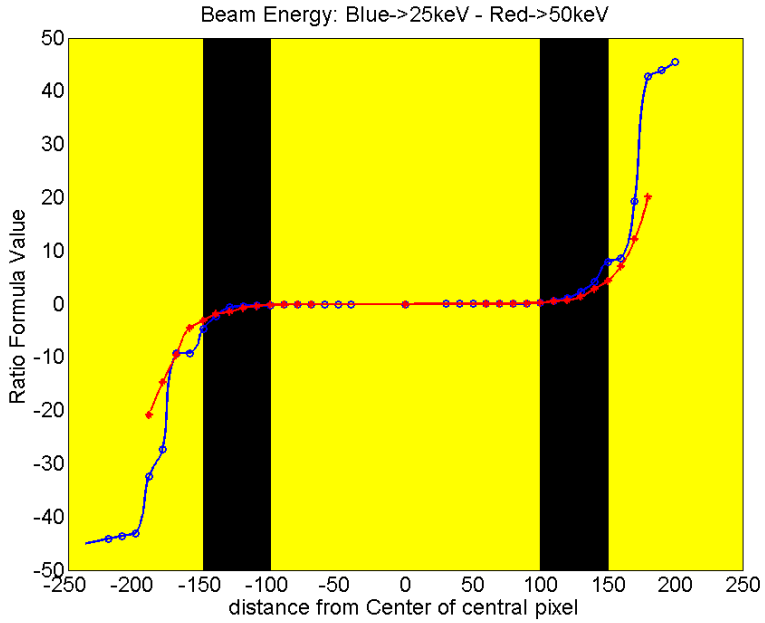

Figure 7-53. Calibration curve R(d) for subpixel correction for 25 keV (blue) and 50 keV(red). Gold regions correspond to the pixel and black regions to gap interpixel (50 μm)

The method was first tested using micro beam data in order to verify its accuracy. The calibration of the method was performed choosing a pixel triplet of the previously reported 25 keV scan. Then data from other triplets of the same scan were used to compare the subpixel positions calculated by the software, and the real beam positions (see Figure 7-54). The method was applied on 10^4 events for each position, and the mean values (and the respective error bar, standard deviation) are plotted in Figure 7-54. Taking into account a pair of neighboring pixels, the following can be stated: I) the method is unable to provide the subpixel position within 70 μm starting from the center of pixels (charge sharing is too weak in these regions); II) the method provides subpixel positioning with a resolution of 30 μm in the remaining region across pixels (i.e. 110 μm between pixels).

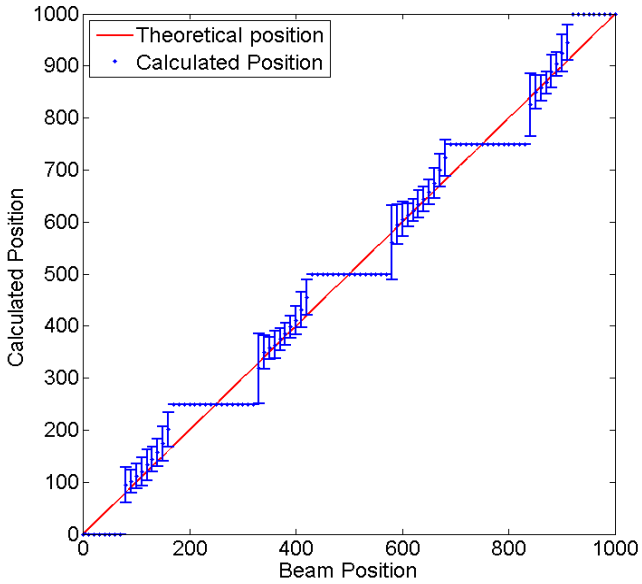

Figure 7-54. Comparison between the real beam position (red) and the calculated subpixel position (blue with error-bar) on 25 keV scan

Lastly the method was applied to the data acquired using a nuclear source. In the following image (Figure 7-55) 2D frames are shown achieved using americium source. The maps show collected charge in grayscale, the red dots are the evaluation of subpixel positioning by using the system described above with 50 keV calibration curve.

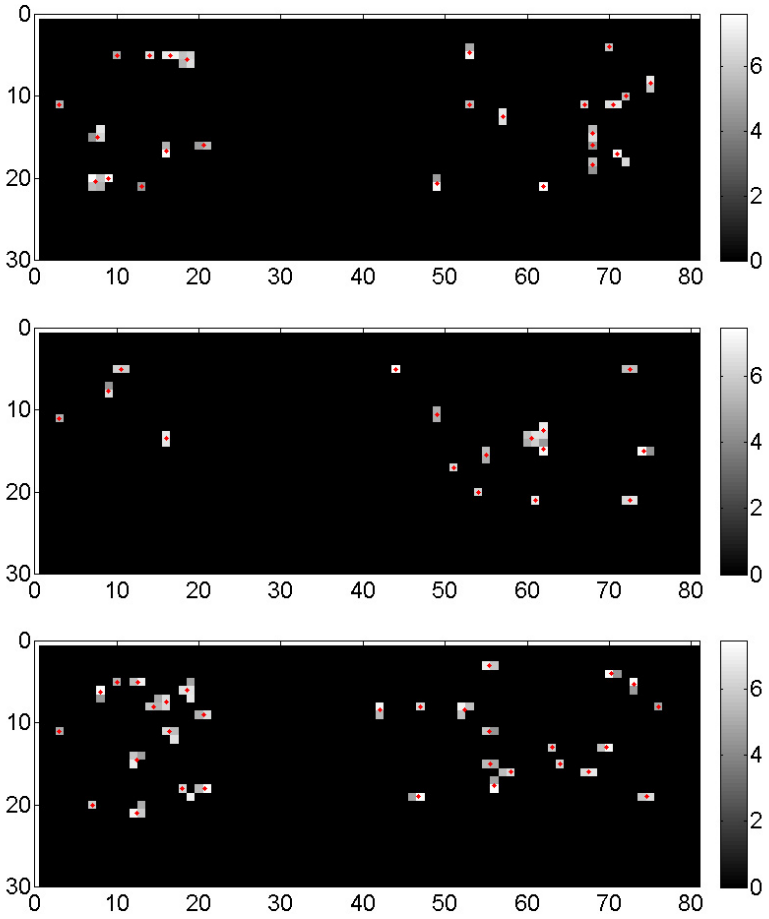

Figure 7-55. Intensity map of a single frame (in logarithmic scale), the red dots are the calculated positions of events

7.4.6 Conclusions and new proposal

The experiments carried out at Diamond Synchrotron were extremely useful and many aspects could be studied and discussed. Briefly, concerning analysis of PIXIE data, the preliminary conclusions are:

- Measurements were made at high rates approaching 1Mcps. The use of digital pulse processing allowed the contribution of charge sharing and pulse pile-up to be minimized allowing high-resolution spectroscopy to be recorded at these fluxes.
- No shifts in the photo-peak positions or degradation of the spectroscopic performance of detectors were observed at these fluxes due to polarization.
- Device product with standard REDLEN materials shows significant electric field non-uniformities on the scale of 100 μm and, in the smallest array studied, a big defects in the central pixel.
- The 2 millimeters thick detector produced by REDLEN with high-flux grade CZT material is more uniform than the other device, and does not present significant defects or distortion even in the smallest array.

Concerning analysis of HEXITEC data, the preliminary conclusions are:

- With CSD the spectral resolution considerably improves and the clutter events generated by charge sharing are removed. Total number of counts is reduced because shared events are not included.
- With CSA spectral resolution improves (not as much as using CSD) and also in this case clutter events are removed and total counts are homogenous also in interpixel regions.
- A method for subpixel resolution based on shared charge ratio is reported and further measurements are necessary (firstly a 2D scan) to optimize this method.

In the next stage of this study we plan on instrumenting the PIXIE detector cathode (see Figure 7-56) to readout the signal created by hole drift in the detector. This information will allow corrections to be applied to spectroscopy at higher energies. Many applications, including science at synchrotrons, require these detectors to work at photon energies > 100 keV. At these energies the depth of interaction (DoI) of the photon in the detector can be significant (> 1 mm) and, due to the poor hole transport properties in CdZnTe, can lead to charge losses that damage performance. By instrumenting both cathode and anode of the detector, it is possible to correct for DoI recovering spectroscopic performance. In this experiment the spatial performance of a novel pixel-strip detector (Figure 7-56-left) will be characterized and it's suitability for synchrotron instrumentation investigated.

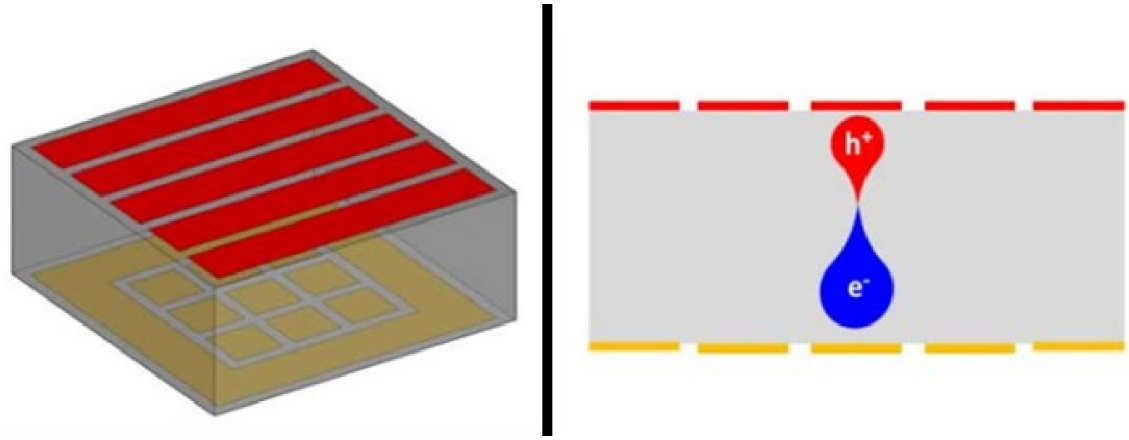

Figure 7-56. Proposed detector with stripped cathode (left) schematic carriers cloud drift (right)

At higher energies the spectroscopic performance of detectors is dependent on the depth of interaction (DoI), i.e. the depth in the detector at which the photon energy is converted into charge carriers. At energies >100 keV photons are able to deposit their energy at depths of >1 mm meaning that the holes can contribute significantly to the detector signal. By measuring and comparing the signals induced in both the cathode and anode of the detector is possible to determine the DoI of the photon which, in turn, provides 3D position information on the position of interaction as well as the ability to correct for any charge loss.

Characterizing the DoI effect in these materials is difficult and requires high quality data with good statistics. The requirement for good statistics makes using a sealed source in the laboratory unsuitable. The relatively high flux of the beamline and the ability to produce X-rays with energies in the range 20–50 keV means it is ideally suited for these measurements. These measurements will make use of the PIXIE-3D system which has recently been developed by STFC and the Cd(Zn)Te detectors have been fabricated by IMEM-CNR. Signals from these PIXIE detectors will be digitized at high speed (100 MHz) using CAEN digitizers provided by the University of Palermo.

The results from this experiment will demonstrate the viability of using a segmented cathode for DoI corrections that provide spatial information and charge-loss corrections when measuring higher energy X-rays in CZT-based detectors. These measurements will represent the first characterization of a CZT pixel-strip hybrid and the understanding gained from this experiment will inform the development of future high energy X-ray and γ-ray detector. These detectors have applications for synchrotron science but also in other application areas like medical and security imaging where higher photon energies allow functional imaging to be made.

7.5 XDrone

XDrone is a project carried out at the SIGNAL group at IMEM CNR and funded by the flagship project "La Fabbrica del Futuro". During my PhD, I was part of the XDrone team. In particular, I directly realized and characterized the CZT detector integrated on the UAV, and cooperated to the realization of the electronic read out. Also, I acquired the patent to operate the UAV according to the ENAC regulations, so that finally I directly took part in the characterization of the final performances of the system (UAV equipped with the CZT detector) in a relevant environment (a service area of a local factory, in the presence of an intense Iridium nuclear source) and in a operation environment (a landfill in Novellara – RE).

7.5.1 Motivation

In the case of a nuclear accident or a terrorist attack involving nuclear material the examination of the contaminated area by hand may not be possible due to the presence of the hazardous material itself. Also, the presence of nuclear or radiological material was sometimes reported in waste disposals, in highly contaminated dismissed industrial area, or in wood or iron stocking plants. In all these cases, the use of a remotely-controlled vehicle for the detection and identification of nuclear or radiological material would be highly recommended in order to preserve the safety of the human operators, as well as to reduce the risk of contamination of the scene.

In last years, the employment of Unmanned Aerial Vehicles (UAV) has been proposed for many civil applications such as aerial photography, search and rescue of people, plants or pipeline inspection, surveillance, agriculture. The UAV market has thus increased in the last years, so that their cost has been constantly reducing. In particular micro-UAVs show a limited cost, together with the possibility to carry a payload that is sufficient for moving sensors and detectors.

Moreover, micro-UAVs are typically multicopters, so that they are able to fly at low altitude, and also to loiter on a target, characteristics highly required in view of detection/identification applications.

In the case of operations in a scene that possibly involves nuclear and radiological (NR) material, the reduction of the time required for the examination of the interested area is always an important issue. Moreover, one of the problems connected with the use of micro-UAV is the limited time of flight allowed by the existing batteries, that is hardly larger then 30 minutes. Before the end of the battery energy, with the present technology the UAV must fly back to a safe zone, where human operators change the batteries.

In collaboration with RimLab (engineering group of Parma University), a novel teleoperation system is proposed to minimize the time required by the UAV to detect the NR material. The system is based on the use of a haptic device providing force feedback to the human operator. Teleoperation of aerial vehicles is complex due to the lack of situation awareness of the operator. Indeed, when only direct visual feedback is available to the operator it is crucial to provide additional information sources, exploiting signals from onboard sensors. In the following, it is shown that force feedback can be used as an additional sensory channel to guide the exploration of the environment. In particular, a haptic rendering algorithm was developed providing an attractive basin around the most intense detected radiation source. In fact, several works investigated the use of UAVs for radiation detection [129] [130] [131] [132] [133]. However, none of the previous works have explored the use of haptic teleoperation for radiation detection. Such potential field approach will help the human operator to keep the UAV close to the radiation source once a target is found.

On the other hand, gamma detectors to be integrated on UAVs must operate at room temperature due to the limited payload of micro-UAVs, and the limited energy availability, must be robust and

have good energy resolution, whenever identification in addition to localization of the nuclear source is required. For these reasons, a CdZnTe detector is the best choice for integration with the UAV. UAV and detector are both well described in their sections.

Several experiments were made to check the prototype: the two main tests are reported in the following sections. Experiments consist firstly of checking the capabilities to individuate and to identify a known nuclear source hidden from the operator eyes and then of flying in a harsh environment how they could be the conditions of future uses.

7.5.2 The prototype

In the Figure 7-57 the overall architecture of the proposed system is shown, software part is based ROS framework. In detection tasks of nuclear sources, the UAV flies at a constant altitude and constant speed. A low velocity set point value is adopted since a high speed would affect geo-referencing of the sensor data. The operator of the haptic device is in charge of guiding the UAV during the hazard search and localization phase by sending motion commands on plane parallel to ground while receiving visuo-haptic feedback. Visual feedback is displayed on a computer screen while a 2D planar force feedback is conveyed through the haptic device connected to a ground station. A second human operator (supervisor), using a standard remote controller, is responsible for take off, landing, setting the altitude set point and he can override, at any time, haptic commands, thereby taking full control of the UAV, as required by the Italian regulation for Unmanned Air Vehicles. Both operators have direct sight of the UAV. The main functions of the ground station are the following: processing motion commands provided by the operator of the haptic device and sending them to the UAV, receiving sensor data from the UAV, computing and rendering both visual and force feedback. Information received by the ground station includes UAV telemetry data (position, speed, height, battery charge, etc...), sent through the UAV radio link, and sensor data from the onboard γ-ray detector (number of photon counts for each energy band in a fixed time frame), sent through a dedicated wireless link.

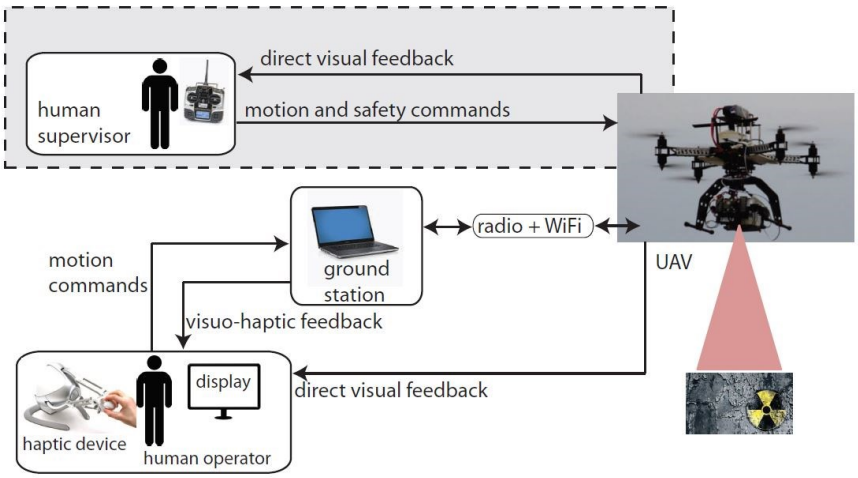

Figure 7-57. Overall architecture of prototype

Assuming a planar environment, the detector will measure a maximum intensity when it is on the vertical of the radiating target. The GPS coordinates of the UAV will be assumed as the coordinates of the radiating part at the ground. The haptic device used in this work is the Novint Falcon. The device has 3 degree of freedom, a position resolution of 63.5 μm and a maximum force feedback capability of about 10 N. The range of motion is about 10 cm^3.

7.5.3 UAV

The UAV adopted in this work (Figure 7-58), is an octocopter in coaxial configuration produced by Virtual Robotix Italia. The payload is up to 4 Kg. Flight time is about 15 minutes. The UAV communicates in real-time to the ground station both telemetry data and sensor data measured by the onboard gamma ray detector. The UAV is built on a light frame whose size is within 550 mm (without propellers). The UAV is equipped with MEMS accelerometer, gyro, magnetometer and GPS sensors. An autopilot system is used, called VRBrain, which supports multiple flying modes like loiter, return to home and guided mode. An integrated high speed data flash is used for logging data. The gamma-ray detector is enclosed in a box and mounted on a two-axes brushless gimbal unit with anti-vibration system. The gimbal unit is controlled by a micro-controller with stabilization software, its size is about 20x15x16 cm^3. An embedded system (Intel Galileo) reads sensor data from the γ-ray detector and sends the data stream to the ground station through a 5 GHz WiFi connection. This solution avoids bandwidth issues on the UAV command channel and it does not affect the UAV autopilot system which runs on a real-time operating system. Two external antennas are connected to the embedded platform allowing a WiFi communication range up to 170 meters.

Figure 7-58. Octocopter with CZT detector

7.5.4 The CZT detector

The purpose of the gamma-ray detector is the individuation and identification of nuclear sources in a wide energy range to reveal most nuclear contaminants that may be dispersed in the environment. The detector must be light and low power consumption. In the first prototype we had used a 20x20x6 mm^3 pixel detector from Redlen. Original contacts were removed and substituted with a planar cathode and a coplanar grid at the anode side, using the technology developed in our lab to realize high quality CZT-based devices. Electroless gold contacts were used to ensure limited leakage current.

Table 7.3 reports the expected number of counts per second revealed by our detector at 2 meters distance from such nuclear sources at different energies. Reported values show that at about 2 meters from the nuclear sources the UAV equipped with the CZT-based detector measures a

number of counts per second that is enough for localizing nuclear sources. The equivalent radiation dose at that distance is the legal threshold for a standard worker.

Nuclear source	Dose	Source activity (Bq)	Expected cps at 2 m
Americium 241	1 mSv/years	$1.2\ 10^8$	955
Cobalt 57	1 mSv/years	$3.5\ 10^7$	270
Cesium 137	1 mSv/years	$6.0\ 10^6$	11

Table 7.3

In the new prototype the detector is changed with four 20x4.5x6 mm^3 stripe detectors cut from a Redlen crystal. We have removed original contacts and deposited a planar cathode and stripes at the anode side for each device (Figure 7-59), by using the technology developed in the last years to realize high quality CZT-based devices. The stripped geometry ensures better spectroscopy with high energy radiations. By using four parallel and identical detectors, each one with dedicated front-end electronics, we can realize additional operations to localize quickly the source. The efficiency is improved of 50% with the new device, resolution is definitely better (less than 3% with ^{137}Cs) and the new electronics designed by Due2Lab allows four analog channel and microcontroller in the same weight of the old box.

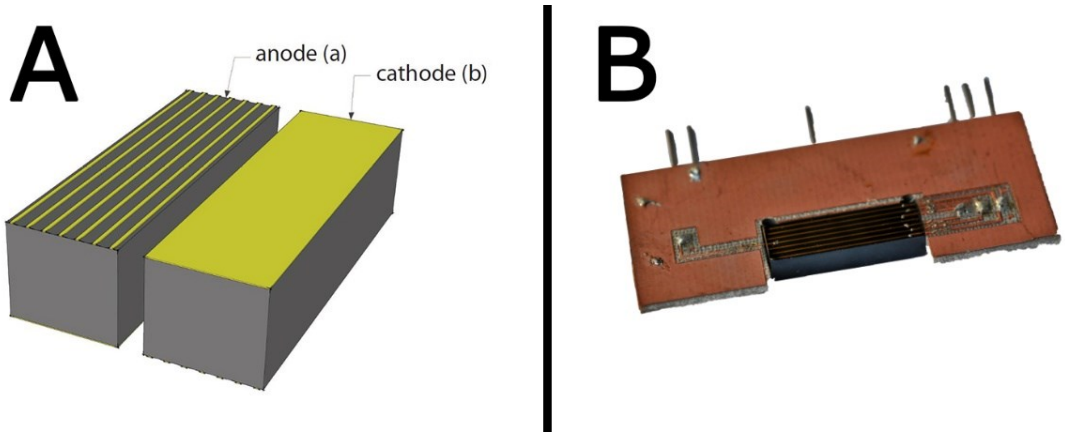

Figure 7-59. Stripes detector: 3D model (A) and real device (B)

As one of the most interesting application of the proposed system is the detection of nuclear sources that can damage operators and workers in industrial or material stocking plants, the new detector is able to measure nuclear sources whose average effective dose is 1 mSv/year at 1 meter distance.

Analog electronics is packaged as illustrated in Figure 7-60. The measurable energy range was from 10 KeV to 1.6 MeV, in order to include the emission gamma lines from the most of the unstable isotopes.

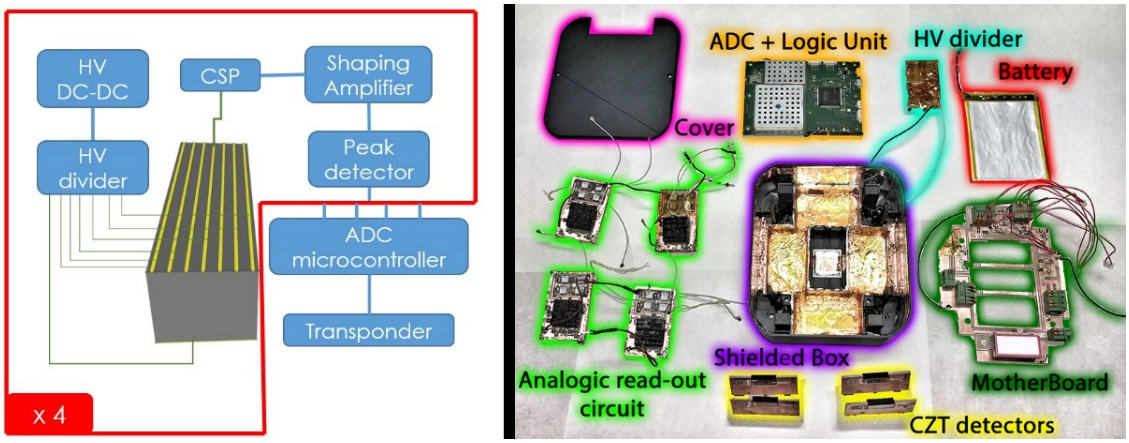

Figure 7-60. Readout electronics: schematic of the system (left) and real electronics where different compounds are highlighted (right)

The system integrate for 2 seconds the incoming events, each pair counts and respective energy band is transmitted to the ground station through the WiFi link. The time required to send a single spectrum to the ground is 200 milliseconds, then the final refresh time is about 2.2 seconds. The gamma-ray detector is enclosed in a shielded box (shown in the middle of Figure 7-60-right) and mounted on a two-axes brushless gimbal unit with anti-vibration system.

Radioactivity data measured by the detector is represented as a histogram of 4096 energy bands. Figure 7-61 reports the comparison between the ^{137}Cs and ^{57}Co emission lines measured by old and new detector box.

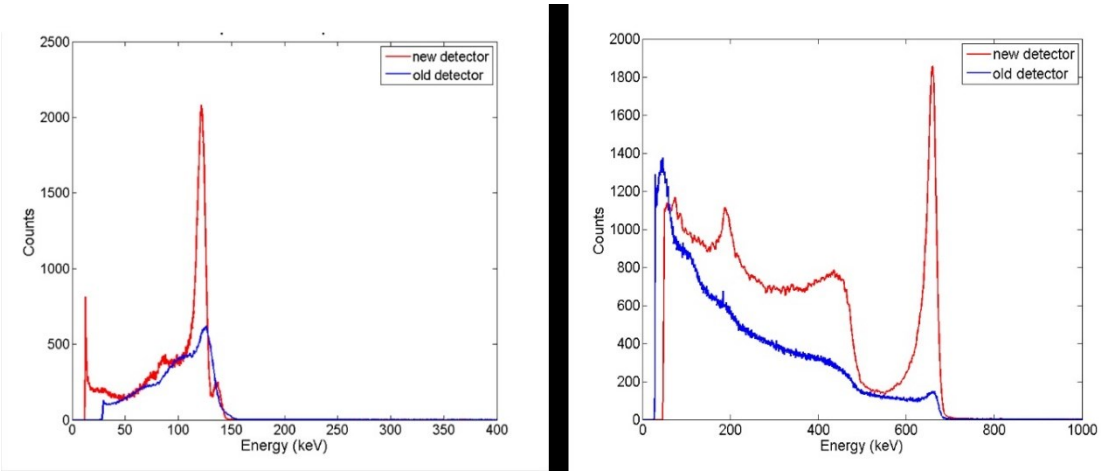

Figure 7-61. Comparison between the old detector (blue) and the new one (red) for both Cobalt 57 (left) and Cesium 137 (right)

7.5.5 Haptic interface

Two control modes (Figure 7-62) have been developed where the operator sends motion commands (via the haptic device tool) and receives force feedback limited to the horizontal plane. In both teleoperation modes there is no direct conversion from the haptic device to the velocity of the UAV (speed is set constant). Moreover, the two teleoperation modes have been designed to map the limited workspace of the haptic device to an arbitrarily large UAV workspace.

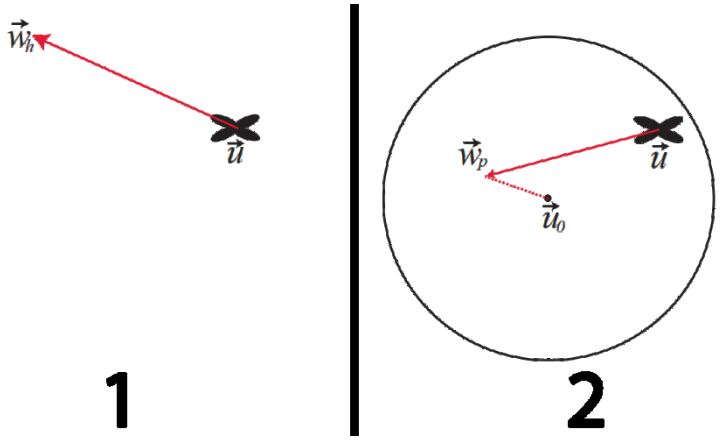

Figure 7-62. Representation of two teleoperation mode: 1) heading mode that allow to drive UAV along a direction; 2) position mode that allow to drive UAV toward a position

In the first teleoperation mode (*heading mode*) position information read by the haptic interface is used to compute the horizontal heading direction of the UAV. In particular, the current displacement of the tool point of the haptic device with respect to its center is converted to a waypoint for the UAV in world coordinates. The UAV flies in guided mode following the current waypoint with head pointing towards the waypoint itself. Each waypoint is not meant to be reached by the UAV as it is continuously updated and placed at a long distance from the current UAV position, thus resulting in a heading-based approach.

The second teleoperation mode is a hybrid approach that allows the operator to switch between the heading-based technique (heading mode), discussed above, and a position to position control technique (*position mode*). Mode switching is achieved by pressing one of the buttons of the haptic device. The position to position control technique, enables a direct mapping between the haptic device to the UAV position around a fixed center of operation. This approach was introduced with the new prototype and allows to drive UAV toward a selected point choose with the joystick.

A force feedback is provided to the operator, acting as a basin of attraction, to let the UAV fly close to the region where the radiation is maximal. Indeed, as the remotely operated UAV travels away from the location of the most intense perceived radiation the haptic device exerts a force in the horizontal direction towards the center of the haptic workspace. If the latest measured radiation intensity is greater than the maximum radiation found so far, the latest radiation intensity is set as the current maximum radiation. The force feedback has a quadratic profile. The user can reset force feedback to zero by pressing a button on the tool point of the haptic device. This feature can be useful when multiple concentrated nuclear sources have to be explored.

The idea is that the heading-based control technique can be used for long transition motions, e.g. when the UAV has to be moved to explore different regions of the environment, while the position mode is helpful when the UAV explores an area in close proximity of a nuclear source.

This approach has been introduced with the new prototype and allows to find quickly and more precisely the nuclear source.

7.5.6 Validation test

Several flights were also performed to test the operation of the haptic interface simulating the presence of nuclear sources.

Finally a experiment was organized using a ^{192}Ir source, normally employed for industrial nondestructive test. The nuclear source was located in a large service area and shielded with a 3 centimeters thick iron container for limiting the dose absorbed by operators. The source was hidden from the operator to simulate a real operational status. The UAV was moved several times in the area flying over the nuclear source in order to test the efficacy of the haptic interface.

During the experiment, the energy spectrum of the nuclear source was also collected and it is shown in Figure 7-63. Even if the ^{192}Ir source was shielded with iron, the spectrum shows the main characteristic emissions of iridium at 470 keV, 600 keV, and 880 keV. The intrinsic spectroscopic capability of the detector enables also the identification of the nuclear source.

Archived footage from described experiment are available via the link:
http://www.bo.cnr.it/imem-old/xdrone/videos.php

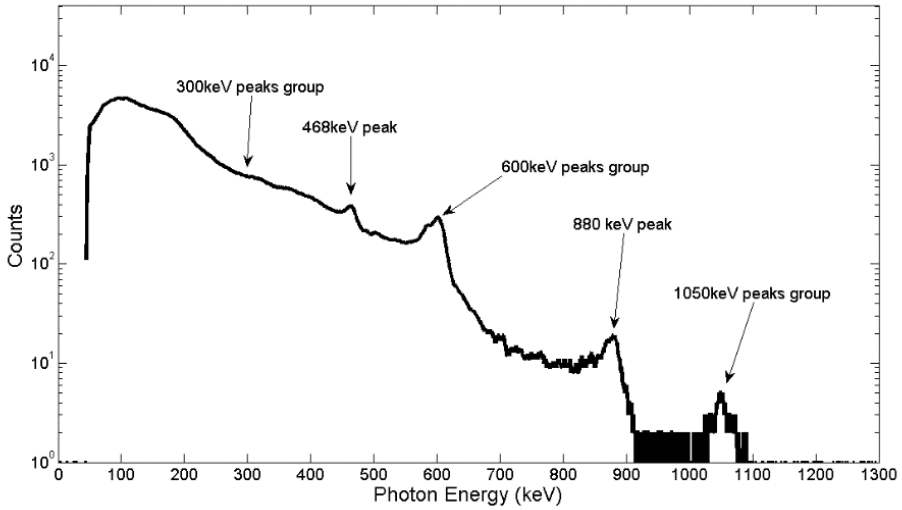

Figure 7-63. ^{192}Ir spectrum measured during the test

A following test has been made in a typical environment where drone could fly to find nuclear sources. Thanks to the ARPA Emilia Romagna (Regional Agency for Environmental Protection in the Emilia-Romagna) we obtained the authorization to fly on a real landfill (S.a.ba.r of Novellara, Italy). The UAV has demonstrated that it is able to move near the ground (less than 2 meters) also on rough terrains and several time faster that a human operator with a Geiger counter.

Archived footage from described experiment are available via the link:
http://www.bo.cnr.it/imem-old/xdrone/videos.php

7.5.7 Conclusions

A UAV was equipped with a CdZnTe-based X-ray detector. A novel haptic teleoperation scheme has been presented which generates an attractive basin around the location of the most intense detected radiation enabling exploration of potentially dangerous areas. A preliminary experiment has been performed where the UAV measured a ^{192}Ir radiation source in a service area. The haptic interface worked properly and the operator (that does not now the siting of source) experienced an attractive force towards the direction of maximum count rate. This operation mode is very effective to minimize the time required to localize a nuclear source on an open area. Moreover, the intrinsic spectroscopy capability of the detector enabled also the identification of the nuclear source. A second experiment has been made in a landfill in a likely operational environment. The UAV has acted well, any flight problem was found. The detector do not measure nothing higher

that the background radiation, how was predictable in a controlled dump. Measured radiation, however, appears weak than the background one, this because the thick layer of garbage played as shield.

New CZT device with stripped anodes based on new gold electroless deposition shows high-energy resolution even at high energies. Field effect geometry strongly improves efficiency and energy resolution (in particular at high energy) if compared with standard pixel detectors. Field effect geometries are strongly recommended in application where efficiency and high-energy resolutions are relevant but spatial resolution is not required.

This prototype was developed within project XDrone, Flagship Project "Factory of the Future" coordinated by the Italian National Research Council (CNR). I want to thank ARPA Emilia Romagna (Regional Agency for Environmental Protection in the Emilia-Romagna), and in particular Roberto Sogni, Emiltest srl, Filippo Panciroli and Giancarla Rossetti, for helping us in the organization of the field experiment with the ^{192}Ir nuclear source. I want also to thank the management of S.a.ba.r landfill in Novellara (RE, Italy) for the kindly willingness.

During the project, I have obtained the UAV license for non critical operations. Moreover, the drone is registered at the ENAC database and assured as wanted by the UAV Italian regulation. The UAV is now exploitable by third parts for real operation, through the website: www.imem.cnr.it/Xdrone.

8 General conclusions

CZT is an interesting semiconductor for x and γ ray detection at room temperature. This characteristic make it useful for several application where cumbersome cooling systems are strongly discouraged or impossible to implement (as in the case of XDrone project). Furthermore the high Z of CdZnTe allows its employment in high-energy spectroscopy (as in space application) with relatively low device thickness. Nevertheless, CZT detectors still present some issues: I) contact deposition typically produce low adherent films that affect the life-time of devices; II) spectroscopic performance of standard devices gets worse when the incoming radiation flux increase (about 10^7photon/cm^2/s); III) pixelated detectors typically show strong sharing effects that further increase with thick devices or high energy radiation.

In these years, we have spent several efforts to improve contacts on CZT-based detectors. Keeping this in mind, different metals were deposited on semiconductor surfaces with different electrode geometries. We have achieved some results that can be summarized according to the following points:

- **Electroless deposition of different metals**. Electroless deposition of gold, platinum and nickel were developed and optimized for CZT. Resulting film are homogenous and show high adhesion. Detectors realized by using these new deposition techniques were analyzed and compared with standard gold contacts deposited in aqueous solution. Interesting results were achieved: in particular nickel turns out to be promising for the realization of ohmic contacts (useful for high radiation flux application) while platinum provides blocking contacts with Schottky barrier higher than gold. Further investigation are necessary to fully understand the behavior of these new contacts for future exploitation.
- **Detector optimized for high radiation flux**. New detectors were realized thanks to the gold electroless deposition based on alcoholic solution. They present very low leakage current even at high voltages, offering the chance to strongly increase the bias voltage for applications where high radiation flux is present. Detailed investigation was performed under high radiation flux (up to 1 Mcps) and good results were obtained from these detectors.
- **Investigation of electric field in different devices and achievement of transport parameters for both carrier types**. Thanks to the LI-TCT combined with a newly developed self-consistent method, it is possible to estimate transport parameters for electrons and holes and to reconstruct electric field profiles of detectors at different bias voltages. Because the method takes into account the role of the weighting field, it is applicable on detectors with any contact geometry, and so also on final devices. The technique separately provides the values of mobility and lifetime and any assumption on the internal electric field is required. LI-TCT is useful to investigate new grown CZT ingots and prototypal devices equipped with novel metal electrodes and/or contact geometries.
- **Investigation of charge sharing effect in pixelated detector**. Pixelated detectors were tested by means of bright light produced by Diamond synchrotron and charge sharing effects on pixels with 500 μm and 250 μm pitch were studied. Effects of charge sharing on both pixel arrays are significant and the digital correction is indispensable even at low flux to obtain high energy-resolution. The use of digital pulse processing also allows to minimize the contributions of charge sharing and pulse pile-up allowing high-resolution spectroscopy at fluxes approaching 1Mcps. Subpixel positioning is appealing to increase the spatial

resolution of the detector and, at the same time, decrease the number of pixels (and then the number of electronic channels). A possible approach of subpixel positioning is suggested and good results were achieved on measurements performed by means of HEXITEC device and nuclear sources.

- **Realization of prototypal UAV equipped with CZT detector for the individuation of nuclear source**. CZT detectors are very interesting also in applications where light (they do not demanded heavy cooling system), compact and low-cost devices are required. Analog readout electronics and special electrode geometries can be employed if spatial resolution is not required and radiation flux does not exceed dozens kcps. Hemispheric-like or strip detectors allow the best trade-off among collection efficiency and spectroscopic resolution even with high-energy radiations. In addition these electrode configurations allow the realization of large volume devices that need electronics with few readout channels. In last years, the employment of Unmanned Aerial Vehicles (UAV) has been proposed for many civil applications. In this landscape, to equip a UAV with a γ-ray detector can be interesting. Light and compact device is required because of limited payload and available space. We equipped UAV with CZT strip detectors reading out them thanks to a 4-channel analog electronics. This device fits well the application demands: it is light and compact, allows to efficiently detect high-energy radiation, works at room-temperature and has low power consumption. The prototype was tested in several experiments acting well also in harsh environments. By combining last technologies of UAV and CZT devices a system lighter than 300 grams could be realized. This is interesting because this weight is the actual limit of law to fly without any license and authorization.

Together with the findings detailed in this thesis, some issues that deserve a better deepening are still present:

- The newly developed electroless platinum contacts are interesting, because show good mechanical adhesion and their barrier height seems to be larger than gold. It would be interesting to prepare high resolution devices.
- Nickel contacts, acting as ohmic electrodes, are interesting for applications where the incoming flux is larger than hundreds of Mcps (medical, industrial and security imaging and tomography). The following step is to realize a CZT detector equipped with nickel contacts and to test it under these extremely high x-ray fluxes.
- LI-TCT was employed to test pixel detectors. As said before, this technique is able to investigate any type of detectors. Also, it allows to know the effective electric field for detector with field effect geometries as hemispheric-like or with stripes. Furthermore, it could be interesting to investigate the electric field of devices under polarization and distortion effects generated by high-flux radiation.
- Charge sharing effects were studied thanks to the synchrotron x-ray beam for low energy radiation. Many applications, including science at synchrotrons, require radiation detectors to work at photon energies greater than 100 keV. At these energies the depth of interaction (DoI) of photons in the detector becomes significant and, due to the poor hole transport properties in CdZnTe, can damage performance. By reading out signal from both the cathode and anodes of the detector, it is possible to correct for DoI recovering spectroscopic performance. The new 3D system is composed of a CZT detector with pixelated anode connected with an old PIXIE ASIC, and stripped cathode connected with a second PIXIE ASIC for the readout of hole signals. This new detector will be tested at Diamond in the next months.
- Subpixel positioning approach was proposed. The HEXITEC system was investigated at Diamond and a calibration curve from shared events allowed us to obtain sub-pixel spatial resolution in one dimension. The correction was tested with good results on measurements acquired with HEXITEC by using nuclear sources. 2D scans at different energies would allow a better characterization of the calibration curve.

Publications

Part of results obtained in during my PhD have been published in different papers and conference proceedings as shown in the following list.

Published papers:

I Gentile Francesco; Ferrara Lorenzo; Villani Marco; Bettelli Manuele; Iannotta Salvatore; Zappettini Andrea; Cesarelli Mario; Di Fabrizio Enzo & Coppedè Nicola
Geometrical patterning of super-hydrophobic biosensing transistors enables space and time resolved analysis of biological mixtures
Scientific reports, Nature Publishing Group, 2016, 6

II Abbene Leonardo; Gerardi Gaetano; Turturici Accurso Antonio; Raso Giuseppe; Benassi Giacomo; Bettelli Manuele; Zambelli Nicola; Zappettini Andrea & Principato Fabio
X-ray response of CdZnTe detectors grown by the vertical Bridgman technique: Energy, temperature and high flux effects
Nuclear Instruments and Methods in Physics Research Section A: Accelerators, Spectrometers, Detectors and Associated Equipment, Elsevier, 2016, 835, 1-12

III Turturici Accurso Antonio; Abbene Leonardo; Gerardi Gaetano; Benassi Giacomo; Bettelli Manuele; Calestani Davide; Zambelli Nicola; Raso Giuseppe; Zappettini Andrea & Principato Fabio
Electrical properties of Au/CdZnTe/Au detectors grown by the boron oxide encapsulated Vertical Bridgman technique
Nuclear Instruments and Methods in Physics Research Section A: Accelerators, Spectrometers, Detectors and Associated Equipment, Elsevier, 2016, 830, 243-250

IV Aleotti Jacopo; Micconi Giorgio; Caselli Stefano; Benassi Giacomo; Zambelli Nicola; Bettelli Manuele & Zappettini Andrea
Detection of Nuclear Sources by UAV Teleoperation Using a Visuo-Haptic Augmented Reality Interface
Sensors, Multidisciplinary Digital Publishing Institute, 2017, 17, 2234

V Benassi Giacomo; Nasi Lucia; Bettelli Manuele; Zambelli Nicola; Calestani Davide & Zappettini Andrea
Strong mechanical adhesion of gold electroless contacts on CdZnTe deposited by alcoholic solutions
Journal of Instrumentation, IOP Publishing, 2017, 12, P02018

VI Pavesi Maura; Santi Andrea; Bettelli Manuele; Zappettini Andrea & Zanichelli Massimiliano
Electric field reconstruction and transport parameter evaluation in CZT X-ray detectors
IEEE Transactions on Nuclear Science, IEEE, 2017

VII Andrea Zappettini, Calogero Leandro Maida, Fabio Gentile, Manuele Bettelli, Marco Villani, Marta Marmiroli, Michela Janni, Nelson Marmiroli, Nicola Coppedé, Roberta Ruotolo and others
An in vivo biosensing, biomimetic electrochemical transistor with applications in plant science and precision farming
Scientific Reports, vol. 7, p. 16195, 2017

VIII Abbene Leonardo; Gerardi Gaetano; Raso Giuseppe; Principato Fabio; Zambelli Nicola; Benassi Giacomo; Bettelli Manuele & Zappettini Andrea
Development of new CdZnTe detectors for room-temperature high-flux radiation measurements
Journal of Synchrotron Radiation, International Union of Crystallography, 2017, 24, 429-438

IX Abbene Leonardo; Principato Fabio; Gerardi Gaetano; Bettelli Manuele; Seller Paul; Veale Matthew C; Zambelli Nicola; Benassi G and Zappettini Andrea
Digital fast pulse shape and height analysis on cadmium zinc telluride arrays for high-flux energy-resolved X-ray imaging
Journal of synchrotron radiation, International Union of Crystallography ,vol. 25, n°1, 2018

Conference proceedings:

I Aleotti Jacopo; Micconi Giorgio; Caselli Stefano; Benassi Giacomo; Zambelli Nicola; Calestani Davide; Zanichelli Massimiliano; Bettelli Manuele & Zappettini Andrea
Unmanned aerial vehicle equipped with spectroscopic CdZnTe detector for detection and identification of radiological and nuclear material
Nuclear Science Symposium and Medical Imaging Conference (NSS/MIC), 2015 IEEE, 2015, 1-5

II Bettelli Manuele; Benassi Giacomo; Nasi Lucia; Zambelli Nicola; Zappettini Andrea; Gombia Enos; Abbene Leonardo; Principato Fabio & Calestani Davide
Mechanically stable metal layers for ohmic and blocking contacts on CdZnTe detectors by electroless deposition
Nuclear Science Symposium and Medical Imaging Conference (NSS/MIC), 2015 IEEE, 2015, 1-3

III Santi Andrea; Piacentini Giovanni; Zanichelli Massimiliano; Bettelli Manuele; Zappettini Andrea & Pavesi Maura
Evaluation of electric field profile and transport parameters in solid-state CZT detectors
Nuclear Science Symposium and Medical Imaging Conference (NSS/MIC), 2015 IEEE, 2015, 1-3

IV Abbene Leonardo; Principato Fabio; Gerardi Gaetano; Benassi Giacomo; Zambelli Nicola Zappettini Andrea; Bettelli Manuele; Seller Paul and Veale Matthew C.
Digital CZT detector system for high flux energy-resolved X-ray imaging
Nuclear Science Symposium, Medical Imaging Conference and Room-Temperature Semiconductor Detector Workshop (NSS/MIC/RTSD), IEEE, 2016, 1-7

V	Abbene Leonardo; Zambelli Nicola; Gerardi Gaetano; Raso Giuseppe; Benassi Giacomo; Bettelli Manuele; Principato Fabio and Zappettini Andrea *High bias voltage CZT detectors for high-flux measurements* Nuclear Science Symposium, Medical Imaging Conference and Room-Temperature Semiconductor Detector Workshop (NSS/MIC/RTSD), IEEE, 2016, 1-6
VI -- not yet published	Abbene Leonardo; Principato Fabio; Gerardi Gaetano; Benassi Giacomo; Zambelli Nicola; Zappettini Andrea; Bettelli Manuele; Seller Paul; Thomas B. and Veale Matthew C. *Microscale X-ray mapping of CZT arrays: spatial dependence of amplitude, shape and multiplicity of detector pulses* Nuclear Science Symposium, Medical Imaging Conference and Room-Temperature Semiconductor Detector Workshop (NSS/MIC/RTSD), IEEE, 2017

Bibliography

[1] G. Vedrenne, J.-P. Roques, V. Schonfelder, P. Mandrou, G. G. Lichti, A. Von Kienlin, B. Cordier, S. Schanne, J. Knodlseder, G. Skinner and others, "SPI: The spectrometer aboard INTEGRAL," *Astronomy \& Astrophysics,* vol. 411, pp. L63--L70, 2003.

[2] S. Del Sordo, L. Abbene, E. Caroli, A. M. Mancini, A. Zappettini and P. Ubertini, "Progress in the development of CdTe and CdZnTe semiconductor radiation detectors for astrophysical and medical applications," *Sensors,* vol. 9, pp. 3491-3526, 2009.

[3] P. Ubertini, F. Lebrun, G. Di Cocco, A. Bazzano, A. J. Bird, K. Broenstad, A. Goldwurm, G. La Rosa, C. Labanti, P. Laurent and others, "IBIS: The Imager on-board INTEGRAL," *Astronomy \& Astrophysics,* vol. 411, pp. L131--L139, 2003.

[4] P. J. Heerden, *The crystal counter [Ph. D. thesis],* Utrecht University, 1945.

[5] S. Babar, "Characterisation of Surface Treated CdZnTe and Thin Film CdTe based Devices," 2016.

[6] J. E. Parks, "The Compton Effect--Compton Scattering and Gamma Ray Spectroscopy," *Department of Physics, University of Tennessee, Knoxville, TN,* 2009.

[7] G. Benassi, "Development of semiconductor compound materials & devices for radiation detection applications," 2014.

[8] Q. Zheng, Preparation and development of CdTe and CdZnTe detectors for gamma ray radiation applications, 2012.

[9] G. F. Knoll, Radiation detection and measurement, John Wiley & Sons, 2010.

[10] J. W. Palmour, J. A. Edmond, H. S. Kong and C. H. Carter, "6H-silicon carbide devices and applications," *Physica B: Condensed Matter,* vol. 185, pp. 461-465, 1993.

[11] A. Raulo, "Miglioramenti spettroscopici in rivelatori a semiconduttore composto per Raggi X e Gamma," 2007.

[12] O. S. Babalola, Dissertation Submitted to the Faculty of the Graduate School of Vanderbilt University In partial fulfillment of the requirements, 2009.

[13] H. Chen, S. A. Awadalla, F. Harris, P. H. Lu, G. Bindley, H. Lenos and B. Cardoso, "Reliability of pixellated CZT detector modules used for medical imaging and homeland security," *Proceedingd of SPIE,* vol. 7079, pp. 707905-1, 2008.

[14] K. C. Mandal, S. H. Kang, M. Choi, A. Kargar, M. J. Harrison, D. S. McGregor, A. E. Bolotnikov, G. A. Carini, G. C. Camarda and R. B. James, "Characterization of Low-Defect CdZnTe and CdTe Crystals for High-Performance Frisch Collar Detectors," *IEEE Transactions on Nuclear Science,* vol. 54, pp. 802-806, 2007.

[15] N. Kubo, S. Zhao, Y. Fujiki, A. Kinda, N. Motomura, C. Katoh, T. Shiga, H. Kawashima, Y. Kuge and N. Tamaki, "Evaluating performance of a pixel array semiconductor SPECT system for small animal imaging," *Annals of nuclear medicine,* vol. 19, p. 633, 2005.

[16] P. M. Shikhaliev, "Energy-resolved computed tomography: first experimental results," *Physics in medicine and biology,* vol. 53, p. 5595, 2008.

[17] J. Kluson, "Environmental monitoring and in situ gamma spectrometry," *Radiation Physics and Chemistry,* vol. 61, pp. 209-216, 2001.

[18] F. H. Ruddy, A. R. Dulloo, J. G. Seidel, F. W. Hantz and L. R. Grobmyer, "Nuclear reactor power monitoring using silicon carbide semiconductor radiation detectors," *Nuclear Technology,* vol. 140, pp. 198-208, 2002.

[19] I. Farella, G. Montagna, A. M. Mancini and A. Cola, *Study on instability phenomena in CdTe diode-like detectors,* 2008, pp. 154-161.

[20] H. Toyama, A. Higa, M. Yamazato, T. Maehama, R. Ohno and M. Toguchi, "Quantitative analysis of polarization phenomena in CdTe radiation detectors," *Japanese journal of applied physics,* vol. 45, p. 8842, 2006.

[21] D. Vartsky, M. Goldberg, Y. Eisen, Y. Shamai, R. Dukhan, P. Siffert, J. M. Koebel, R. Regal and J. Gerber, "Radiation induced polarization in CdTe detectors," *Nuclear Instruments and Methods in Physics Research Section A: Accelerators, Spectrometers, Detectors and Associated Equipment,* vol. 263, pp. 457-462, 1988.

[22] D. J. Williams, "B2. 1 Densities and lattice parameters of CdTe, CdZnTe and CdTeSe," *Properties of Narrow Gap Cadmium-based Compounds,* 1994.

[23] T. E. Schlesinger, J. E. Toney, H. Yoon, E. Y. Lee, B. A. Brunett, L. Franks and R. B. James, "Cadmium zinc telluride and its use as a nuclear radiation detector material," *Materials Science and Engineering: R: Reports,* vol. 32, pp. 103-189, 2001.

[24] N. Peyghambarian, S. W. Koch and A. Mysyrowicz, Introduction to semiconductor optics, Prentice-Hall, Inc., 1993.

[25] D. Kranzer, "Hall and drift mobility of polar p-type semiconductors. II. Application to ZnTe, CdTe, and ZnSe," *Journal of Physics C: Solid State Physics,* vol. 6, p. 2977, 1973.

[26] D. J. Olego, J. P. Faurie, S. Sivananthan and P. M. Raccah, "Optoelectronic properties of Cd1-x Zn x Te films grown by molecular beam epitaxy on GaAs substrates," *Applied physics letters,* vol. 47, pp. 1172-1174, 1985.

[27] K.-L. Giboni and E. Aprile, "Evaluation of CdTe detectors with Schottky contacts for imaging applications," *Nuclear Instruments and Methods in Physics Research Section A: Accelerators, Spectrometers, Detectors and Associated Equipment,* vol. 416, pp. 319-327, 1998.

[28] A. Zappettini, M. Zha, L. Marchini, D. Calestani, R. Mosca, E. Gombia, L. Zanotti, M. Zanichelli, M. Pavesi, N. Auricchio and others, "Boron oxide encapsulated vertical Bridgman grown CdZnTe crystals as X-ray detector material," *IEEE Transactions on Nuclear Science,* vol. 56, pp. 1743-1746, 2009.

[29] H.-Y. Shin and C.-Y. Sun, "Temperature-gradient-solution grown CdTe crystals for γ-ray detectors," *Journal of crystal growth,* vol. 186, pp. 67-78, 1998.

[30] H. Chen, S. A. Awadalla, J. Mackenzie, R. Redden, G. Bindley, A. E. Bolotnikov, G. S. Camarda, G. Carini and R. B. James, "Characterization of Traveling Heater Method (THM) Grown CdZnTe Crystals," *IEEE Transactions on Nuclear Science,* vol. 54, pp. 811-816, 2007.

[31] Z. Li, J. H. Peterson, A. Yeckel and J. J. Derby, "Analysis of the effects of a rotating magnetic field on the growth of cadmium zinc telluride by the traveling heater method under microgravity conditions," *Journal of Crystal Growth,* vol. 452, pp. 17-21, 2016.

[32] T. E. Schlesinger and R. B. James, "Semiconductors for Room Temperature Nuclear Applications, Vol. 43," 1995.

[33] A. Zappettini, M. Zha, M. Pavesi and L. Zanotti, "Boron oxide fully encapsulated CdZnTe crystals grown by the vertical Bridgman technique," *Journal of Crystal Growth,* vol. 307, pp. 283-288, 2007.

[34] Q. Zheng, F. Dierre, M. Ayoub, J. Crocco, H. Bensalah, V. Corregidor, E. Alves, R. Fernandez-Ruiz, J. M. Perez and E. Dieguez, "Comparison of radiation detector performance for different metal contacts on CdZnTe deposited by electroless deposition method," *Crystal Research and Technology,* vol. 46, pp. 1131-1136, 2011.

[35] W. Sang, J. Wei, Z. Qi, L. Wanwan, M. Jiahua, T. Jianyong and Q. Yongbiao, "Primary study on the contact degradation mechanism of CdZnTe detectors," *Nuclear Instruments and Methods in Physics Research Section A: Accelerators, Spectrometers, Detectors and Associated Equipment,* vol. 527, pp. 487-492, 2004.

[36] Y. Nemirovsky, A. Ruzin, G. Asa, Y. Gorelik and L. Li, "Study of contacts to CdZnTe radiation detectors," *Journal of Electronic Materials,* vol. 26, pp. 756-764, 1997.

[37] Q. Li, W. Jie, L. Fu, X. Wang and X. Zhang, "Metal--CdZnTe contact and its annealing behaviors," *Applied surface science,* vol. 253, pp. 1190-1193, 2006.

[38] Q. Zheng, F. Dierre, V. Corregidor, J. Crocco, H. Bensalah, J. L. Plaza, E. Alves and E. Dieguez, "Electroless deposition of Au, Pt, or Ru metallic layers on CdZnTe," *Thin Solid Films,* vol. 525, pp. 56-63, 2012.

[39] A. M. Mancini, A. Quirini, L. Vasanelli, E. Perillo, E. Rosato, G. Spadaccini and E. Barbarino, "Rutherford backscattering analysis of electroless gold contacts on cadmium telluride," *Journal of Applied Physics,* vol. 53, pp. 5785-5788, 1982.

[40] H. Chen, S. A. Awadalla, P. Marthandam, K. Iniewski, P. H. Lu, G. Bindley and others, *CZT device with improved sensitivity for medical imaging and homeland security applications,* vol. 7449, 2009, p. 744902.

[41] A. E. Bolotnikov, S. E. Boggs, C. M. H. Chen, W. R. Cook, F. A. Harrison and S. M. Schindler, "Properties of Pt Schottky type contacts on high-resistivity CdZnTe detectors," *Nuclear Instruments and Methods in Physics Research Section A: Accelerators, Spectrometers, Detectors and Associated Equipment,* vol. 482, pp. 395-407, 2002.

[42] C.-Y. Wu, "Interfacial layer-thermionic-diffusion theory for the Schottky barrier diode," *Journal of Applied Physics,* vol. 53, pp. 5947-5950, 1982.

[43] A. Rose, "Space-charge-limited currents in solids," *Physical Review,* vol. 97, p. 1538, 1955.

[44] W. Shockley, "Currents to conductors induced by a moving point charge," *Journal of applied physics,* vol. 9, pp. 635-636, 1938.

[45] S. Ramo, "Currents induced by electron motion," *Proceedings of the IRE,* vol. 27, pp. 584-585, 1939.

[46] P. D. Yoder, K. Gärtner and W. Fichtner, "A generalized Ramo--Shockley theorem for classical to quantum transport at arbitrary frequencies," *Journal of Applied Physics,* vol. 79, pp. 1951-1954, 1996.

[47] A. Castoldi, "Signal formation in radiation detectors: Ramoś theorem and its application to practical cases," 2011.

[48] M. Groza, H. Krawczynski, I. I. I. Alfred Garson, J. W. Martin, K. Lee, Q. Li, M. Beilicke, Y. Cui, V. Buliga, M. Guo and others, "Investigation of the internal electric field in cadmium zinc telluride detectors using the Pockels effect and the analysis of charge transients," *Journal of Applied Physics,* vol. 107, p. 023704, 2010.

[49] A. Milani, E. Bocchi, A. Zappettini, S. M. Pietralunga and M. Martinelli, "Characterization of electro-optic shielding effect in bulk CdTe: In crystals," *Journal of crystal growth,* vol. 214, pp. 913-917, 2000.

[50] A. Santi, G. Piacentini, M. Zanichelli, M. Bettelli, A. Zappettini and M. Pavesi, *Evaluation of electric field profile and transport parameters in solid-state CZT detectors,* 2015, pp. 1-3.

[51] M. Zanichelli, M. Pavesi, A. Zappettini, L. Marchini, N. Auricchio, E. Caroli and M. Manfredi, "Characterization of bulk and surface transport mechanisms by means of the photocurrent technique," *IEEE Transactions on Nuclear Science,* vol. 56, pp. 3591-3596, 2009.

[52] A. Santi, "Transport modeling and measurements in solid state photo-detectors," 2017.

[53] Z. He, "Review of the Shockley--Ramo theorem and its application in semiconductor gamma-ray detectors," *Nuclear Instruments and Methods in Physics Research Section A: Accelerators, Spectrometers, Detectors and Associated Equipment,* vol. 463, pp. 250-267, 2001.

[54] O. Frisch, "British atomic energy report," *BR-49,* vol. 65, 1944.

[55] A. E. Bolotnikov, N. M. Abdul-Jabbar, S. Babalola, G. S. Camarda, Y. Cui, A. Hossain, E. Jackson, H. Jackson, J. R. James, A. L. Luryi and others, "Optimization of virtual Frisch-grid CdZnTe detector designs for imaging and spectroscopy of gamma rays," *Invited Paper, in Proceedings of SPIE Hard X-Ray and Gamma-Ray Detector Physics IX,* vol. 6702, pp. 670603-1, 2007.

[56] A. E. Bolotnikov, G. S. Camarda, G. A. Carini, G. W. Wright, D. S. McGregor, W. McNeil and R. B. James, "New results from performance studies of Frisch-grid CdZnTe detectors," pp. 33-45, 2004.

[57] P. N. Luke, "Unipolar charge sensing with coplanar electrodes-application to semiconductor detectors," *IEEE Transactions on Nuclear Science,* vol. 42, pp. 207-213, 1995.

[58] P. N. Luke, "Single-polarity charge sensing in ionization detectors using coplanar electrodes," *Applied Physics Letters,* vol. 65, pp. 2884-2886, 1994.

[59] Z. He, "Potential distribution within semiconductor detectors using coplanar electrodes," *Nuclear Instruments and Methods in Physics Research Section A: Accelerators, Spectrometers, Detectors and Associated Equipment,* vol. 365, pp. 572-575, 1995.

[60] J. Ryan, J. R. Macri, M. L. McConnell, B. K. Dann, M. L. Cherry, T. Guzik, F. Doty, B. A. Apotovsky and J. F. Butler, "Large-area submillimeter resolution CdZnTe strip detector for astronomy," 1995.

[61] C. M. Stahle, A. M. Parsons, L. M. Bartlett, P. Kurczynski, J. F. Krizmanic, L. M. Barbier, S. D. Barthelmy, F. B. Birsa, N. A. Gehrels, J. L. Odom and others, "CdZnTe strip detector for arcsecond imaging and spectroscopy," in *SPIE's 1996 International Symposium on Optical Science, Engineering, and Instrumentation*, 1996.

[62] K. Zanio, "Use of various device geometries to improve the performance of CdTe detectors," *Revue de Physique Appliqueé,* vol. 12, pp. 343-347, 1977.

[63] T. H. Prettyman, "Theoretical framework for mapping pulse shapes in semiconductor radiation detectors," *Nuclear Instruments and Methods in Physics Research Section A: Accelerators, Spectrometers, Detectors and Associated Equipment,* vol. 428, pp. 72-80, 1999.

[64] F. P. Doty, H. B. Barber, F. L. Augustine, J. F. Butler, B. A. Apotovsky, E. T. Young and W. Hamilton, "Pixellated CdZnTe detector arrays," *Nuclear Instruments and Methods in Physics Research Section A: Accelerators, Spectrometers, Detectors and Associated Equipment,* vol. 353, pp. 356-360, 1994.

[65] H. B. Barber, D. G. Marks, B. A. Apotovsky, F. L. Augustine, H. H. Barrett, J. F. Butler, E. L. Dereniak, F. P. Doty, J. D. Eskin, W. J. Hamilton and others, "Progress in developing focal-plane-multiplexer readout for large CdZnTe arrays for nuclear medicine applications," *Nuclear Instruments and Methods in Physics Research Section A: Accelerators, Spectrometers, Detectors and Associated Equipment,* vol. 380, pp. 262-265, 1996.

[66] H. H. Barrett, J. D. Eskin and H. B. Barber, "Charge transport in arrays of semiconductor gamma-ray detectors," *Physical Review Letters,* vol. 75, p. 156, 1995.

[67] J. C. Kim, S. E. Anderson, W. Kaye, F. Zhang, Y. Zhu, S. J. Kaye and Z. He, "Charge sharing in common-grid pixelated CdZnTe detectors," *Nuclear Instruments and Methods in Physics Research Section A: Accelerators, Spectrometers, Detectors and Associated Equipment,* vol. 654, pp. 233-243, 2011.

[68] J. S. Iwanczyk, E. Nygard, O. Meirav, J. Arenson, W. C. Barber, N. E. Hartsough, N. Malakhov and J. C. Wessel, "Photon counting energy dispersive detector arrays for x-ray imaging," *IEEE transactions on nuclear science,* vol. 56, pp. 535-542, 2009.

[69] A. Brambilla, P. Ouvrier-Buffet, G. Gonon, J. Rinkel, V. Moulin, C. Boudou and L. Verger, "Fast CdTe and CdZnTe semiconductor detector arrays for spectroscopic X-ray imaging," *IEEE Transactions on Nuclear Science,* vol. 60, pp. 408-415, 2013.

[70] L. Abbene, G. Gerardi, G. Raso, F. Principato, N. Zambelli, G. Benassi, M. Bettelli and A. Zappettini, "Development of new CdZnTe detectors for room-temperature high-flux radiation measurements," *Journal of Synchrotron Radiation,* vol. 24, pp. 429-438, 2017.

[71] Cremat, "Why use charge sensitive preamplifiers?," [Online]. Available: http://www.cremat.com/why-use-csps/.

[72] fast comtec, "CR-200 Gaussian shaping amplifier," [Online]. Available: https://www.fastcomtec.com/products/preamps-hybrids-and-special-products/cr-200-shaping-amplifier/.

[73] L. Abbene, G. Gerardi, G. Raso, S. Basile, M. Brai and F. Principato, "Energy resolution and throughput of a new real time digital pulse processing system for x-ray and gamma ray semiconductor detectors," *Journal of Instrumentation,* vol. 8, p. P07019, 2013.

[74] L. Abbene, G. Gerardi, A. A. Turturici, G. Raso, G. Benassi, M. Bettelli, N. Zambelli, A. Zappettini and F. Principato, "X-ray response of CdZnTe detectors grown by the vertical Bridgman technique: Energy, temperature and high flux effects," *Nuclear Instruments and Methods in Physics Research Section A: Accelerators, Spectrometers, Detectors and Associated Equipment,* vol. 835, pp. 1-12, 2016.

[75] L. Abbene and G. Gerardi, "High-rate dead-time corrections in a general purpose digital pulse processing system," *Journal of synchrotron radiation,* vol. 22, pp. 1190-1201, 2015.

[76] F. Y. Daniel and J. A. Fessler, "Mean and variance of single photon counting with deadtime," *Physics in medicine and biology,* vol. 45, p. 2043, 2000.

[77] Y. Eisen, I. Mardor, A. Shor, Z. Baum, D. Bar, G. Feldman, H. Cohen, E. Issac, R. Haham-Zada, S. Blitz and others, "NUCAM3-a gamma camera based on segmented monolithic CdZnTe detectors," *IEEE Transactions on Nuclear Science,* vol. 49, pp. 1728-1732, 2002.

[78] M. C. Veale, S. J. Bell, D. D. Duarte, A. Schneider, P. Seller, M. D. Wilson and K. Iniewski, "Measurements of charge sharing in small pixel CdTe detectors," *Nuclear Instruments and Methods in Physics Research Section A: Accelerators, Spectrometers, Detectors and Associated Equipment,* vol. 767, pp. 218-226, 2014.

[79] D. D. Duarte, "Charge share corrections and low energy noise performance in a small pixel CdTe detector," 2012.

[80] W. K. Warburton, "An approach to sub-pixel spatial resolution in room temperature X-ray detector arrays with good energy resolution," *MRS Online Proceedings Library Archive,* vol. 487, 1997.

[81] M. Burks, E. Jordan, E. Hull, L. Mihailescu and K. Vetter, "Signal interpolation in germanium detectors for improved 3-D position resolution," vol. 2, pp. 1114-1118, 2004.

[82] D. G. Marks, H. B. Barber, H. H. Barrett, J. Tueller and J. M. Woolfenden, "Improving performance of a CdZnTe imaging array by mapping the detector with gamma rays," *Nuclear Instruments and Methods in Physics Research Section A: Accelerators, Spectrometers, Detectors and Associated Equipment,* vol. 428, pp. 102-112, 1999.

[83] J. S. Vickers and S. Chakrabarti, "Silicon-anode detector with integrated electronics for microchannel-plate imaging detectors," *Review of scientific instruments,* vol. 70, pp. 2912-2916, 1999.

[84] J. Jakubek and J. Uher, "Fast neutron detector based on TimePix pixel device with micrometer spatial resolution," in *Nuclear Science Symposium Conference Record (NSS/MIC), 2009 IEEE*, 2009.

[85] T. Narita, J. E. Grindlay, J. Hong and F. C. Niestemski, "Anode readout for pixellated CZT detectors," in *Optical Science and Technology, SPIE's 48th Annual Meeting*, 2004.

[86] Y. Zhu, S. E. Anderson and Z. He, "Sub-pixel position sensing for pixelated, 3-d position sensitive, wide band-gap, semiconductor, gamma-ray detectors," *IEEE Transactions on Nuclear Science,* vol. 58, pp. 1400-1409, 2011.

[87] M. J. Bosma, M. Can and J. Visser, *Development of edgeless high-Z sensors for endless medical detectors.*

[88] P. Seller, S. Bell, R. J. Cernik, C. Christodoulou, C. K. Egan, J. A. Gaskin, S. Jacques, S. Pani, B. D. Ramsey, C. Reid and others, "Pixellated Cd (Zn) Te high-energy X-ray instrument," *Journal of Instrumentation,* vol. 6, p. C12009, 2011.

[89] G. D. Geronimo, W. Chen, J. Fried, Z. Li, D. A. Pinelli, P. Rehak, E. Vernon, J. A. Gaskin, B. D. Ramsey and G. Anelli, "Front-end ASIC for high resolution X-ray spectrometers," in *Nuclear Science Symposium Conference Record, 2007. NSS07. IEEE*, 2007.

[90] M. C. Veale, S. J. Bell, L. L. Jones, P. Seller, M. D. Wilson, C. Allwork, D. Kitou, P. J. Sellin, P. Veeramani and R. C. Cernik, "An ASIC for the study of charge sharing effects in small pixel CdZnTe X-ray detectors," *IEEE Transactions on Nuclear Science,* vol. 58, pp. 2357-2362, 2011.

[91] M. D. Wilson, R. Cernik, H. Chen, C. Hansson, K. Iniewski, L. L. Jones, P. Seller and M. C. Veale, "Small pixel CZT detector for hard X-ray spectroscopy," *Nuclear Instruments and Methods in Physics Research Section A: Accelerators, Spectrometers, Detectors and Associated Equipment,* vol. 652, pp. 158-161, 2011.

[92] F. Principato, G. Gerardi, A. A. Turturici and L. Abbene, "Time-dependent current-voltage characteristics of Al/p-CdTe/Pt x-ray detectors," *Journal of Applied Physics,* vol. 112, p. 094506, 2012.

[93] A. A. Turturici, L. Abbene, G. Gerardi and F. Principato, "Electrical characterization of CdTe pixel detectors with Al Schottky anode," *Nuclear Instruments and Methods in Physics Research Section A: Accelerators, Spectrometers, Detectors and Associated Equipment,* vol. 763, pp. 476-482, 2014.

[94] G. C. Shwartz, Handbook of semiconductor interconnection technology, CRC Press, 2006.

[95] A. IPC-TM-650 TEST METHODS MANUAL.

[96] A. Cola, I. Farella, A. M. Mancini and A. Donati, "Electric field properties of CdTe nuclear detectors," *IEEE Transactions on Nuclear Science,* vol. 54, pp. 868-872, 2007.

[97] P. J. Sellin, G. Prekas, J. Franc and R. Grill, "Electric field distributions in CdZnTe due to reduced temperature and x-ray irradiation," *Applied Physics Letters,* vol. 96, p. 133509, 2010.

[98] K. Hecht, "Zum Mechanismus des lichtelektrischen Primärstromes in isolierenden Kristallen," *Zeitschrift fur Physik A Hadrons and Nuclei,* vol. 77, pp. 235-245, 1932.

[99] J. Franc, P. Hoschl, E. Belas, R. Grill, P. Hlidek, P. Moravec and J. Bok, "CdTe and CdZnTe crystals for room temperature gamma-ray detectors," *Nuclear Instruments and Methods*

in Physics Research Section A: Accelerators, Spectrometers, Detectors and Associated Equipment, vol. 434, pp. 146-151, 1999.

[100] A. Santi, M. Zanichelli, G. Piacentini, M. Pavesi, A. Cola and I. Farella, "An original method to evaluate the transport parameters and reconstruct the electric field in solid-state photodetectors," *Applied Physics Letters,* vol. 104, p. 193503, 2014.

[101] M. Pavesi, A. Santi, M. Bettelli, A. Zappettini and M. Zanichelli, "Electric field reconstruction and transport parameter evaluation in CZT X-ray detectors," *IEEE Transactions on Nuclear Science,* 2017.

[102] A. Zappettini, A. Santi, M. Bettelli, G. Piacentini, M. Zanichelli and M. Pavesi, "Laser Induced Transient Current Technique as a Powerful Tool to Determine Charge Transport Properties, Electric Field and Weighing Field Distribution in CdZnTe Detectors," 2016.

[103] W. Xiaoqin, J. Wanqi, L. Qiang and G. Zhi, "Surface passivation of CdZnTe wafers," *Materials science in semiconductor processing,* vol. 8, pp. 615-621, 2005.

[104] H. Bensalah, J. L. Plaza, J. Crocco, Q. Zheng, V. Carcelen, A. Bensouici and E. Dieguez, "The effect of etching time on the CdZnTe surface," *Applied Surface Science,* vol. 257, pp. 4633-4636, 2011.

[105] V. G. Ivanits'Ka, P. Moravec, J. Franc, Z. F. Tomashik, P. I. Feychuk, V. M. Tomashik, L. P. Shcherbak, K. Mašek and P. Höschl, "Chemical etching of CdTe in aqueous solutions of H2O2-HI-citric acid," *Journal of Electronic Materials,* vol. 36, pp. 1021-1024, 2007.

[106] S. Wenbin, W. Kunshu, M. Jiahua, T. Jianyong, Z. Qi and Q. Yongbiao, "A novel two-step chemical passivation process for CdZnTe detectors," *Semiconductor science and technology,* vol. 20, p. 343, 2005.

[107] M. J. Mescher, T. E. Schlesinger, J. E. Toney, B. A. Brunett and R. B. James, "Development of dry processing techniques for CdZnTe surface passivation," *Journal of electronic materials,* vol. 28, pp. 700-704, 1999.

[108] A. Etcheberry, F. Iranzo-Marin, E. Novakovic, R. Triboulet and C. Debiemme-Chouvy, "Contribution to the understanding of the CdTe and Cd1- yZnyTe surface chemistry," *Journal of crystal growth,* vol. 184, pp. 213-217, 1998.

[109] A. Małecki and A. Micek-Ilnicka, "Electroless nickel plating from acid bath," *Surface and Coatings Technology,* vol. 123, pp. 72-77, 2000.

[110] M. C. Chase, E. Grace and A. R. Brenner, "NICKEL PLATING CHEMICAL REDUCTION," *UNITED STATE PATENT OFFICE,* pp. 2,532,233, 1947.

[111] A. Brenner and others, *Electroless deposition of nickel,* Google Patents, 1960.

[112] M. V. Sullivan and J. H. Eigler, "Electroless nickel plating for making ohmic contacts to silicon," *Journal of the electrochemical Society,* vol. 104, pp. 226-230, 1957.

[113] G. Benassi, L. Nasi, M. Bettelli, N. Zambelli, D. Calestani and A. Zappettini, "Strong mechanical adhesion of gold electroless contacts on CdZnTe deposited by alcoholic solutions," *Journal of Instrumentation,* vol. 12, p. P02018, 2017.

[114] A. A. Turturici, L. Abbene, G. Gerardi, G. Benassi, M. Bettelli, D. Calestani, N. Zambelli, G. Raso, A. Zappettini and F. Principato, "Electrical properties of Au/CdZnTe/Au detectors

grown by the boron oxide encapsulated Vertical Bridgman technique," *Nuclear Instruments and Methods in Physics Research Section A: Accelerators, Spectrometers, Detectors and Associated Equipment,* vol. 830, pp. 243-250, 2016.

[115] M. Bettelli, G. Benassi, L. Nasi, N. Zambelli, A. Zappettini, E. Gombia, L. Abbene, F. Principato and D. Calestani, "Mechanically stable metal layers for ohmic and blocking contacts on CdZnTe detectors by electroless deposition," in *Nuclear Science Symposium and Medical Imaging Conference (NSS/MIC), 2015 IEEE*, 2015.

[116] A. Santi, M. Bettelli, A. Zappettini and M. Pavesi, *Carrier diffusion coefficient in compensated tellurides for high energy detection,* 2017.

[117] L. Abbene, F. Principato, G. Gerardi, M. Bettelli, P. Seller, M. C Veale, N. Zambelli, G. Benassi and A. Zappettini, *Digital fast pulse shape and height analysis on CZT arrays for high flux energy-resolved X-ray imaging,* 2017.

[118] J. Aleotti, G. Micconi, S. Caselli, G. Benassi, N. Zambelli, D. Calestani, M. Zanichelli, M. Bettelli and A. Zappettini, "Unmanned aerial vehicle equipped with spectroscopic CdZnTe detector for detection and identification of radiological and nuclear material," in *Nuclear Science Symposium and Medical Imaging Conference (NSS/MIC), 2015 IEEE*, 2015.

[119] J. Aleotti, G. Micconi, S. Caselli, G. Benassi, N. Zambelli, M. Bettelli and A. Zappettini, "Detection of Nuclear Sources by UAV Teleoperation Using a Visuo-Haptic Augmented Reality Interface," *Sensors,* vol. 17, p. 2234, 2017.

[120] E. J. Morton, M. A. Hossain, P. De Antonis and A. M. D. Ede, "Investigation of Au--CdZnTe contacts using photovoltaic measurement," *Nuclear Instruments and Methods in Physics Research Section A: Accelerators, Spectrometers, Detectors and Associated Equipment,* vol. 458, pp. 558-562, 2001.

[121] Z. Deng, Y. Li, Y. Liu, W. Zhu and L. Zhang, "low noise charge sensitive preamplifier A250 for CZT detector readout," *Nuclear Electronics and Detection Technology,* vol. 27, pp. 1103-1105, 2007.

[122] D. S. Bale and C. Szeles, "Nature of polarization in wide-bandgap semiconductor detectors under high-flux irradiation: Application to semi-insulating Cd 1- x Zn x Te," *Physical Review B,* vol. 77, p. 035205, 2008.

[123] C. Szeles, S. A. Soldner, S. Vydrin, J. Graves and D. S. Bale, "CdZnTe semiconductor detectors for spectroscopic x-ray imaging," *IEEE Transactions on Nuclear Science,* vol. 55, pp. 572-582, 2008.

[124] K. Taguchi and J. S. Iwanczyk, "Vision 20/20: Single photon counting x-ray detectors in medical imaging," *Medical physics,* vol. 40, 2013.

[125] L. Marchini, A. Zappettini, E. Gombia, R. Mosca, M. Lanata and M. Pavesi, "Study of surface treatment effects on the metal-CdZnTe interface," *IEEE Transactions on Nuclear Science,* vol. 56, pp. 1823-1826, 2009.

[126] S. E. Anderson, B. Donmez and Z. He, "Sub-pixel position resolution in pixelated semiconductor detectors," vol. 2, pp. 1569-1576, 2007.

[127] G. Montemont, S. Lux, O. Monnet, S. Stanchina and L. Verger, "Studying Spatial Resolution of CZT Detectors Using Sub-Pixel Positioning for SPECT," *IEEE Transactions on Nuclear Science,* vol. 61, pp. 2559-2566, 2014.

[128] D. Meier, C. Gheorghe, T. M. Johansen, S. Mikkelsen and G. Maehlum, "Interpolation in a pixellated CZT γ-radiation detector," in *Nuclear Science Symposium and Medical Imaging Conference (NSS/MIC), 2011 IEEE*, 2011.

[129] K. Boudergui, F. Carrel, T. Domenech, N. Guenard, J.-P. Poli, A. Ravet, V. Schoepff and R. Woo, "Development of a drone equipped with optimized sensors for nuclear and radiological risk characterization," in *Advancements in Nuclear Instrumentation Measurement Methods and their Applications (ANIMMA), 2011 2nd International Conference on*, 2011.

[130] R. A. Cortez, X. Papageorgiou, H. G. Tanner, A. V. Klimenko, K. N. Borozdin, R. Lumia and W. C. Priedhorsky, "Smart radiation sensor management," *IEEE Robotics |& Automation Magazine,* vol. 15, 2008.

[131] J. Han, Y. Xu, L. Di and Y. Chen, "Low-cost multi-UAV technologies for contour mapping of nuclear radiation field," *Journal of Intelligent |& Robotic Systems,* pp. 1-10, 2013.

[132] K. Kurvinen, P. Smolander, R. Pollanen, S. Kuukankorpi, M. Kettunen and J. Lyytinen, "Design of a radiation surveillance unit for an unmanned aerial vehicle," *Journal ot environmental radioactivity,* vol. 81, pp. 1-10, 2005.

[133] R. Pollanen, H. Toivonen, K. Perajarvi, T. Karhunen, T. Ilander, J. Lehtinen, K. Rintala, T. Katajainen, J. Niemela and M. Juusela, "Radiation surveillance using an unmanned aerial vehicle," *Applied radiation and isotopes,* vol. 67, pp. 340-344, 2009.

[134] S. A. Awadalla, M. Al-Grafi and K. Iniewski, "High voltage optimization in CdZnTe detectors," *Nuclear Instruments and Methods in Physics Research Section A: Accelerators, Spectrometers, Detectors and Associated Equipment,* vol. 764, pp. 193-197, 2014.

[135] P. J. Sellin, A. W. Davies, A. Lohstroh, M. E. Ozsan and J. Parkin, "Drift mobility and mobility-lifetime products in CdTe: Cl grown by the travelling heater method," *IEEE transactions on nuclear science,* vol. 52, pp. 3074-3078, 2005.